Prediction of process induced shape distortions and residual stresses in large fibre reinforced composite laminates

With application to Wind Turbine Blades

Nielsen, Michael Wenani; Løgstrup Andersen, Tom; Nielsen, Per Hørlyk; Branner, Kim; Hattel, Jesper Henri

Publication date:
2013

Document Version
Publisher's PDF, also known as Version of record

Prediction of process induced shape distortions and residual stresses in large fibre reinforced composite laminates

- With application to Wind Turbine Blades

Ph.D. Dissertation

by

Michael Wenani Nielsen

Supervisor: Prof. Jesper H. Hattel

Department of Mechanical Engineering

Technical University of Denmark, DTU

2012

Department of Mechanical Engineering
Technical University of Denmark

Preface

The work underlying this thesis har been carried out from December 2009 to November 2012 in the Process Modelling Group at the Department of Mechanical Engineering (MEK) at the Technical University of Denmark (DTU). The work was supervised by Professor Jesper H. Hattel (MEK/DTU) to whom I am most indebted for his engagement, inspiration, immense competences and guidance, and for providing good research conditions and facilities for our research group. The work is also co-supervised by Senior Development Engineer Tom Løgstrup Andersen, Senior Scientist Kim Branner, and Senior Development Engineer Per Hørlyk Nielsen, all from the Department of Wind Energy (WIND/DTU).

Acknowledgements are directed towards colleagues and friends in the Process Modelling Group for their support during the thesis period and many research and non-research related discussions. Furthermore, special gratitude is given to Dr. Jacob W. Schmidt for our joint work on use of embedded fiber optic sensors for strain monitoring and his indispensable contribution, dedication and energy during our fruitful collaboration. I would like to thank the research technicians at the Fiberlab at Risø Campus DTU Jacob Christensen, Christian H. Madsen and Jonas K. Heininge, as well as Development Engineer Christen M. Markussen for their support and invaluable suggestions during all the experimental studies conducted in this work. I would furthermore like to thank LM Wind Power A/S for their collaboration on the wind turbine blade root section case study, in particular Dr. Torben K. Jacobsen, Madhava Khoteshwara and Jesper Garm.

Finally, I want to thank my friends, family and most importantly my financé Lene for their support and motivation throughout the period.

The present work has been funded by the Danish Energy Agency through the Energy Technology Development and Demonstration Program (EUDP). The supported EUDP-project is titled "Demonstration of new blade design using manufacturing process simulations", journal no. 64009-0094. The support is gratefully acknowledged.

Abstract

The present thesis is devoted to numerical modelling of thermomechanical phenomena occurring during curing in the manufacture of large fibre reinforced polymer matrix composites with thick laminate sections using vacuum assisted resin transfer moulding (VARTM[1]). The main application of interest in this work is modelling manufacturing induced shape distortions and residual stresses in commercial wind turbine composite blades. Key mechanisms known to contribute to shape distortions and residual stress build-up are reviewed and the underlying theories used to model these mechanisms are presented. The main mechanisms of thermal-, chemical- and mechanical origin are; (i) the thermal expansion mismatch of the constitutive composite materials, layer and tooling, (ii) chemical cure shrinkage of the composite matrix material and (iii) the tooling (i.e. the mould, inserts etc.) influence on the composite part.

In the modelling approach taken in the current study, 1D and 3D thermomechanical models are utilized. A 1D thermomechanical model in a finite difference (FD) framework, capable of predicting heat transfer, internal heat generation, cure degree development, as well as process induced in-plane strains and residual stresses is initially presented. This 1D model is the framework for the first attempt at a void growth model, capable of predicting the laminate through-thickness discretized void size distribution, as a function of processing parameters.

Using a 3D thermomechanical finite element (FE) model in ABAQUS, different constitutive modelling approaches are investigated, including a cure hardening instantaneous linear elastic (CHILE) approach, a viscoelastic approach and a path-dependent approach. The latter is a limiting case of viscoelasticity. These approaches are investigated with regards to their accuracy in predicting process induced strain and stress development in thick section laminates during curing, and more precisely regarding the evolution of the composite thermoset polymer matrix mechanical behaviour during the phase transitions experienced during curing. The different constitutive approaches are utilized in various case studies and compared, where possible, to experimental results from measured *in situ* internal total strains in laminates using embedded fibre Bragg grating (FBG) sensors. Due to reasonable model accuracy, ease of implementation and use of relatively simply obtained material characterization data, the CHILE and path-dependent approaches are found to be most favorable. It is shown that use of the viscoelastic approach to accurately predict process induced strains and stresses in modelling manufacturing cases where mild tooling constraints on the composite part exist, is not viable. In a final case study, process

[1] Also known as Vacuum Infusion or Vacuum Infusion Resin Transfer Moulding

induced shape distortions in a commercial wind turbine blade root subsection, courtesy of LM Wind Power A/S, are analyzed using the CHILE constitutive approach. It is shown how large non-uniform through-thickness part thermal- and corresponding cure gradients are the main driving factors for process induced shape distortions.

Resumé

Nærværende afhandling omhandler numerisk modellering af termomekaniske forhold under hærdning af store fiberforstærkede polymer kompositter med tykke laminater i vakuuminfusionsprocessen (VARTM). Fokus er på modellering af fremstillingsinducerede tøjninger og residualspændinger i kommercielle vindmøllevinger. Indledningsvis præsenteres de underliggende mekanismer for disse tøjninger og spændinger samt de teorier, der anvendes til at modellere dem. Mekanismerne er af termisk, kemisk samt mekanisk oprindelse og kan primært tilskrives: (i) forskellen i den termiske udvidelseskoefficient mellem fiberforstærkningsmaterialet, resinen samt værktøjsmaterialet, (ii) det kemisk inducerede volumetriske svind under resinens hærdning og (iii) værktøjsindflydelsen, fx fra kontakt mellem formværktøjet og emnet. Herefter præsenteres de udviklede 1D og 3D termomekaniske modeller. Den 1D termomekaniske model er baseret på en finite difference (FD) formulering og bruges her til at forudsige effekten af den latente varme, der frigives under hærdningsprocessen, herunder hærdningsgradens udvikling samt udviklingen af proces-inducerede tøjninger og spændinger i de betragtede laminatkompositter. 1D modellen anvendes ydermere som basis for en porøsitetsmodel, der kan modellere luftboblers udvikling og størrelse i gennem laminattykkelsen som funktion af procesparametrene. Den termomekaniske model i 3D er baseret på finite element (FE) metoden i det kommercielle program ABAQUS og anvendes til at implementere og undersøge forskellige konstitutive modeller, bl.a. en hærdningsaf-hængig lineærelastisk model, en fuld viskoelastisk model og en simpel historieafhængig model. Sidstnævnte er en forsimpling af viskoelasticitet. Det undersøges, hvor præcise disse konstitutive modeller er til at simulere udviklingen af procesinducerede tøjninger og spændinger i tykke laminater, herunder specielt hvor nøjagtigt de kan modellere den termohærdende resins faseovergang kendetegnet ved det tilhørende hærdningsforløb. Efter dette præsenteres en eksperimentel undersøgelse, hvor de tre forskellige konstitutive modeller anvendes til at forudsige procesinducerede tøjninger i en laminatplade, som sammenholdes med tilsvarende eksperimentelle tøjninger målt ved hjælp af indstøbte optiske fibre med FBG sensorer. Det ses, at den hærdningsafhængige lineærelastiske model samt den historieafhængige model er bedst egnede til modellering af den betragtede hærdningsproces. Det vises ydermere, at i de fremstillingstilfælde, hvor værktøjets indflydelse på kompositemnet ikke er signifikant, er der ingen tegn på viskoelastisk materialeopførsel, hvorfor det ikke er nødvendigt at bruge en fuld viskoelastisk beskrivelse i sådanne tilfælde. I en afsluttende undersøgelse analyseres udviklingen af procesinducerede tøjninger og restspændinger i en kommerciel vindmøllevinges rodsektion fra LM Wind Power A/S. Det vises, at store termiske gradienter og tilsvarende store hærdningsgradienter igennem

emnets tykkelse er hovedårsagerne til de anselige forskydninger og ændringer i emnets geometri, der udvikles under hærdningsforløbet.

List of abbreviations

CHILE	Cure Hardening Instanteneous Linear Elastic (constitutive model)
CLT	Classical Laminate Theory
CTE	Coefficient of Thermal Expansion
CV	Control Volume
DSC	Differential Scanning Calorimetry
DTG	Draw Tower Grating
FEM	Finite Element Method
FBG	Fibre Bragg Grating
FRP	Fibre Reinforced Polymer
FVM	Finite Volume Method
GFRP	Glass Fiber Reinforced Polymer
PD	Path-dependent (constitutive model)
RTM	Resin Transfer Moulding
SCFM	Self-Consistent Field Micromechanics
VARTM	Vacuum Assisted Resin Transfer Moulding
UD	Uni-directional
VE	Viscoelastic (constitutive model)
WLF	Williams Landel Ferry (equation)

List of symbols

Roman symbols

a_T,$a_{T,\alpha}$	Temperature shift function, temperature and cure dependent shift function
A	Pre-exponential factor (cure kinetics model)
C	Diffusion constant
C_p	Heat capacity
C_{ijkl}	Stiffness tensor
E	Youngs modulus
E_m^o	Unrelaxed matrix material modulus
E_m^∞	Fully relaxed matrix material modulus
E_a	Apparent activation energy of the cure reaction
H_T	Total heat of reaction or reaction enthalpy
H_R	Residual heat of reaction
H^{Cond}	Conductivity weighting function
H^{Cap}	Capacity weighting function
G	Shear modulus
k	Thermal conductivity
K	Arrhenius expression parameter
K_ε,K_T	Strain- and temperature sensitivity factors
M, N	Laminate bending moment and normal load
$\dot{q}$,$\dot{Q}'''$	Heat conduction equation source terms
R	Universal gas constant
R^{Cond}	Heat flow conductive resistance
S_{ijkl}	Compliance tensor
S_{ijkl_m}	Internal state variable (viscoelastic model)
Tr	Transformation matrix
T	Temperature
$\bar{T}$	Known (prescribed) temperature
T_{cure}	Cure temperature
T_g	Glass transition temperature
T_{go}	T_g of polymer monomer
$T_{g\infty}$	T_g of fully cured polymer
V_f	Fiber volume fraction
V_{Sh}^T	Resin total volumetric shrinkage
u, v, w	Spatial coordinate velocity terms
x, y, z	Spatial coordinate direction annotations

Greek symbols

α	Degree of cure
α_{gel}	Degree of cure at gelation
α_{ref}	Reference degree of cure
α^{cte}	Coefficient of thermal expansion
β_{ij}	Internal stave variable tensor
ε_{ij}	Strain tensor
$\dot{\varepsilon}$	Strain rate
ε^{ch}	Chemical Strain
ε^{mech}	Mechanical or elastic Strain
ε^{Pr}	Process Strain
ε^{th}	Thermal Strain
ε^{Tot}	Total Strain
ε^{o}	Laminate mid-layer global strain
η	Viscosity
γ_{lv}	Void bubble surface tension
λ	Material constant in DiBenedetto equation
λ_B	Bragg wavelength
κ	Laminate mid-layer curvature
ν	Poissons ratio
σ_{ij}	Stress tensor
σ_{ij}^{R}	Stress residual tensor
θ	Spring-in angle or fibre orientation angle
ρ	Density
τ	Relation time
ξ	Reduced time
Π, Θ, Φ	Spherical coordinate system body force components

Contents

Appended publications

Paper I

M.W. Nielsen, J.H. Hattel, T.L. Andersen, K. Branner, P.H. Nielsen,
A 1D coupled curing and visco-mechanical void growth model of thick thermosetting composite laminates, Proc.: 18^{th} International Conference of Composite Materials (ICCM), Korea, 2011.

Paper II

M.W. Nielsen, J.H. Hattel, T.L. Andersen, K. Branner, P.H. Nielsen,
Experimental Determination and Numerical Modelling of Process Induced Strains and Residual Stresses in Thick Glass/Epoxy Laminate, Proc.: 15^{th} European Conference of Composite Materials (ECCM), Italy, 2012.

Paper III

M.W. Nielsen, J.W. Schmidt, J.H. Hattel, T.L. Andersen, C.M. Markussen,
In situ Measurement Using FBGs of Process-Induced Strains During Curing of Thick Glass/Epoxy Laminate Plate: Experimental Results and Numerical Modelling, Wind Energy, DOI: 10.1002/we.1550, 2012. In Press.

Paper IV

M. W. Nielsen, J. W. Schmidt, J. H. Høgh, J. P. Waldbjørn, J. H. Hattel, T. L. Andersen, C. M. Markussen,
Life cycle strain monitoring from manufacturing to failure in GFRP laminates using embedded FBG sensors, Journal of Composite Materials, DOI: 10.1177/0021998312472221, 2012. In Press.

Other appended works

Technical Report I

M.W. Nielsen, *Implementation of Temperature- and Cure Dependent Viscoelastic Curing Model*, Technical University of Denmark, 2011.

Non-appended works

M.W. Nielsen, J.W. Schmidt, J.H. Hattel
Prediction of internal strains during curing, post-curing and demoulding of thick glass/epoxy composite - Analysis of different constitutive models, Proc.: 6^{th} International Conference on Advanced Computational Engineering and Experimenting (ACE-X), Istanbul, Turkey, 2012.

J.P. Waldbjørn, J.H. Høgh, J.W. Schmidt, C. Berggreen, H. Stang, M. W. Nielsen
Strain and Deformation Control by Fibre Bragg Grating and Digital Image Correlation, Strain, Submitted in December 2012 - Under Review.

I. Baran, C. Tutum, J.H. Hattel, M.W. Nielsen,
Process induced residual stresses and distortions in pultrusion, Composite Part B: Engineering, Submitted November, 2012 - Under Review.

M. W. Nielsen, *Technical Report: In Situ Strain Monitoring in Composites using embedded FBG sensors*, Technical University of Denmark, 2011.

M. W. Nielsen, *Confidential Technical Report: Prediction of process induced shape distortions and residual stresses in LM 48.8P3 blade root section*, Technical University of Denmark, 2012.

Chapter 1

Introduction

A general introduction to the current thesis is presented in this chapter. The process generally utilized for the manufacture of large fibre reinforced polymer (FRP) composite structures is presented followed by the current challenges faced during the manufacture of large commercial wind turbine blades. Following this, the motivation for the current study is presented as well as the project objectives and thesis outline.

1.1 Manufacture of large FRP composite structures

FRP matrix composite materials have found widespread use in the manufacture of large energy critical structural applications where low weight and high stiffness and strength play an important role in material selection. In the wind energy industry, use of FRP composites (from here on "composites") in large commercial wind turbine blades has surpassed all other materials, as a majority of wind turbine blade manufacturers currently use composites for both the load-carrying and airfoil sections of the blades [12, 40, 90]. Composite structures offer a low weight-to-stiffness ratio and user-defined high durability and strength. Application-defined properties are also more readily obtained, compared to when using metals and alloys, by tailoring the composite lay-up fiber directions, thicknesses and fiber/matrix combinations according to the mechanical, thermal, electrical or aesthetic requirements. However, in commercial applications, these advantages are often shunned by their base costs, since the manufacture of large composite structures is heavily labour-intensive [69, 109].

During the manufacture of composites in general, the reinforcement fiber material is moulded into a desired shape by impregnation of the fibers with a liquid polymer called the matrix material. The matrix is typically an adhesive polymer such as a thermosetting epoxy or polyester resin. During the moulding process, liquid polymer is applied to the fibre and allowed to solidify until a structural solid combination of these materials is gained resembling the mould geometry. This solidification process is termed *curing*. Many different variations of this basic process exist, for instance Compression Moulding, Pultrusion, Filament Winding, Resin Transfer Moulding (RTM), Vacuum Assisted Resin Transfer Moulding (VARTM), Structural Reaction Injection Moulding (SRIM), to name

a few [69]. Focus is subsequently directed towards the manufacture of large composite structures using VARTM.

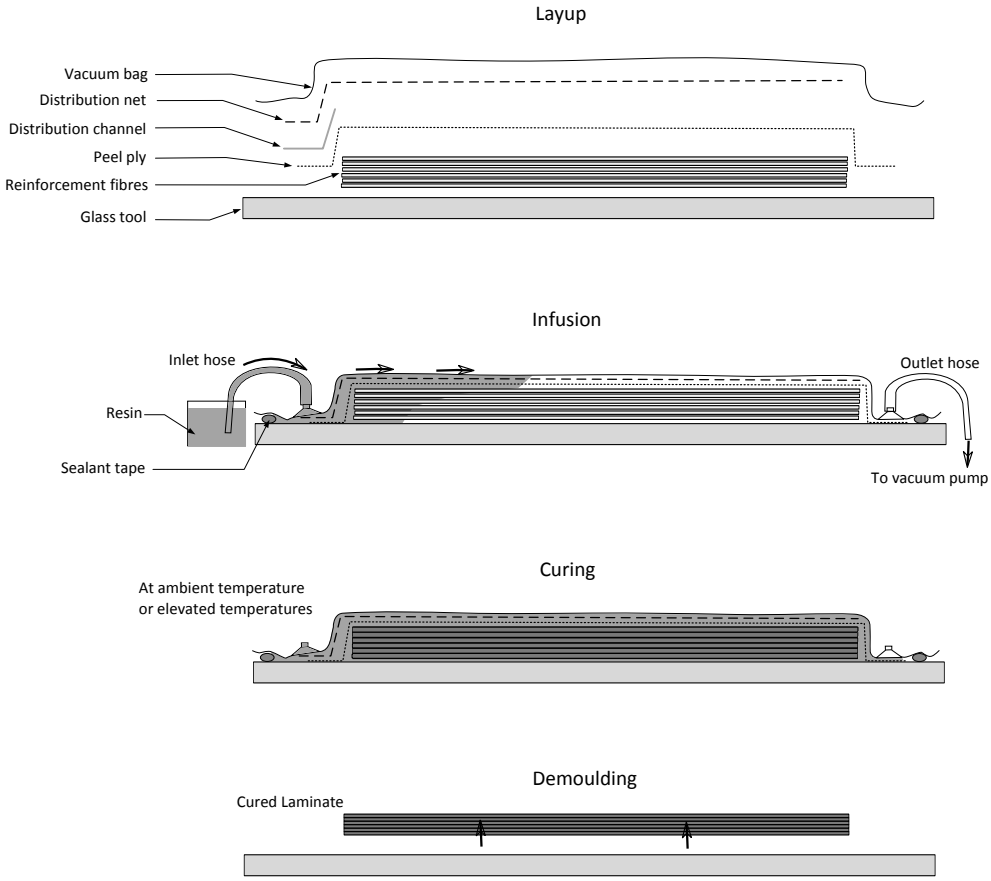

Figure 1.1: *Schematic of the VARTM process comprising of layup, infusion, curing and demoulding stages*

The VARTM resin infusion process has been developed as an efficient low-cost method for the manufacture of large composite structures and offers a cheaper alternative to conventional RTM, as the use of costly metal moulds is avoided. Instead, in VARTM a single sided hard mould is used and the upper half of the conventional RTM mould is replaced by an airtight vacuum bag, see Fig. 1.1, why the process is also simply termed “vacuum infusion”. In the manufacture of large structures, the single hard mould is usually also a composite itself, to keep production costs down [90]. During the process, reinforcement fiber fabric is laid in the mould to form a preform. Inlet and outlet hoses are placed as well as various flow-assisting media, depending on the part size and design. Following this, the mould is sealed shut by the vacuum bag using adhesive sealant tapes. Vacuum pressure is then applied expelling air from the preform assembly after which any eventual air leaks are eliminated. To commence infusion, the inlet hose is opened and resin is allowed to flow into the mould/vacuum bag cavity and impregnate the reinforcement fibers. The driving force for the resin flow is the pressure difference at the flow front, which also offers a hydrostatic pressure state on the entire part compacting the reinforcement fibers. This also helps increase the fiber volume fraction and the stiffness of the part [89]. During infusion, the ultimate goal is to fill all spaces which exist between the fiber fabric

with resin; i.e. between the fiber tows, and within the fiber tows. As the architecture of the structure and preform become more complex, the ability to fill every region in the mould cavity becomes increasingly difficult [63]. Once the reinforcement fibers are fully wetted, the inlet hose is closed and any excess resin is allowed to flow out of the wet preform, still under vacuum pressure. The part may then be cured at ambient temperature or in an oven/autoclave at elevated temperatures as prescribed by the resin manufacturer. Once the composite is adequately cured the part and mould are separated and subsequent post-processing or assembly is undertaken.

At a first glance, the vacuum infusion process may seem faily straight-forward. However, the combination of geometric non-uniformity, large thicknesses, elevated temperature cure cycles and the highly non-linear resin phase transition characteristics make the process complex to control and avoid induced shape distortions and residual stress build-up.

The constituent composite materials used in wind turbine blade laminates typically comprise of 70-75% E-glass reinforcement fibres by weight and thermoset epoxy or unsaturated polyester resin as the matrix. However, as the need to develop longer blades arise, some blade manufacturers look towards incorporating more carbon fibre reinforced composites for increased stiffness [90]. Blades are generally moulded in sub-components, then assembled using high performance structural adhesives.

1.2 Motivation

During manufacturing, one of the common challenges met is the development of process induced shape distortions and residual stress build-up within the manufactured specimen. Moreover, the ability to increase production throughput is dependent on how rapidly parts are cured and can be released from the large expensive moulds without damaging or changing the geometry due to insufficient curing. Where there is a shortcoming in experience or during development of radically different new parts, a demand for more computer-aided process outcome prediction- and control tools exists. Currently, no references exist of thermomechanical numerical process modelling efforts devoted to wind turbine blade structures.

In other processes, for instance metal casting, being able to predict and account for the local microstructure evolution during solidification as well as the development of residual stresses and distortions using numerical simulation models, has long been of scientific interest [29, 55]. Similarly, in composites processing, the final composite part's quality and shape is dependent on the thermal- and cure history during manufacturing, not to mention the influence of tool/part interactions and constraints. As shortly mentioned earlier, the mechanisms governing this can be highly non-linear making the process outcome difficult to predict and control. Using process models, prediction of the process and final part degree of cure, geometry and mechanical properties is possible, allowing for more accurate predictions of the process outcome than would otherwise be possible. Hence process models can significantly help avoid costly trial-and-error approaches during the

product development phase and in manufacturing, especially when new designs, materials or process conditions are investigated.

1.3 Objectives

The general objective of the current work is to apply numerical process models for the prediction of induced strains and residual stresses during the manufacture of large composite structures. Focus is devoted towards thermo-mechanical modelling of the curing process of materials representative of those applied in the manufacture of commercial composite wind turbine blades. Furthermore, different modelling approaches, constitutive models and experimental techniques are investigated with the objective of understanding the various mechanisms taking place during the process and which models best predict process outcomes.

Although numerical modelling efforts have at large existed within the field of composites processing, in the current study focus is dedicated towards applications within the manufacture of large commercial wind turbine blades with thick laminate sections and alternative cure cycles.

Since only thermomechanical aspects of the process will be considered in the current study, flow related phenomena will not be addressed. Hence it is generally assumed that in curing models, the part of interest is perfectly filled, has uniform material properties and that no voids or porosities exist, unless stated otherwise.

1.4 Thesis overview

The current thesis is divided into three main parts. Part I concerns a general introduction and overview of the problem matter, Part II is committed to various modelling theoretical aspects and Part III deals with modelling implementation and application cases. Finally some concluding remarks are presented. These parts are subdivided into the following chapters:

PART I
Chapter 1: Thesis introduction, motivation and overview.

Chapter 2: A review of the origins and mechanisms involved in the development of process induced shape distortions and residual stresses during composites manufacturing is given.

PART II
Chapter 3: This chapter is devoted to the general modelling theory used in this work. Fundamental theories for modelling heat transfer, resin cure kinetics, voids growth and mechanical constitutive models are presented and discussed.

Chapter 4: In this chapter, different mechanical composites process modelling constitutive approaches are presented and compared, including linear elastic, viscoelastic and a path-dependent constitutive models. Some of the details discussed in this chapter complement studies in the appended Paper II and Technical Report I.

PART III

Chapter 5: A 1D thermomechanical model is presented here for the calculation of process induced stresses and strains during curing. Furthermore, a voids growth model is presented, which is the basis of work covered in the appended Paper I.

Chapter 6: The implementation and validation of a 3D thermomechanical curing model is presented in this chapter. The different user-defined subroutines used in the commercial finite element software tool ABAQUS are presented, along with analytical and numerical validation cases.

Chapter 7: In this chapter, two modelling case studies are presented, concerning process induced strain predictions in thick laminate plates and an analysis of the origins of manufacturing shape distortions in a commercial wind turbine blade root section. Some details covered here within are seen in the appended Paper III. Furthermore, an introduction to the experimental in situ strain monitoring techniques utilized for comparitive purposes is also given, based on works in Paper III and IV.

Chapter 8: As the current study is not based on a specific single problem as such, general concluding remarks are presented in this chapter as a summary of the work covered in the thesis. Furthermore, recommendations and perspectives for further modelling studies are given.

An overview of the key modelling and experimental work carried out within the research period is presented in Fig. 1.2, showing also the relation to the appended works.

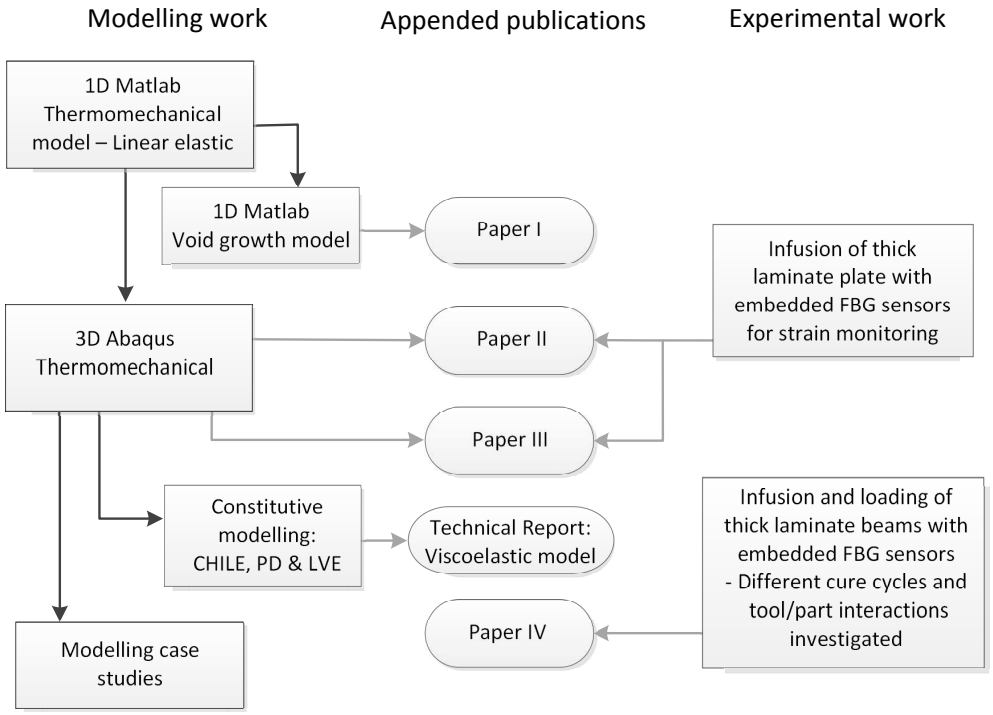

Figure 1.2: *Schematic of modelling- and experimental work flow during the PhD study, along with the relation to appended publications.*

Chapter 2

Mechanisms of shape distortions and residual stress in VARTM

The use of numerical process models to predict the thermal and mechanical response of composite structures during processing has gained interest in the last 3 decades [8, 21, 52, 64]. Of particular interest within these studies is the prediction of part temperatures and cure degree development during processing, not to mention shape distortions governed by the free expansion or contraction of the composite material. This chapter reviews the origins and mechanisms involved in the development of shape distortions and residual stresses during the manufacture of composites. Since flow related phenomena lie beyond the scope of this thesis, only aspects related to the curing stage of the process are considered, i.e. thermal, chemical and mechanical phenomena.

First, some preliminary definitions are presented, after which an introduction to curing state transitions in thermosetting polymers is presented. This is the backbone for understanding how a majority of the mechanisms that influence shape distortions and residual stress build-up. After this, effects of thermal- and cure shrinkage (chemical) origin are covered. Lastly, the influence of tool/part interactions and other processing aspects are reviewed.

2.1 Preliminary definitions

In general, composite materials consist of multiple layers of fibre/matrix materials, that are bonded together to form a laminate. The different layers are termed plies or laminae. Each lamina is normally orthotropic and consists of three orthogonal principle axes dependent of the principle reinforcement fiber direction, see Fig. 2.1. Hence the lamina is the building block of the composite material [109]. By stacking the laminae in different directions, structural properties can be tailored to meet the application of interest. According to the stacking sequence, balanced or unbalanced laminates can be formed, with or without symmetry. For balanced laminates, shear loads and strains are uncoupled from normal loads and strains, i.e. no bend-twist coupling exists [109]. Symmetric layups

exist only if the mid-plane forces and strains are uncoupled from bending strains and moments. For instance, a $[0°,90°]_s$ lay-up results in a balanced symmetric laminate. In the mechanics of laminated composites, a general assumption is that the lamina (layers) of the laminate are perfectly bonded [109].

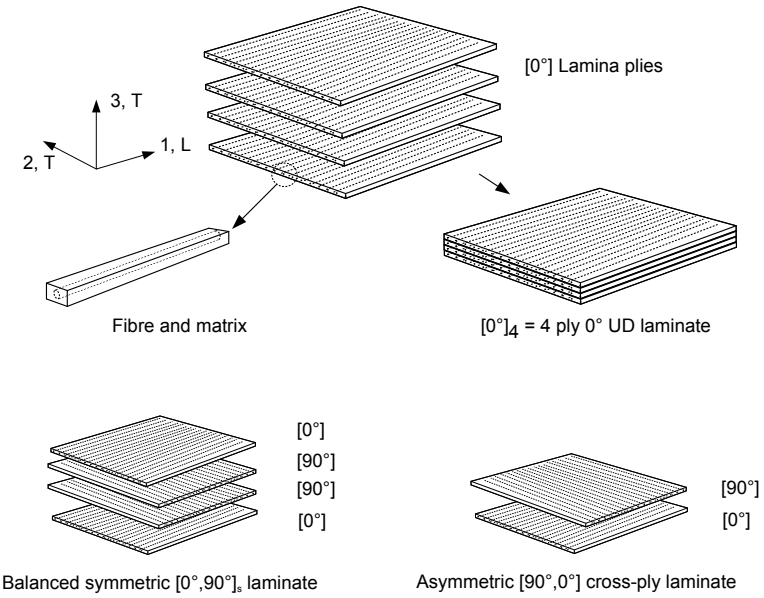

Figure 2.1: *Illustration of a laminate plate assembly comprising here of 4 uni-directional (UD) laminae. The coordinate axes notations L and T denote the principle fiber longitudinal and transverse directions respectively. Examples of balanced, symmetric and asymmetric laminates are also seen.*

In composite residual stress analyses, two types of stresses are generally distinguished between [69, 109]:

- **Micromechanical stresses**: These stresses are defined as the stresses that arise between the fibre and matrix material as a result of differences in the coefficient of thermal expansion (CTE), moduli and degree of anisotropy of the fiber and matrix materials. This mismatch can cause both longitudinal and transverse "*Intra*laminar" stresses within each ply. These stresses are difficult to evaluate and are generally very small in magnitude, hence they are generally disregarded in the analysis of large-scale deformations.
- **Macromechanical stresses**: These so-called *lamination* residual stresses are present within the individual ply of a laminate consisting of multi-plies of different angles. The residual stresses in the laminate arise, for instance from the difference between the ply CTEs in the longitudinal and transverse directions. Lamination residual stresses are known to promote the onset of transverse layer cracking and delamination and often cause serious warping in asymmetric laminates. Macromechanical stresses are "*Inter*laminar" stresses i.e. between or among plies.

Subsequently, various themomechanically related phenomena taking place during the manufacture of composites are presented. The descriptions are structured, where pos-

sible, according to the above given definitions. But first an introduction to thermosetting polymer state transitions during curing is presented.

2.2 Thermoset polymer state transitions during cure

In some VARTM processes, heat is applied to the composite material during resin infusion or during curing directly through the mould or in autoclave ovens. Curing is the term given to describe polymer solidification during cross-linking. During curing, thermoset resins evolve from liquids of low molecular weight to solids with fully developed 3D cross-linked networks. Cross-links can be formed by chemical reactions that are initiated by curing agents, temperature, pressure or radiation [6]. The cross-linking and branching action results in a loss in the polymers ability to move as individual polymer chains, consequently resulting in an increase in viscosity. During a typical process cycle, initially the resin viscosity drops upon the application of heat, passes through a region of maximum flow and then begins to increase again as the chemical reactions commence and the average length- and degree of cross-linking between the constituent oligomers[1] increases. This point is known as the gelation point and is characterized by the material transition from a viscous liquid to a rubbery solid exhibiting viscoelastic-type behavior. Consequently, an increase in stiffness is experienced after the onset of gelation allowing the material to be able to sustain strains and stresses without flowing [52, 108]. After gelation, the mobility of the polymer system gradually becomes limited as the resin micro-structure becomes fixed. Upon further curing during the process the transition of the material from a rubbery- to a glassy elastic-like solid state occurs, known as vitrification. In order for this to occur, usually an increase in temperature is necessary such that the cure temperature T_{cure} is larger than the resin glass transition temperature T_g [3, 24]. During curing a decrease in volume is experienced due to the forming of single bonds - attributed to change in inter-atomic spacing between molecules in solution [83]. Due to this, the sum of the energies of the polymer are less than the sum of the energies of the individual monomers [6]. Hence an exothermic reaction takes place as energy is released in the form of heat.

In Fig. 2.2 a Time-Temperature-Transformation (TTT) cure diagram for a thermosetting polymer is shown as proposed by J. Gillham [24]. This diagram describes the dependency of thermoset polymer state transition on temperature and time. The T_g of thermosets is dependent on the cure degree and can be determined using the DiBenedetto equation, given in its original form as[39]:

$$\frac{T_g - T_{go}}{T_{g\infty} - T_{go}} = \frac{\lambda\alpha}{1-(1-\lambda)\alpha} \tag{2.1}$$

where T_{go} is the T_g of the resin monomer, λ is a material constant and α is the degree of cure, expressed as a variable that varies from 0 to 1, with 0 corresponding to uncured and 1 to a fully cured polymer with a totally developed 3D cross-link network.

[1] Polymer that contains 2, 3 or 4 monomers

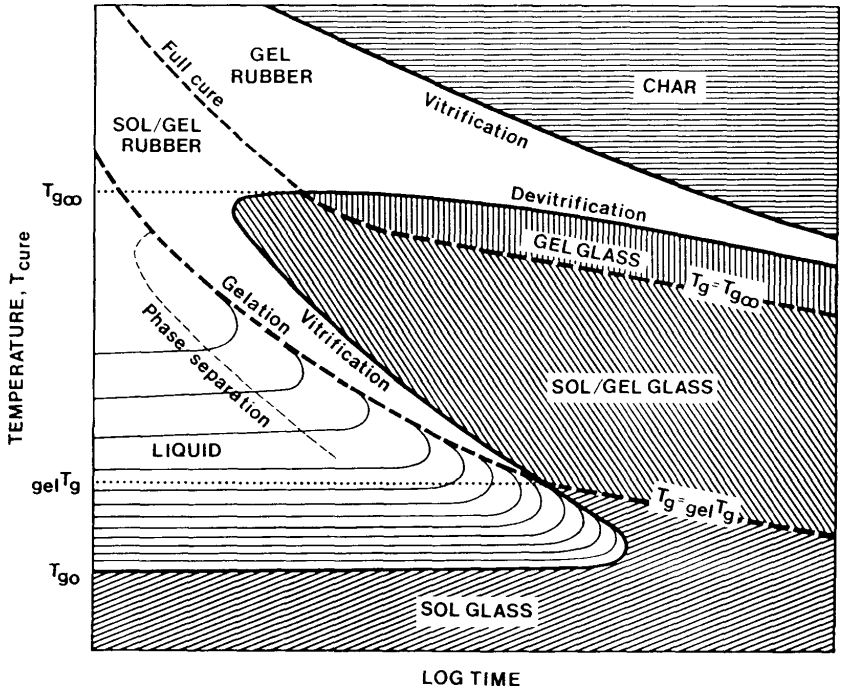

Figure 2.2: *Time-Temperature-Transformation (TTT) isothermal cure diagram for a thermosetting resin system, showing three critical temperatures, $T_{g\infty}$, ${}_{gel}T_g$, T_{g0}, and the distinct states of matter for the cure temperature T_{cure}. $T_{g\infty}$ is the ultimate glass transition temperature, ${}_{gel}T_g$ is the temperature at which gelation and vitrification occurs simultaneously and T_{g0} is the initial glass transition temperature of the reactants. [24]*

The TTT-diagram in Fig. 2.2 provides a framework for understanding the curing characteristics of thermosetting polymers. Some of the more important features of the diagram are summarized subsequently [24]:

- The general curing process involves gelation, vitrification, full cure (and sometimes devitrification) in that order. Devitrification, due to thermal degradation, marks the lifetime of the material to support a substantial thermal load.
- For reactions where T_g rises substantially, the glass transition temperature of the fully cured network, $T_{g\infty}$, can be surpassed, causing devitrification and the transition back to a gelled rubber state.
- When the cure temperature T_{cure}>T_g, the thermoset is in a liquid or rubbery state with low stiffness. After gelation, the material is in a glassy solid state when T_{cure}<T_g, with a higher modulus.
- Shrinkage stresses due to volume contraction of the resin on cure can first develop after gelation above ${}_{gel}T_g$ and above vitrification below ${}_{gel}T_g$.
- Full cure is attained most readily by reaction temperatures above $T_{g\infty}$, and more slowly by curing below $T_{g\infty}$ to the full-cure line of the TTT cure diagram.

For applications where cure at elevated temperatures is necessary, the TTT-diagram can be used as a tool for process optimization by helping achieve the correct schedule for the curing process [71, 108].

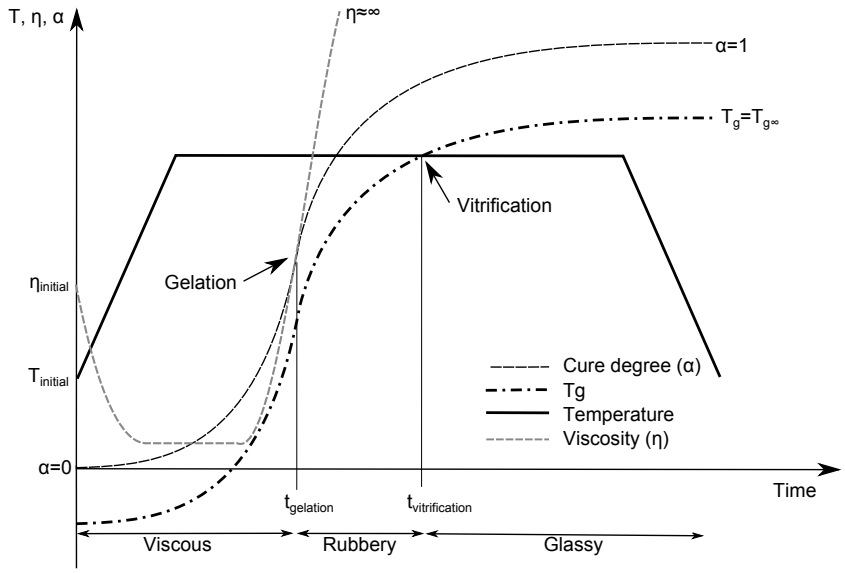

Figure 2.3: *Schematic of a fictive cure cycle example, showing cure degree, glass transition temperature and resin viscosity development as a function of temperature and time. The gelation and vitrification points are marked.*

Throughout the current work, three main resin states will generally be considered; (i) viscous liquid state prior gelation, (ii) rubbery solid state after gelation exhibiting solid viscoelastic-type behaviour, and (iii) glassy solid state after vitrification exhibiting short term elastic-solid like behaviour. A cure cycle example is illustrated in Fig. 2.3, showing the cure degree, glass transition temperature and resin viscosity development as a function of the process temperature. During these three main states, the resin undergoes large changes in its thermal and mechanical properties, most significantly in its thermal expansion and modulus [39, 47, 53, 94, 96].

While the behaviour presented above is general for thermoset polymers, some differences may exist between curing characteristics of epoxy and polyester resins. Knowing the different polymer matrix material states, the factors affecting the development of shape distortions and residual stresses are reviewed henceforth.

2.3 Stresses and distortions of thermal origin

As earlier mentioned, VARTM is in most cases conducted at elevated temperatures, either as a result of external heating or due to heat generation from the exothermic reaction. Due to this, differential thermal expansion effects are inevitable and known to be one of the major contributors to stress build-up. Residual stresses of thermal origin will subsequently be presented either as stresses at the micro- or macro level.

One of the driving factors at the micromechanical level is the much higher coefficient of thermal expansion (CTE) of polymer matrix materials as compared to reinforcement fibres. Some examples are presented in Tab. 2.1. The large difference in constituent material CTEs, along with the orthotropic nature of expansion of some fibres, are known to lead to the development of residual stresses at the microscale level [21, 45, 50, 77, 102, 105]. These stresses are usually most significant during the cooling phase of processing, where the resin stiffness is fully developed and can in worst case result in failure through matrix cracking [111]. One effect of the low (and sometimes negative) CTEs of (stiff) fibre materials, as shown in Tab. 2.1, is that they severely constrain contraction of the (softer) matrix during cooling. For instance, upon uniform cooling of a glass/epoxy UD laminate, the higher matrix CTE would result in longitudinal tensile stresses in the matrix, while longitudinal compressive stresses would develop in the reinforcement fibre in order to uphold equilibrium [100]. However, Nedele et al. [76] and Wisnom et al. [105] found that residual stresses at a micromechanic level may not normally readily cause distortions, as they may arise at a very local scale such that deforming effects are averaged out over the larger volume of the material. However, various studies state that the expansional mismatch of the matrix and fibre material gives rise to residual stresses within the plies after fabrication which can be sufficiently high to cause intraply or matrix cracking even before any load is applied [68].

At a macromechanical level, differences in effective interlaminar expansion behaviour in the longitudinal and transverse directions can cause differential in-plane stresses throughout the laminate layup, for instance in laminates with unbalanced non-symmetric layups. These stresses can lead to distortions even in flat plates [27] and result in twist in laminates with angle plies [52].

Reinforcement fibre	**CTE (x 10^{-6} $^{\circ}C^{-1}$)**
Carbon - HS (high strength)	α_L = -0.5 to -0.1
	α_T = 7 to 12
Carbon - HM (high modulus)	α_L = -1.2 to -0.5
	α_T = 7 to 12
Glass: E-glass	4.7 to 5.0
Glass: S-glass	5.6
Matrix$^{(a)}$	
Epoxies	55 to 90
Polyester	50 to 100

$^{(a)}$: Values for fully cured (glassy state) resins

Table 2.1: *Linear coefficients of thermal expansion (CTE) of fibres and fully cured matrix materials [50]. Unidirectionally (UD) oriented fibres composites have two effective CTEs; α_L and α_T in the longitudinal and transverse directions respectively. It is clear that a great mismatch exists between the different fibre and matrix materials.*

The thermal expansion behaviour for thermosetting resins have been reported to be approximately 2-3 times higher in the viscous and rubbery state as compared to the glassy state [46, 47, 92]. While this may cause larger free expansion of unconstrained laminates, the effect on development of stresses in rubbery state of constrained laminates is small due to the low matrix stiffness in this state. This was shown in cure investigations by Lange et al. [56] for thermoset resin cured above $T_{g\infty}$, where stresses were only shown to

develop during the cooling stage below T_g. However, if unconstrained, free expansion in rubbery state may result in large shape distortions.

While cure cycle heating and cooling effects may result in insignificant gradients through the laminate thickness, for thick composite laminates or cases where the mould has poor heat transfer properties, large gradients can promote residual stress build-up and distortions. These effects are described later in Section 2.6.

2.4 Stresses and distortions of chemical shrinkage origin

The curing reaction is accompanied by a decrease in the matrix material volume. The reaction between the reactive groups of the molecules lead to an increase of the molar weight of the resin macromolecules, corresponding to a volumetric shrinkage. Epoxy resins are known to exhibit a total volumetric cure shrinkage of 3-7% [47, 88, 105], while a total volumetric shrinkage ranging between 6-10% has been reported for standard unsaturated polyester resins [9, 33, 67, 84].

Chemical shrinkage strains can result in stress development at the micromechanical level. Prior gelation, while the resin is in the viscous state, cure shrinkage occurs without stress development. As different thermoset polymers gel at different stages of curing, the amount of chemical shrinkage that can induce stress development varies. Hence reductions in cure-induced stresses are experienced when a greater volume shrinkage of the matrix occurs in liquid state, leaving a smaller fraction of the total shrinkage to contribute to the stress build up after gelation [15]. This is for instance possible for polyester resins as they are known to gel earlier than epoxy resins [92]. For instance, the gelation degree of cure for an unsaturated polyester resin used in RTM was determined by Kenny et al. [45] to be just α_{gel}=0.088, while RTM epoxy resins are reported to gel at as high as $\alpha_{gel} >$0.7 [59, 101].

Chemical shrinkage of resins in the macromechanic scale can also play an important role. Studies by Holmberg et al. [38] and Prasatya et al. [80] show that these effects cannot be ignored. Prasatya et al. showed numerically that approximately 30% of the total process induced residual stress build-up in neat resin samples owes to cure shrinkage. For UD laminates, large shape distortions can occur in the transverse direction of the reinforcement fibre due to better freedom of contraction, as behaviour in this direction is mainly matrix dominated. Russel et al. [86] state that 30-95% of residual stresses in aerospace grade epoxy can contribute from cure shrinkage also and not only thermal strains. From this it is clear that cure shrinkage can play a large role in the final part geometry and stress state. Chemical shrinkage induced strains are easily distinguishable as strains arising at isothermal process periods, i.e. when thermal effects are constant, as is seen in work by Crasto et al. [15].

2.5 Influence of tool/part interaction

Process induced stresses can develop during VARTM where thermal and mechanical driven effects play a role. Effects develop under the circumstance that the part and mould are forced together due to the hydrostatic vacuum pressure and weight of the part. The main driving factor behind stress development are the differential strains between the mould and part (from hereon “tool/part”) due to differences in material thermal expansion behaviour and shrinkage. The difference in tool/part expansion can result in shear interaction along the contact interface. This is known to induce residual stresses in the part if a stiff mould tool is used, which can lead to warpage after demoulding [23, 99]. While these stresses are partly avoided in the manufacture of large composite structures by use of less stiff composite moulds, geometry, thickness and fibre volume fraction, can vary within the part, making stress development during processing inevitable. Even for identical composite tool and part configurations, stresses are known to develop due to the changing physical properties of the uncured part during processing [41].

Tool/part interface interactions are of particular interest when considering thick laminate composites as large non-uniform distributions of in-plane shear stresses can arise due to constraints at the tool/part interface [18, 22, 105]. Various studies propose the following general mechanisms for warpage/distortion due to tool/part interactions with differential expansion behaviour [22, 82, 99]:

- (a) Upon heating, the laminate is stretched due to the thermal expansion of the (stiffer) tool. Plies close to the contact interface are in tension more than plies away from the tool.
- (b) As the part is not fully cured, interply-slippage result in through-thickness gradients in the ply stresses. These stress gradients become locked-in upon curing.
- (c) Upon demoulding, the stresses are relieved through warpage distortions as the part is no longer in equilibrium with the tool.

The above mentioned points are illustrated in Fig. 2.4.

2.6 Other factors

2.6.1 Cure cycle design

For processes conducted at elevated temperatures, the cure cycle temperature design can also influence residual stress build-up and shape distortions. Implementation of long cure cycles at elevated temperatures are known to minimize residual stress levels during moulding [52][100]. This is due to the viscoelastic nature of thermosets at elevated temperatures (especially in the rubbery state) where large stress relaxation can occur [72]. During curing, temperature dwells are normally used in order to obtain uniform temperatures in the part after the initial heating stage[27]. Long dwell periods are typically

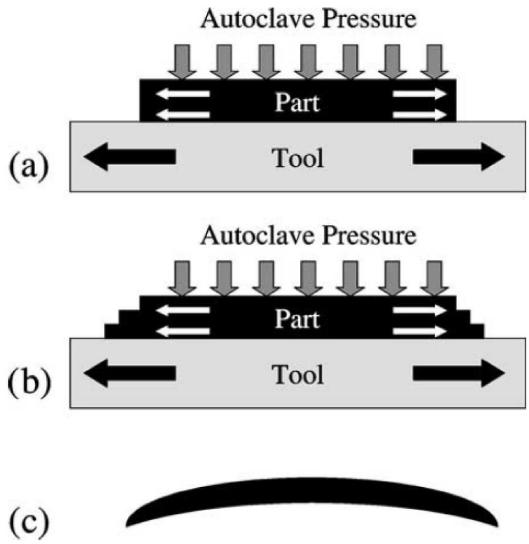

Figure 2.4: *Schematic of mechanism resulting in part warpage as a result of tool/part interaction [82, 99].*

implemented at matrix gelation temperatures and effectively result in stress relaxation of the matrix material which is dependent of T_g and the cure degree [53].

Implementation of *smart cure cycles* can also help reduce residual stresses by use of specific cooling and reheating steps during curing to trigger different transition states [51]. Studies by Crasto et al. [15] and Russell et al. [86] showed that the process temperatures can be controlled, such that the thermal expansion and cure shrinkage strains cancel each other out, effectively keeping the matrix material volume somewhat constant, which helps reduce cure induced strains. Two conditions, necessary to minimize cooling stress build-up are, having a low peak cure temperature and low heating/cooling rates [85]. However, these two conditions conflict with the general industry goal of low process times.

2.6.2 Composite thickness

Inherent difficulties exist in the manufacture of thick-section composites. The low thermal conductivity of thick composite sections greatly constrains the use of rapid heating and cooling cure schedules. These difficulties arise from the highly non-linear nature of the reaction kinetics taking place in the thermosetting resin during curing. As the interior of the uncured composite part heats up, the exothermic reaction starts by releasing energy (heat) at a faster rate than the material's ability to conduct this heat away from the region. The increase in temperature helps to further accelerate the curing reaction resulting in an even faster energy release. As a result the process can rapidly become unstable causing a thermal spike phenomenon [49, 70], resulting in highly non-uniform temperature gradients within the part.

The thickness of the laminate affects the magnitude of induced residual stresses as thick-walled parts have been shown to experience larger residual stresses [9]. Furthermore,

prediction of residual stresses in thick-walled geometries is harder than in thin-walled laminates where near uniform through-thickness temperatures are experienced and uniform through-thickness in-plane stress/strain assumptions can be made. Larger residual stresses arise as a result of larger variations of cured and uncured regions through the part thickness. This is a result of fully cured regions constraining the cure shrinkage at uncured regions which can lead to significant tensile stresses in the interior region, equilibrated by compressive stresses in the exterior region[98].

2.6.3 Fibre volume fraction

Almost all effective laminate thermal and mechanical properties are dependent of the laminate fibre volume fraction. Hence variations in fibre content from part to part due to poor manufacturing control can result in substantial differences in the end product behaviour. Similarly, the inhomogeneous distribution of fibre and matrix within a part, usually proned to exist in parts with complex geometries, can significantly influence the process outcome also. For instance, Hubert [36] showed that resin flow phenomena in angle profiles can result in resin-rich or resin-poor regions at curved sections depending on the mould type (i.e. negative or positive print). Sung and Hilton [91] showed that the fibre content in thick laminates affected the maximum exothermic temperature peak and degree of cure.

2.6.4 Void content

Voids are known to exist in composite laminates as a result of entrapped air and other volatiles during infusion, for instance between compacted fibre tows [57, 106]. Formation of voids can also arise due to nucleation effects driven by the diffusion of moisture that is dissolved in the resin matrix material during curing into existing void bubbles, typically under elevated temperature conditions [4, 26, 43]. An attempt to model the through-thickness non-uniform void growth due to transient processing effects is investigated in the appended Paper I. It was shown that large through-thickness thermal gradients can result in non-uniform void dimensions.

While the mechanisms behind the formation of voids are still not fully understood [26], the effects are well known. Voids have been reported to have a detrimental effect on the strength and fatigue life of composite laminate structures [7, 61]. Several authors have also reported that voids in composites accelerate crack initiation and propagation [35, 64, 104]. Liu et al. [61] investigated the void content effect on carbon/epoxy laminate mechanical properties. It was found that a decrease of approximately 20% in shear-, flexural- and tensile strength was observed with an increase in void content by approximately 2.6%. Similar tendencies are also observed for the flexural- and tensile moduli as well as the inter-laminar shear strength (ILSS). As voids clearly have an effect on the mechanical behaviour of composites and the constituent material volume fractions, their existence in composites indirectly influences residual stress build-up and shape distortions.

2.7 Summary of mechanisms

An attempt at summarizing the mechanisms and factors presented in this chapter is presented in Fig. 2.5. With inspiration from the work by Svanberg [92] and Wisnom [105], along with the references presented above, the different factors affecting process induced shape distortions and residual stress build-up are classified according to how large or small their effects are.

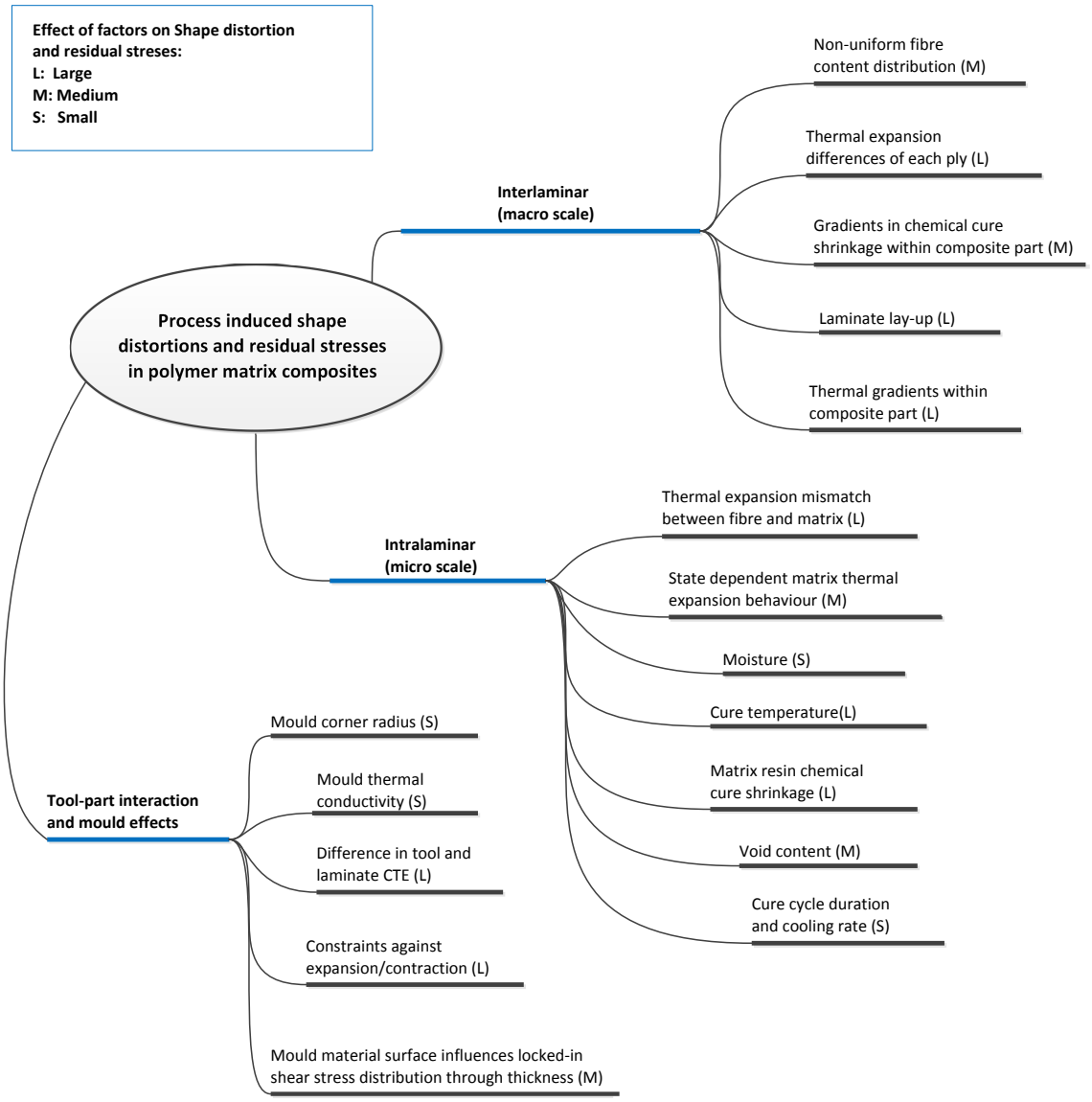

Figure 2.5: *Schematic summarizing the mechanisms and factors influencing process induced residual stress build-up and shape distortions in composites.*

Chapter 3

General modelling theory

In this chapter, the fundamental models governing the thermo-chemo-mechanical phenomena occurring during composites manufacturing are presented. Through use of these models, we wish to predict the shape distortion and residual stress inducing mechanisms numerically. The term thermo-chemical is used subsequently to categorize modelling aspects relating to thermal and chemical (curing reaction) phenomena. First, general heat conduction is presented, naturally followed by thermoset polymer cure kinetics models used to express the degree of cure evolution and heat generation during resin cross-linking. Following this, general mechanical constitutive relations specific for orthotropic and transversely isotropic materials are presented. Cartesian systems x, y, z coordinates are used when referring to the global coordinate system for the laminate and composite, whereas $1, 2, 3$ are primarily used as a local coordinate system for the lamina, with 1 representing the fiber direction, 2 transverse to the fiber and 3 the out-of-plane direction.

3.1 Thermo-chemical modelling

Before calculation of process-induced stresses and strains is possible, knowledge of the heat transfer for the part (and tool) is required. The principle governing equation for heat conduction is Fourier's equation [29]:

$$\rho C_p \frac{\partial T}{\partial t} = k_x \left(\frac{\partial^2 T}{\partial x^2} \right) + k_y \left(\frac{\partial^2 T}{\partial y^2} \right) + k_z \left(\frac{\partial^2 T}{\partial z^2} \right) + \dot{Q}''' \tag{3.1}$$

where T is the temperature, t is the time and x, y, z represent spatial coordinates in the Cartesian system. $\dot{Q}'''$ is the heat source term representing the internal volumetric heat generation rate occurring during resin phase transition[1]. ρ, C_p, and k_i are the effective composite material density, specific heat and thermal conductivity respectively- assumed

[1]The triple prime used to describe the heat source term denotes per unit volume.

constant here. These effective properties are obtained by the rule of mixture [84]:

$$\begin{aligned} C_p &= C_{pr}(1 - V_f) + C_{pf}V_f \\ \rho &= \frac{\rho_r \rho_f}{\rho_r(1 - V_f) + \rho_f V_f} \\ k &= \frac{k_r k_f}{k_r(1 - V_f) + k_f V_f} \end{aligned} \tag{3.2}$$

where the subscripts r and f denote resin and fibre properties and V_f is the fibre volume fraction. In Eq. 3.1 the source term $\dot{Q}'''$ is naturally zero when modelling heat conduction of model parts other than the composite being cured. $\dot{Q}'''$ is determined by the total reaction enthalpy H_T during curing and the cure rate $\frac{d\alpha}{dt}$ as:

$$\dot{Q}''' = \rho H_T (1 - V_f) \frac{d\alpha}{dt} \tag{3.3}$$

Kinetic models are used to express the cure kinetics behaviour of a polymer. These models are classified into mechanistic and phenomenological models. The latter are more empirically based and widely accepted in composites process modelling as they are determined by fitting coefficients to experimental material characterization data [87]. Kinetic models are usually first- or second order partial differential equations generally relating the cure rate to functions of temperature and cure degree as [24, 64, 84]:

$$\frac{d\alpha}{dt} = K(T) \cdot f(\alpha) \tag{3.4}$$

involving a conversion function $f(\alpha)$, which describes the shape of the heat flow curve (reflecting the type of reaction), and an Arrhenius-type relation for the reaction temperature dependency given as:

$$K(T) = A \cdot exp\left[\frac{-E_a}{RT}\right] \tag{3.5}$$

In Eq. 3.5 A is the pre-exponential factor, E_a is the apparent activation energy of the cure reaction, R is the universal gas constant and T is the temperature. Empirically, the transient degree of cure $\alpha(t)$, at a material point is generally assumed to be dependent of the ratio of the cumulative heat liberated from the chemical reaction, $H(t)$, to the total heat of the reaction (or reaction enthalpy) H_T, expressed as:

$$\alpha(t) = \frac{H(t)}{H_T} \tag{3.6}$$

The heat liberated at any point in time t is expressed in integral form as:

$$H(t) = \int_0^t \frac{1}{\rho_m} \left(\frac{dq}{dt}\right) dt \tag{3.7}$$

where dq/dt is the rate of heat generation from the cure reaction and ρ_m is the matrix material density. H_T is the accumulated heat for the whole reaction, commonly determined using Differential Scanning Calorimetry (DSC).

In Eq. 3.4, the conversion function $f(\alpha)$ used depends on the thermoset polymer. Different types of cure reaction formulations exist for thermoset resins, either in the form of nth order models, autocatalytic models, or a combination of both [9, 87]. Which model to use can be determined by examining heat flow measurements (e.g. from DSC). A bell-shaped heat flow profile as a function of time is generally representative of autocatalytic-type reactions, where the cure rate dα/dt = 0 at the initial stages of curing and achieves a maximum rate during intermediate stages of curing. Alternatively, if dα/dt starts from a maximal point early in the reaction and decreases towards zero with time, nth order expressions are used [87]. nth order conversion functions are expressed as [70, 87]:

$$f(\alpha) = (1 - \alpha)^n \tag{3.8}$$

where n is the reaction order. In contrast, autocatalytic conversion expressions are expressed as [70, 110]:

$$f(\alpha) = \alpha^m(1 - \alpha)^n \tag{3.9}$$

where m and n are reaction orders determined experimentally. Kamal & Sourour [42] proposed an autocatalytic model, for curing reactions where the initial reaction rate (at $\alpha = 0$) may not be zero. This model is widely used in numerous studies for thermosetting epoxies and unsaturated polyester resins given as [9, 14, 41, 44, 45, 107]:

$$\frac{d\alpha}{dt} = (K_1 + K_2\alpha^m)(1 - \alpha)^n \tag{3.10}$$

where the parameters K_1 and K_2 are defined for $i = 1, 2$ by the Arrhenius expression in Eq. 3.5. An autocatalytic kinetic model including a diffusion factor was proposed by Hubert et al. [37] for epoxy resins. The diffusion factor accounts explicitly for the transition of the cure mechanisms from being kinetically controlled to diffusion controlled towards the end of the curing reaction, expressed as:

$$\frac{d\alpha}{dt} = \frac{1}{1 + exp\left[C(\alpha(\alpha_{C0} + \alpha_{CT}T))\right]} K\alpha^m(1 - \alpha)^n \tag{3.11}$$

where the diffusion parameters include the diffusion constant C, the critical cure degree at absolute zero temperature α_{C0} and the degree of cure accounting for the increase in the critical degree of cure with resin temperature α_{CT}. This model is well suited for epoxy resins with high ultimate glass transition temperatures.

While many other models for specific polymer curing behaviour exist, the examples given above are widely used within thermoset resin process modelling applications. Having expressions for the thermochemical behaviour of the composite during curing, other temperature and cure degree properties can be determined readily in an incremental manner well suited for numerical implementation.

A note on the robustness of the cure kinetics characterization methods is necessary. Due to the highly non-linear phenomenological cure rate expressions presented above, determination of precise material parameters, for instance in the Arrhenius expressions, can be cumbersome. Hence values found in the literature for identical resins might not always be consistent, even for identical stoichiometric ratios of resin and hardener/catalyst.

3.2 Mechanical modelling

While Chapter 4 is devoted to the different constitutive models used in the current study, general elastic theories governing the stress-strain relations in composites are presented henceforth.

As composite structures are neither homogeneous nor isotropic, their mechanical properties depend on the orientation of the composing materials and layup architecture. Mechanical property definitions at the micro- and macromechanic scales are therefore sometimes used [69]:

- Micromechanic level - Interaction of constituent materials are expressed at a micro scale where micromechanic formulations are used to describe the thermal and mechanical (elastic) characteristics of each lamina.
- Macromechanic level - The response of the composite material to mechanical and thermal loads are expressed at a macroscopic scale typically using “lumped” models representative of global effective properties. Here the material is generally assumed to be homogeneous in the respective coordinate directions, and orthotropic elasticity equations are usually used to calculate strains and stresses.

Many different approaches exist for determining composite micromechanic behavior, such as rule-of-mixtures (ROM), self-consistent mechanics approaches [32], numerical method approximations using representative volume elements (RVE), the boundary element method (BEM) [20] or Semi-empirical methods [109]. In this work, the self-consistent field model (SCFM) proposed by Whitney and Hermans [30, 103] is used for the calculation of effective elastic constants. SCFM is known to offer realistic approximations of effective lamina properties and the basic relations used for deriving the elastic constants for transversely isotropic material behaviour is presented in detail in [9, 41]. Knowing the effective global material mechanical properties, constitutive relations can be applied. Hooke’s generalized law describes the constitutive relation between stresses and elastic strains, characterizing the material and its reaction to applied loads, expressed as:

$$\sigma_{ij} = \mathbf{C}_{ijkl}\varepsilon_{kl} \qquad \text{or} \qquad \varepsilon_{ij} = \mathbf{S}_{ijkl}\sigma_{kl} \tag{3.12}$$

for $i, j, k, l = 1, 2, 3$ or x, y, z. Eq. 3.12 is valid for linear elastic homogeneous materials. $\mathbf{C}$ is the stiffness tensor and $\mathbf{S}$ the compliance tensor with the common relation $\mathbf{S}$=$\mathbf{C}^{-1}$. A lamina is defined as a thin orthotropic layer of a composite material; the smallest element at a macroscopic level used to build a composite laminate [109]. For an orthotropic material, Hooke’s generalized law reduces to:

$$\begin{bmatrix}\sigma_{11}\\ \sigma_{22}\\ \sigma_{33}\\ \sigma_{23}\\ \sigma_{31}\\ \sigma_{12}\end{bmatrix} = \begin{bmatrix}C_{11} & C_{12} & C_{13} & 0 & 0 & 0\\ C_{12} & C_{22} & C_{23} & 0 & 0 & 0\\ C_{13} & C_{23} & C_{33} & 0 & 0 & 0\\ 0 & 0 & 0 & C_{44} & 0 & 0\\ 0 & 0 & 0 & 0 & C_{55} & 0\\ 0 & 0 & 0 & 0 & 0 & C_{66}\end{bmatrix} \begin{bmatrix}\varepsilon_{11}\\ \varepsilon_{22}\\ \varepsilon_{33}\\ 2\varepsilon_{23}\\ 2\varepsilon_{31}\\ 2\varepsilon_{12}\end{bmatrix} \tag{3.13}$$

whereby a reduction of the total number of stiffness components needed to describe the material behaviour from 81 for an anisotropic material to 12 components is achieved. For an orthotropic material the following material engineering constants are used [109]: E_1, E_2, E_3, ν_{12}, ν_{21}, ν_{13}, ν_{31}, ν_{23}, ν_{32}, G_{12}, G_{13} and G_{23}, such that the stiffness matrix becomes:

$$C = \begin{bmatrix} \frac{1-\nu_{23}\nu_{32}}{E_2E_3\Delta} & \frac{\nu_{21}+\nu_{31}\nu_{23}}{E_2E_3\Delta} & \frac{\nu_{31}+\nu_{21}\nu_{32}}{E_2E_3\Delta} & 0 & 0 & 0\\ \frac{\nu_{12}+\nu_{13}\nu_{32}}{E_3E_1\Delta} & \frac{1-\nu_{31}\nu_{13}}{E_3E_1\Delta} & \frac{\nu_{32}+\nu_{31}\nu_{12}}{E_3E_1\Delta} & 0 & 0 & 0\\ \frac{\nu_{13}+\nu_{12}\nu_{23}}{E_1E_2\Delta} & \frac{\nu_{23}+\nu_{13}\nu_{21}}{E_1E_2\Delta} & \frac{1-\nu_{12}\nu_{21}}{E_1E_2\Delta} & 0 & 0 & 0\\ 0 & 0 & 0 & 2G_{23} & 0 & 0\\ 0 & 0 & 0 & 0 & 2G_{31} & 0\\ 0 & 0 & 0 & 0 & 0 & 2G_{12} \end{bmatrix} \tag{3.14}$$

where:

$$\Delta = \frac{1-\nu_{12}\nu_{21}-\nu_{23}\nu_{32}-\nu_{31}\nu_{13}-2\nu_{12}\nu_{23}\nu_{31}}{E_1E_2E_3} \tag{3.15}$$

As UD laminates are transversely isotropic, we assume that the 2-3 plane is isotropic, hence E_2=E_3, ν_{12}=ν_{13}, ν_{21}=ν_{31}, ν_{23}=ν_{32} and G_{12}=G_{13}. Furthermore:

$$\begin{aligned} G_{23} &= \frac{E_2}{2(1+\nu_{23})},\\ \nu_{21} &= \frac{E_2}{E_1}\nu_{12} \quad \text{and} \quad \nu_{23} = \nu_{12}\frac{1-\nu_{21}}{1-\nu_{12}} \end{aligned} \tag{3.16}$$

Composite laminae are commonly very thin, hence a state of plane stress can be assumed to prevail. In this case, all out-of-plane normal- and shear stress components become negligible (i.e. $\sigma_3$3=σ_{23}=σ_{31}=0). This further reduces Eq. 3.13 to:

$$\begin{bmatrix}\sigma_{11}\\ \sigma_{22}\\ \sigma_{12}\end{bmatrix} = \frac{1}{1-\nu_{12}\nu_{21}} \begin{bmatrix}E_1 & \nu_{21}E_1 & 0\\ \nu_{12}E_2 & E_2 & 0\\ 0 & 0 & G_{12}(1-\nu_{12}\nu_{21})\end{bmatrix} \begin{bmatrix}\varepsilon_{11}\\ \varepsilon_{22}\\ 2\varepsilon_{12}\end{bmatrix} \tag{3.17}$$

A transversely isotropic material is hence fully described using only 5 independent material properties.

3.2.1 Process-induced strain increments

Process-induced strain increments refer to the structural strains induced as a result of the chemical cure shrinkage and thermal strains. These are presented henceforth. Note that in this section, the derivations presented are both applicable in the local or global coordinate systems.

Chemical strain increment

As the resin cures, a change in volume associated with the reaction takes place. This volumetric shrinkage relates to a chemically induced contraction strain in the resin. The change in specific volume of a cubic volume element can be described in terms of its normal strain components ($\varepsilon_{11}, \varepsilon_{22}$ and ε_{33}). Experimentally, the specific total volumetric shrinkage of resins V_{sh}^T can be determined , among other methods, by dynamic mechanical analysis (DMA), thermal mechanical analysis (TMA) or gravimetric methods [47, 60, 67]. Assuming uniform strain contraction, the incremental isotropic shrinkage strain in a neat resin matrix sample $\Delta\varepsilon_m$ can be found as:

$$\Delta\varepsilon_m = \sqrt[3]{1 + \Delta V_m} - 1 \tag{3.18}$$

where ΔV_m is the incremental specific change in volume of the matrix. Some studies assume a linear relation between ΔV_m and the cure degree [9]:

$$\Delta V_m = \Delta\alpha \cdot V_{sh}^T \tag{3.19}$$

However, some resins have been shown to exhibit varying shrinkage behaviour during the curing reaction. Johnston [41] proposed an alternative approach, replacing V_{sh}^T in the previous equation with:

$$V_{sh} = \begin{cases} 0 & \alpha < \alpha_{c1} \\ A_{sh} \cdot \alpha_s + (V_{sh}^T - A_{sh})\alpha_s^2 \quad \text{for} & \alpha_{c1} \leq \alpha \leq \alpha_{c2} \\ V_{sh}^T & \alpha \geq \alpha_{c2} \end{cases} \tag{3.20}$$

where α_{c1} and α_{c2} are the critical cure degrees marking assumed bounds of shrinkage during curing and A_{sh} is a factor accounting for the non-linear cure degree dependency. α_s is expressed as:

$$\alpha_s = \frac{\alpha - \alpha_{c1}}{\alpha_{c2} - \alpha_{c1}} \tag{3.21}$$

Knowing the incremental isotropic shrinkage strain $\Delta\varepsilon_m$ in Eq. 3.18, the incremental longitudinal and transverse chemically induced shrinkage strains $\Delta\varepsilon^{ch}$ can be determined for

a composite material (or each laminae) using SCFM for UD continuous fiber composites. The chemically induced incremental longitudinal strain is expressed as:

$$\Delta\varepsilon_1^{ch} = \frac{\Delta\varepsilon_m E_m(1-V_f)}{E_f V_f + E_m(1-V_f)} \tag{3.22}$$

where E_m and E_f are the matrix and reinforcement fiber Youngs modulus. Having calculated the longitudinal chemical strain increment, the transverse strain increment is determined as:

$$\Delta\varepsilon_2^{ch} = (\Delta\varepsilon_m + \nu_{12m}\cdot\Delta\varepsilon_m)(1-V_f) - (\nu_{12f}V_f + \nu_{12m}(1-V_f))\Delta\varepsilon_1^{ch} \tag{3.23}$$

where ν is the Poisson's ratio. For UD fiber laminates, transversly isotropic conditions prevail hence $\Delta\varepsilon_3^{ch} = \Delta\varepsilon_2^{ch}$.

Thermal strain increment

Thermal strain increments are calculated in a similar manner, based on the temperature change and the composite effective thermal expansion coefficient α^{cte}. In general, for an isotropic material the thermal strain increment $\Delta\alpha^{cte}$ is calculated as:

$$\Delta\varepsilon^{th} = \alpha^{cte}\cdot\Delta T \tag{3.24}$$

However, for orthotropic materials the effective lamina thermal expansion coefficient α_i^{cte} for $i = 1,2,3$ is dependent of the matrix and fiber thermal expansion, mechanical properties and fiber volume fraction. Using SCFM, the effective laminate longitudinal CTE is determined as [103]:

$$\alpha_1^{cte} = \frac{\alpha_{1f}^{cte}E_{1f}V_f + \alpha_m^{cte}E_m(1-V_f)}{E_{1f}V_f + E_m(1-V_f)} \tag{3.25}$$

where α_f^{cte} and α_m^{cte} are the fiber and matrix thermal expansion coefficients respectively. The transverse effective thermal expansion coefficients are hence:

$$\begin{aligned}\alpha_2^{cte} &= (\alpha_{2f}^{cte} + \nu_{12f}\cdot\alpha_{1f}^{cte})V_f + (\alpha_m^{cte} + \nu_{12m}\cdot\alpha_m^{cte})(1-V_f) \\ &\quad - [\nu_{12f}V_f + \nu_{12m}(1-V_f)]\alpha_1^{cte} \qquad (3.26)\\ \alpha_3^{cte} &= \alpha_2^{cte} \qquad (3.27)\end{aligned}$$

Note that the presented expressions depend on the reinforcement fabric architecture, hence the equations shown above are only valid for transverse isotropic material behaviour.

Total process induced strain increment

The total process induced strain increments are found as a sum of the chemical and thermal strain increments:

$$\Delta\varepsilon_i^{Pr} = \Delta\varepsilon_i^{ch} + \Delta\varepsilon_i^{th} \tag{3.28}$$

for i = 1,2,3 or x, y, z.

3.2.2 Effective plate loads and laminate deformations using CLT

Classical laminate theory (CLT) approaches can provide good approximations of the overall laminate behaviour and individual ply mechanical response in cases where the laminate cross-section is uniform and the laminate part thickness is small compared to other dimensions. An illustration of the CLT interrelations which exist between local and global in-plane stresses and strains as well as force- and moment resultants is presented in Fig. 3.1. Assuming that the process induced strains are known according to the previous section (i.e. ε_1^{Pr} and ε_2^{Pr}), the effective plate loads (N and M) can be calculated from the strain induced deformations that would be experienced by each lamina. By utilizing the relations presented in Fig. 3.1, calculation of corresponding in-plane laminate global stresses and strains is possible. However, note that where, in normal CLT calculations, one usually wishes to determine laminate stresses or strains from prescribed normal forces or bending moments, in the following a different approach is taken starting with the process induced strains as proposed by Bogetti & Gillespie [9].

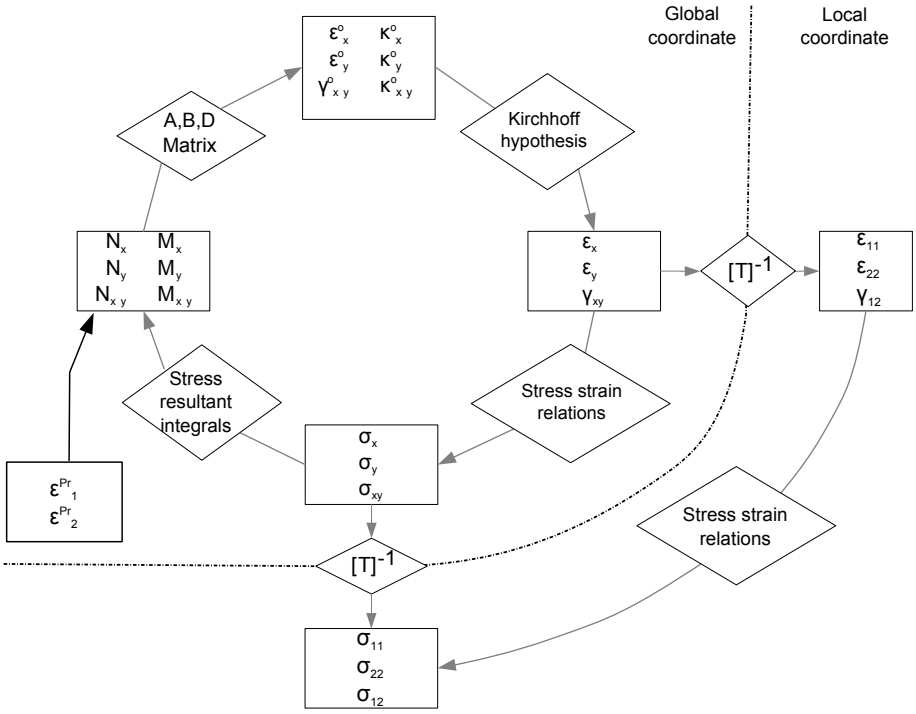

Figure 3.1: *Classical laminate theory interrelations.*

The total local strain for a lamina (index l) is the sum of elastic, thermal and chemical strains:

$$\varepsilon_l^T = \varepsilon_l^{el} + \varepsilon_l^{th} + \varepsilon_l^{ch} = \varepsilon_l^{el} + \varepsilon_l^{Pr} \tag{3.29}$$

where ε^{el}, ε^{th} and ε^{ch} are the elastic, thermal expansion and chemical shrinkage strain components. For each lamina the local in-plane strains are:

$$\begin{pmatrix} \varepsilon_{11}^{T} \\ \varepsilon_{22}^{T} \\ \gamma_{12}^{T} \end{pmatrix} = \begin{pmatrix} \varepsilon_{11}^{el} \\ \varepsilon_{22}^{el} \\ \gamma_{12}^{el} \end{pmatrix} + \begin{pmatrix} \varepsilon_{11}^{Pr} \\ \varepsilon_{22}^{Pr} \\ \gamma_{12}^{Pr} \end{pmatrix} \tag{3.30}$$

or similarly using Eq. 3.17:

$$\begin{pmatrix} \varepsilon_{11}^{T} \\ \varepsilon_{22}^{T} \\ \gamma_{12}^{T} \end{pmatrix} = \begin{bmatrix} S_{11} & S_{12} & 0 \\ S_{12} & S_{22} & 0 \\ 0 & 0 & S_{66} \end{bmatrix} \begin{pmatrix} \sigma_{11} \\ \sigma_{22} \\ \sigma_{12} \end{pmatrix} + \begin{pmatrix} \varepsilon_{11}^{Pr} \\ \varepsilon_{22}^{Pr} \\ \gamma_{12}^{Pr} \end{pmatrix} \tag{3.31}$$

Note that $\gamma_{ij} = 2\epsilon_{ij}$ are the engineering strains. Inversion of the compliance tensor above results in the local stiffness tensor $\boldsymbol{C}_l$. Following appropriate transformation using the transformation matrix ***Tr***, the global lamina stiffness and process strains are determined as:

$$\mathbf{Q} = \mathbf{Tr}\ \mathbf{Q}_l\ \mathbf{Tr}^t \tag{3.32}$$

$$\varepsilon = (\mathbf{Tr}^{-1})^t\ \varepsilon_l \tag{3.33}$$

where:

$$\mathbf{Tr} = \begin{bmatrix} cos^2\theta & sin^2\theta & -2sin\theta cos\theta \\ sin^2\theta & cos^2\theta & 2sin\theta cos\theta \\ sin\theta cos\theta & -sin\theta cos\theta & cos^2\theta - sin^2\theta \end{bmatrix} \tag{3.34}$$

where θ is the angle of the local fiber longitudinal rotation compared to the global coordinate system. Having information of the global lamina process induced strains and stiffness, from laminate theory the normal loads and bending moments are found as:

$$\mathbf{N} = \sum_{i=1}^{n} \int_{z_{i-1}}^{z_i} \sigma_i dz = \sum_{i=1}^{n} \mathbf{Q}_i \int_{z_{i-1}}^{z_i} \varepsilon_i^{el} dz = \sum_{i=1}^{n} \mathbf{Q}_i \int_{z_{i-1}}^{z_i} (\varepsilon^0 + z\kappa - \varepsilon^{Pr}) dz \tag{3.35}$$

$$\mathbf{M} = \sum_{i=1}^{n} \int_{z_{i-1}}^{z_i} \sigma_i z dz = \sum_{i=1}^{n} \mathbf{Q}_i \int_{z_{i-1}}^{z_i} \varepsilon_i^{el} z dz = \sum_{i=1}^{n} \mathbf{Q}_i \int_{z_{i-1}}^{z_i} z(\varepsilon^0 + z\kappa - \varepsilon^{Pr}) dz \tag{3.36}$$

where ***N***=$[N_x, N_y, N_{xy}]^t$ and ***M***=$[M_x, M_y, M_{xy}]^t$ and n is the number of plies. In Eq. 3.35 and Eq. 3.36, ε^0 is the laminate middle surface global strain, κ is the curvature of the middle plane and z_i the through-thickness distance of each of the i^{th} lamina from the middle plane, as illustrated in Fig. 3.2. *Kirchhoff's hypothesis* is considered when bending the laminate in order to calculate the strain in each ply, for instance in the x-direction as:

$$\varepsilon_x = \varepsilon_x^0 + z\kappa_x \tag{3.37}$$

In this way, considering the in-plane laminate loads and bending moments, each effective lamina in-plane strain and curvature is expressed using Kirchhoff's hypothesis. Eq. 3.35 and Eq. 3.36 can be written in short using the well known **ABD** matrix components as:

$$\mathbf{N} = \mathbf{A}\varepsilon^0 + \mathbf{B}\kappa - \mathbf{N}^{Pr} \tag{3.38}$$

$$\mathbf{M} = \mathbf{B}\varepsilon^0 + \mathbf{D}\kappa - \mathbf{M}^{Pr} \tag{3.39}$$

The normal loads and bending moments from the curing process are then treated similarly to ordinary external forces following:

$$\mathbf{N}^{Pr} = \sum_{i=1}^{n} \mathbf{Q}_i \int_{z_{i-1}}^{z_i} \varepsilon_i^{Pr} dz \tag{3.40}$$

$$\mathbf{M}^{Pr} = \sum_{i=1}^{n} \mathbf{Q}_i \int_{z_{i-1}}^{z_i} \varepsilon_i^{Pr} z dz \tag{3.41}$$

Knowing the effective plate loads (**N, M**) from Eq. 3.38 and Eq. 3.39 as well as the laminate stiffness matrix **[A,B,D]**, ε_x^0 and κ_x can be determined:

$$\begin{pmatrix} \varepsilon_x^o \\ \kappa_x \end{pmatrix} = \begin{bmatrix} \mathbf{A} & \mathbf{B} \\ \mathbf{B} & \mathbf{D} \end{bmatrix}^{-1} \begin{pmatrix} \mathbf{N} \\ \mathbf{M} \end{pmatrix} \tag{3.42}$$

where:

$$[\mathbf{A,B,D}] = \sum_{i=1}^{n} \mathbf{Q}_i \left[(z_i - z_{i-1}), \frac{1}{2}(z_i^2 - z_{i-1}^2), \frac{1}{3}(z_i^3 - z_{i-1}^3) \right] \tag{3.43}$$

A is the extensional stiffness matrix, **B** is the coupling matrix and **D** is the bending stiffness matrix which all are sub-matrices in the lamina stiffness matrix **Q** and z_i is the distance from the laminate line of symmetry (in the thickness direction) to the respective lamina. Hence by determining the global laminate strain and curvature (ε^0 and κ) in Eq. 3.42, an expression for the total lamina strain is found using Eq. 3.37 after which the effective global stresses for each lamina can be readily determined. As will be shown later in the thesis, these calculations can be applied in an incremental manner in a 1D thermomechanical model such that transient stresses as well as process induced residual stresses and strains in a laminate plate can be determined.

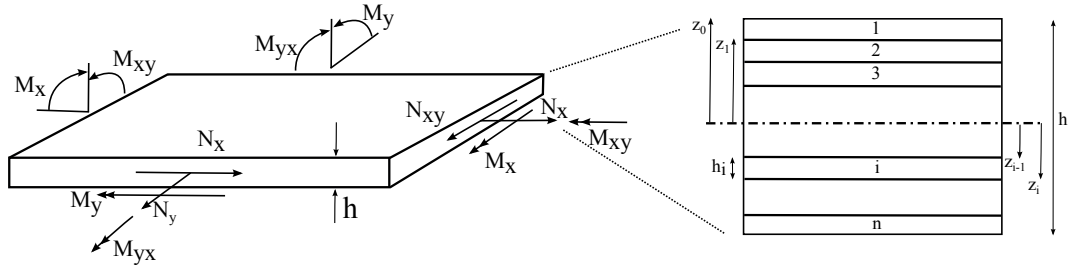

Figure 3.2: *In-plane normal load and bending moment notation (left) and through-thickness geometry of an n-layered laminate (right) [109]*

3.3 Summary

In this chapter, general thermomechanical modelling theory has been presented for the calculation of process induced strains and stresses. This has been done in general 3D

notation as well as for a 1D application using the well known classical laminate theory. In their current form, the constitutive relations presented are linear elastic, which does not totally represent the behaviour of the composite material during curing. In the following chapter, constitutive material models are discussed.

Chapter 4

Constitutive models

This chapter is dedicated to the different constitutive modelling approaches investigated that govern the cure dependent instantaneous stress-strain relation of the composite during curing. Of specific interest is how the change in resin mechanical behavior during cure is expressed. Three approaches are presented; (i) a linear elastic approach, (ii) a viscoelastic approach and (iii) a path-dependent approach. Note that a detailed description of the viscoelastic model can be found in the appended Technical Report I. The different approaches are presented subsequently after which a discussion of the pros and cons of each approach is given, as well as a brief evaluation of which modelling cases these best are applicable for. Since the mechanical properties of the composite reinforcement fibres remain relatively constant throughout manufacturing, which is a general assumption in most works [9, 41, 46, 92], focus subsequently is on modelling the matrix material behavior.

4.1 Linear Elastic models

Although the matrix resin is known to exhibit viscoelastic mechanical behavior throughout much of processing (which means also that the composite exhibits viscoelastic behavior in matrix dominated directions), a majority of process induced stress analysis work utilize elastic constitutive models [25, 28]. The two main reasons behind this is the complexity of viscoelastic models and the heavy material characterization necessary to correctly model the material, and secondly the ability of elastic models to offer reasonable predictions of the residual stress build-up during the cooling phase where in most cases the matrix is in glassy state.

One of the earliest linear elastic approaches presented for composites process modelling was proposed by Bogetti and Gillespie [9] based on an α-mixing rule. In this model, a linear dependence between the resin stiffness evolution and the cure degree α is assumed, such that the instantaneous isotropic resin (matrix) modulus E_m is expressed as [9]:

$$E_m = (1 - \alpha_{mod})E_m^o + \alpha_{mod}E_m^\infty + \gamma\alpha_{mod}(1 - \alpha_{mod})(E_m^\infty - E_m^o) \tag{4.1}$$

where

$$\alpha_{mod} = \frac{\alpha - \alpha_{gel}^{mod}}{\alpha_{diff}^{mod} - \alpha_{gel}^{mod}} \qquad \text{for} \qquad (-1 < \gamma < 1) \tag{4.2}$$

In the above, E_m^o and E_m^∞ are the fully uncured and fully cured temperature dependent resin moduli respectively. α_{gel}^{mod} and α_{diff}^{mod} represent the bounds of cure where the resin modulus develops, resembling in most cases the gelation and vitrification cure degree. The parameter γ is introduced to quantify the competing mechanisms between stress relaxation and chemical hardening - increasing γ corresponds to a more rapid increase in modulus at a lower cure degree [9]. For the model presented above, E_m^o and E_m^∞ are assumed constant, with the general assumption being that E_m^∞ corresponds to the fully cured glassy state Young's modulus at room temperature and while the uncured modulus E_m^o is simply chosen as an arbitrary small value or assumed to be equal E_m^∞/1000, meant to correspond to the polymer modulus in rubbery state [9, 92]. The corresponding instantaneous resin shear modulus is simply:

$$G_m = \frac{E_m}{2(1+\nu_m)} \tag{4.3}$$

where Poisson's ratio of the resin, ν_m, is assumed constant due to the fact that the largest deviations in Poisson's ratio occur at very low cure degrees, i.e. where the material modulus is still undeveloped [46]. In essence, E_m and G_m are a function of time and cure degree, but only indirectly a function of temperature through the cure degree. In some works, as a first approximation, Eq. 4.1 is used assuming $\gamma = 0$ and the bounds of cure α_{gel}^{mod} and α_{diff}^{mod} equal 0 and 1 respectively [34]. An example of the resin modulus development during cure using the linear elastic model is presented in Fig. 4.1 for a fictive cure case. A linear dependency is clearly seen between the cure degree and the modulus developments with time, i.e similar curve profiles are exhibited.

The instantaneous linear elastic approach presented above offers a simple method for process stress and strain predictions. However, since most mechanical properties are assumed to be constant once the resin is fully cured, irrespective of time or temperature, the approach can be said to offer an upper bound approximation to process induced stresses as stress-relaxation behaviour in the polymer matrix resin is not accounted for. Furthermore, material parameters are taken from elastic tests performed at room temperature. Hence overestimation of stresses is common [41].

Johnston [41] modified the linear elastic model proposed by Bogetti and Gillespie, incorporating temperature dependency. This is done by taking advantage of the relationship between the resin cure degree and the glass transition temperature T_g. The main effect of the included temperature dependency is the ability to model softening at elevated temperatures. The proposed model follows [41]:

$$E_m' = \begin{cases} E_m^o & \\ E_m^o + \frac{T^* - T_{C1}^*}{(T_{C2}^* - T_{C1}^*)}(E_m^\infty - E_m^o) & \text{for} \\ E_m^\infty & \end{cases} \begin{matrix} T^* < T_{C1}^* \\ T_{C1}^* \le T^* \le T_{C2}^* \\ T^* > T_{C2}^* \end{matrix} \tag{4.4}$$

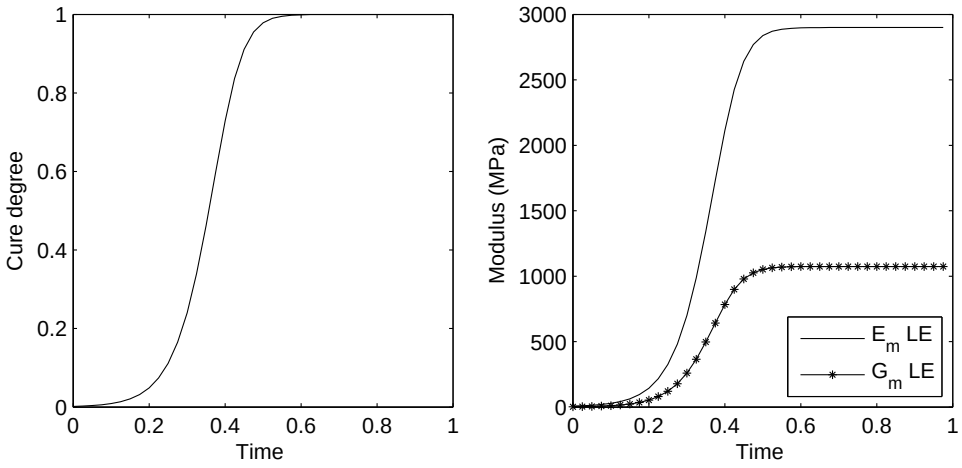

Figure 4.1: *Example of linear elastic (LE) approach matrix modulus development as a function of the cure degree*

$$E_m = E'_m[1 - a_{Er}(T - T_0)] \tag{4.5}$$

where T_{C1} and T_{C2} are the critical temperatures marking the bounds determining the linear variation of the modulus with T^*, defined as:

$$T^* = (T_g^0 + a_{Tg} \cdot \alpha) - T \quad \textit{and} \quad T_{C1}^* = T_{C1a}^* + T_{C1b}^* \cdot T \tag{4.6}$$

In the above, the temperature T^* can also simply be modelled as $T^* = T_g - T$. The remaining constants in the equations above are fitting parameters used to capture experimental data. In essence, Eq. 4.4 expresses a two-step temperature- and cure degree dependent resin modulus which also allows softening of the gelled resin once the cure temperature T is large enough to allow T^* to be smaller than the critical temperature T_{C2}. Physically this represents increasing the temperature of the vitrified resin resulting in transition back from glassy to rubbery state. The approach above has been coined as a Cure Hardening Instantaneous Linear Elastic (CHILE) resin model. This designation indicates that the modulus of the instantaneous linear elastic resin increases monotonically with the progression of cure [41]. An example of the cure dependent resin modulus development when using the CHILE approach is presented in Fig. 4.2. As opposed to the linear elastic model shown in Fig. 4.1, a step change in the modulus is seen.

Fig. 4.3 shows an example of resin modulus development as a function of temperature and cure degree for the CHILE model. The model is capable of capturing opposing effects of temperature-softening and cure-hardening, hence the name. Later in this chapter, an example of CHILE modulus development for a specific material case is presented.

For both the simple linear elastic and CHILE approaches presented above, the instantaneous resin mechanical properties calculated are used to update the effective composite material properties using the SCFM micromechanic approach. Following this, stress increments are determined as:

$$\Delta\sigma_{ij} = C_{ijkl}(\alpha, T)\Delta\varepsilon_{kl} \tag{4.7}$$

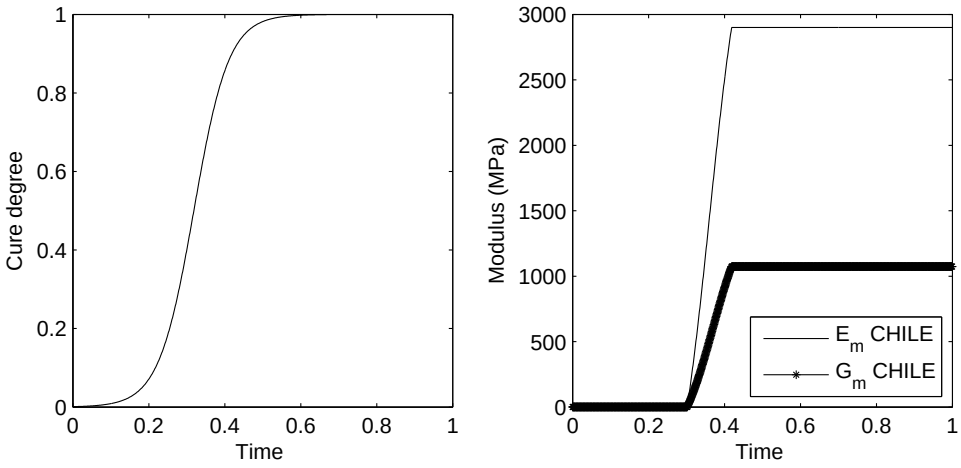

Figure 4.2: *Example of CHILE approach matrix modulus development as a function of the cure degree*

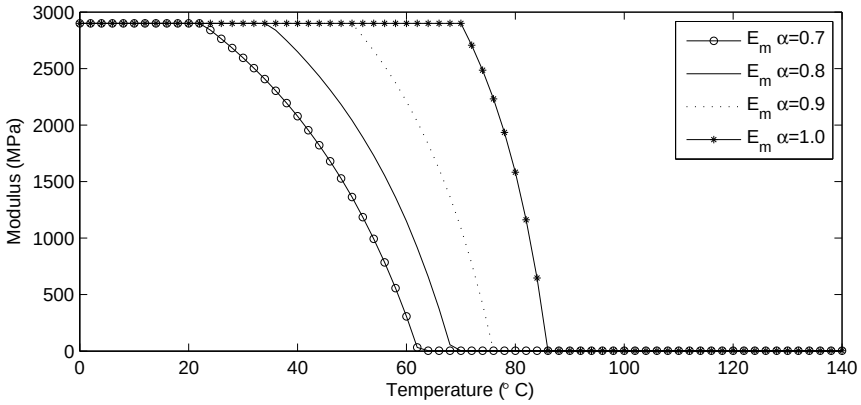

Figure 4.3: *Example of CHILE approach matrix modulus development as a function of temperature and the cure degree*

using the cure- and temperature dependent stiffness matrix C and the elastic strain increment. Hence the new stress at time $t + \Delta t$ is updated following:

$$\sigma_{ij}(t + \Delta t) = \sigma_{ij}(t) + \Delta\sigma_{ij} \tag{4.8}$$

where t is the current time and Δt is the time increment.

4.2 Viscoelastic models

In the current study, the need to investigate viscoelastic constitutive models arises from the following key arguments when considering the manufacture of large composite structures, such as those present in commercial wind turbine blades:

1. The thick laminate sections present optimal conditions for high curing peak temperatures due to the exothermic reaction during cross-linking. Thus curing in elevated temperatures due to external heating or internal effects is highly expected.

2. The large size and laminate thickness of the composite structures requires longer manufacturing cure times than otherwise necessary for smaller and thinner composites. Hence, long process periods are anticipated.

The above stated points lead to the notion that in some applications within VARMT of large composite structures, curing is carried out over long durations at elevated temperatures. As a result of this, viscoelastic behaviour is inevitably exhibited in the thermoset matrix material, hence use of viscoelastic constitutive models may be more accurate than the CHILE approach.

Various viscoelastic constitutive models have been proposed previously for the prediction of process induced stresses and strains in composites. Among the most significant works at a macromechanical scale are White and Kim [53, 54, 102], Prasatya et al. [80] and Ruiz and Trochu [84]. Investigations at a micromechanic level have also been carried out by Weitsman [100] and with similar formulations fore damage-coupled VE behaviour by Dai [16, 17]. Viscoelastic models have the capability of allowing more precise expressions of the mechanical behaviour of resin dominated composite properties but have the great disadvantage of being complex and computationally heavy, when compared to simpler elastic models. Regarding the complexity, appropriate characterization of the viscoelastic response of a polymer composite material is quite complex when considering rate and temperature effects. Characterization complexity is further increased when cure dependency is also of interest. Although several authors have proposed different characterization methodologies directly on composites or neat resins, and successfully applied these to models using temperature- and cure dependent shift factors, [80, 88, 102], viscoelastic formulations still remain computationally heavy due to the requirement of memory resources needed for the allocation of internal state variables that are saved at each model integration point. The accuracy of these models depends on how well material property variables fit experimental data - usually increasing the number of discrete fitting variables increases accuracy, equally increasing memory requirements as well as the need for experimental work to determine these variables.

Viscoelastic constitutive models generally exist in differential- or integral form. Due to apparent disadvantages with differential formulations for complex materials, see e.g. Technical report I, mainly integral formulations are used, as will be done here. To describe the behaviour of a linear viscoelastic material in integral form, the Boltzman superposition principle is applied (also referred to as *Duhamel*'s integral). The constitutive equation is given as [11]:

$$\sigma(t) = \int_0^t E(t-t')\frac{\partial \varepsilon(t')}{\partial t'}dt' \tag{4.9}$$

In the equation above, the stress output of a viscoelastic material at time t is expressed as a sum of the output for each individual time increment up to the current time t. In order to do this, material linearity is assumed [11]. In Eq. 4.9, a mathematical expression

for the relaxation modulus $E(t)$ is needed. When modelling epoxy resins (isotropic), the relaxation modulus $E_m(t)$ can be modelled using a Prony series representation of a Wiechert standard linear solid as [80, 88]:

$$E_m(t) = E_m^{\infty} + (E_m^0 - E_m^{\infty}) \sum_{i=1}^{n} w_i \cdot exp\left[-\frac{t}{\tau_i}\right] \tag{4.10}$$

where E_m^{∞} is the fully relaxed resin modulus, E_m^o is the unrelaxed resin modulus, w_i are weight fitting factors, τ_i are relaxation times and n is the number of Maxwell spring-damper elements in series, illustrated in Fig. 4.5. The use of a Wiechert spring-damper model to represent resins is adequate because thermosetting polymers exhibit a bound in stress relaxation due to unbreakable cross-links in the polymer structure, in the model represented by the linear spring element. Alternatives to Prony series type models have also been proposed. Kim and White [53] used a power law representation to describe the relaxation modulus of a epoxy resin, given as:

$$E_m(t) = E_m^o \cdot exp\left[-\left(\frac{t}{\tau_i}\right)^b\right] \tag{4.11}$$

where b is a material constant and τ_p is the peak relaxation time. However, it was found that a single value of b is not sufficient to represent the entire stress relaxation transition behaviour of the epoxy over a wide temperature range, making the power law formulation unsuitable for process modelling cases at high elevated temperatures. Ruiz & Trochu [84], modified the power-law formulation for a polyester resin, resulting in a simple precise model for the relaxation modulus without the use of extensive least-square fitting techniques for the determination of Prony series data, given as:

$$E(t) = E^u \cdot exp\left[-\Omega_1(t+\tau_0)^{\Omega_2}\right](t+\tau_0)^{-\Omega_3} \tag{4.12}$$

where Ω_1,Ω_2 and Ω_3 are fitting parameters, and τ_0 is the reference relaxation time. However, determination of these constants was found to be cumbersome, requiring special experimental techniques, discussed in [84]. Common for the above mentioned formulations is that shift functions are needed to capture the influence of cure hardening or temperature softening on the material relaxation time.

The influence of temperature on the relaxation behaviour of polymers is commonly accounted for by the Time-Temperature-Superposition-Principle. This principle builds upon the notion that time and temperature effects on a polymer are similar and this is useful when determining polymer master curves [72]. Mathematically, the time-temperature equivalence can be expressed as [39, 72]:

$$E(t, T_1) = E(t/a_T, T_2) \tag{4.13}$$

stating that the modulus at time t at one temperature T_1 is equal to the modulus at temperature T_2 at the time $t = t/a_T$, where a_T is the temperature shift function. The shift factor is generally found using the WLF equation (from M.L. Williams, R.F. Landel and J.D. Ferry [39]):

$$log(a_T) = log\left(\frac{\tau(T)}{\tau(T_{ref})}\right) = \frac{-C_1(T - T_{ref})}{C_2 + (T - T_{ref})} \tag{4.14}$$

where the C_1 and C_2 are constants and have the "universal" values of 17.44 and 51.6 respectively under the assumption that the glass transition temperature T_g is used as the reference temperature T_{ref}. Having an expression for the shift factor a_T, temperature dependence can now be implemented and Eq. 4.9 can be rewritten as:

$$\sigma(t) = \int_0^t E_{T_0}(\xi(t) - \xi(t'))\frac{\partial \varepsilon}{\partial t'}dt' \tag{4.15}$$

where $\xi(t)$ and $\xi(t')$ are the so called *reduced times* defined as:

$$\xi(t) \equiv \int_0^t \frac{1}{a_T}\zeta \quad and \quad \xi(t') \equiv \int_0^{t'} \frac{1}{a_T}\zeta \tag{4.16}$$

Essentially the function of the shift factor is to make "time run *faster* or *slower*" depending on the difference between the current temperature and reference temperature, and likewise for the cure degree. An in-depth description of the mechanisms are found in the appended Technical Report I. A polymer's T_g can be determined as the point where the material exhibits a change in its thermal expansion behaviour as a result of the change in the material properties at gelation, see e.g. [11, 39, 72]. At this material discontinuity, Ferry (1961) noted that the WLF equation is known to be only valid above the T_g. A shift factor below the T_g is developed based on Arrhenius activation energy equation, which is more valid [11]:

$$log(a_T) = log\frac{\tau(T)}{\tau(T_g)} = -\frac{E_a}{2.303R}\left(\frac{1}{T} - \frac{1}{T_g}\right) \tag{4.17}$$

where E_a is the activation energy and R is the gas constant. To account for effects above and below T_g, i.e. combined WLF and Arrhenius behaviour, a generalized Vogel equation is used [88]:

$$log(a_T) = log\frac{\tau(T)}{\tau(T_g)} = \frac{C}{T - T_\infty} - \frac{C}{T_{ref} - T_\infty} \tag{4.18}$$

where C is a constant, T_∞=0K is the absolute temperature and T_{ref} is the reference temperature for the viscoelastic master curve of the fully cured material ($\alpha = 1.0$). In a similar manner, the effects of the cure degree (or $conversion$) can be accounted for by applying time-conversion superposition, using a cure shift factor a_α as done by Simon, McKenna & Sindt [88]:

$$log(a_\alpha) = log\left(\frac{\tau(T_g(\alpha))}{\tau(T_g(\alpha_{ref}))}\right) = -\left(\frac{C}{T_g(\alpha) - T_\infty} - \frac{C}{T_g(\alpha_{ref}) - T_\infty}\right) \tag{4.19}$$

where cure degree-dependent glass transition temperatures are used. Assuming that the reference cure degree α_{ref}=1.0 and that T_{ref}=$T_g(\alpha_{ref})$, then the cure shift factor a_α and temperature shift factor a_T can be combined to give:

$$log(a_{T,\alpha}) = log\left(\frac{\tau(T, T_g(\alpha))}{\tau(T_{ref}, T_g(\alpha_{ref}))}\right) = \frac{C}{T - T_\infty} - \frac{C}{T_g(\alpha_{ref}) - T_\infty} \tag{4.20}$$

In the above equation, cure degree dependence is included by having a cure dependent glass transition temperature given by the DiBenedetto equation. Using the DiBenedetto equation, cure dependency is introduced in the WLF equation. Hence the relaxation modulus (Equation Eq. 4.10) would become:

$$E(\alpha, T, t) = E^{\infty} + (E^{o} - E^{\infty}) \sum_{i=1}^{n} w_i \cdot exp\left[-\frac{t}{a_{T,\alpha} \cdot \tau_i}\right] \tag{4.21}$$

An alternative approach is proposed by Kim & White [53]. Experimental testing of an epoxy resin at different cure degrees revealed that the peak stress relaxation time τ_p increases as the degree of cure increases. Assuming that this is also true for the stress relaxation behaviour at any cure degree, an expression for the discrete relaxation time at any cure degree was formulated, using discrete relaxation times at a reference degree of cure [53]:

$$log(\tau_i(\alpha)) = log(\tau_i(\alpha_{ref})) + [f'(\alpha) - (\alpha - \alpha_{ref}) log(\lambda_i')] \tag{4.22}$$

where τ_i is each discrete relaxation time, α_{ref} is the reference degree of cure where the stress relaxation is known and:

$$f'(\alpha) = \frac{T_g(\alpha)}{T_g(\alpha_{ref})} - 1 \tag{4.23}$$

$$\lambda_i' = \frac{\tau_p(\alpha_{ref})}{\tau_i(\alpha_{ref})} \tag{4.24}$$

where $\tau_p(\alpha_{ref})$ is the peak relaxation time at the reference cure degree. Having a cure dependent expression for the relation times, a separate temperature shift factor is used:

$$log(a_T) = c_1(\alpha)T + c_2(\alpha) \tag{4.25}$$

where:

$$c_1(\alpha) = -a_1 \cdot exp\left[\frac{1}{\alpha - 1}\right] - a_2 \tag{4.26}$$

$$c_2(\alpha) = -T_{ref} \cdot c_1(\alpha) \tag{4.27}$$

where a_1 and a_2 are constants. Hence the relaxation modulus (Equation Eq. 4.10) in this case would become:

$$E(\alpha, T, t) = E^{\infty} + (E^{o} - E^{\infty}) \sum_{i=1}^{n} w_i \cdot exp\left[-\frac{t}{a_T \cdot \tau_i(\alpha)}\right] \tag{4.28}$$

Common for the approaches presented above is that no formal proof of validity is present in the literature for the combination of degree of cure with time-temperature superposition, though the WLF-type expressions are very popular. In the subsequent sections however, the model proposed by Kim & White [53] is used due to its well accounted experimental background.

For illustrative purposes, the relaxation modulus development as a function of temperature and cure degree is shown in Fig. 4.4, using Eq. 4.28, for the prony series data is presented in Tab. 4.1. The given data is fit to the room temperature relaxation modulus of an infusion epoxy resin system. In Fig. 4.4 thermal softening and cure hardening (i.e. curve shift to the right) is clearly seen.

Element	τ_i (min)	w_i
1	1.92E1	0.059
2	2.92E2	0.066
3	8.99E3	0.083
4	9.5E3	0.018
5	9.93E3	0.014
6	9.94E3	0.362
7	1.05E4	0.324
8	1.99E4	0.049
9	2.22E4	0.025

Table 4.1: *Prony series data used in the calculation of neat resin relaxation modulus presented in Fig. 4.4*

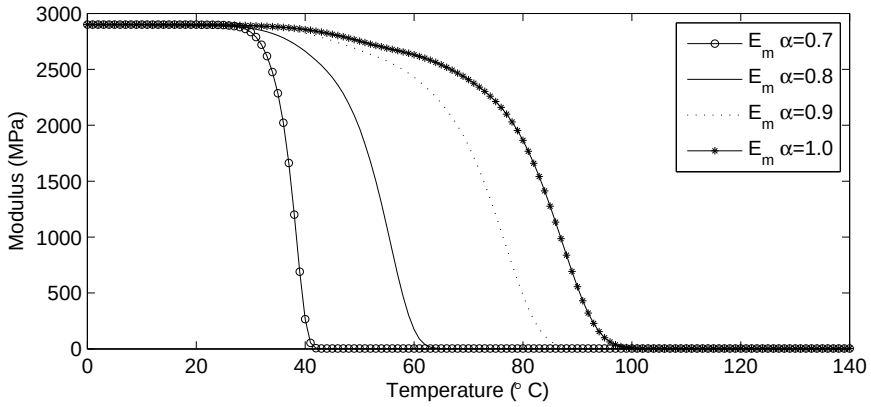

Figure 4.4: *Example of viscoelastic relaxation modulus development as a function of temperature and the cure degree*

Customary for all viscoelastic models however, is that the entire history of the material needs to be accounted for in order to accurately describe the current stress or strain state. If the integral expressions presented above in their current form are to be implemented within the framework of an FE model at each integration point as time marches forward it would be computationally expensive. Hence, recursive formulations for viscoelastic models exist in literature, designed for numerical implementation, see e.g [17, 102, 113]. These recursive formulations enable a more efficient approach through storage of previous time step history state variables only, as opposed to recalculation of the entire time span with each new increment. In the current work, an incremental constitutive viscoelastic formulation proposed by Zocher [112] is used due to the following key arguments:

- The incremental formulation is accomplished in closed-form, resulting in a simple recursive relationship accounting for material history in the form of linear algebraic equations

- A constant strain rate during each time step is assumed, as opposed to constant stress or strain, resulting in a model capable of predicting relaxation- and creep-type behaviour simultaneously
- Lastly, the formulation allows for simple change of the phenomenological mechanical model used, be it a generalized Kelvin model, Wiechert model etc. Along this line simple adjustment of the number of damper and spring elements used in these models is possible.

Elaborating on the second bullet above, viscoelastic formulations where a constant stress over each time step is assumed, are known to offer good creep predictions but are poor in predicting stress relaxation behaviour. Alternatively, formulations where a constant strain is assumed, adequately predict relaxation behaviour but are poor at creep predictions [113]. In using a constant strain rate assumption, these disadvantages are avoided [112].

The resin time- temperature- and cure dependency is modelled using Eq. 4.10 and effective composite properties are found using SCFM. Reduced time is used according to Eq. 4.16 and subdivided into discrete intervals such that the new reduced time $\xi_{n+1} = \xi_n + \Delta\xi$. The general three-dimensional integral-form constitutive equation using reduced time is given as [11, 112]:

$$\sigma_{ij}(\xi) = \int_0^{\xi} C'_{ijkl}(\xi - \xi') \frac{\partial \varepsilon_{kl}(\xi')}{\partial \xi'} d\xi' \tag{4.29}$$

where:

$$\xi(t) \equiv \int_0^t \frac{1}{a_{T,\alpha}} \zeta \quad and \quad \xi(t') \equiv \int_0^{t'} \frac{1}{a_{T,\alpha}} \zeta \tag{4.30}$$

are reduced times dependent on temperature and cure degree, and the stiffness matrix:

$$C'_{ijkl} = C^{\infty}_{ijkl} + \frac{1}{\Delta\xi} \sum_{m=1}^{N} \eta_{ijkl_m} \left(1 - exp \left[-\frac{\Delta\xi}{\tau_m} \right] \right) \tag{4.31}$$

The equations above represent a Wiechert model, see Fig. 4.5, with N elements (not to be confused with FEM elements). The viscosity of each discrete element is determined as $\eta_{ijkl_m} = \tau_m \cdot C_{ijkl_m}$, where C_{ijkl_m} are discrete Weichert model stiffnesses. In Eq. 4.30, $a_{T,\alpha}$ is the temperature- and cure dependent shift functions. Eq. 4.29 can be expressed incrementally as:

$$\Delta\sigma_{ij} = C'_{ijkl} \Delta\varepsilon_{kl} + \Delta\sigma^R_{ij} \tag{4.32}$$

The stress residual is given as [112]:

$$\Delta\sigma^R_{ij} = -\sum_{m=1}^{N} \left(1 - exp \left[-\frac{\Delta\xi}{\tau_m} \right] \right) S_{ijkl_m}(\xi_n) \tag{4.33}$$

where the internal state variable is defined as:

$$S_{ijkl_m}(\xi_n) = exp\left[-\frac{\Delta\xi}{\tau_m}\right] S_{ijkl_m}(\xi_n - \Delta\xi) + \eta_{ijkl_m}\dot{\varepsilon_{kl}}\left(1 - exp\left[-\frac{\Delta\xi}{\tau_m}\right]\right) \tag{4.34}$$

where $S_{ijkl_m}(\xi_n - \Delta\xi)$ is the "old" internal state variable from the previous time step. In the above equations, a key assumption is the constant strain rate approximation between each time step:

$$\frac{\partial\varepsilon_{kl}(\xi')}{\partial\xi'} \approx \dot{\varepsilon_{kl}} \equiv \frac{\Delta\varepsilon_{kl}}{\Delta\xi} \tag{4.35}$$

where $\Delta\varepsilon_{kl}/\Delta\xi$ is known from the previous step at reduced time ξ_n. Having an expression of the stress increment, the new stress can be updated at the end of each time step as:

$$\sigma_{ij}(\xi_{n+1}) = \sigma_{ij}(\xi_n) + \Delta\sigma_{ij} \tag{4.36}$$

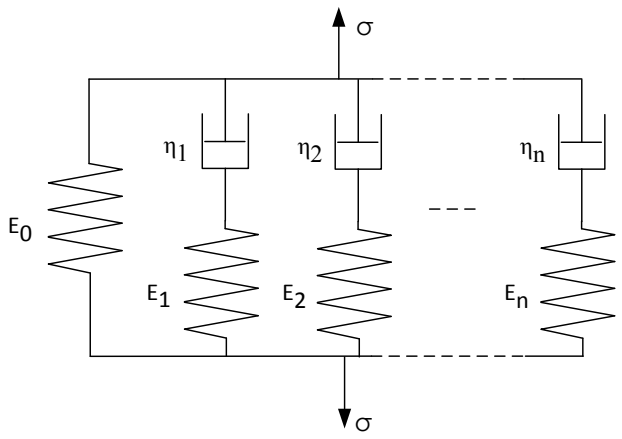

Figure 4.5: *Example of Wiechert-type model consisting of a linear spring with n-1 Maxwell elements in series.*

In other works [16, 17] a similar approach using a constant strain rate assumption is used with the exception that the general state of stress is subdivided into deviatoric and dilatatoric stress tensors. Separating the stress tensor into dilatational (volumetric) and deviatoric components is a result of the observation that viscoelastic deformations in polymers are predominantly a result of changes in shape [11]. Hence volumetric effects can be neglected simplifying the problem.

4.3 Path-dependent model

Svanberg [92] proposed a path-dependent constitutive model derived from a linear viscoelastic constitutive formulation. The path-dependent approach is a limiting case of linear viscoelasticity where material rate dependence is replaced by a path dependence on the temperature and cure degree. This is enabled through use of the material temperature during the cure process and the corresponding matrix glass transition temperature T_g. In

effect by constantly evaluating which material state the matrix material is in, depending on the matrix T_g and the cure temperature. This is expressed constitutively as [92]:

$$\sigma = \begin{cases} C^r_{ijkl}(\varepsilon^{Tot}_{kl} - \varepsilon^{Pr}_{kl}) & \text{for } T \leq T_g(\alpha) \\ C^g_{ijkl}(\varepsilon^{Tot}_{kl} - \varepsilon^{Pr}_{kl}) - (C^g_{ijkl}C^r_{ijkl})(\varepsilon^{Tot}_{kl} - \varepsilon^{Pr}_{kl}) & \text{for } T < T_g(\alpha) \end{cases} \tag{4.37}$$

where C^r_{ijkl} and C^g_{ijkl} are the rubbery and glassy state stiffness tensors corresponding to the fully relaxed and unrelaxed stiffnesses. ε^{Tot}_{kl} are the total strains. The cure dependent glass transition temperature can be determined using the DiBenedetto equation (see Eq. 2.1). In order to allow numerical implementation, incrementalization of the constitutive model is necessary, expressed as [92]:

$$\Delta\sigma = \begin{cases} C^r_{ijkl}(\Delta\varepsilon^{Tot}_{kl} - \Delta\varepsilon^{Pr}_{kl}) - \beta_{ij}(t + \Delta t) & \text{for } T \leq T_g(\alpha) \\ C^g_{ijkl}(\Delta\varepsilon^{Tot}_{kl} - \Delta\varepsilon^{Pr}_{kl}) & \text{for } T < T_g(\alpha) \end{cases} \tag{4.38}$$

where the internal history state variable $\beta_{ij}(t + \Delta t)$ at the new time increment is updated as [92]:

$$\beta_{ij}(t + \Delta t) = \begin{cases} 0 & \text{for } T \leq T_g(\alpha) \\ \beta_{ij}(t) + (C^g_{ijkl}C^r_{ijkl})(\varepsilon^{Tot}_{kl} - \varepsilon^{Pr}_{kl}) & \text{for } T < T_g(\alpha) \end{cases} \tag{4.39}$$

Using Eq. 4.39 the stress history is accumulated at temperatures below T_g and fully relaxed above T_g when the material state transition from glassy to rubbery state occurs. During this transition, the material stiffness is also reduced to resemble behaviour in the rubbery state.

The prerequirements needed for the path-dependent model to be valid are [92, 95]:

- The material should exhibit linear elastic behavior in the glassy and the rubbery state regimes, i.e. constant mechanical properties in these states exist
- Heating rates through the devitrification transition (i.e. the glass to rubber transition) are large enough and cooling rates through vitrification are slow enough to exclude explicit rate dependence. In other words, an instantaneous transition occurs.

The apparent advantages with the path-dependent approach is the ability to model stress relaxation behaviour for cure processes at elevated temperatures, or for instance where post curing is utilized, through the β history state variable without the need for cumbersome viscoelastic mechanical characterization data. In a similar manner as with the previous constitutive approaches, an example of the path-dependent model temperature and cure dependency is given in Fig. 4.6. An instantaneous reduction in the modulus (not to be confused with stress relaxation) is exhibited once $T > T_g$, shown as the sharp reduction in the modulus as the temperature is increased.

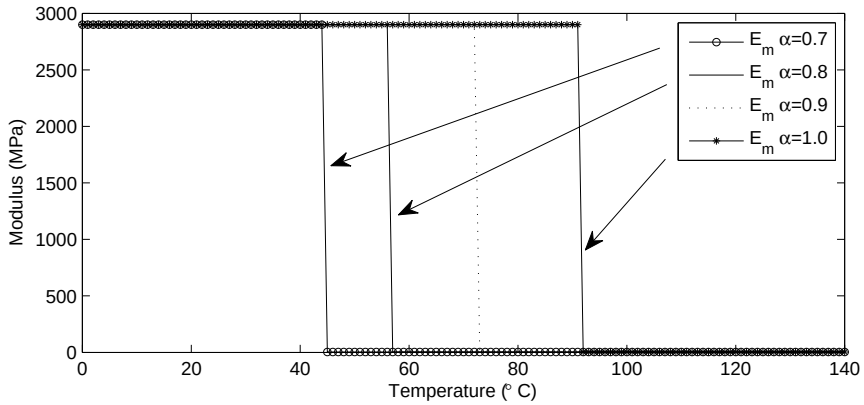

Figure 4.6: *Example of Path-dependent modulus development as a function of temperature and the cure degree*

To summarize, the approaches presented in this chapter are compared to each other in Fig. 4.7 and overlaid with the relaxation modulus development of a DGEBA[1] infusion epoxy resin (called "Hexion RIM135") with an amine curing agent from Momentive^{TM}. This epoxy is commonly used in the manufacture of wind turbine blades.

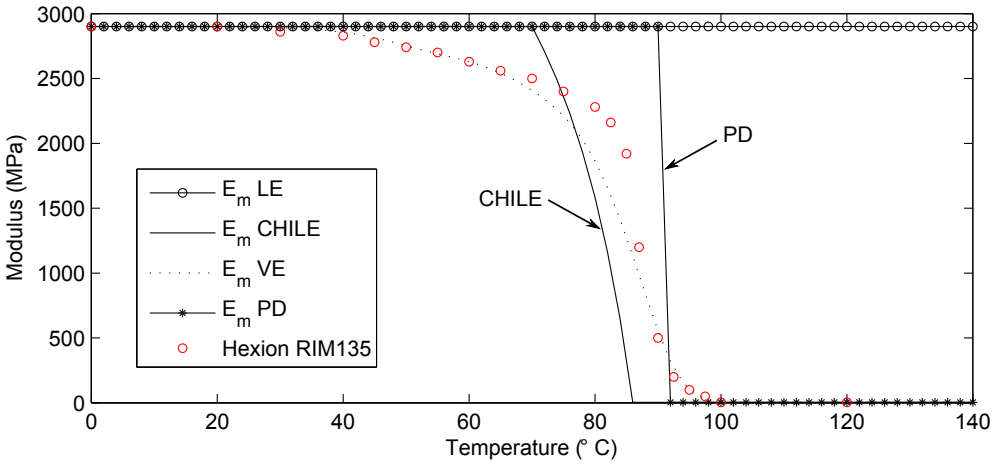

Figure 4.7: *Summary of the different constitutive models modulus development as a function of temperature for a cure degree α=1.0 overlaid with the fully cured relaxation modulus of an epoxy resin (Hexion RIM135).*

In Fig. 4.7, it is seen that the viscoelastic (VE) model offers the best approximation of the modulus development as a function of temperature. The much simpler CHILE approach in general captures the main behaviour of the epoxy quite well, but with shortcomings throughout the entire transition regime. The path dependent approach (PD) exhibits an instantaneous shift in stiffness not offering any approximation of the transition region, which is expected and was also stated as one of the model assumptions. Lastly, since no temperature dependency exists in the simple linear elastic (LE) model, no changes in the modulus is experienced, irrespective of the temperature. It may seem that the CHILE model offers the best accuracy, besides the VE model, but selection of the correct fitting

[1]Diglycidyl Ether Bisphenol-A

parameters used in Eq. 4.4 to Eq. 4.6 is left to the user if no cure dependent relaxation data exists a priori. Hence the possibility of underestimating the matrix material stiffness development is present.

A comparison of model predictions of manufacturing induced strains in a thick laminate plate using the different constitutive models presented above, is conducted in Chapter 6 and Chapter 7, as well as in the appended Paper II.

4.4 Summary

In this chapter, different constitutive approaches have been presented for modelling the matrix stiffness evolution during curing. These include (i) a simple linear elastic model only dependent on the resin cure degree, (ii) a cure hardening instantaneous linear elastic (CHILE) model taking simple temperature dependency into account, (iii) a viscoelastic approach including temperature and cure degree based rate dependency and finally (iv) a path-dependent model which is a limiting case of the viscoelastic approach. The different models will be analyzed for different modelling cases subsequently in the thesis.

Chapter 5

1D Modelling

In this chapter, a 1D thermomechanical model is presented for the calculation of in-plane process induced residual stresses and strains during curing, driven by through-thickness temperature and cure gradients within a laminate plate. In the manufacture of large composite structures such as wind turbine blades, a majority of the structural parts exist in the form of laminate plate sections, hence the choice of considering a simple plate. The term *plate* is used in this context defining a thin[1] structure where a state of plane stress prevails, allowing stresses in the thickness direction to be neglected. The 1D model presented in this chapter is the basis of the work in the appended Paper I, concerning a coupled curing and visco-mechanical void growth model in thick thermosetting composite laminates. The 1D model is also used in Papers III and V for the determination of thermal heat transfer coefficients through inverse modelling.

First, the model is presented with focus on the thermal and mechanical approach used for model implementation in MATLAB[2]. After this, validation examples are given by model prediction comparisons with the work by Bogetti and Gillespie [9]. Finally, the case of modelling void growth during composites processing in a 1D discretized domain is presented.

5.1 Introduction to 1D laminate model

A UD laminate plate is considered, as previously presented in Fig. 2.1 in Section 2.1. The basis of a single dimensional thermomechanical model, where the direction of interest is through the laminate thickness (i.e. global z-coordinate) requires the following assumptions to be valid:

- The laminate plate length and width are much larger than the plate thickness, hence a state of plane stress exists
- The dominant heat flow direction exists in the plate through-thickness direction

[1] Small thickness compared to other dimensions

[2] MATLAB is a registered trademark of Math Works

- All loading and material properties in the in-plane longitudinal (x-direction) and transverse (y-direction) respectively, remain constant
- Only changes in loading (thermal) and mechanical material behaviour occur in the plate thickness direction

A general description of the model structure and the different calculation steps and considerations taken are presented henceforth, divided in the thermal- and mechanical modelling steps respectively. In Fig. 5.1, the thermal and mechanical discretization of the 1D problem is illustrated, for the simple case of symmetric thermal boundary conditions. The problem assumed is the uniform surface heating of a laminate plate, for instance placed in an autoclave oven for cure.

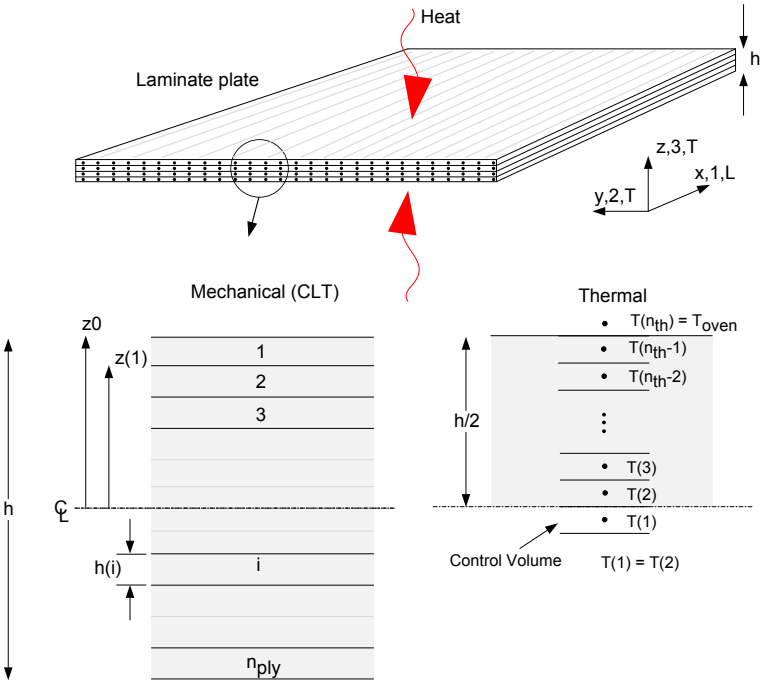

Figure 5.1: *Schematic of 1D problem showing the respective mechanical Classical Laminate Theory (CLT) and thermal problem discretization and boundary conditions assumed.*

5.1.1 Thermal model

The general modelling approach used is consistent with similar 1D investigations [9, 62, 64], however, in the current work the thermal model is discretized spatially in a finite volume framework with a backward Euler finite difference time discretization, see e.g. [29] for details. For the 1D analysis considered, Fourier's heat conduction equation presented in Eq. 3.1 is reduced to 1D:

$$\rho C_p \frac{\partial T}{\partial t} = k_z \left(\frac{\partial^2 T}{\partial z^2} \right) + \dot{Q}''' \tag{5.1}$$

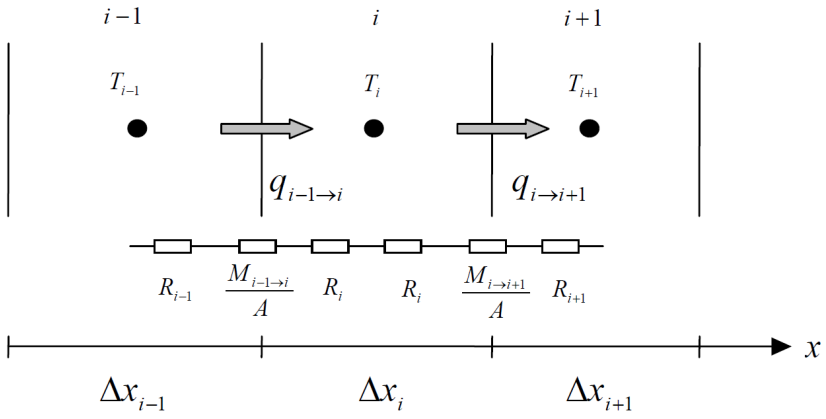

Figure 5.2: *Schematic of heat balance in 1D Cartesian control volume in the x-coodinate [29]*

considering heat conduction in the z-direction only. A 1D Cartesian discretization through the laminate thickness is considered, discretized using n_{th} number of control volumes (CV) for the thermal problem. The principle of heat conservation is used by taking the heat balance for each CV as illustrated in Fig. 5.2. Any change in the heat content pr. time unit equals the sum of the heat fluxes into the CV plus any internal heat generation that may occur. This is expressed for the i'th CV as [29]:

$$V_i(\rho C_p)_i \frac{\partial T_i}{\partial t} = q_{i-1\to i} - q_{i\to i+1} + \dot{Q}_i \tag{5.2}$$

where V_i is the CV volume, $\dot{Q}_i$ is the internal heat generation and the heat flux q is expressed as:

$$q_{i-1\to i} = -\frac{T_i - T_{i-1}}{R_{i-1\to i}} \quad \text{and} \quad q_{i\to i+1} = -\frac{T_{i+1} - T_i}{R_{i\to i+1}} \tag{5.3}$$

for the flux into CV i from $i-1$ and out of CV i to $i+1$. In Eq. 5.3, the concept of thermal resistance is used where the combination of thermal conductivity, material thickness and area are considered together as the resistance to heat flow, defined as [29]:

$$R_{th}^{Cond} = \frac{\Delta z}{k_z A_{xy}} \tag{5.4}$$

where the resistance sub- and superscript denote thermal conduction resistance, Δz is the heat flow distance and A is the surface area perpendicular to the heat flow direction, i.e. on the xy-plane. A coupling in series is carried out of all resistance terms present in the heat flow direction within and between each CV. Inserting this expression for the resistances in and out of the CV (see Fig. 5.2), discretizing the time derivative and dividing by the surface area Eq. 5.2 is rewritten as:

$$\Delta x_i(\rho C_p)_i \frac{\Delta T_i}{\Delta t} = \frac{T_{i-1} - T_i}{\frac{\Delta z_{i-1}}{2k_{i-1}} + \frac{\Delta z_i}{2k_i} + \frac{M_{i-1\to i}}{A}} + \frac{T_{i+1} - T_i}{\frac{\Delta z_i}{2k_i} + \frac{\Delta z_{i+1}}{2k_{i+1}} + \frac{M_{i\to i+1}}{A}} + \frac{\dot{Q}_i}{A} \tag{5.5}$$

As illustrated in Fig. 5.2, the temperatures are calculated at the control volume center, hence the heat flow distance Δz for each resistance term is halved. In this work constant material properties are considered, as well as a uniform CV discretization through the thickness of the laminate, hence the following notation is also valid: $(\rho C_{p,i})$=ρC_p, k_i=k and Δx_i=Δx. Furthermore, the interface resistance (i.e. $M_{i-1\rightarrow i}/A$ and $M_{i\rightarrow i+1}/A$) is only non-zero at the boundaries where thermal contact may be present. However, if the heat transfer coefficient h is known a priori[3], the interface resistance term is simply:

$$\frac{M_{i-1\rightarrow i}}{A} = \frac{1}{h \cdot A} \tag{5.6}$$

In the next step, conductivity and capacity weighting functions are used, defined respectively as [29]:

$$H_i^{Con} = \frac{1}{\frac{\Delta z_{i-1}}{2k_{i-1}} + \frac{\Delta z_i}{2k_i} + \frac{M_{i-1\rightarrow i}}{A}} \tag{5.7}$$

and

$$H_i^{Cap} = \frac{\Delta z_i (\rho C_p)_i}{\Delta t} \tag{5.8}$$

These weighting functions are substituted into Eq. 5.5 resulting in the reduced heat balance equation:

$$H_i^{Cap} \Delta T_i = H_i^{Con}(T_{i-1} - T_i) + H_{i+1}^{Con}(T_{i+1} - T_i) + \frac{\dot{Q}_i}{A} \tag{5.9}$$

In Eq. 5.9, the heat balance for the i'th CV is expressed in a form that is fit for numerical implementation. Since the problem we wish to solve consists of a highly non-linear heat generation term due to the equations expressing the cure kinetics of the resin material (presented earlier in Section 3.1), an implicit formulation is chosen, thus avoiding any limitations that may arise when using the explicit method regarding choice of simulation time step Δt. Using an implicit formulation for the current 1D problem is not considered to be a problem, since computation times are still quite fast, as will be discussed later in the chapter. Solution using an implicit formulation requires expressing the right-hand side of Eq. 5.9 at the new time level of calculation, i.e. $t + \Delta t$ as well as expanding ΔT as follows:

$$H_i^{Cap}(T_i^{t+\Delta t} - T_i^t) = H_i^{Con}(T_{i-1}^{t+\Delta t} - T_i^{t+\Delta t}) + H_{i+1}^{Con}(T_{i+1}^{t+\Delta t} - T_i^{t+\Delta t}) + \frac{\dot{Q}_i^{t+\Delta t}}{A} \tag{5.10}$$

An equation with 3 unknowns ($T_{i-1}^{t+\Delta t}, T_i^{t+\Delta t}, T_{i+1}^{t+\Delta t}$) now exists. Eq. 5.10 is rewritten, isolating terms that will be designated as solution coefficients, for the respective unknowns:

$$-H_i^{Con} T_{i-1}^{t+\Delta t} + (H_i^{Cap} + H_i^{Con} + H_{i+1}^{Con}) T_i^{t+\Delta t} - H_{i+1}^{Con} T_{i+1}^{t+\Delta t} = H_i^{Cap} T_i^t + \frac{\dot{Q}_i^{t+\Delta t}}{A} \tag{5.11}$$

[3]Not to be confused with the thickness of each ply, shown in Fig. 5.1

or alternatively:

$$a_i \cdot T_{i-1}^{t+\Delta t} + b_i \cdot T_i^{t+\Delta t} + c_i \cdot T_{i+1}^{t+\Delta t} = d_i \tag{5.12}$$

where

$$\begin{aligned} a_i &= -H_i^{Con} \\ b_i &= H_i^{Cap} + H_i^{Con} + H_{i+1}^{Con} \\ c_i &= -H_{i+1}^{Con} \\ d_i &= H_i^{Cap} T_i^t + \frac{\dot{Q}_i^{t+\Delta t}}{A} \end{aligned} \tag{5.13}$$

Note that no iterations due to the thermal properties' dependency on temperature are performed, i.e the coefficients a_i, b_i, c_i and d_i for $i = 1, ..., n_{th}$ are expressed using the known temperatures $T_1^t, ..., T_{n_{th}}^t$ at the current time t. This is conducted in an equation system consisting of $n_{th} - 1$ equations for the *inner* CV nodes in the discretized region as well as 2 equations for the boundaries.

Initially, symmetric through-thickness thermal and geometric conditions are considered, hence only heat conduction and cure kinetics calculations are carried out for half of the laminate thickness and results are mirrorred across the mid plane for use in the mechanical calculations. However, this condition can simply be changed to consider the entire laminate thickness in the thermal calculations, if non-symmetric boundary temperatures or tooling is considered. The temperature at the laminate plate boundary, i.e. the top plate surface is known ($\bar{T}(n_{th})$ in Fig. 5.1), hence a Dirichlet thermal boundary condition is applied at the boundary control volume $CV(n_{th})$. At the plate thickness center line, the Neumann condition is applied as it is assumed that no heat flux across the center line exists due to symmetry, i.e. $q_{1\to 2} = 0$. This is implemented for the boundary- and center-line CV as:

$$\begin{aligned} i = n_{th}: &\quad T_{n_{th}} = \bar{T}_{n_{th}}(t) \quad \Rightarrow \quad a_{n_{th}} = 0 \quad b_{n_{th}} = 1 \quad d_{n_{th}} = \bar{T}_{n_{th}}(t) \\ i = 1: &\quad q_{1\to 2} = T_1 - T_2 = 0 \quad \Rightarrow \quad b_i = 1 \quad c_i = -1 \quad d_i = 0 \end{aligned} \tag{5.14}$$

The equations are collected in a system of equations of triagonal matrix form and solved using Gauss elimination or matrix left division in MATLAB for the temperatures below:

$$\begin{bmatrix} b_1 & c_1 & & & & \\ a_2 & b_2 & c_2 & & & \\ & \cdots & \cdots & \cdots & & \\ & & \cdots & \cdots & \cdots & \\ & & & a_{n-1} & b_{n-1} & c_{n-1} \\ & & & & a_{n_{th}} & b_{n_{th}} \end{bmatrix} \cdot \begin{bmatrix} T_1^{t+\Delta t} \\ T_2^{t+\Delta t} \\ \cdots \\ \cdots \\ T_{n-1}^{t+\Delta t} \\ T_{n_{th}}^{t+\Delta t} \end{bmatrix} = \begin{bmatrix} d_1 \\ d_2 \\ \cdots \\ \cdots \\ d_{n-1} \\ d_{n_{th}} \end{bmatrix} \tag{5.15}$$

Hence the *new* temperatures at each CV can be determined. To summarize, the equations presented above are solved numerically for each (thermal problem) CV. Throughout, the heat source term is solved as presented earlier in Section 3.1, for each CV corresponding to the laminate part, prior calculation of the new temperatures using the old cure degree and temperature from the previous time step.

5.1.2 Mechanical model

Knowing the updated temperatures and cure degree, mechanical model calculations can be conducted. First, each lamina's micromechanic properties at the new time step $t + \Delta t$ is determined using updated temperature- and/or cure dependent mechanical properties . Recall that most of the polyester resin mechanical properties are cure- and temperature dependent. Updating material properties is therefore done prior the micromechanics calculations. The mechanical model approach then follows the CLT approach presented earlier in Chapter 3, Section 3.2.2. The laminate thickness of interest is discretized according to the number of plies and process induced strains and stresses are calculated for each ply as well as the entire laminate. Special care is taken in distinguishing between lamina local and global calculation steps, taking the appropriate transformations depending on the layup design into account.

An overview of the model structure including both the thermal and mechanical calculations conducted during each increment in time is presented in Fig. 5.3. Knowing the new temperature and cure degree, Eq. 3.18 to Eq. 3.43 can be solved. At the end of each calculation increment, residual stresses are determined as a summation of the current stress and stress increments. Model validation cases are presented subsequently.

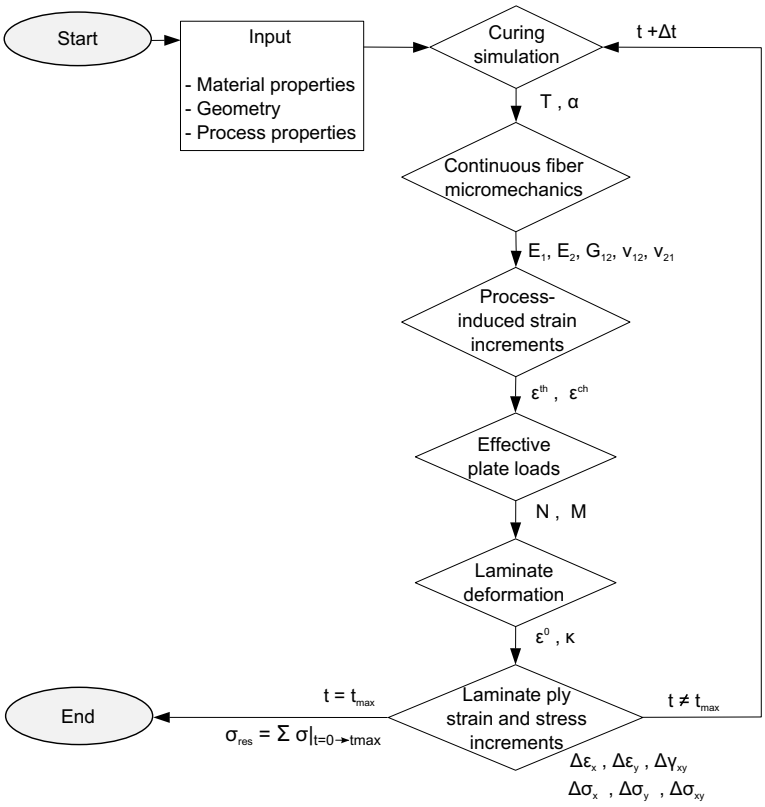

Figure 5.3: *1D thermomechanical process induced stress and strain model flow diagram. The model flow is similar to that proposed in [9]*

5.2 1D Matlab model validation

In the 1D model validation, a symmetric layup comprising of $[0]_{n_{ply}}$ UD plies are considered. The matrix Youngs modulus follows the simple linear elastic formulation presented in Chapter 4, i.e. Eq. 4.1 to Eq. 4.3 using a constant Poisson's ratio. As a first approximation, the number of CVs in the model coincide with the number of lamina in the ply stack. Unless stated otherwise, the total laminate thickness is 25.4[mm] coinciding with 30 plies. A glass/polyester composite laminate is investigated with the material properties given in Tab. 5.1.

Property	Unit	**Glass/Polyester**
ρ	[kg/m^3]	1890
C_p	[J/(W°C)]	1260
k_z	[W/(m°C)]	0.2163
Resin Modulus		**Polyester resin**
E_m^o	[MPa]	2.757
E_m^∞	[MPa]	2.757 E3

Table 5.1: *Glass/epoxy laminate effective thermal properties and resin mechanical properties [9]*

As stated earlier in Section 3.1, polyester and epoxy resins exhibit different cure kinetics behaviour. An autocatalytic type cure rate equation is used:

$$\frac{d\alpha}{dt} = \left(A \cdot exp\left[\frac{-E_a}{RT}\right] \right) \alpha^m \cdot (1-\alpha)^n \tag{5.16}$$

where the respective kinetics parameters are given in Tab. 5.2.

Property	Unit	**Polyester resin**
m		0.524
n		1.476
A	[s^{-1}]	6.167 E20
E_a	[J/mol]	1.674 E5
H_r	[J/kg]	77.5 E3
V_{sh}^T	[%]	6

Table 5.2: *Cure kinetic and chemical shrinkage parameters [9]*

The glass/polyester composite contains CYCOM 4102 polyester resin reinforced with E-glass fibers with a 54% fiber volume fraction. Fiber and resin effective mechanical properties are summarized in Tab. 5.3.

Property	Unit	**Glass**	**Polyester**
$E_1 = E_2$	[MPa]	7.308 E4	Eq. 4.1
$\nu_{12} = \nu_{13} = \nu_{23}$		0.22	0.40
$G_{12} = G_{13} = G_{23}$	[MPa]	2.992 E4	Eq. 4.3
$\alpha_1 = \alpha_2$	[1/°C]	5.04 E-6	72.0 E-6

Table 5.3: *Constituent fiber and resin mechanical properties [9]*

The prescribed cure cycle used in the validation case for the cure of glass/polyester is illustrated in Fig. 5.4 along with the temperature and cure degree evolution predictions at

the laminate top ply ($n_{th}-1$), at the center ($n=2$) and between these layers, i.e. a quarter of the thickness from the top. In the figure, one clearly sees the temperature overshoot representative of the exothermic reaction taking place resulting in an increase in internal temperatures. This is effectively the result of poor thermal conduction properties and high heat generation rates. The corresponding cure degree evolution in Fig. 5.4(right) shows that an inside-out curing occurs with the laminate center achieving full cure prior the regions near the surface.

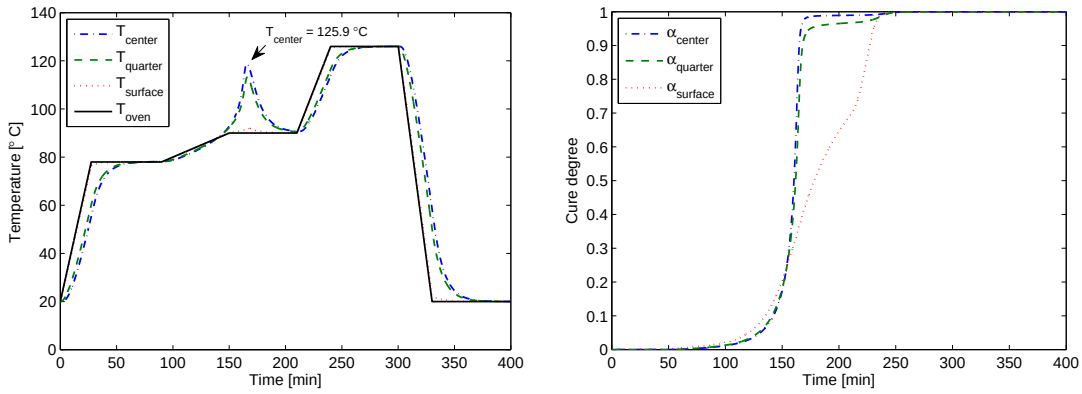

Figure 5.4: *(left) Cure cycle used for Glass/Polyester. (right) Cure degree predictions.*

5.2.1 Sensitivity analysis

A mesh and time step sensitivity analysis is carried out for the thermal solution to see which influence the number of CVs used and the choice of calculation time step has on the predicted temperatures and cure degree. This is only done for the thermal model as effects are primarily expected here due to the use of the implicit formulation and the highly non-linear cure rate expression. Moreover, the results from the thermal model are the main drivers for the mechanical model which in essence is a quasi-steady state model.

Mesh sensitivity analysis results at time t=164[min] where the peak exothermic reaction occurs are seen in Fig. 5.5(left), for the maximum obtained temperature and corresponding through-thickness average cure degree using $\Delta t = 1$[s]. Convergence is exhibited as the number of CVs is increased. It is seen that the use of 1 CV to represent each laminate ply (30 in all) is not a poor approximation in order to achieve reasonable results (when $\Delta t = 1[s]$). A CV:ply ratio of 1:1 is therefore used henceforth. Result sensitivity to time step size is also investigated using 30 CVs, seen in Fig. 5.5(right) for the through-thickness temperatures at time $t = 164$[min]. A slight overestimation of the temperatures is seen when $\Delta t > 0.1$[s] is used. However, for comparative purposes in the subsequent section with the results from Bogetti & Gillespie [9], the same time step size as used in [9] equal $\Delta t = 1$[s] is used. The elapsed calculation times during the time step size analysis are summarized in Tab. 5.4. Note that the times shown also include the mechanical calculations for a total process time of 400[min].

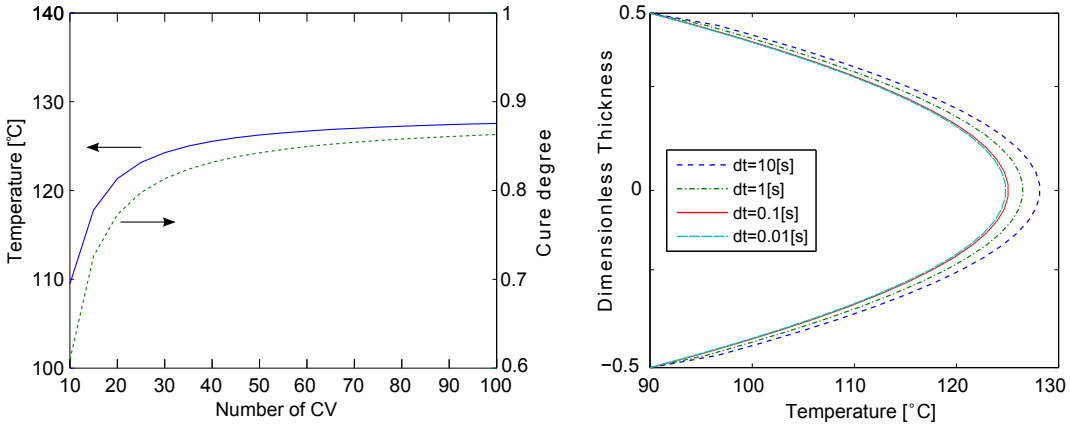

Figure 5.5: *Mesh sensitivity analysis of thermal solution showing (left) the development of the peak temperature and cure degree after 164[min] as a function of the number of control volumes. (right) The through-thickness temperature distribution at t=164[min] as a function of time step size (dt) is seen.*

Δt [s]	Elapsed time [s]
0.01	3584.54
0.1	337.01
1	33.77
10	3.43

Table 5.4: *Calculation times using different time step sizes.*

5.2.2 Temperature and cure degree prediction comparisons

The through-thickness temperature distribution for different laminate thicknesses after 164[min] is shown in Fig. 5.6(left) for results by Bogetti and Gillespie [9]. The maximum temperature achieved by the 25.4mm thick laminate here is app. 127°C. Similar results for the 1D Matlab model are seen in Fig. 5.6(right), where a peak temperature of 125.9°C for the 25.4mm thick laminate is achieved. Hence, good agreement between model predictions using a similar discretization and time step size as in [9] is achieved.

In Fig. 5.6 it is visible that the 50.8[mm] laminate is still being heated as its temperature at the center is lower than the temperatures at the boundaries. Contrary to this, for the thinner laminates, the laminate temperature at the center is higher than at the boundaries as cross-linking and the exothermic reaction at the center has started. Similar degree of cure distributions at time 164[min] are seen in Fig. 5.7. The cure degree is highest in the 25.4[mm] laminate at 164[min] because the cure rate is highest for this particular temperature cycle and laminate thickness. Moreover, it is seen that the 50.8[mm] laminate is still under-cured at its center, compared to the thinner laminates, showing the influence of the thickness on the cure rate and exothermic reaction. Obtained results from the 1D model coincide well with that of Bogetti et al. [9].

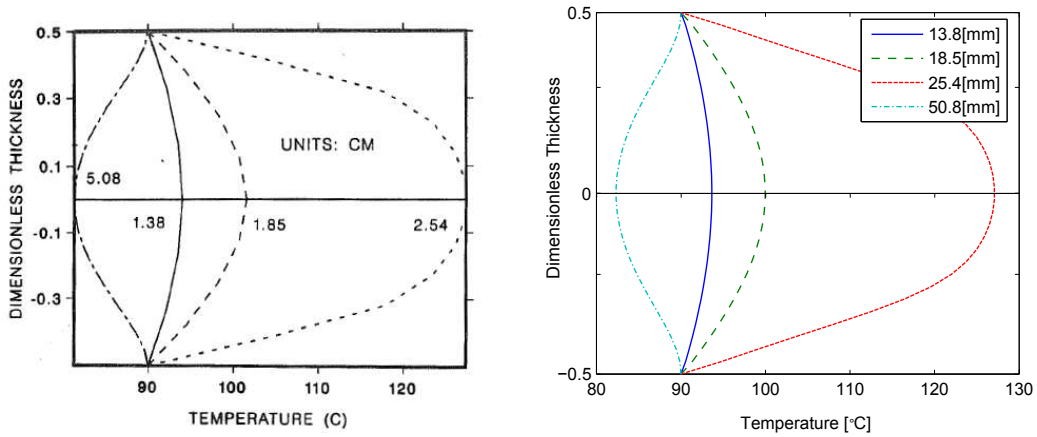

Figure 5.6: *(left) Temperature distributions in glass/polyester laminates after 164[min] [9]. (right) 1D model temperature distribution at same process time.*

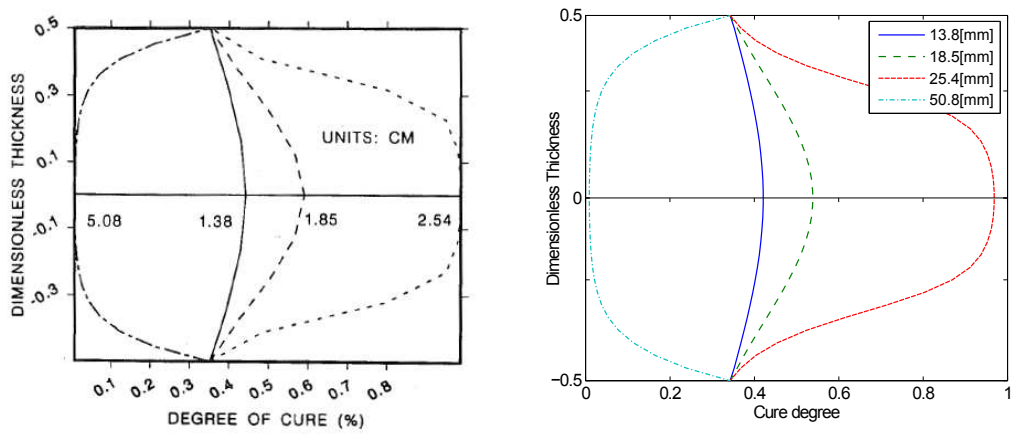

Figure 5.7: *(left) Degree of cure distributions in glass/polyester laminates at 164min [9]. (right) 1D Model results.*

5.2.3 Transverse residual stress predictions

Residual process-induced in plane transverse stress distributions for different laminate thicknesses up to 25.4[mm] from Bogetti et. al and the 1D MATLAB model are compared in Fig. 5.8, where good agreement exists. The final through-thickness in-plane transverse residual stress distribution is seen to exhibit compressive stresses at the laminate plate center and tensile stresses towards the boundaries. This is mainly driven by the higher thermal strains experienced at the center of the plate, due to the high peak temperatures, as presented earlier.

From the result comparisons carried out it can be said that the thermomechanical 1D model works well. The model is subsequently used for void growth modelling.

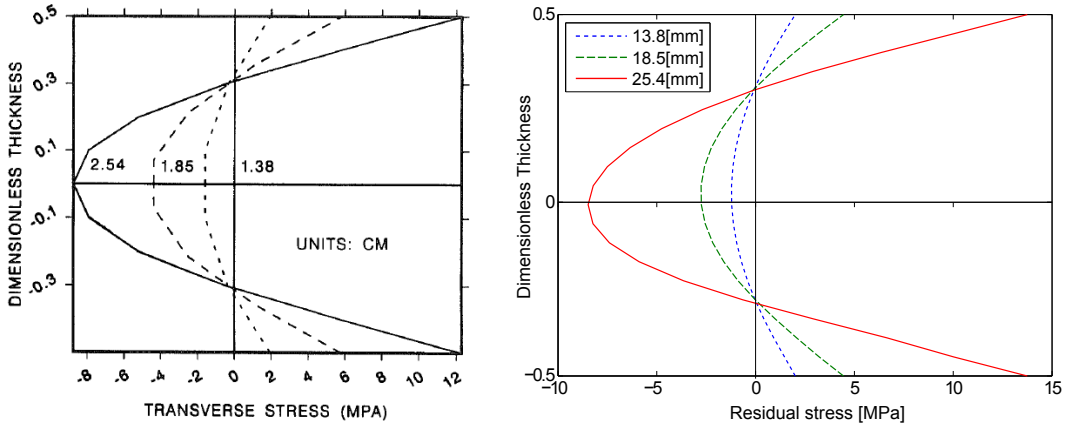

Figure 5.8: *(left) Residual process-induced in-plane transverse stress distributions($t \leq 25.4$mm) [9] and (right) 1D MATLAB model transverse residual stress predictions at the end of the cure cycle.*

5.3 Void growth

In this section, a void-growth model is implemented in the 1D model in a through-thickness spatially discretized manner and is the basis of the appended Paper I. Several models for the growth prediction of a single void bubble in matrix rich regions within a composite exist, e.g. [43, 58, 64, 106]. Of the most significant include studies by Kardos et al. [43], who proposed a general time-dependent diffusion-controlled void growth model as well as a model of the void stability at equilibrium as a function of pressure and temperature. Ledru et al. [58] presented a coupled visco-mechanical and diffusion model to predict the final void size post resin polymerization. In Ledru's model the resin viscosity variation during cure, as a function of temperature and cure degree is taken into account, as well as the process- and gas void pressure difference and gas temperature variation for a unit cell spherical void. Common for the above mentioned references is that only a single representative void is modelled, similar to common representative volume element (RVE) studies.

In the current study, a visco-mechanical void growth model is implemented, mainly inspired by work by Ledru et al. [57, 58], originally adapted from studies by Wood and Bader [106] and Kardos et al. [43]. Originally, the void growth model considered is also largely developed by Amon and Denson [4]. Subsequently, void growth is assumed to follow perfect gas law behaviour as a first approximation, without taking transport of species (volatiles) across the void/resin interface into account through diffusion. As a novelty, an attempt to predict processing effects is conducted by implementing the void model in a spatially discretized through-thickness domain of the laminate plate model previously introduced in this chapter.

5.3.1 Void growth in viscous media

Consider a spherical gas bubble developing in a polymer matrix, see Fig. 5.9, representing a void in resin rich regions within a composite laminate. Isotropic expansion or contraction of the void is assumed, hence the bubble size variation is described using the radial velocity component only ($v = [u, 0, 0]^T$). Hence, non-isotropic growth, that could arise due to influence from fibers in the fibre/matrix regions, is neglected.

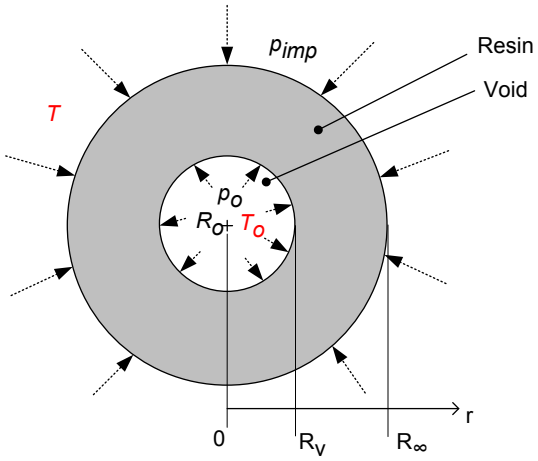

Figure 5.9: *Schematic of void gas bubble surrounded by resin with an imposed surrounding pressure p_{imp} and temperature T. Also seen is the initial void pressure, radius and temperature; p_o, R_o and T_o.*

The spherical void is in equilibrium when the pressure difference Δp between the void and the surrounding resin is equal to the bubble surface tension γ_{lv} given as a function of the void radius by the relation:

$$\begin{aligned} \Delta p &= \gamma_{lv}\left(\frac{1}{R_x}+\frac{1}{R_y}\right) \Rightarrow \\ \Delta p &= p_g - p_{imp} = \gamma_{lv}\left(\frac{2}{R_v}\right) \end{aligned} \tag{5.17}$$

where capital R_v denotes the void radius and p_g is the void gas pressure. Note that $R_v = R_x = R_y$. From incompressibility (volume constancy) we have the relation:

$$\varepsilon_{rr} + \varepsilon_{\theta\theta} + \varepsilon_{\varphi\varphi} = 0 \tag{5.18}$$

where each strain component can be expressed using strain-displacement relations in spherical coordinates [10]:

$$\begin{aligned} \varepsilon_{rr} &= \frac{\partial u}{\partial r} \\ \varepsilon_{\theta\theta} &= \frac{u}{r} + \frac{1}{r}\frac{\partial v}{\partial \theta} \\ \varepsilon_{\varphi\varphi} &= \frac{u}{r} + \frac{v}{r}cot\theta + \frac{1}{r\cdot sin\theta}\frac{\partial w}{\partial \varphi} \end{aligned} \tag{5.19}$$

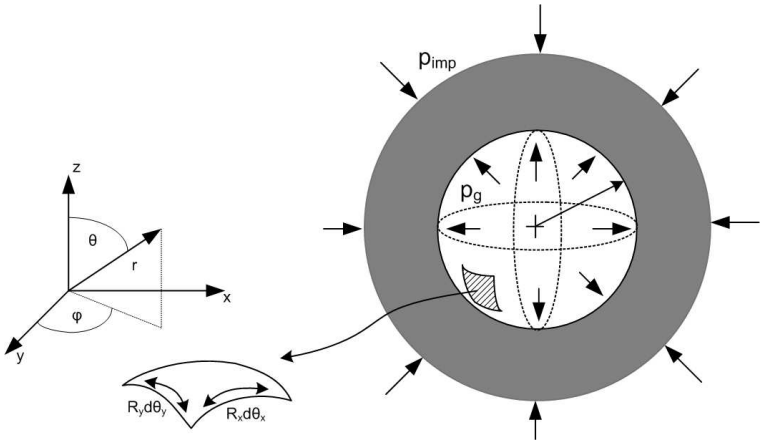

Figure 5.10: *Schematic of the void in a spherical coordinate system showing surface tension relations for an arbitrary void surface region.*

In Eq. 5.19 u, v, w denote velocity terms in the spherical coordinate system r, θ, φ. As only a change of the bubble radius is experienced during growth/contraction, the above is simplified to:

$$\begin{aligned} \varepsilon_{rr} &= \frac{\partial u}{\partial r} \\ \varepsilon_{\theta\theta} &= \varepsilon_{\varphi\varphi} = \frac{u}{r} \end{aligned} \tag{5.20}$$

hence:

$$\begin{aligned} \varepsilon_{rr} + \varepsilon_{\theta\theta} + \varepsilon_{\varphi\varphi} &= 0 \\ \Rightarrow \frac{\partial u}{\partial r} + 2\frac{u}{r} &= 0 \\ \Rightarrow \frac{\partial u}{\partial r} &= -2\frac{u}{r} \end{aligned} \tag{5.21}$$

From the above, the strain rate tensor $\underline{\underline{\dot{\varepsilon}}}$ can then be expressed, noting that no shear strains and shear strain rates exist:

$$\underline{\underline{\dot{\varepsilon}}} = \frac{u}{r}\begin{bmatrix} -2 & 0 & 0 \\ 0 & 1 & 0 \\ 0 & 0 & 1 \end{bmatrix} \tag{5.22}$$

From separation of variables, u is isolated:

$$\begin{aligned} \int \frac{du}{dr} = \int -2\frac{dr}{r} \Rightarrow \ln u = -2\ln r + c \Rightarrow \\ u = \exp(-2\ln r + c) = r^{-2} \cdot c \end{aligned} \tag{5.23}$$

where c is an integration constant. The radial velocity u can be expressed as $\Delta R_v/\Delta t = \dot{R}_v$, hence $u(R_v)$=$\dot{R}_v$. Following Eq. 5.23, this gives:

$$u(R_v) = \dot{R}_v = \frac{1}{R_v^2} \cdot c \Rightarrow c = \dot{R}_v R_v^2 \Rightarrow$$
$$u = \frac{1}{r^2}\dot{R}_v R_v^2 \tag{5.24}$$

The strain rate tensor can then be rewritten as:

$$\underline{\underline{\dot{\varepsilon}}} = \frac{\dot{R}_v R_v^2}{r^3}\begin{bmatrix} -2 & 0 & 0 \\ 0 & 1 & 0 \\ 0 & 0 & 1 \end{bmatrix} \tag{5.25}$$

where $\dot{R}_v$ is the void growth rate. In Spherical coordinates, equilibrium equations are given as [10]:

$$\frac{\partial \sigma_{rr}}{\partial r} + \frac{1}{r}\frac{\partial \sigma_{r\theta}}{\partial \theta} + \frac{1}{r\sin\theta}\frac{\partial \sigma_{r\varphi}}{\partial \varphi} + \frac{1}{r}[2\sigma_{rr} - \sigma_{\theta\theta} - \sigma_{\varphi\varphi} + \sigma_{r\theta}\cot\theta] + \Pi = 0 \tag{5.26}$$

$$\frac{\partial \sigma_{r\theta}}{\partial r} + \frac{1}{r}\frac{\partial \sigma_{\theta\theta}}{\partial \theta} + \frac{1}{r\sin\theta}\frac{\partial \sigma_{\theta\varphi}}{\partial \varphi} + \frac{1}{r}[(\sigma_{\theta\theta} - \sigma_{\varphi\varphi})\cot\theta + 3\sigma_{r\theta}] + \Theta = 0 \tag{5.27}$$

$$\frac{\partial \sigma_{r\varphi}}{\partial r} + \frac{1}{r}\frac{\partial \sigma_{\theta\varphi}}{\partial \theta} + \frac{1}{r\sin\theta}\frac{\partial \sigma_{\theta\varphi}}{\partial \varphi} + \frac{1}{r}[3\sigma_{r\varphi} + 2\sigma_{\theta\varphi}\cot\theta] + \Phi = 0 \tag{5.28}$$

where Π, Θ and Φ are the body-force components in the r, θ and φ directions. For the isotropic problem at hand, Π=Θ=Φ=θ=φ=0, greatly simplifying the equations above to:

$$\frac{\partial \sigma_{rr}}{\partial r} + \frac{1}{r}[2\sigma_{rr} - \sigma_{\theta\theta} - \sigma_{\varphi\varphi}] = 0$$
$$\sigma_{\theta\theta} = \sigma_{\varphi\varphi} \tag{5.29}$$

The boundary conditions at the limits, represented by the void surface/resin interface and the surrounding resin boundary, (see Fig. 5.9) dictate that:

$$\sigma_{rr}(R_v) = -p_g + \frac{2\gamma_{lv}}{R_v}$$
$$\sigma_{rr}(R_\infty) = -p_{imp} \tag{5.30}$$

which are found using the Laplace-Young relationship where surface tension forces γ_{lv} are taken into account as well as the internal void gas pressure p_g and imposed hydrostatic pressure p_{imp}. In the case of VARTM, no external hydrostatic pressure is applied, as would be the case in autoclave RTM. Hence, p_{imp} corresponds to the atmospheric pressure. Finally, the polymer resin is assumed to exhibit Newtonian behaviour expressed constitutively via the Cauchy tensor as:

$$\underline{\underline{\sigma}} = 2\eta\underline{\underline{\dot{\varepsilon}}} - p\underline{\underline{I}} \Rightarrow$$
$$= 2\eta\frac{\dot{R}_v R_v^2}{r^3}\begin{bmatrix} -2 & 0 & 0 \\ 0 & 1 & 0 \\ 0 & 0 & 1 \end{bmatrix} - p\begin{bmatrix} 1 & 0 & 0 \\ 0 & 1 & 0 \\ 0 & 0 & 1 \end{bmatrix} \tag{5.31}$$

where η is the resin viscosity. Inserting Eq. 5.25 in Eq. 5.31 we get:

$$\sigma_{rr} = -4\eta\frac{\dot{R}_v R_v^2}{r^3} - p_{imp}$$
$$\sigma_{\theta\theta} = \sigma_{\varphi\varphi} = 2\eta\frac{\dot{R}_v R_v^2}{r^3} - p_{imp} \tag{5.32}$$

The visco-mechanical coupling in the void growth model is achieved by expressing the resin viscosity as a function of the cure degree and temperature, expressed by [57]:

$$\eta(T,\alpha) = \eta_g \cdot \exp\left[-\frac{C_1(T-T_{go})}{C_2+T-T_o}\right]\left(\frac{\alpha_{gel}}{\alpha_{gel}-\alpha}\right)^a \tag{5.33}$$

which is a combination of the Williams-Landel-Ferry (WLF) expression and the Castro and Macosko conversion term. η_g is the resin viscosity at gelation, C_1 and C_2 are WLF model parameters and α_{gel} is the gelation cure degree. A viscosity limit of 10e6[Pa s] is used, corresponding to solidification of the resin [57].

Having an expression for the resin viscosity as a function of cure and temperature, the equilibrium- and constitutive equations presented earlier, as well as the applied boundary conditions are used to obtain a 1st order differential equation:

$$\frac{\dot{R}_v}{R_v(t)} - \frac{p_g(t) - p_{imp}(t)}{4\eta(T,\alpha)} + \frac{\gamma_{lv}}{2\eta(T,\alpha)R_v(t)} = 0 \tag{5.34}$$

where the void gas pressure p_g at time t is:

$$p_g(t) = p_o\frac{T(t)}{T_o}\left(\frac{R_o}{R_v(t)}\right)^3 \tag{5.35}$$

p_o, T_o and R_o are the initial void pressure, temperature and radius respectively. The 1st order non linear differential equation Eq. 5.34 is solved implicitly for the void radius at each control volume in a similar incremental fashion as described earlier in the thermo-mechanical 1D model. Close attention should be paid when determining the roots for the solution of Eq. 5.34. Once the prescribed viscosity limit of 10e6[Pa s] is reached during curing, it is assumed that the void size follows the expansion/contraction behaviour of the resin. As first, the influence of the resin cure shrinkage is disregarded such that only resin thermal expansion is considered:

$$R_v(t) = R_{v@\eta_{max}} + R_{v@\eta_{max}}(\alpha_{CTE}\cdot\Delta T) \tag{5.36}$$

where $R_{v@\eta_{max}}$ is the void radius when the viscosity limit is reached.

Using the approach above, a model is presented capable of predicting the expected average void growth at discrete regions through the thickness of a laminate as a function of processing parameters (p_{imp}, T) and the corresponding resin viscosity evolution dependent on the cure degree within the part. Diffusion across the void bubble interface is not taken into account, hence the influence of neighbouring voids is disregarded. The main model assumptions are as follows:

- Constant isotropic thermal material properties are assumed
- Voids are assumed to be initially present in the resin after infusion during VARTM as a result of gas bubbles being trapped in the inter-tow spaces
- An initial mean void radius (R_o) and distribution is assumed through the laminate thickness
- The gas void is assumed to be perfectly spherical
- The perfect gas law applies for describing the gas inside the void
- No diffusion takes place, i.e. void and resin are assumed to be non-miscible.

5.3.2 Void growth predictions

A 40.0[mm] thick glass/epoxy laminate plate is considered using similar symmetric thermal boundary conditions as presented in Section 5.2. The epoxy resin cure rate is modelled using the Kamal and Sourour model expressed in Eq. 3.10, Section 3.1. The model material parameters used for the resin cure kinetics and cure-dependent viscosity presented in Eq. 5.33, are summarized in Tab. 5.5. An initial uniform void distribution corresponding to one void pr. control volume is assumed, with an initial radius R_o=10[μm] and pressure p_o=1.1E5[Pa]. The initial radius corresponds to void radius measurements in viscous epoxy resin conducted by Ledru [57]. The initial temperature is set to 20°C and the void bubble surface tension force is set to γ_{lv}=0.05[Pa.m], a value commonly taken in literature [43, 58].

Property	Unit	**Epoxy resin**
m	-	0.51
n	-	1.49
A_1	[s^{-1}]	1528
A_2	[s^{-1}]	1.6
$E_{a,1}$	[kJ/mol]	59.4
$E_{a,2}$	[kJ/mol]	26.3
H_r	[J/kg]	198.9
η_g	[Pa.s]	10E12
T_{go}	[K]	235
α_g	-	0.345
C_1	-	29.9
C_2	-	30.0
a	-	2.1

Table 5.5: *Void growth model cure kinetics and viscosity parameters, taken from [57].*

In Fig. 5.11 the temperature cycle at the laminate surface as prescribed in the model is seen. The temperatures at the laminate thickness center and between the center and surface (quarter) are also seen. The temperature peaks at app. t=3000[s] and 9000[s] are a result of the exothermic heat generation which is not fully released in one go, hence the two temperature overshoots. The cure degree evolution at the same points are also presented. A similar inside-out through-thickness cure evolution as presented in the 1D thermal validation case is seen.

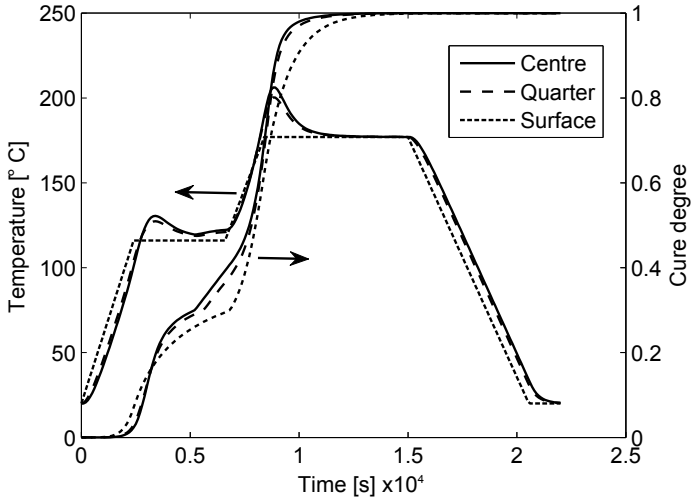

Figure 5.11: *Temperature and cure degree at different laminate through-thickness regions.*

The corresponding cure and temperature dependent resin viscosity development is seen in Fig. 5.12 (left). Initially, a decrease in resin viscosity is seen due to the corresponding increase in temperature, seen in Fig. 5.11. As the process continues and curing initiates, an increase in viscosity occurs, physically representing the densification of the resin molecular structure upon gelation. The prescribed viscosity limit of 10e6[Pa.s] was reached shortly after (at app. 0.6E4[s]), first at the center of the laminate due to the high curing rate in this region. The non-uniform through-thickness temperatures and cure degree development are the driving factors behind the slightly non-uniform through-thickness void growth evolution, seen in Fig. 5.12m(right). As the resin is not fully cured at the laminate surface after approximately t=5000[s], only an increase in void radius is experienced here due to the second temperature ramp starting at time t=6600[s]. However, the most significant contribution to the increase in void radius is the initial increase in temperature before the first dwell. Hence, selecting an appropriate temperature cycle with lower peak temperatures could assist in reducing the final void size. This would however conflict with the wish for higher processing throughput as longer cure cycles would be necessary to ensure sufficient curing at lower temperatures.

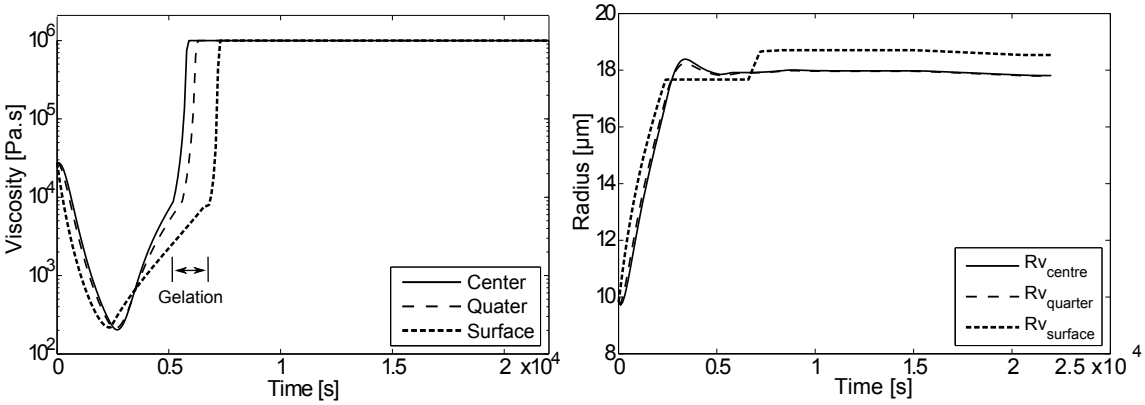

Figure 5.12: *(left) Resin viscosity development during the cure cycle shown in Fig. 5.11, and (right) the corresponding predicted void radius development.*

A more detailed presentation of results including a parameter study of laminate thickness and cure cycle effects on the through-thickness predicted void size distribution is found in the appended Paper I. Unfortunately, it was not possible to properly verify the implemented gas diffusion effects across the void bubble/resin interface successfully in the current work due to lack of sufficient information in terms of comparative experimental values. The diffusion behaviour is based on Fick's second law.

As a closing remark, the importance of the ability to predict void growth in composites is important, considering reports on the detrimental effects on the strength and fatigue life that voids pose on composite structures [7, 61]. For instance, Liu et al. [61] investigated the void content effect on carbon/epoxy laminate mechanical properties, where a decrease of app. 20% in shear-, flexural- and tensile strength was observed with an increase in void content of app. 2.6%. Voids have also been reported to accelerate crack initiation and propagation in laminates, see e.g [2, 35, 104]. Hence the ability to model void growth and its influence on part strength and fatigue is of great interest. The 1D model presented earlier builds on a number of assumptions and is a first attempt at modelling void size distirbution as a function of processing effects. Therefore, in its current form the model may not be directly applicable in a full 3D curing modelling framework, for analysis of large composite structures.

5.4 Summary

In this chapter, a 1D thermomechanical curing model was presented and validated using various test cases. The model is capable of predicting temperature- and cure degree profiles through the thickness of a composite laminate during cure, not to mention the development of process induced laminate in-plane strains and residual stresses. The 1D model is also used as a framework for a void growth model used to predict through-thickness visco-mechanically coupled void growth, dependent on processing parameters (pressure and temperature) and the cure degree development at discrete points through the laminate thickness. While the void growth model is not addressed later in the thesis, the 1D thermal model is used for thermal boundary condition fitting purposes, as discussed in Chapter 7.

Chapter 6

3D Modelling

In the previous chapter, a 1D thermomechanical curing and void growth model was presented. Although this simple model offers many capabilities for modelling thermal and mechanical effects in laminate plate structures, the model is inadequate once complex geometries, boundary conditions or loading scenarios are considered. In this chapter, a 3D thermomechanical model is presented. First, an overview of the numerical implementation framework is given, conducted using the commercial finite element software package ABAQUS[1]. User-subroutines are utilized to accommodate the mechanisms and theories presented in the previous chapters. Following this, some validation cases are presented, used to ensure correct implementation of the subroutine algorithms. Finally simple modelling case studies are presented, for the prediction of process induced strains and stresses in composite laminate plates during curing.

6.1 Numerical implementation

6.1.1 User-subroutines

In ABAQUS, user-subroutines can be included for specific modelling applications to help increase the functionality of several standard ABAQUS built-in capabilities for which the usual data input methods may be too restrictive or insufficient. These subroutines are typically written in FORTRAN code. An overview of the general flow in a typical analysis in ABAQUS is seen in Fig. 6.1, where the different subroutines that can be included are shown in red. During each analysis increment, iteration steps are carried out where the global stiffness matrix and reaction forces are defined and updated. These are solved for the nodal displacements where, once a converged solution is found, the next analysis increment can commence. A close-up of the subroutines governing the constitutive behavior of the materials, as well as boundary conditions and loads in the analysis is presented in Fig. 6.2 for typical ABAQUS/Standard (implicit formulation) analyses. It is seen that prior to the definition of the new loads, the incremental stresses and strains are determined.

[1] ABAQUS is a registered trademark of Simulia, Dassault Systemes

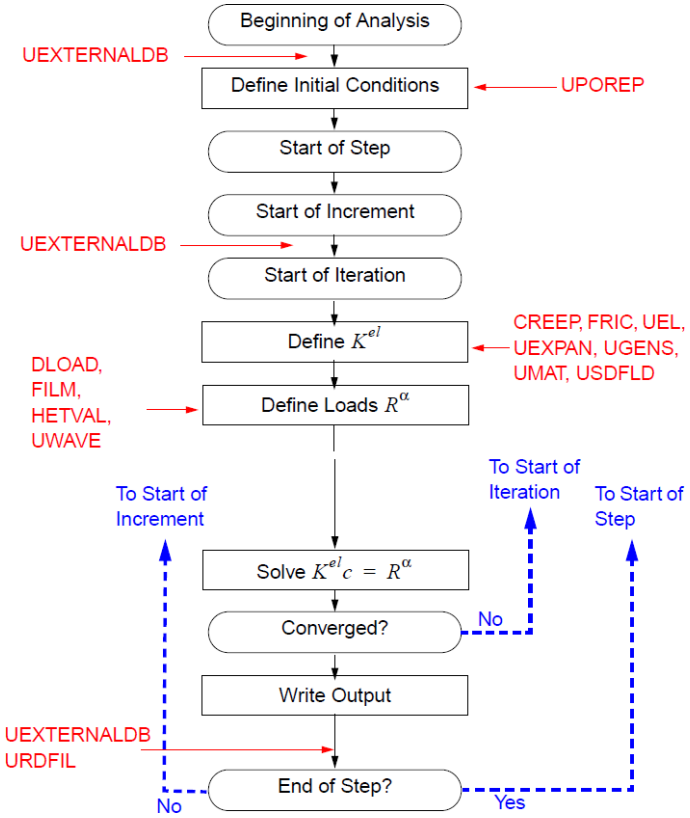

Figure 6.1: *Global analysis flow in ABAQUS/Standard showing the different subroutines available (in red) and where, during the analysis increments and iterations, these subroutines are used [97].*

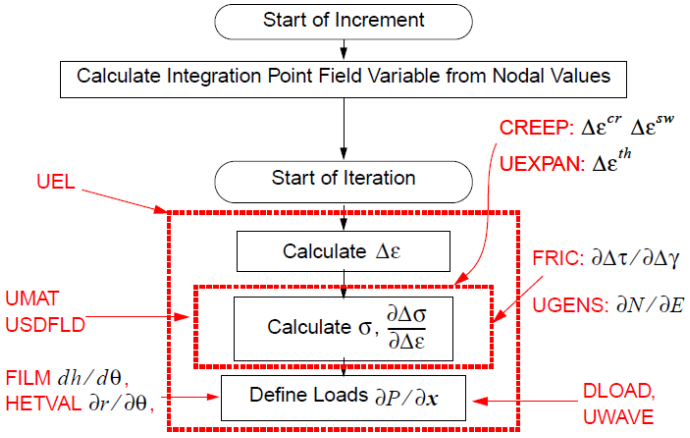

Figure 6.2: *A more detailed overview of analysis steps in ABAQUS/Standard [97]*

In the current study, the following user-subroutines are used:

- *HETVAL* - used to define a heat flux due to internal heat generation in a material in heat transfer analyses
- *UEXPAN* - used to define incremental thermal (or other) strains, as functions of temperature, predefined field variables and state variables

- *UMAT* - a user-material subroutine in ABAQUS that can be used to define the mechanical constitutive behavior of a material

A short overview of the requirements of the above-named subroutines is given subsequently.

HETVAL

In HETVAL, definition of the internal heat generation of a material as a function of a state variable (for instance cure degree) is possible. During an analysis increment, the HETVAL subroutine is called at all integration points for which the material definition contains volumetric heat generation in a heat transfer analysis, coupled temperature-displacement, or other coupled thermal analysis procedures [1]. Information of each integration point's temperature, temperature increment and user defined state variables, as well as the solution time increment, total time etc. is passed into HETVAL at each increment start. From this information, calculation of the internal heat generation can be done such that the heat flux and rate of change of the heat flux per temperature change can be defined [1]. In this work, the resin cure rate and volumetric heat generation during curing is defined in HETVAL.

UEXPAN

The UEXPAN subroutine is used to define incremental thermal strains when a material's thermal expansion is too complex to model with the standard thermal expansion option in ABAQUS [1]. Similar to HETVAL, the UEXPAN subroutine is called at all integration points in which the material contains user-subroutine defined thermal expansion, and twice per material point in each iteration during coupled temperature-displacement analyses. In UEXPAN, the incremental thermal strains $\Delta\varepsilon_{ij}^{th}$ are to be defined. The number of strain components defined depends on the model used, for instance isotropic (1), orthotropic (3) or anisotropic (6) [1]. In this work, cure- and temperature dependent orthotropic thermal expansion and chemical cure shrinkage behavior are defined in UEXPAN.

UMAT

As seen from the flow diagrams in Fig. 6.1 and Fig. 6.2, the UMAT subroutine allows the user to calculate any specific material constitutive behavior by expressing the stress σ and material Jacobian matrix $\partial\Delta\sigma/\partial\Delta\varepsilon$ at each integration point for each simulation increment. In ABAQUS, a range of information is passed into UMAT at the beginning of an analysis increment. These include the current stresses, strains and strain increments, as well as other state variables. It is then necessary to execute three tasks [1, 19]:

1. Determine the new stresses at the end of the time increment, $\sigma(t_n + \Delta t)$

2. Define the material Jacobian stiffness matrix, $\partial\Delta\sigma/\partial\Delta\varepsilon$
3. Update any solution-dependent state variables used at the end of the increment, e.g. the stress residual σ_{ij}^{R} or internal state variable β_{ij}, presented earlier in Chapter 4

In the first iteration of an increment all of the user subroutines are called twice. During the first call the initial stiffness matrix is formed using the initial configuration of the model in the analysis. During the second call a new stiffness, based on the updated configuration of the model is created [97].

During a mechanical analysis increment, the equations of motion together with the constitutive law form an equation system, consisting of an initial boundary problem and a partial differential equation. The relevant constitutive information is supplied by the user in UMAT before being passed to ABAQUS for solution [97]. Starting from a state of equilibrium at time t_c (subscript 'c' denotes current time), ABAQUS applies the defined loads (thermal, mechanical etc.) occurring within the time increment Δt, and an initial guess (unless loading is given as a displacement in one increment) is made for the strain increment $\Delta\varepsilon_c$. In UMAT, the new Cauchy stress tensor $\sigma(t_c + \Delta t)$ is updated according to the constitutive law used, as well as with the derivative of stress with respect to the strain increment (Jacobian J or $\partial\Delta\sigma/\partial\Delta\varepsilon$). With this information, a new value for the strain increment is calculated and the whole procedure is iterated until the solution converges. In the current work, the SCFM calculations and constitutive approaches used are defined in UMAT.

6.2 Subroutine validation

In order to verify that the subroutines are implemented properly, different tests are conducted.

6.2.1 Temperature and cure degree predictions

The HETVAL subroutine is compared to 1D model predictions from MATLAB. This is done for 1D and 3D cases in ABAQUS for similar conditions as in the 1D MATLAB model, see Fig. 6.3. Note that the MATLAB model uses a finite volume method (FVM) framework, as opposed to ABAQUS where the finite element method (FEM) is used. This may give slight discrepancies in predicted temperatures as in FVM, temperatures are calculated at the control volume center, while this is done at element nodal points in FEM, typically situated at the element boundaries, illustrated as circles in Fig. 6.3. However, with an adequate discretization of the spatial domain, this should not be an issue.

For all three models evaluated, similar material and thermal properties for a glass/polyester composite are used as well as the temperature cure cycle presented earlier in Section 5.2. Furthermore, adiabatic conditions at the domain boundaries are considered. In the ABAQUS 3D model, linear 8-node brick elements (DC3D8) are used, while the 1D ABAQUS model consists of 2-node heat transfer link (DC1D2) elements. Furthermore,

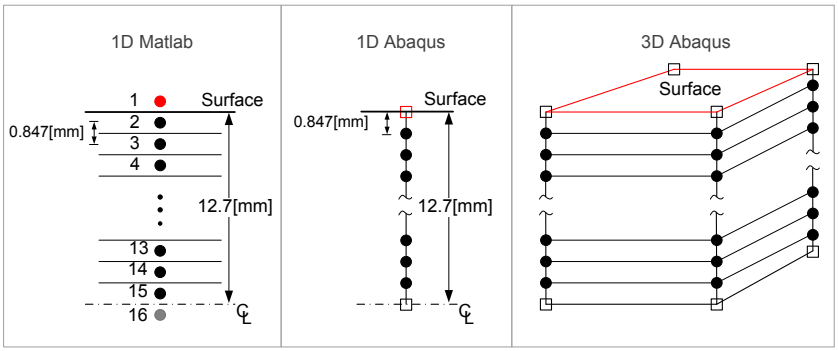

Figure 6.3: *Discretization of the spatial modelling domain in the 1D MATLAB FVM model, and comparative 1D- and 3D ABAQUS FEM models. The red nodes/surfaces represent the regions following a prescribed temperature cycle.*

similar simulation settings, as in the MATLAB model are used; i.e. t_{max}=24000[s] and a constant time increment Δt=1[s].

Results

Comparisons of model temperature and cure degree development predictions are shown in Fig. 6.4, at the laminate surface and through-thickness center. In general all models agree well with each other. In Fig. 6.4(left) slightly higher peak temperatures at the laminate center are predicted by the ABAQUS models as a result of the center nodes being exactly at the through-thickness center symmetry line, while this is not the case for the MATLAB model (see in Fig. 6.3) which is a half control volume off center.

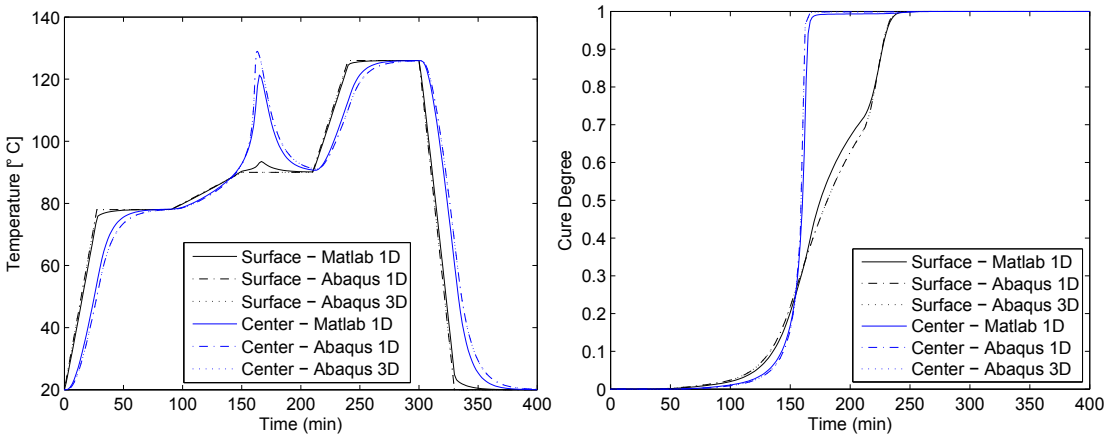

Figure 6.4: *(left) 1D and 3D model temperature predictions at the laminate surface and center, and (right) similar cure degree predictions.*

In Fig. 6.4(right), good agreement between the models exists at the surface and center of the plate thickness, albeit a corresponding higher cure degree gradient at the laminate center in the ABAQUS results between 150-200[min] is seen. The difference is driven by the slightly higher temperature at the center in the ABAQUS model, as mentioned previ-

ously. The HETVAL subroutine works well as temperature and cure degree calculations are as expected for both 1D and 3D cases.

6.2.2 Constitutive behavior

The UMAT subroutine is tested using single- and multiple element(s), for uniaxial and shear loading conditions. For simple test cases, comparisons with closed-form solutions are also possible. Multiple element test cases are chosen to ensure that "free" nodal points, which are not directly subjected to boundary conditions or loads, behave correctly [19]. Shear tests are also conducted since uniaxial loading does not take shear terms in the material stiffness matrix into account. This is also important in order to ensure that the use of engineering shear strains, which ABAQUS uses in UMAT, is applied correctly.

Case 1: Static tensile and shear tests - isotropic

In the following tests, 4-node shell elements with reduced integration (S4R) are used, see Fig. 6.5. Hence, the tests are essentially in 2D, but also apply for 3D cases.

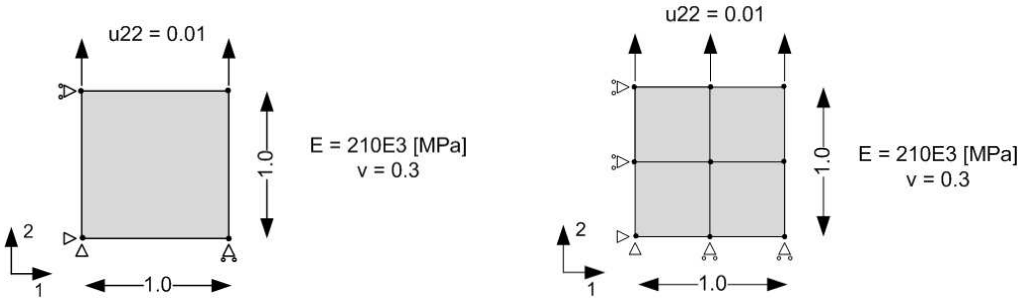

Figure 6.5: *Single and multiple element tensile test cases assuming plane stress conditions. Prescribed displacements of 0.01[m] at the upper boundary are seen.*

For the tensile test cases illustrated in Fig. 6.5, the stress in the normal axis 2 is found analytically as:

$$\begin{aligned} \varepsilon_{22} &= \frac{\Delta l}{L} = \frac{0.01[m]}{1[m]} = 0.01 \\ \sigma_{22} &= E\varepsilon_{22} = 210E3 \cdot 0.01 = 2.1E3[\text{MPa}] \end{aligned} \tag{6.1}$$

Correspondingly, the negative strain in the normal 1 direction is:

$$\varepsilon_{11} = -\nu\varepsilon_{22} = -0.3 \cdot 0.01 = -0.003 \tag{6.2}$$

As a plane stress state prevails, and no shear exists:

$$\varepsilon_{33} = \varepsilon_{12} = \sigma_{11} = \sigma_{33} = \sigma_{12} = 0 \tag{6.3}$$

Using the programmed UMAT routine in ABAQUS, the following results are achieved for both single and multiple element cases:

σ_{11} [MPa]	0	ε_{11}	-3.0E-3
σ_{22} [MPa]	2100	ε_{22}	1.0E-2
σ_{12} [MPa]	0	ε_{12}	0

which agrees well with the analytical calculations. In the multiple element test case, the displacement of the middle "free" node is found as:

$$u_{2@center} = \frac{1}{2}u_{22} = 5.0E\text{-}3[\text{m}] \tag{6.4}$$

which is also found in ABAQUS. i.e the free node displacements are also satisfactory.

In the shear tests, small deformations are assumed, hence $\|\Delta u\| << 1$. Furthermore, the following prevails: σ_{33}=ε_{33}=ε_{22}=0. The shear test cases for the single and multiple element examples are illustrated in Fig. 6.6.

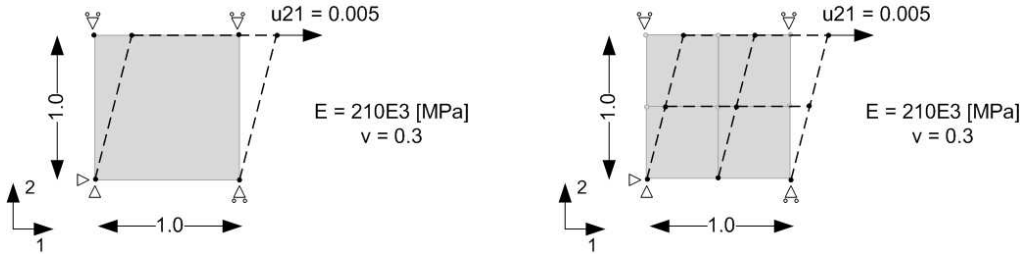

Figure 6.6: *Single and multiple element shear test cases assuming plane stress conditions*

From ABAQUS the following results are achieved for both single and multiple element cases using the standard elastic material model and the UMAT subroutine, with very good agreement:

ABAQUS Standard			
σ_{11} [MPa]	2.990E2	ε_{11}	1.295E-3
σ_{22} [MPa]	8.969E1	ε_{22}	2.633E-20 $\approx$ 0
σ_{12} [MPa]	2.992E2	ε_{12}	3.705E-3
UMAT			
σ_{11} [MPa]	2.991E2	ε_{11}	1.296E-3
σ_{22} [MPa]	8.974E1	ε_{22}	1.645E-20 $\approx$ 0
σ_{12} [MPa]	2.991E2	ε_{12}	3.704E-3

From the results, no difference is seen between the standard Abaqus solution and the programmed UMAT code. Hence the subroutine works satisfactorily in both tension and shear for single and multiple element cases.

Case 2: Static tensile tests - Transversely isotropic

In this section, similar tests as those shown in Fig. 6.5 and Fig. 6.6 are conducted for transversely isotropic material behavior, representing a UD laminate. The aim is to ver-

ify the continuous fiber micromechanics model implemented in UMAT. Tensile tests are conducted using the following material properties for the fiber and matrix materials:

Fiber		Matrix	
E_f [GPa]	73.080	E_m [GPa]	2.757
ν_f	0.22	ν_m	0.40
Fibre volume fraction	54%	-	

From the micromechanics calculations, the following equivalent material parameters are calculated:

E_1 [GPa]	40.889	E_2 [GPa]	8.525
ν_{12}	0.295	ν_{21}	0.062
G_{12} [GPa]	1.196		

Knowing that the strain in the 2-direction from the displacement loading is ε_{22}=1.0E-2, see Fig. 6.5, the corresponding strain in the 1-direction is ε_{11}=$-\nu_{21}\varepsilon_{22}$=-0.062·1.0E-2 = -6.16E-4 and all shear is null. The stresses are hence:

$$\begin{bmatrix}\sigma_{11}\\ \sigma_{22}\\ \sigma_{12}\end{bmatrix} = \frac{1}{1-\nu_{12}\nu_{21}}\begin{bmatrix}E_1 & \nu_{21}E_1 & 0\\ \nu_{12}E_2 & E_2 & 0\\ 0 & 0 & G_{12}(1-\nu_{12}\nu_{21})\end{bmatrix}\begin{bmatrix}\varepsilon_{11}\\ \varepsilon_{22}\\ \varepsilon_{12}\end{bmatrix} \Rightarrow$$
$$= \begin{bmatrix}\approx 0\\ 85.245\\ 0\end{bmatrix} \text{[MPa]} \tag{6.5}$$

As the plate is not constrained in the 1-direction, $\sigma_{11} \approx 0$[MPa]. Using the above given material properties in UMAT, a similar analysis is done in ABAQUS, giving:

σ_{11} [MPa]	-5.572-13 ≈ 0	ε_{11}	-6.06E-4
σ_{22} [MPa]	83.940	ε_{22}	1.0E-2
σ_{12} [MPa]	-2.24E-15 ≈ 0	ε_{12}	-7.5E-19 ≈ 0

which are similar to the analytical results. The validation tests carried out in this section show good agreement with analytical and 1D model predictions. The model can therefore be used for more complex realistic curing procedures.

6.3 Curing of composite laminate angle profile

For the final validation case, a well described modelling and experimental study by Svanberg [92, 93] is adapted. Svanberg used the PD approach to predict the spring-in of a woven laminate 90° angle bracket after demoulding. In a similar manner, predictions of the same composite part spring-in will be conducted in this section, using the three different constitutive models presented in Chapter 4, i.e CHILE, PD and VE. Initially, this is

done for a similar woven layup as in Svanberg using only the PD approach, after which model predictions using all three approaches are analyzed for a UD layup laminate angle profile. The profile considered is illustrated in Fig. 6.7 and measures 150mm in width. In [93] the laminate is vacuum infused on a steel mould with internal heating/cooling chambers and a vacuum bag on the free laminate side.

The laminate profile is modelled using a sequentially coupled thermomechanical analysis in ABAQUS where two main mechanical boundary conditions are considered; (i) a free standing case and (ii) a fixed case at the tool/part interface, also seen in Fig. 6.7. In the *free standing* case, unconstrained expansion and contraction is allowed and rigid body motion is constrained. In the *fixed* case, all nodes along the laminate tool/part interface are fully constrained, resembling perfect bonding to a tool with negligible expansion. Using these two conditions, the need to model the tool is avoided, hence only the laminate is modelled. However, in doing so, any tool influence in real life on the induced distortions is disregarded.

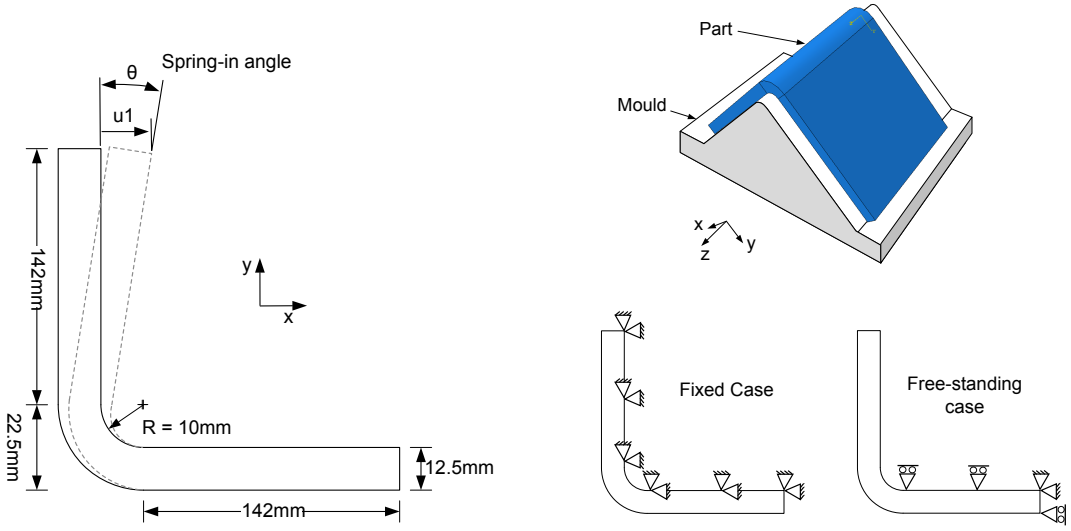

Figure 6.7: *Schematic of laminate angle profile considered (not to scale), tooling configuration in real life and mechanical boundary conditions considered.*

The laminate layup consists of woven glass fibre fabric, with a final fibre volume fraction of V_f=56%. Effective mechanical properties for the woven laminate considered in the analysis, are shown in Tab. 6.1 in both glassy and rubbery state [93]. Using these properties, the effective stiffness matrices in the glassy and rubbery state are constructed directly in the CHILE, PD and VE model subroutines, without the need of micromechanics calculations. The total volumetric shrinkage for the resin considered is 7%. For brevity, the thermal analysis model settings and properties are omitted here, but found in full in [93]. The temperature cycle during curing and post-curing, as well as the corresponding cure degree development at the angle profile mid-width through-thickness points (a-c) is presented in Fig. 6.8. It is seen that the temperature cycle generally depicts a heating stage, a temperature overshoot due to the exothermic reaction, a temperature hold and a cooling stage. In the post-curing cycle no temperature overshoot is seen as almost all latent heat is already released during the first heating stage. Due to the simulated heating from the surface in contact with the heated mould, temperatures at point (a) are generally

higher than at the remaining points, except between app. 3-4E3[s] into the process where the cure exothermic reaction results in higher temperatures at the laminate mid-thickness point (c).

Property		Glassy state	Rubbery state
E_x=E_y	[GPa]	26.2	21.4
E_z	[GPa]	10.1	2.7
ν_{xy}		0.094	0.0021
ν_{xz}=ν_{yz}		0.46	0.83
G_{xy}=G_{yz}	[GPa]	3.0	0.033
G_{xz}	[GPa]	2.9	0.033
α_x=α_y	[10^{-6}°C^{-1}]	13.9	5.4
α_z	[10^{-6}°C^{-1}]	58.7	229.0
β_x=β_y		-3.2·10^{-3}	-7.4·10^{-5}
β_z		-1.9·10^{-2}	-3.2·10^{-2}

Table 6.1: *Mechanical properties of woven glass/epoxy laminate with V_f=56% [93]. $\alpha_{x,y,z}$ are the thermal expansion coefficients and $\beta_{x,y,z}$ are the chemical shrinkage constants, given for the global material directions.*

Results

As mentioned earlier, two boundary conditions are considered; (i) free-standing and (ii) fixed. In the case of the fixed boundary conditions, after the cure cycle simulation is completed, demoulding is simulated by simply suppressing part mechanical constraints. For both cases, the spring-in angle of the angle profile is calculated using the tip displacement u_1 illustrated in Fig. 6.7. In Fig. 6.9, the PD model spring-in predictions are presented for both boundary condition cases. Also shown are the development of the cure- and glass transition temperatures at laminate point (c). When considering the free standing case first, spring-in develops once gelation occurs after app. 250[s]. At this point in time cooling is taking place after the exothermic reaction, as well as cure shrinkage. This contraction results in an increase in spring-in, which is further increased during the cure cycle cooling stage. For the fixed case, no displacement occurs, hence stresses build-up within the laminate. Upon demoulding, a large increase in spring-in is seen for the fixed case, due to the release of tensile stresses along the laminate profile length. During the second heating ramp under post curing, the same initial negative gradient in the spring-in angle is seen in both cases, due to thermal expansion resulting in an opening of the profile angle again. However, once $T_{cure} > T_g$ residual stresses in the fixed case are totally released, seen by the sudden increase in spring-in for the fixed case, after which both cases follow the same pattern. The sudden increase in spring-in during this transition is a result of the instantaneous stress relaxation of internal stresses in the fixed case. Note that no similar instantaneous relaxation in the free-standing case occurs due to the very small stresses built-up during curing. Comparisons to Svanberg's numerical and experimental results are given in Tab. 6.2.

Fig. 6.10 presents the integrated chemical shrinkage strain increments throughout the cure and post-cure cycle at nodal points N:304 and N:376 corresponding to points (a) and

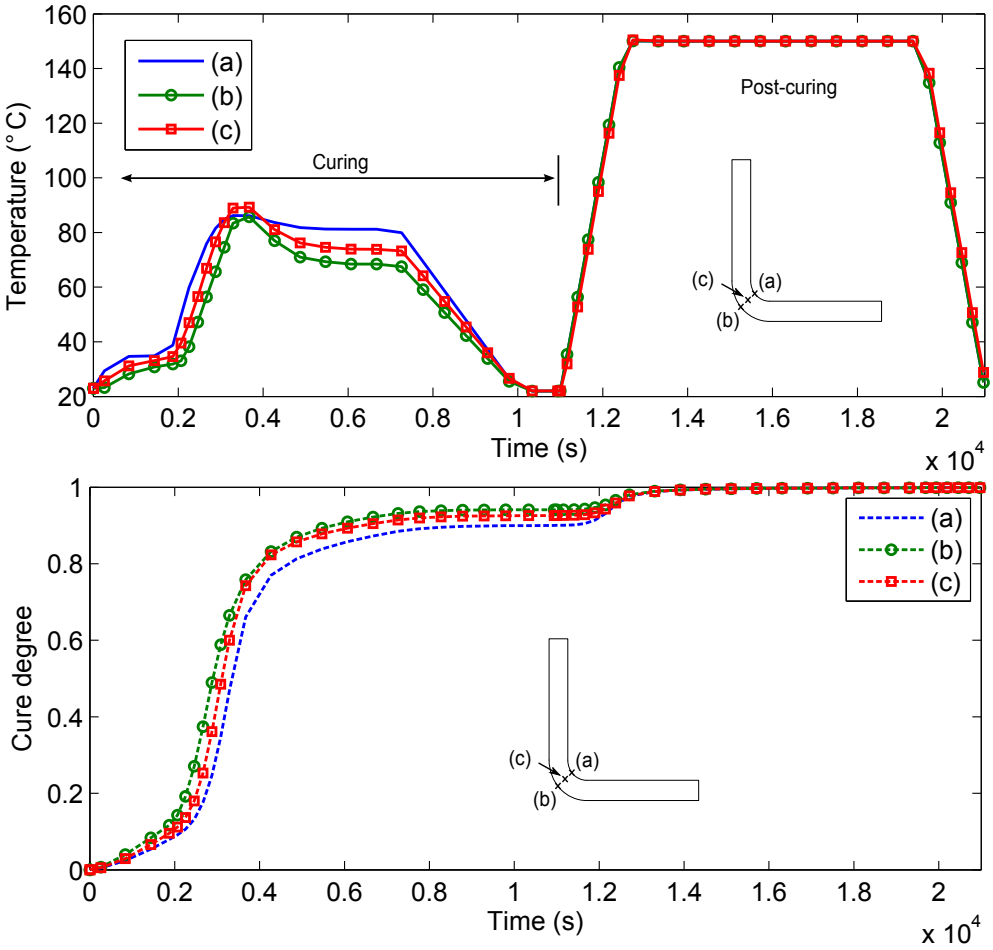

Figure 6.8: *(Top) Temperature profile and (Bottom) cure degree development experienced at the laminate mid-width through-thickness points (a-c).*

Process stage	Experimental [93]	Model [93]	Current study
Curing	1.0±0.1	1.4	1.38
Post-curing	1.1±0.05	1.2	1.16

Table 6.2: Spring-in angle (in degrees) comparisons between experimental and numerical values from [93] and current study predictions using the PD approach for the free standing case.

(b). Also shown are the cure degree developments at corresponding points. The cure shrinkage dependency on the cure degree development is clearly seen. Due to the higher temperatures at point (a) (see Fig. 6.8, a higher cure rate is exhibited here, resulting in faster shrinkage. It is clearly seen how through-thickness thermal gradients facilitate non-uniform curing, which in turn result in non-uniform shrinkage. A similar analysis of the integrated thermal strain increments is seen in Fig. 6.11, overlaid temperatures at similar points. Thermal strains are null until gelation occurs at app. 2.5E3[s]. After this thermal contraction is exhibited during cooling after the exothermic reaction and the first cooling stage to the ambient temperature. A difference is seen between the results at the two nodal points, due to the higher temperatures at point (a), resulting in slight thermal expansion prior final contraction during the cooling stage. However, due to the larger change in

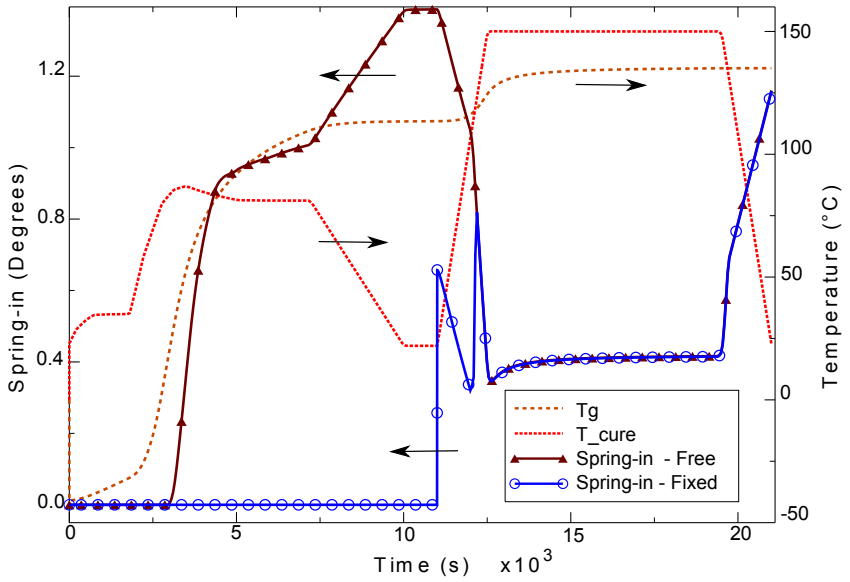

Figure 6.9: *PD model spring-in angle predictions during curing and post curing. Also shown are representative model cure temperature and glass transition temperatures at point (c).*

temperature, larger negative strains are experienced at N:376. During the post-curing cycle, a change in the strain gradient is seen, corresponding to the change in state from glassy to rubbery where higher matrix thermal expansion behaviour exists. From Fig. 6.11 it is clearly shown how negative thermal strains develop, even though the initial and final part temperatures are the same.

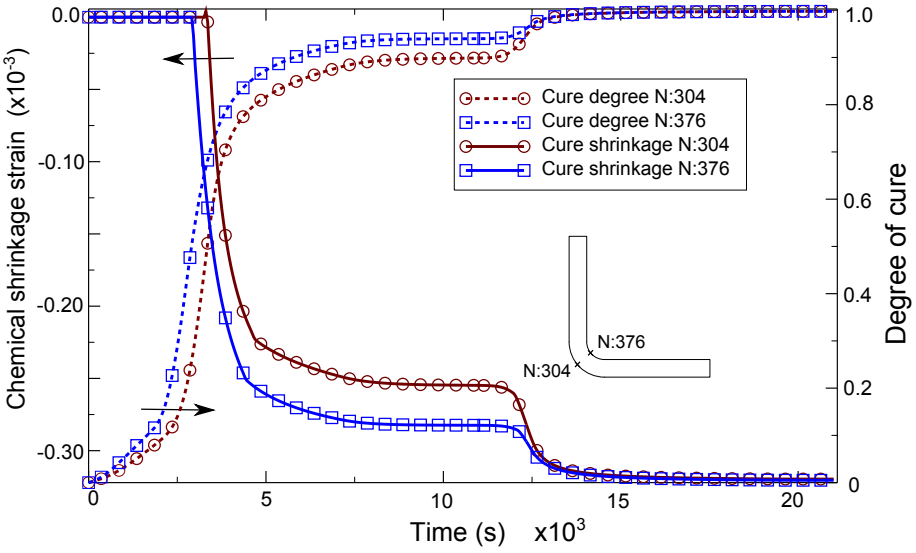

Figure 6.10: *Chemical shrinkage strain development during curing and post curing overlaid the cure degree development, seen at the mid-width nodal points N:376 and N:304.*

From the results shown in Fig. 6.10 and Fig. 6.11, the total process induced strains are calculated as the sum of the thermal and chemical strains.

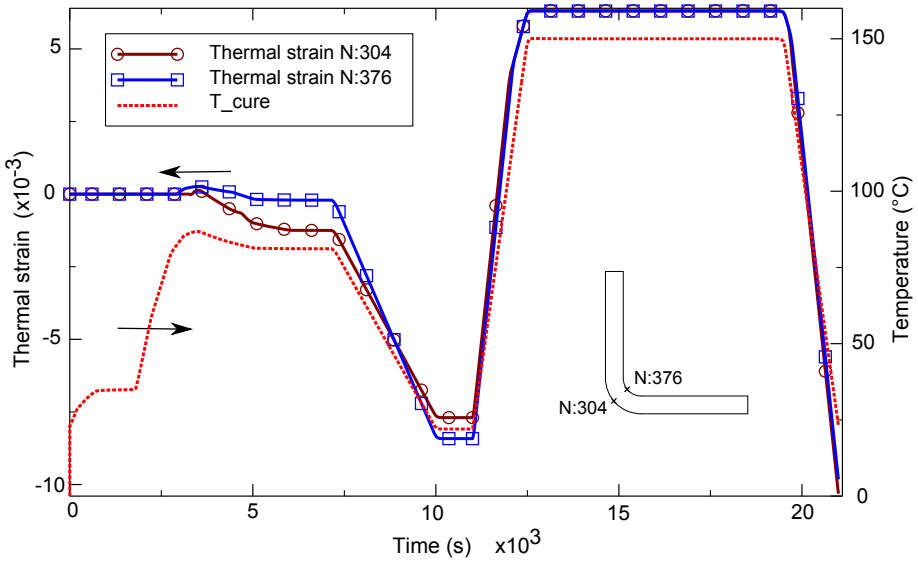

Figure 6.11: *Thermal strain development during curing and post curing overlaid representative temperature development, seen at the mid-width nodal points N:376 and N:304.*

Finally, in the following comparison of the different constitutive approaches, the same thermal conditions are considered for all cases, as previously presented. Thus, process induced strains (i.e. chemical and thermal) are also similar. In this manner, any eventual differences in model spring-in predictions are purely a result of the constitutive approach used. Fig. 6.12 presents the spring-in predictions using the CHILE and VE approaches for the considered mechanical boundary condition cases during the cure cycle. For the VE analyses, different fictive relaxation times ("tau") are used, for the sake of comparison. Note that in the VE approach, the temperature- and cure dependent shift factor is adapted from Prasatya et al. [80]. A calculation period corresponding to 5000[s] after demoulding is allowed, to capture stress relaxation or creep effects.

In Fig. 6.12 almost identical spring-in predictions for the free-standing case are seen for all models. This is understandable since process induced strains are equivalent to total strains in the absence of mechanical strains. However, in the fixed case, similar spring-in predictions are achieved after demoulding by the CHILE model, as compared to the PD approach used earlier in Fig. 6.9. It is also seen how larger spring-in predictions for the fixed case are obtained when using a viscoelastic approach with a very small relaxation time where internal stresses are relaxed rapidly. By increasing the relaxation time, a more elastic-type response is achieved. However, even though the relaxation times depicted are fictive, they clearly show the potential of the viscoelastic approach in matters where rate dependency is wished analyzed. The VE model also indicates here that not all internal stresses are readily released upon demoulding.

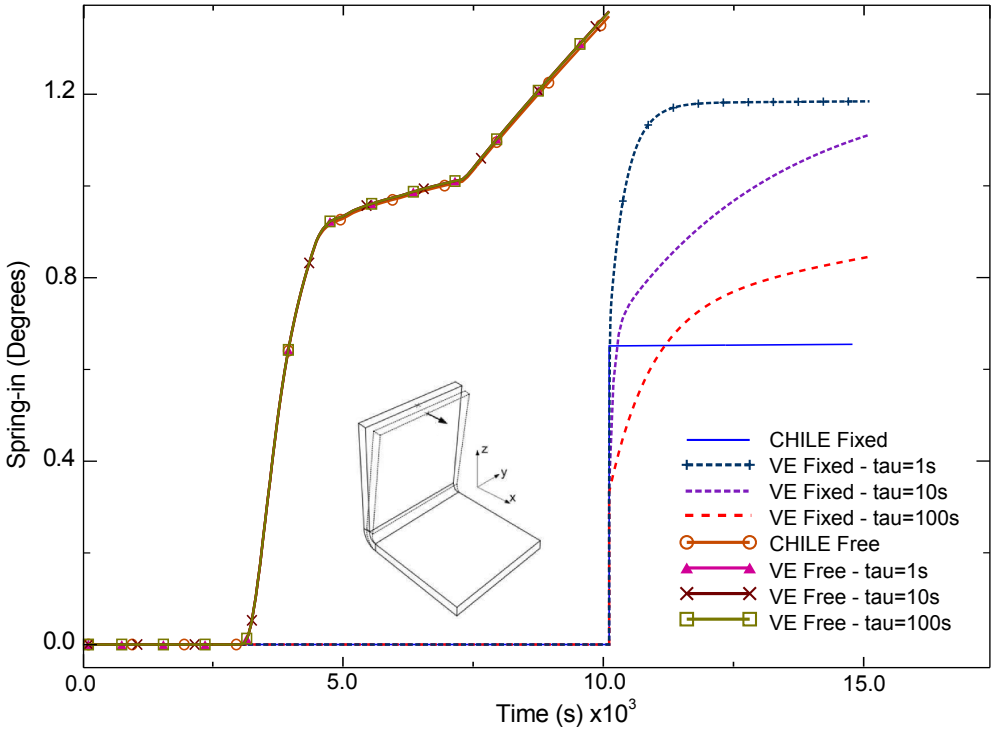

Figure 6.12: *Spring-in predictions using the CHILE model and Viscoelastic (VE) model with different relaxation times (tau) for the free-standing and fixed boundary condition cases.*

6.4 Summary

In this chapter, the implemented 3D model was tested and validated for different analytical, experimental and numerical cases. An attempt at showing the pros and cons of the different constitutive models has also been made, albeit this is done in the VE case using fictive material behaviour. A detailed study of the viscoelastic approach for composites process modelling is found in the appended Technical Report, where for instance, detailed descriptions of the workings of the concept of reduced time, shift functions and relaxation behaviour of thermoset resins is presented and discussed.

Chapter 7

Modelling Case Studies

In this chapter, different modelling case studies are presented. The first concerns predictions of process induced strains in a thick glass/epoxy laminate plate where comparisons to *in situ* strain measurements from embedded optical fibre Bragg grating (FBG) sensors are made. The second case study focuses on an investigation of shape distortions and residual stress build-up in a commercial wind turbine blade root section during curing, courtesy of LM Wind Power A/S, Lunderskov, Denmark.

7.1 Case 1: Process-induced strains in thick laminate plate

The internal strain development during curing of a thick laminate plate at elevated temperatures using a long cure cycle is analyzed. One of the objectives with the study is to evaluate how accurate the CHILE and PD constitutive modelling approaches are at predicting the internal strain development, in what is essentially a viscoelastic problem. This is done by comparison of the 3D model total strain predictions with experimentally determined *in situ* strains within the laminate part, using embedded fibre optic sensors. From this, a direct comparison can be made with model predictions of how thermal expansion- and chemical shrinkage strains develop within the laminate throughout the process, as well as the influence of tooling.

The work presented in this section is the basis of the studies conducted in the appended Papers II and III, generally concerning numerical modelling and experimental *in situ* strain monitoring of process induced strains in thick glass/epoxy laminates.

The modelling approach presented in this case study is twofold; First, a 1D thermal model is used to determine accurate cure kinetics and heat transfer conditions for the problem. This is done due to the lack of initially available resin cure kinetics material data for the epoxy resin used. Once appropriate thermal and cure kinetics parameters are determined, 3D thermomechanical models are employed for the determination of process strains and stresses.

7.1.1 Introduction to FBG sensor principle

FBG sensors have been used succesfully in a number of studies for strain and temperature monitoring in composites, e.g. [18, 48, 78, 79]. An optical fibre with an axial Bragg grating, back-reflects light when a broadband light spectrum is transmitted from a source through the optical fibre. The Bragg grating is a pattern created in the core of the optical fibre which acts as wavelength selective mirrors [66, 78]. The reflected light spectrum, which is transmitted into an interrogator for data acquisition, is centered on the predefined Bragg-wavelength λ_B according to the Bragg equation [66]:

$$\lambda_B = 2n_{eff}\Lambda \tag{7.1}$$

where n_{eff} is the effective index of refraction and Λ is the Bragg period of the grating. A schematic of a generic strain monitoring setup is seen in Fig. 7.1 showing data acquisition of the back-reflected light wavelength signla λ_{ref} from an arbitrary embedded FBG sensor.

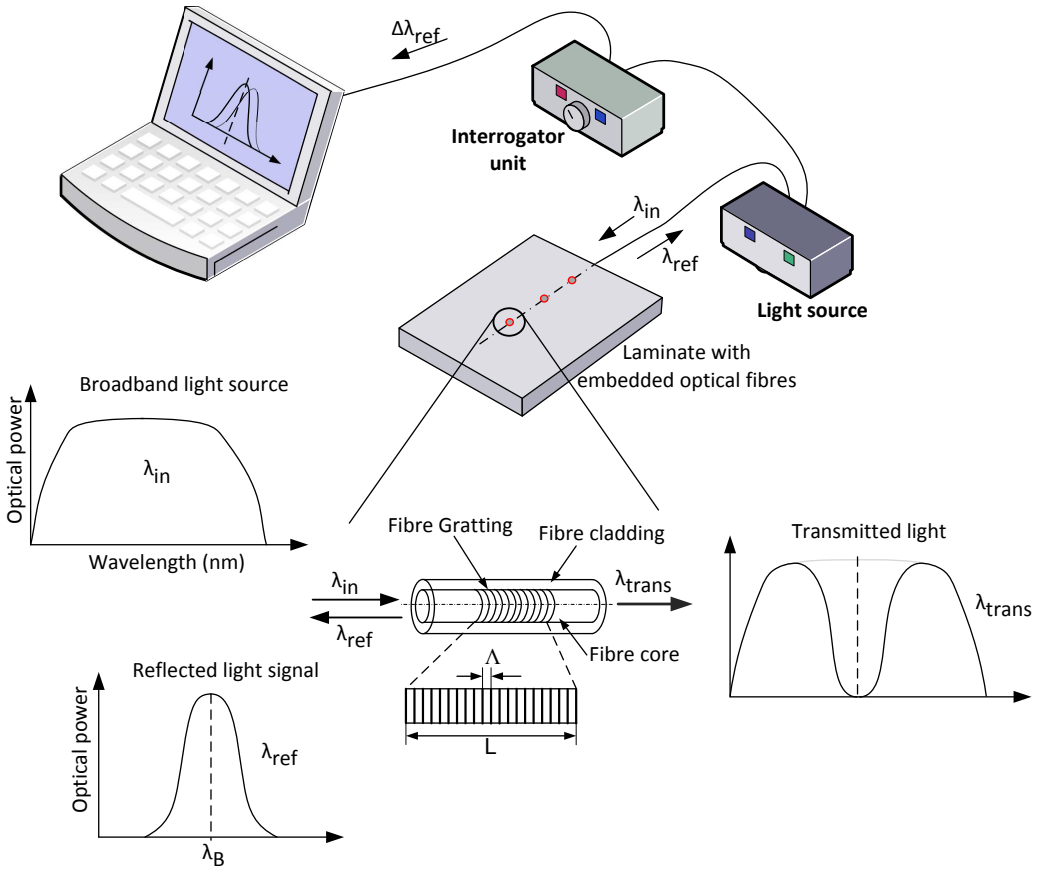

Figure 7.1: *Schematic of strain monitoring setup with embedded optical fibres and FBG sensor principle.*

When the FBG is embedded in a host material, and perfect bonding is assumed to exist between the optical fibre and the host material, any thermal or mechanical straining of the

host results in a linear variation of the Bragg wavelength, expressed as [66, 73]:

$$\begin{aligned}\Delta\lambda_B &= \lambda_B^0(K_\varepsilon[\Delta\varepsilon_{app}^{host} + \Delta\varepsilon_{th}^{host}] + K_T\Delta T) \Rightarrow \\ &= \lambda_B^0(K_\varepsilon\Delta\varepsilon_{tot} + K_T\Delta T)\end{aligned} \tag{7.2}$$

where λ_B^0 is the initial unstrained grating wavelength, K_ε and K_T are the mechanical strain- and temperature sensitivity factors, respectively. If the temperature at the vicinity of the strain monitoring region is known, the host material total strain increment in Eq. 7.2 can be readily determined. In various works, separately embedded thermocouples are used for this purpose [48, 79], an approach which is also adapted in the current study.

In this work, silica optical fibres provided by FOS&S, Belgium, with draw tower grating (DTG©) are used. The optical fibres are clad with an Ormocer© coating resulting in a final cladding diameter of 125μm. DTG FBGs are known to exhibit little variation in strain-optic coefficients when loaded which is advantageous in order to uphold linearity [79]. Furthermore, the coating helps reduce sensitivity to external transverse loading increasing the accuracy of the axial strain measurements. In this work, the silica optical fibre strain sensitivity factor K_ε is equal to 0.775E-6$\mu\varepsilon^{-1}$. K_ε is known to be between 0.77 and 0.78E-6$\mu\varepsilon^{-1}$ [18, 48, 79]. Furthermore, it has been reported that the strain sensitivity does not exhibit temperature dependency between 0-180°C [75] which lies well in the temperature range of the current study. K_T is a product of the optical fibre coefficient of thermal expansion α_{OF} and the thermo-optic coefficient ξ. α_{OF} of a silica optical fibre is equal to 5.5E-6°C^{-1} and is fairly close to the CTE of the composite reinforcement glass fibre (app. 5.04E-6°C^{-1}). K_T is equal to 6.27°C^{-1}. The sensitivity factors are determined through calibration tests.

7.1.2 Experimental procedure

A glass/epoxy UD laminate plate measuring 400x600mm consisting of 52-layers UD E-glass fibre mats with a nominal area weight of 1246g/m^2 was vacuum infused on a 10mm tempered glass plate, pre-coated with release agent, resulting in a final laminate thickness of app. 46mm. Note that although this is considered fairly thick in many composite applications, laminate sections with a thickness of upto 150mm are known to exist in large wind turbine blades. Epikote RIMR135/RIMH137 epoxy resin and hardener was used as the matrix material, developed for the wind turbine industry. The epoxy is a diglycidyl ether of bisphenol-A (DGEBA) resin with an amine curing agent. A schematic of the experimental infusion setup and laminate layup is given in Fig. 7.2. Prior infusion, various sensors were embedded within the dry preform; three J-type (Fe-CuNi) 2x0.5mm thermocouples (T_1,T_2 and T_3) and three optical fibres (FBG$_{Top}$,FBG$_{Center}$ and FBG$_{Bottom}$), each consisting of three FBG sensors interspaced along the optical fibre by 150mm. The sensors were placed at the bottom, center and top planes of the laminate plate, as illustrated in Fig. 7.2(a) and (b). The optical fibres are placed transverse to the main reinforcement fibre direction in order to capture the matrix-driven process strains. To ensure that the optical fibres remain where placed during the process, the fibres are woven into the reinforcement fibre fabric using the loose backing fibres from an adjacent ply, see Fig. 7.3. The entire layup (laminate and 10mm thick tempered glass plate) is placed on an electric

heating plate (1000x1500mm) with a digital temperature control unit, where the infusion process takes place.

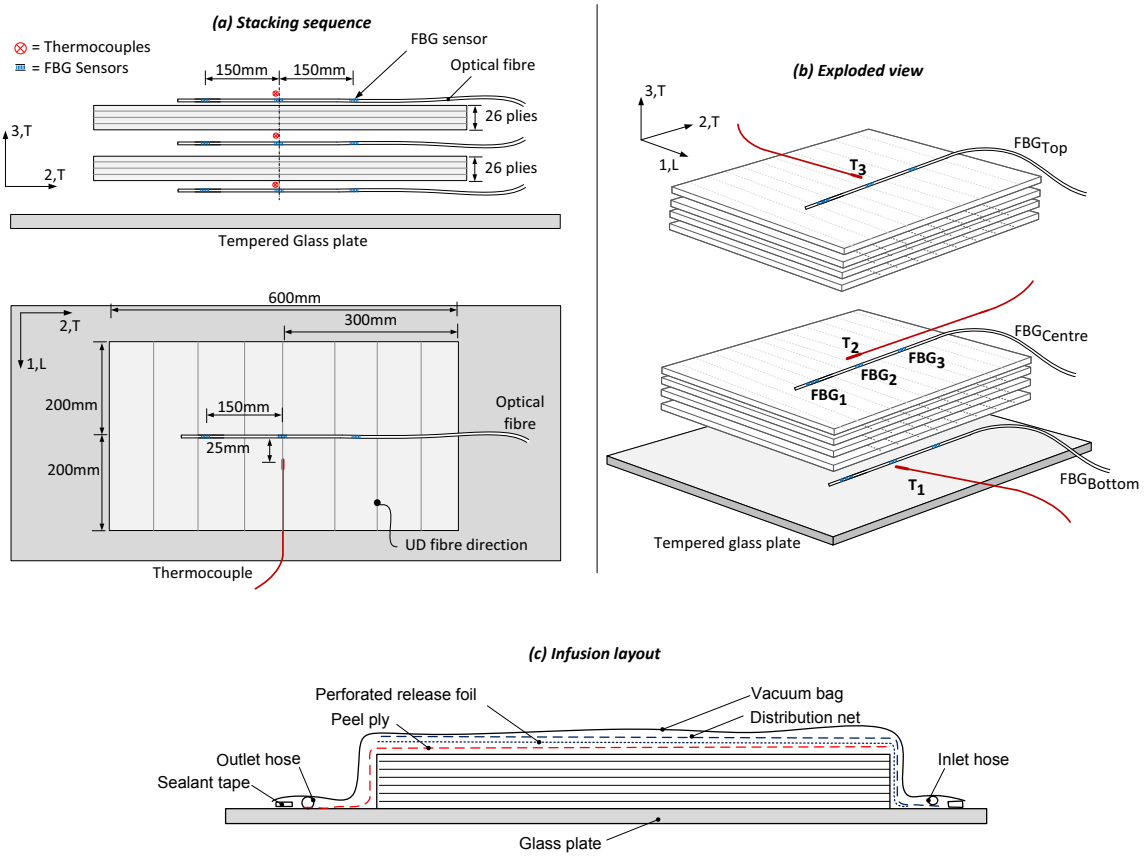

Figure 7.2: *Schematic of (a) the experimental laminate stacking sequence, (b) exploded view showing the position of embedded sensors and (c) experimental infusion setup.*

During the entire infusion and curing process, data was logged from the FBG sensors as well as all three thermocouples using an I-MON E Interrogator from Ibsen Photonics and a digital thermometer, respectively. Strain measurements from all three embedded optical fibres (bottom, center and top plane) were only carried out at specific intervals: i) after vacuum bagging, ii) prior applying vacuum at the outlet, iii) after infusion and cooling and iv) after demoulding. Due to the number of input channels, in situ strain measurements during infusion and curing could only be conducted from a single optical fibre, hence the mid-layer embedded optical fibre FBG_{Center} was chosen.

Experimental results

Fig. 7.4 presents the measured temperatures during infusion and curing, logged by the embedded thermocouples ($T_1 - T_3$) and the room- and heat plate surface temperatures (T_4 and T_5), respectively. The temperatures at the laminate plate bottom T_1 are initially highest due to the heat plate. Likewise, temperatures at the laminate top T_3 are lowest due to free convection to the surroundings. Changes in curve gradients at points (A), (B) and (C) are seen as the resin flow front reaches the thermocouples. After this, an increase in

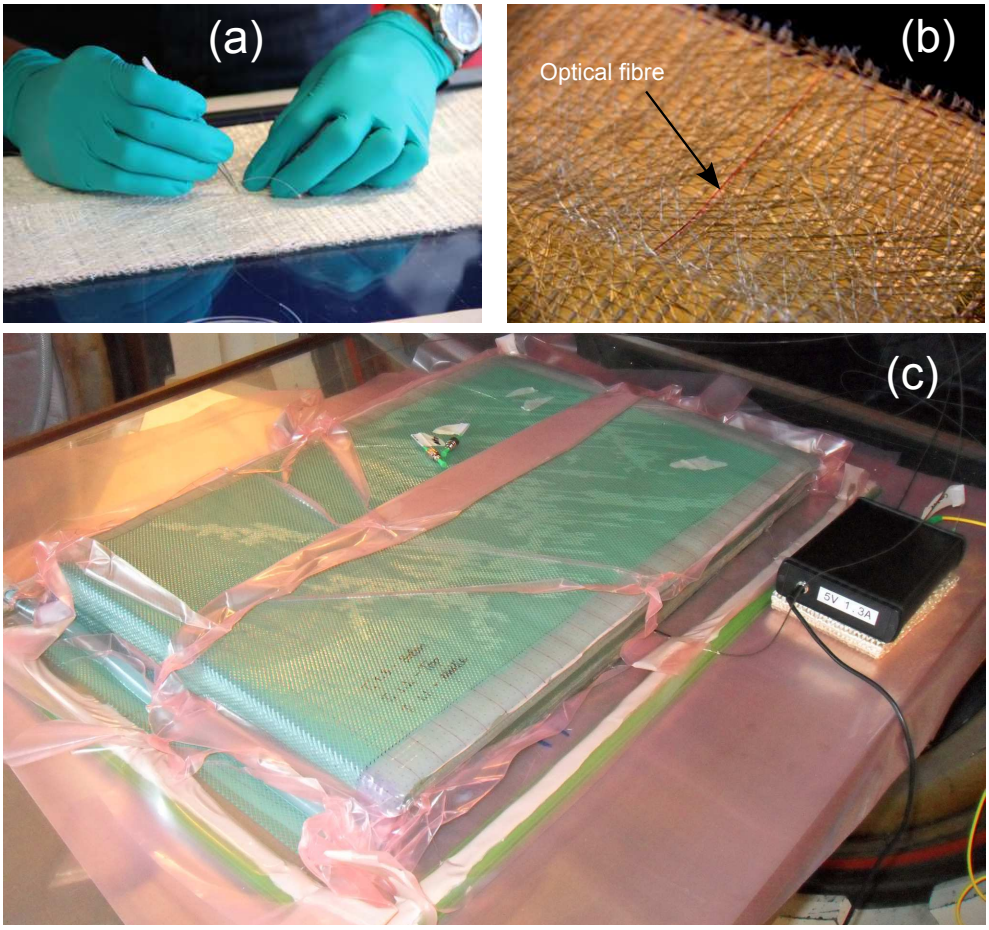

Figure 7.3: *(a) Optical fibre placement by weaving through individual reinforcement fabric backing fibres. (b) Optical fibre after placement and (c) laminate on heat plate prior infusion after sensor embedment, layup and vacuum bagging.*

temperature is experienced as a result of the onset of curing and the exothermic reaction heat release. The exothermic reaction induces the highest temperatures at the center of the thick laminate. After the exothermic reaction peaks, the laminate plate cools back to a steady state temperature upheld by the heat plate. Note that the heat plate is set at a constant temperature of app. 40°C, but due to poor thermal contact and convective cooling, a slightly lower temperature is measured by T_5. After app. 1050 minutes, the heat plate is turned off and the laminate plate cools by natural convection.

The corresponding in situ laminate transverse total strain variation $\Delta\varepsilon_{tot}$ during the process at the laminate mid-plane is seen in Fig. 7.5. The strain development generally corresponds to the temperature history presented in Fig. 7.4, mainly due to the effects of thermal expansion and contraction. The variations in strain measurements early in the process upto app. 70 minutes, are due to the resin flow front progression during infusion, which the embedded FBG sensors also are capable of monitoring. However, perfect strain transfer between the optical fibre and the viscous resin material is not fully developed early in the process, why interpretation of any deviations in measured strains should be done with caution prior resin gelation. Due to thermal expansion strains during

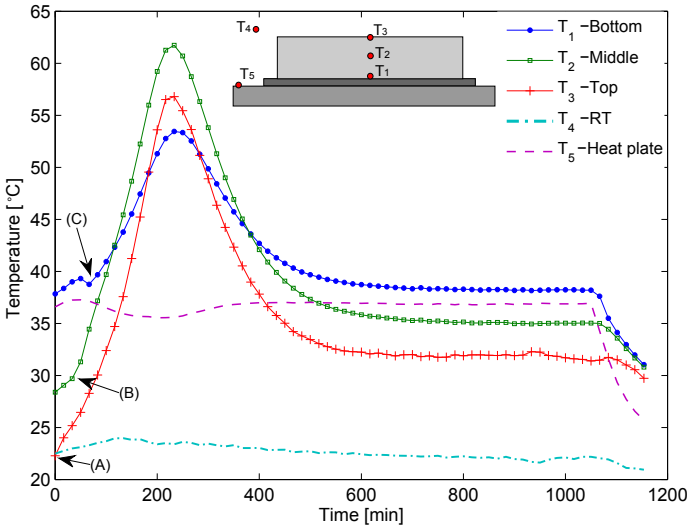

Figure 7.4: *Experimentally determined thermocouple temperatures during infusion and curing of glass/epoxy laminate plate, measured within the plate ($T_1 - T_3$), the ambient temperature (T_4) and on the heat plate surface (T_5).*

the exothermic reaction, positive strain increments arise. After this, the laminate cools and negative strain increments are seen from all three sensors. Note that chemical cure shrinkage also occurs, which further contributes to the negative strain increments. This is also seen during the early stages of the temperature hold (after app. 600minutes) where a slight negative gradient still is present in the measurements even though temperatures in Fig. 7.4 are constant. After this, the final cooling stage takes place and an increase in negative strains is measured due to thermal contraction.

The total transverse strains after demoulding were measured from all the embedded optical fibres (FBG$_{Bottom}$, FBG$_{Mid}$ and FBG$_{Top}$) and are summarized in Tab. 7.1, along with the final mid-plane strains after curing, prior demoulding (shown in brackets). The measured final process-induced residual strains are all negative, largest at the top plane and smallest at the bottom plane where the plate is constrained by the glass tool. Furthermore, the final total strains are seen to be largest near the infusion inlet at FBG$_1$ and smallest near the outlet. This indicates that, differences exist in measurements along the same line (axial direction of embedded fibre) at the same laminate plane and not alone through the thickness.

	FBG$_{Top}$	FBG$_{Mid}$	FBG$_{Bottom}$
FBG$_1$ (near inlet)	-3.15	-2.39 (-1.64)	-1.15
FBG$_2$	-2.85	-2.29 (-1.51)	-0.79
FBG$_3$ (near outlet)	-3.02	-2.19 (-1.44)	-0.12

Table 7.1: *Total transverse strain measurements at room temperature after demoulding. Also seen are the strains prior demoulding at the laminate plate mid-plane in brackets. All values given in x10^{-3}*

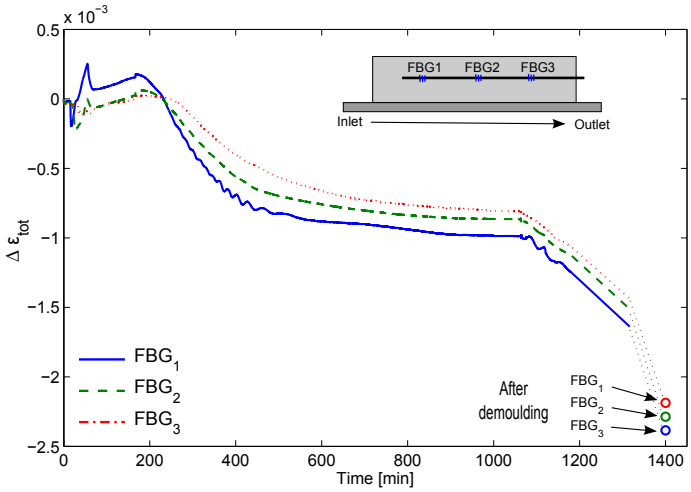

Figure 7.5: *Experimentally determined in situ total transverse strains during infusion and curing from embedded optical fibre FBG sensors at the laminate mid-plane.*

7.1.3 1D Thermal model

The 1D thermal model is adapted here in order to determine the cure kinetics behaviour of the epoxy resin used, which is not well documented a priori in the literature. Moreover, the cure kinetics parameters reported for identical DGEBA epoxies do not agree well, even for similar resin/hardener stoichiometric ratios, see e.g. [13, 74]. In the model, temperatures and the cure degree evolution are calculated as per the approach presented earlier in Section 5.1.1, and compared to the experimentally determined temperatures.

Boundary conditions

The experimentally measured temperatures at the laminate surfaces (T_1 and T_3 in Fig. 7.4) are used as prescribed boundary temperatures in the model. Hence the Dirichlet conditions for known boundary temperatures $\bar{T}$ are used [29]:

$$\begin{aligned} i = n_{th}: \quad & T_{n_{th}} = \bar{T}_{n_{th}}(t) \quad \Rightarrow \quad a_{n_{th}} = 0 \quad b_{n_{th}} = 1 \quad d_{n_{th}} = \bar{T}_{n_{th}}(t) \\ i = 1: \quad & T_1 = \bar{T}_1(t) \quad \Rightarrow \quad b_i = 1 \quad c_i = 0 \quad d_i = \bar{T}_1(t) \end{aligned} \tag{7.3}$$

Knowing the thermal boundary conditions, the cure kinetic behaviour of the matrix material is approximated using inverse modelling by fitting the predicted laminate mid-layer temperature to the experimentally measured values (i.e. T_2 in Fig. 7.4). This approach has also been successfully used in [93] and essentially omits the need to model the vacuum bag and tool with appropriate heat transfer coefficients, which can be cumbersome to determine. However, if the resin cure kinetics behaviour were to be used in other applications, DSC analysis is advisable, in order to capture more generic curing behaviour at other temperatures.

Results

The epoxy resin cure rate is modelled using the Kamal and Sourour autocatalytic expression (see Eq. 3.10). The determined cure kinetics parameters and thermal model properties in the through-thickness direction that result in a satisfactory agreement with experimental temperatures, are summarized in Tab. 7.2. Using these properties, the resulting temperature and cure degree model predictions determined at the laminate plate center are seen in Fig. 7.6. The predicted temperature development corresponds well with the experimental data using the material data summarized in Tab. 7.2. Near full cure is achieved quite early in the process, which means that the constant temperature dwell prior cooling could be shortened if a faster cure cycle was wished. However, the long temperature dwell was specifically chosen to investigate if any significant viscoelastic creep would occur. In Fig. 7.4 it should be noted that the initial 50 minutes of the measured temperature history, during resin infusion, was disregarded in Fig. 7.6 - i.e. the simulation is started when it is assumed that the reinforcement fabric is totally saturated. Mesh sensitivity analyses showed that only a temperature variation of 0.76 °C of the mid-plane exothermic peak temperature was obtained when using between 10 and 52 control volumes through the thickness, with the latter coinciding with one CV per ply. When using 10 CVs, the 1D elapsed calculation time is 23.78s, using a constant time step size Δt=1s. The corresponding 52 CV model, with the same time step size, takes 59.18s. Although this is more than double the calculation time, the model is still very fast, barring in mind that 63.0E3 calculation increments are carried out. Using the determined thermochemical properties, 3D modelling is conducted.

Property	Unit	Value
ρ	[kg/m^3]	1855
C_p	[J/(W°C)]	1240
k_z	[W/(m°C)]	0.24
m		0.78
n		1.12
A_1	[s^{-1}]	3.89E-6
A_2	[s^{-1}]	2.24E-3
$E_{a,1}$	[kJ/mol]	16.28
$E_{a,2}$	[kJ/mol]	11.08
H_r	[kJ/kg]	450.0

Table 7.2: *Glass/epoxy laminate through-thickness thermal properties and resin cure kinetics parameters used in the 1D thermal model.*

7.1.4 3D Thermomechanical model

Sequentially coupled thermomechanical analyses are conducted using the CHILE and PD constitutive approaches. As mentioned in Section 4.2, determination of viscoelastic process modelling parameters for the resin behaviour is complex, especially if accurate cure and temperature dependent shift function approximations are to be made. Hence in the current study, analyses using only the CHILE and PD approaches are conducted, and evaluated against any viscoelastic behaviour seen from the experimental results.

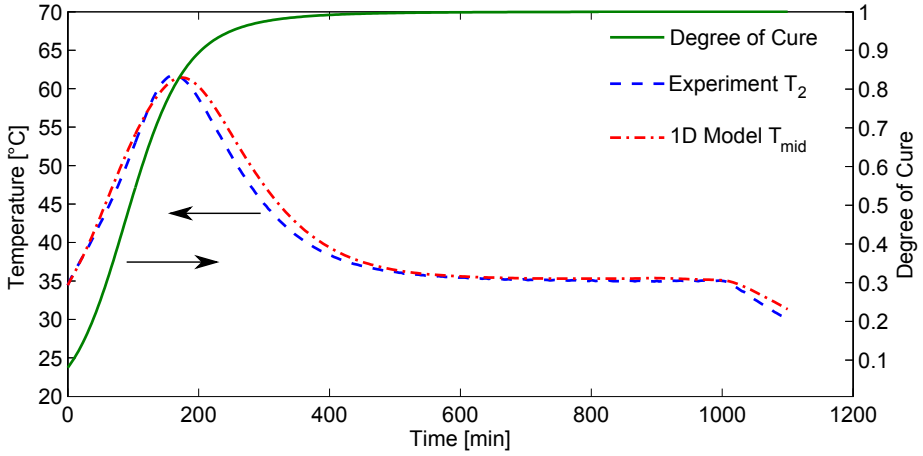

Figure 7.6: *Comparison of 1D model temperature predictions and experimentally determined mid-layer temperature development. Also seen is the corresponding cure degree evolution as predicted by the 1D model.*

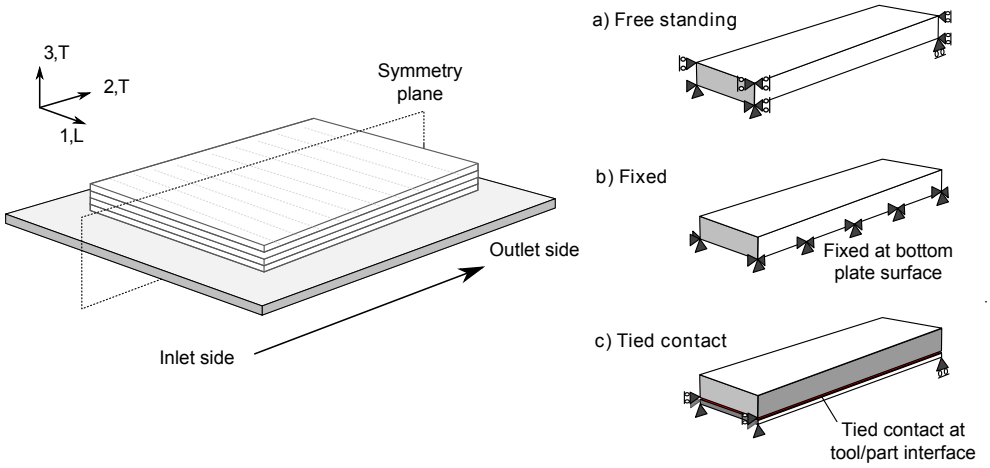

Figure 7.7: *3D model symmetry conditions and mechanical boundary conditions considered in the mechanical analyses.*

Boundary conditions

Similar thermal boundary conditions are prescribed in the 3D model as in the 1D model at the laminate plate top and bottom surface. In doing so, it is assumed that any in-plane variations in temperature in real life between, for instance, the infusion inlet and outlet hose is negligible. This assumption is justified by the relatively large heat flow through the plate thickness direction compared to the other directions. Three different mechanical BCs are employed on the laminate plate; (a) free standing, (b) fixed at the laminate bottom (tool/part interface) and (c) a tied contact condition at the tool/part interface by modelling the tool also, see Fig. 7.7. The tied contact condition allows the influence of tool thermal expansion and contraction to be included. This is known to be a major factor resulting in distortions and warpage in cases where much stiffer tools are used as compared to the composite part. In this way, a middle-ground between the free-standing and fixed conditions can be analyzed. Symmetry is assumed on the 2-3 plane (or yz-plane) and demoulding simulations are conducted for the tied and fixed boundary cases. This condi-

tion may not be completely valid as seen earlier in the differences in experimental strains along the infusion direction, but is considered to be insignificant. The tool temperature in the tied case is set to follow the laminate bottom layer temperature.

A total of 15x5x7 linear brick elements are used for the laminate plate and 15x5x1 elements for the 10mm thick tempered glass plate. 8-node linear heat transfer brick (DC3D8) and 8-node linear brick (C3D8) elements are used in thermal and mechanical analyses respectively. A mesh sensitivity analysis using a model with a finer mesh by a factor of 4 in each direction (i.e. 60x60x28 elements) revealed no significant difference in results at the laminate mid-thickness center region. Analyses with quadratic elements with reduced integration (C3D20R) were also carried out, revealing similar results. Some mechanical BC related stress singularities were reduced using the finer mesh, but no significant difference in mid plane strains were seen, hence the linear elements are used henceforth due to lower calculation times.

Mechanical material properties

The mechanical properties used for the E-glass and epoxy resin considered are summarized in Tab. 7.3, properties are given both in glassy state and rubbery state (in brackets). Also given are the CHILE model constants used. These parameters are fit to the Hexion RIM135 resin relaxation modulus behaviour, given by the manufacturer, and presented earlier in Fig. 4.7.

Property	Unit	**E-Glass**	**Epoxy resin**$^{(a)}$
E	[GPa]	73.0	2.9 (2.9E-3)
ν		0.22	0.38 (0.49)
α_{cte}	[x10°C^{-1}]	5.04	65.41 $^{(b)}$ (α_{cte}·2.5)
V_{sh}^{T}	[%]	-	7$^{(c)}$
CHILE approach		E_m **parameters**	
T_{c1}	[°C]	84.0	
T_{c2}	[°C]	100.4	
a_{Er}	[°C]	178.0	
α_{c1}		0.055	
α_{c2}		0.651	

$^{(a)}$:Values given in glassy state and rubbery state in brackets
$^{(b)}$: Experimentally determined using embedded FBGs (See Paper III, Section 4.3)
$^{(c)}$: Assumed value, conservatively based on literature [47, 95, 105]

Table 7.3: *Constituent glass fibre and RIM135/137 epoxy resin mechanical properties used in the 3D models. Also given are the CHILE model constants used in Eq. 4.4*

As opposed to the CHILE approach, in the PD approach the instantaneous transition between rubbery and glassy state is only governed by the current cure temperature and glass transition temperature T_g given by the DiBenedetto equation (see Eq. 2.1). In this equation the resin parameters T_{go} and T_g are equal to 0.0 and 84.0°C respectively, while λ is 0.44. Moreover, the gelation cure degree α_{gel} is needed to describe the liquid to rubbery state transition. For similar DGEBA-type epoxy resins with amine curing agents, the gelation cure degree has been reported to lie between 0.45 and 0.63 [31, 65]. Hence, a conservative value of α_{gel}=0.5 is chosen.

Results and discussions

The predicted in situ total transverse strains at the laminate center are compared to the experimentally determined strain (FBG_2) at the laminate mid-plane in Fig. 7.8. Initially, this is solely presented for the CHILE approach for all three boundary condition cases. The fixed boundary condition case is seen to result in very small strains, while the free standing case is seen to result in an overestimation. In the case of the tied boundary condition, a good approximation to the experimentally measured strains is observed, with the best agreement early in the process. However, as the resin cures, the strain development goes from being driven by the tool expansion, to being driven by the induced thermal and chemical shrinkage laminate strains. In Fig. 7.8 one can also observe the non-constant curve gradient of the experimental results (FBG_2) between app. 500 and 1050minutes, as compared to the tied model predictions. From Fig. 7.6 earlier, it was predicted that the resin is almost fully cured after app. 500minutes. Hence, the curved through-thickness stress gradient observed from the experimental measurements is therefore not caused by residual chemical shrinkage, as the cross-links are already fully developed. This complies with reports that chemical shrinkage in epoxy resins mainly occurs prior vitrification [41, 46]. Hence the negative increase in transverse total strains during the constant temperature hold may be attributed to viscoelastic creeping of the composite matrix and not residual cure shrinkage. Unfortunately, the CHILE approach does not account for this slight creeping behaviour. However, it is likely that some slippage at the tool/part interface is also taking place.

The influence of the tempered glass plate is visible upon cooling (between app. 1050-1300 minutes) where a smaller gradient of the strains using the tied case is predicted, compared to the experimental results. This is due to the lower CTE of the tempered glass plate (9.0E-6$^{\circ}C^{-1}$) as compared to the transverse CTE of the laminate plate in the glassy state (46.07E-6$^{\circ}C^{-1}$). The differences in cool-down strain gradients between the model and experiment may therefore be due to slipping interactions occurring at tool/part interface, which is not accounted for in the mould using the tied boundary condition.

The final transverse total strains after demoulding are also seen in Fig. 7.8. Here, model strain predictions for both the tied and fixed cases are seen to overestimate the demoulding strains determined experimentally. This may be due to an overestimation of stresses due to the boundary conditions used and the lower total strain magnitude, or due to lack of capturing viscoelastic stress relaxation effects. Strains after demoulding using the tied boundary conditions at all the regions corresponding to the experimental embedded FBG sensor points are compared to experimental values in Tab. 7.4, i.e. for FBG_1, FBG_2 and FBG_3 at the top, middle and bottom of the laminate plate. Note that FBG_1 and FBG_3, have identical results in the model due to symmetry along the length of the laminate in the model. Hence, one value is presented only representing both FBG_1 and FBG_3. Strain predictions using the tied condition are seen to agree somewhat with experimental values at the laminate top and middle layer, but large differences are seen at the laminate bottom near the tool/part interface. The small strains determined experimentally at the bottom of the laminate at FBG_3 near the outlet hose was found to be due to slight unwetted regions. However, the differences in results at the plate bottom at FBG_2 are still significant and believed to owe to the simple boundary conditions used in the model.

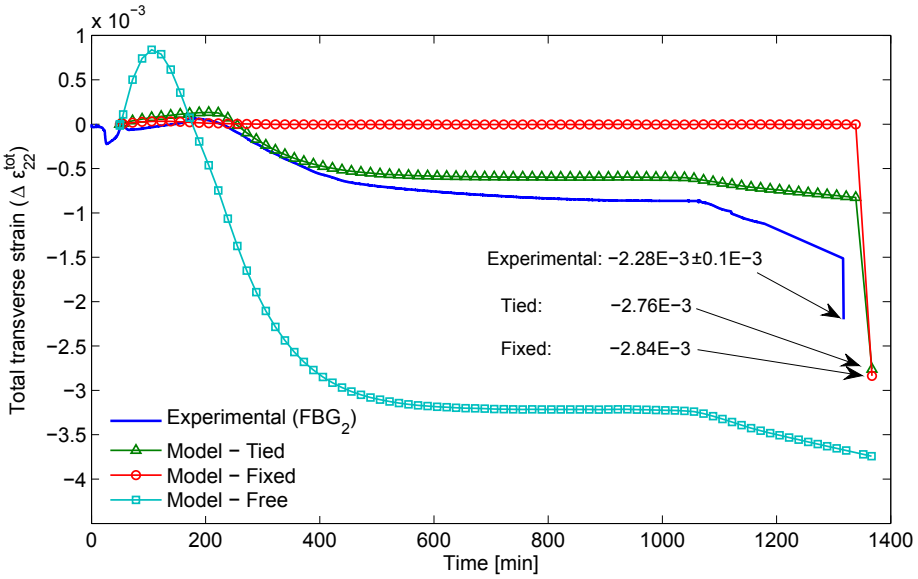

Figure 7.8: *CHILE model total transverse strain predictions using the free, fixed and tied mechanical boundary conditions, compared to experimental strains at the laminate plate mid-plane center. Final part strains after demoulding are also shown.*

	Top		**Mid**		**Bottom**	
	Exp.	Model	Exp.	Model	Exp.	Model
FBG_1	-3.15E-3		-2.39E-3		-1.15E-3	
FBG_3	-3.02E-3	-2.80E-3	-2.18E-3	-2.88E-3	-0.11E-3	-2.79E-3
FBG_2	-2.85E-3	-2.72E-3	-2.28E-3	-2.76E-3	-0.79E-3	-2.77E-3

Table 7.4: *Comparisons of CHILE model (using tied BC) and experimentally determined transverse strains after demoulding.*

The nature of the variation in transverse strains upon demoulding is analyzed by comparing the tied and fixed model transverse stresses along paths corresponding to the sensor positions in Fig. 7.9 for the laminate and plate (left) and for the laminate stresses alone (right), before and after demoulding. Due to the more stringent constraints posed by the fixed condition, larger stresses are developed after curing in the laminate. These stresses are tensile, due to the *hard* constrain restricting chemical shrinkage and thermal contraction during cooling after gelation. However, in the tied case, lower stresses are seen due to the compliance of the tool, which the laminate is in equilibrium with prior demoulding. For both cases, once the mechanical constraints are suppressed, simulating demoulding, the stresses fall drastically and are almost null. Slight gradients in the through-thickness stresses are also seen in Fig. 7.9 (right), resulting in larger tensile stresses at the laminate top for the fixed case, and largest tensile stresses at the laminate mid region for the tied case. These through-thickness gradients are discussed subsequently, by analyzing the total- and elastic transverse strain development during curing at the laminate center-line top and bottom points, as well as the corresponding transverse stresses, presented for the fixed case in Fig. 7.10 and for the tied case in Fig. 7.11.

In Fig. 7.10, the fixed constraints at the laminate plate bottom result in negligible total strains at the bottom of the plate and very small total strains at the top. Early in the

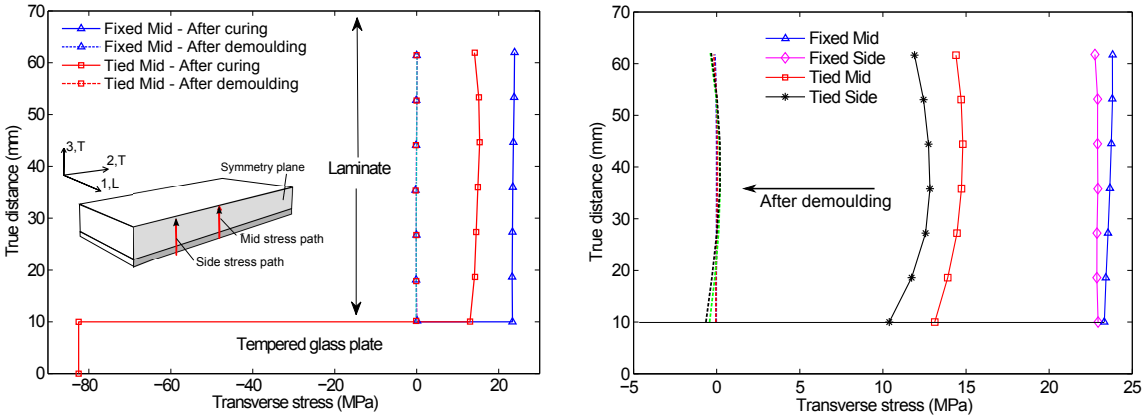

Figure 7.9: *Through thickness laminate transverse stresses after curing and after demoulding, for the fixed and tied mechanical boundary condition cases using the CHILE approach. (left) Seen only for the mid-line path and (right) shown in detail for mid- and side-line paths in laminate part only.*

process, negative elastic strains develop due to thermal expansion upon heating (note that if $\varepsilon^{Total} \approx 0 \Rightarrow \varepsilon^{elastic} = -\varepsilon^{thermal}$). Upon gelation, the matrix is able to sustain stresses, seen as the beginning of stress development after app. 10E3s. However, by this time in the process, the exothermic reaction has peaked and thermal contraction as well as chemical shrinkage result in tensile stress development due to tooling constraints hindering contraction. Recall in Fig. 7.4, that temperatures were seen to be highest at the laminate mid and bottom region, and lowest at the top due to free convection. Hence the smaller thermal strain increments result in larger process induced strains ($\varepsilon^{Pr} = \varepsilon^{th} + \varepsilon^{ch}$, where ε^{ch} is negative), which in turn result in larger tensile stresses at the plate top for this particular case. When a similar analysis of the strain and stress development is conducted for the tied case in Fig. 7.11, it is seen that the total strain development due to the expansion and contraction of the glass tool results in lower elastic strains and stresses. However, it is now easy to understand why the stresses shown in Fig. 7.9 (right) are largest in tension at the laminate mid region, since these are mainly a result of higher thermal strains at the plate center due to the highest peak temperatures achieved here during the exothermic reaction.

The PD approach is also shortly investigated subsequently. A comparison of the PD and CHILE approach is given for the transverse strain predictions, overlaid with the experimental in situ strains, see Fig. 7.12. Strain predictions are also seen app. 150mm from the center line, representing strains at FBG_1 and FBG_3. The two approaches result in quite similar strain predictions, though slightly larger negative strains are achieved by the PD approach. This is however not a result of any instantaneous stress relaxation (recall the use of the internal state variable β_{ij} in the PD approach), but rather a result of the transition from rubbery to glassy state occurring later in the process than in the CHILE approach. This is seen when analyzing the temperatures governing the resin modulus transition during the process, i.e T^* for CHILE and $T_g(\alpha)$ for PD, presented in Fig. 7.13. The PD approach remains in the rubbery state until T_g crosses the cure temperature T. The same transition is governed in the CHILE approach by the temperature T^* and the fitted bounding temperature T_{c1}, which occurs before $T_g(\alpha) \geq T$. As a result, larger thermal

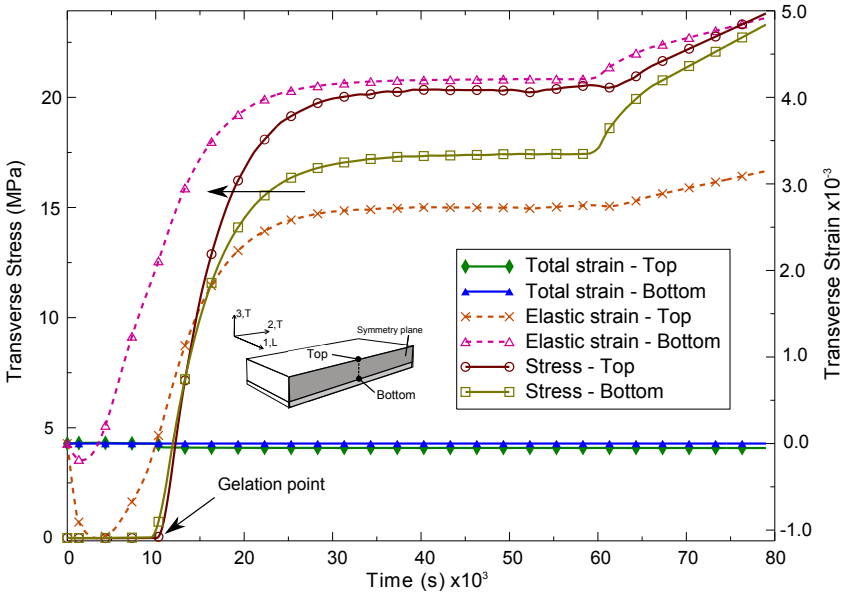

Figure 7.10: *Development of total and elastic transverse strains at the laminate center-line top and bottom point, during curing when using fixed boundary conditions. Also seen are the corresponding transverse stresses.*

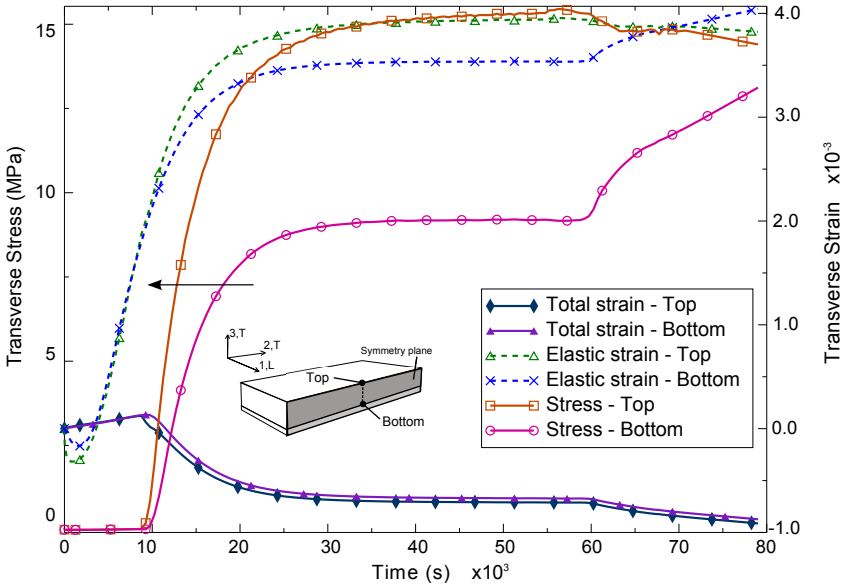

Figure 7.11: *Development of total and elastic transverse strains at the laminate center-line top and bottom point, during curing when using tied boundary conditions at the tool/part interface. Also seen are the corresponding transverse stresses.*

contraction occurs in a longer period in the PD model since a higher resin CTE exists in rubbery state. However, after the rubbery to glassy transition, both models follow similar behaviour because the cure temperature does not exceed T^* nor $T_g(\alpha)$.

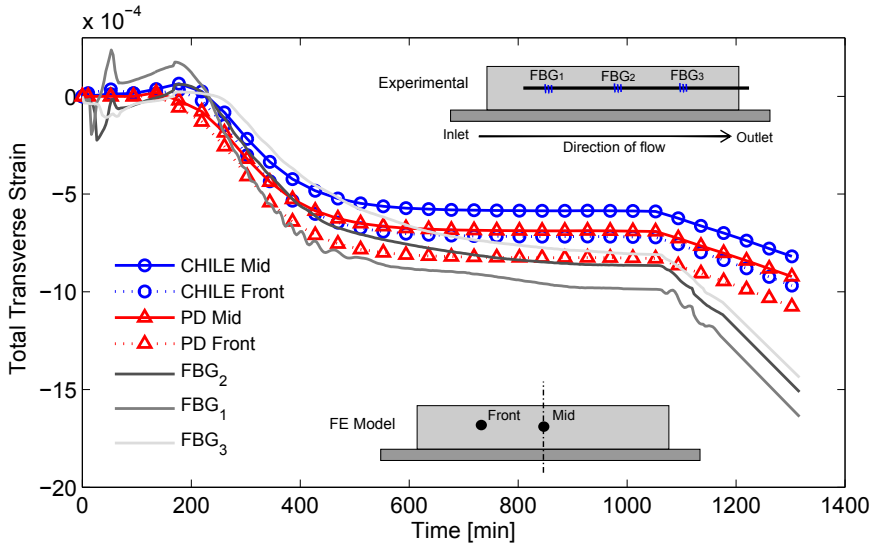

Figure 7.12: *Comparison of PD and CHILE transverse strains.*

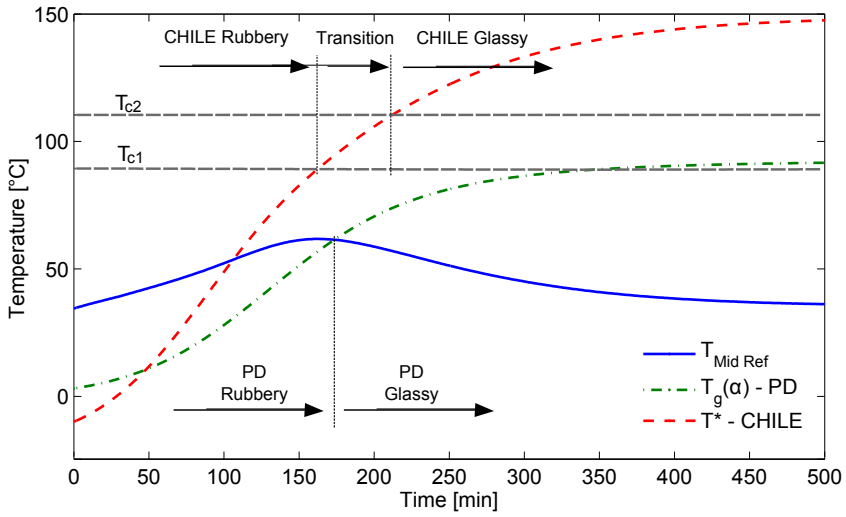

Figure 7.13: *Comparison of the temperatures governing the resin rubbery to glassy state transitions in the PD and CHILE constitutive approaches.*

From the total strain prediction presented in Fig. 7.12, no further need to analyze model differences between the PD and CHILE approach is needed for this specific case study, as model predictions are quite similar.

In the appended Paper III, further investigations are found of the laminate thickness influence on process induced strains. Furthermore, analyses where the tempered glass tool plate is replaced by different corresponding composite tools, representative of mould materials used in the manufacture of large composite components, are conducted.

7.2 Case 2: Process induced shape distortions in blade root section

Process-induced shape distortions and residual stresses are investigated in a wind turbine blade root section during curing, courtesy of LM Wind Power A/S. The root section analyzed is the LM48.8 blade root, a subcomponent in blades used on 2.5-3.2MW wind turbines. The root substructure represents one half of the entire blade root section. A schematic of the substructure is seen in Fig. 7.14. Due to confidentiality, specific details concerning part geometry and materials used are omitted. Moreover, the results presented in this case study are normalized with respect to maximum achieved values.

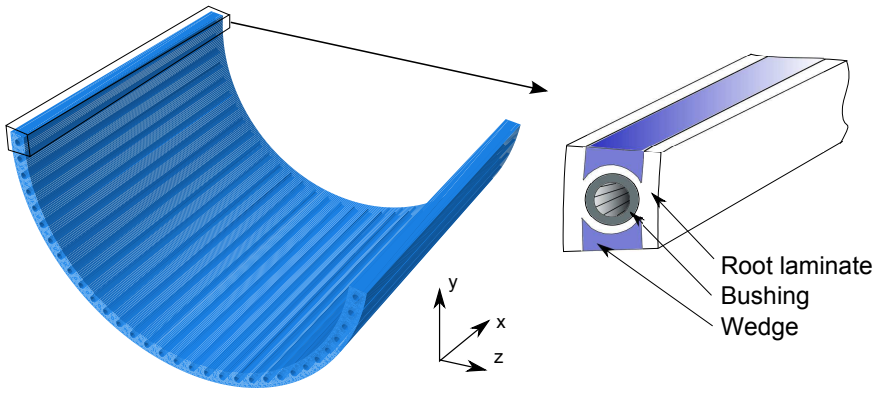

Figure 7.14: *Root substructure comprising of 32 inserts, that are built up of 3 main material subsections; steel bushing, a composite root laminate and pultruded wedges*

The material subsections presented in Fig. 7.14 represent a simplified version of the actual root section geometry and material composition. The basic function of the material subsections are as follows:

Bushings: The bushings enable mounting of the blade structure to the wind turbine rotor hub. The bushings comprise of pre-milled threaded steel cylindrical inserts. In this study, the bushings are modelled as cylindrical uniform cross-sectioned parts that run the entire length of the root substructure.

Pultruded composite wedges: The pultruded wedges are situated between each bushing and mutually separate them. The wedges are prefabricated composite parts used to ensure a more cost-effective lamination process [5]. In the model, the wedges also run the entire length of the substructure with a constant cross-section.

Composite root laminate: The root laminate comprises primarily of unidirectional (UD) composite fabric, situated in-between and around each bushing and wedge. The root laminate is in-mould cured, after lay-up and placement of all the individual substructure components are conducted.

7.2.1 Problem of interest

The analysis problem of interest concerns the development of manufacturing-induced distortions during in-mould curing of the root substructure. Geometric measurements of the roundness on 5 manufactured blade root specimens were conducted by LM Wind Power. The measure of roundness is here defined as the largest difference in the maximum and minimum circumscribed circle diameters. Nominal measurement results of the distance between opposing bushing center-points along the root circumference are presented in Fig. 7.15 as a function of the bushing number, starting from the blade trailing edge side. A variation of the diameter around the root circumference exists, with the general tendency that the smallest diameter is measured near the blade trailing edge and leading edge. It is also at these regions that the root section halves are assembled after curing using structural adhesives. In Fig. 7.15(left), the allowable tolerances are also shown, marked as dashed lines, corresponding to an allowable tolerance of 6.52E-2%. Hence deviations in the diameter larger than allowed are experienced, post manufacturing.

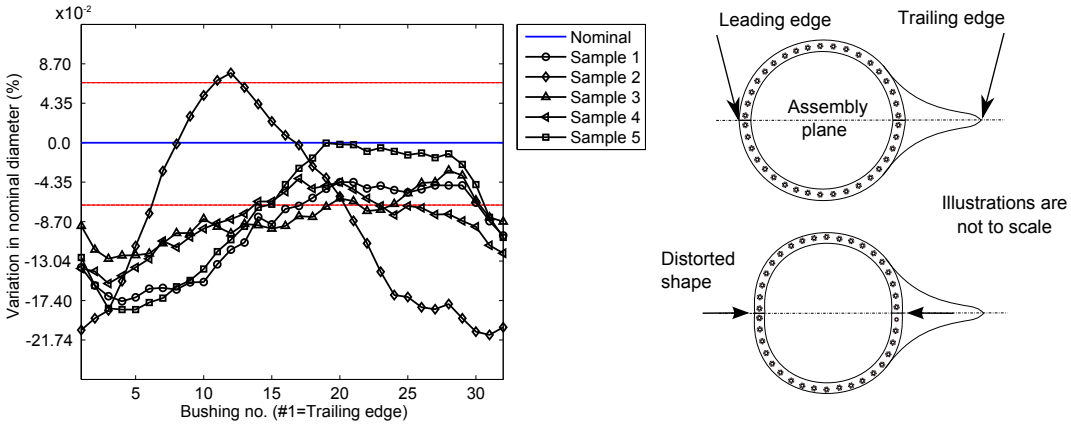

Figure 7.15: *(left) Nominal root section roundness variation data courtesy of LM Wind Power, (right) schematic of assembly plane with leading and trailing edge, along with distorted shape (not to scale).*

7.2.2 Analysis goals

A thermomechanical process modelling analysis of the curing stage during manufacturing of the blade root substructure is conducted. From this, predictions of final part shape distortions are derived and the driving mechanisms determined. As seen in Fig. 7.14, the root model comprises of 32 *beam-like* parts, assembled around each discrete bushing. These individual beams will be refered to as “Beam Elements” henceforth. These parts are assembled in the model accordingly using surface and edge constraints.

In the current case study, the thermomechanical analysis of shape distortions and residual stress development is conducted using a CHILE constitutive model.

7.2.3 Manufacturing conditions and materials

During the moulding process, a female mould representing the desired aerodynamic outer contours of the root section is used, see Fig. 7.16 (left). For large composite structures, manufacturing costs are reduced by using composite moulds, as opposed to costly steel moulds. In the layup phase, after the lower layers of the root laminate composite fabric are laid, the bushings are secured in place by a steel tooling, see Fig. 7.16 (right), before the pultruded wedges and remaining reinforcement fabric are placed around each bushing. Securing the bushings in place is vital in order to uphold the tolerances necessary for eased installation of the final blade assembly on the rotor hub on site. Hence, the main external mechanical constraints during manufacturing exist from contact to the mould surface and constraints from tooling on each bushing.

After the entire layup process is completed, resin distribution channels and a vacuum bag is placed, prior to infusion. These parts do not pose any significant constraint on the manufactured part and are therefore excluded in the curing model. Curing is conducted at ambient temperature without external heating, which is normally used to accelerate resin gelation and cross-linking. This is possible because a low temperature thermosetting resin system is used, containing inhibitors and initiators that are specifically designed to control the resin cross-linking behaviour.

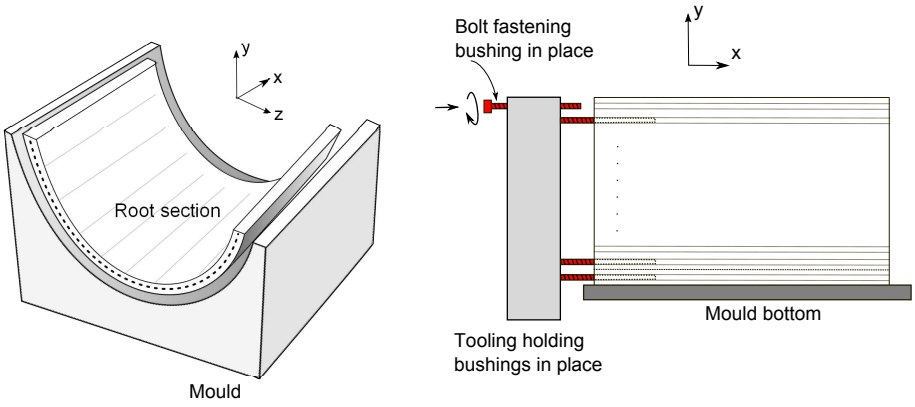

Figure 7.16: *Schematic of root section moulding assembly with mould part (left) and tooling constraints (right).*

Due to lack of experimental resin cure kinetics characterization data, e.g from DSC, approximations of the thermoset resin cure characteristics are adapted from literature for similar low-temperature curing resins. This is necessary in order to reduce the number of unknown model material parameters. In the approach used, first a cure kinetics model representative of curing times corresponding to that experienced by LM is chosen. After this, the reaction enthalpy of the given resin system is adjusted so as to match the peak temperatures experienced by LM in real life, corresponding to 80-90°C. Hence in the first step, the cure degree evolution for similar low temperature thermoset resins in works by Kamal & Sourour [42], Haider et al. [67] and Pusatcioglu et al. [81] are analyzed. These three sources are chosen due to the complete array of cure kinetics parameters available. The isothermal cure degree and cure rate evolution at 30°C and 30°C are presented in Fig. 7.17 and Fig. 7.18 for the resin systems presented in the above references.

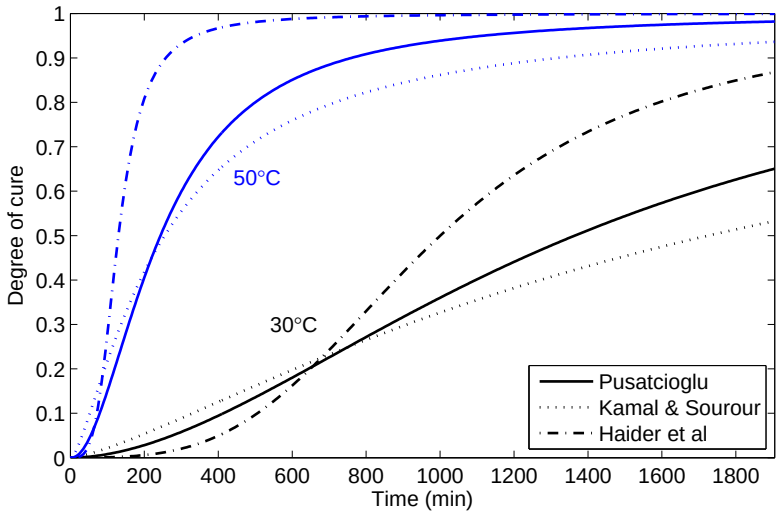

Figure 7.17: *Cure degree development low temperature curing resins from literature at 30 and 50°C*

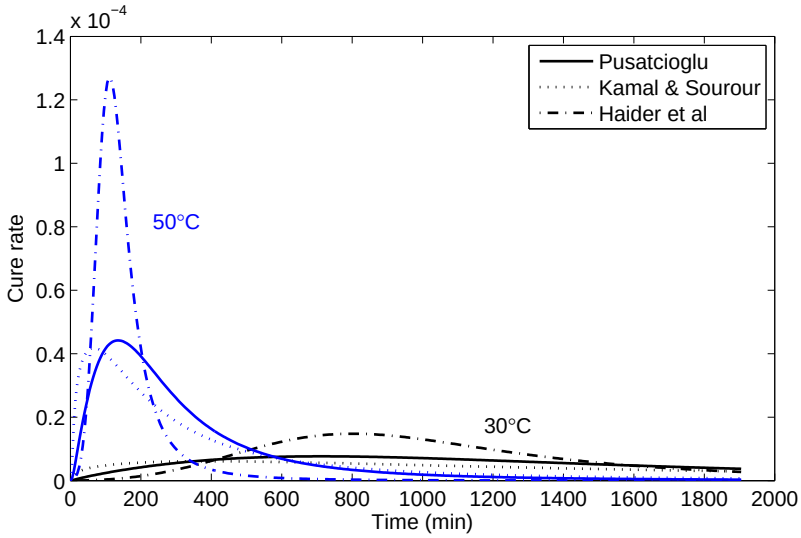

Figure 7.18: *Cure rate development of low temperature curing resins from literature at 30 and 50°C*

From Fig. 7.17 and Fig. 7.18 it is seen that the model proposed by Haider et al. is the fastest reacting resin system, approaching full cure for both the prescribed temperatures first. LM Wind Power A/S assumes that the root section curing process span lies in the vicinity of 5-6 hours. Hence a similar low temperature resin system is needed that approximates these cycle times. The model proposed by Haider is chosen as a first approximation in the subsequent analysis, as it is assumed that the kinetics behaviour best approximates the desired process cycle times. In essence, with the approach taken in this study, the actual kinetics behaviour is not of prime interest. The total reaction enthalpy H_T of the resin system is instead adjusted during the thermal analysis, until corresponding curing peak temperatures in the root section are obtained, as experienced in real life

to lie within 80-90°C. As of this, it is worth mentioning that the isothermal curing scenarios depicted in Fig. 7.17 and Fig. 7.18 are not entirely representative of the expected process curing conditions, as an increase in temperature due to the exothermic reaction is not accounted for here since the temperature is held constant, see e.g. Eq. 3.5. Due to the nature of the autocatalytic cure kinetics behaviour of the resin, this rise in temperature can rapidly accelerate the cure rate, which only further increases the latent heat release rate. Hence by analyzing the cure kinetics behaviour for the given temperatures in Fig. 7.17 and Fig. 7.18, an idea of which behaviour to expect for non-isothermal temperature conditions is gained.

7.2.4 Geometry and boundary conditions

The simplified uniform cross-section analysis model of the root section means that the analysis can also be carried out as a 2D problem. This is illustrated in Fig. 7.19(a-b). Hence a 2D model is considered taking geometric and boundary condition symmetry into account. In Fig. 7.19(c), a closer view of the different material regions around a representative bushing is shown. A slightly larger root laminate thickness exists towards the mould side surface as compared to at the inner surface. This difference in thickness can influence the uniformity of through-thickness temperatures and cure degree, as will be discussed later in this section.

In the model, boundary conditions for the sequentially coupled thermal and mechanical analysis are prescribed. The aim of the thermal analysis is to approximate the peak temperatures experienced by LM during production of the blade root section. Knowing the temperatures, realistic cure degree predictions can be obtained using the resin material data chosen earlier.

Thermal boundary conditions are replicated by considering heat loss to the surroundings at three main surfaces, (i) at the root section inner (free) surface, (ii) the bushing/tool interface surface and (iii) the root/mould interface surface. This is illustrated in Fig. 7.20. In the thermal analysis, 2 main fitting parameters are considered in order to achieve peak temperatures corresponding to 80-90°C during curing. These parameters include the resin total reaction enthalpy H_T, which is not specifically known *a priori*, and approximated surface heat transfer coefficients at the surfaces illustrated in Fig. 7.20. The conditions governing heat loss at the inner surface in Fig. 7.20 are significantly different to those at the bushing and mould contact surfaces. At the inner surface a thin boundary layer exists in real life, consisting of the infusion distribution net, peel ply, flow channels, vacuum bag etc. This effective thin layer exhibits low thermal resistance and a corresponding low thermal capacity in contrast to for instance the mould in contact with the outer surface or the tooling restraining the bushings. To replicate these different boundary conditions, various surface film condition scenarios are investigated using different heat transfer coefficients, presented in Tab. 7.5. By using surface film conditions, the need to model surrounding materials in contact is omitted. The choice of values presented in the table arise from the following arguments:

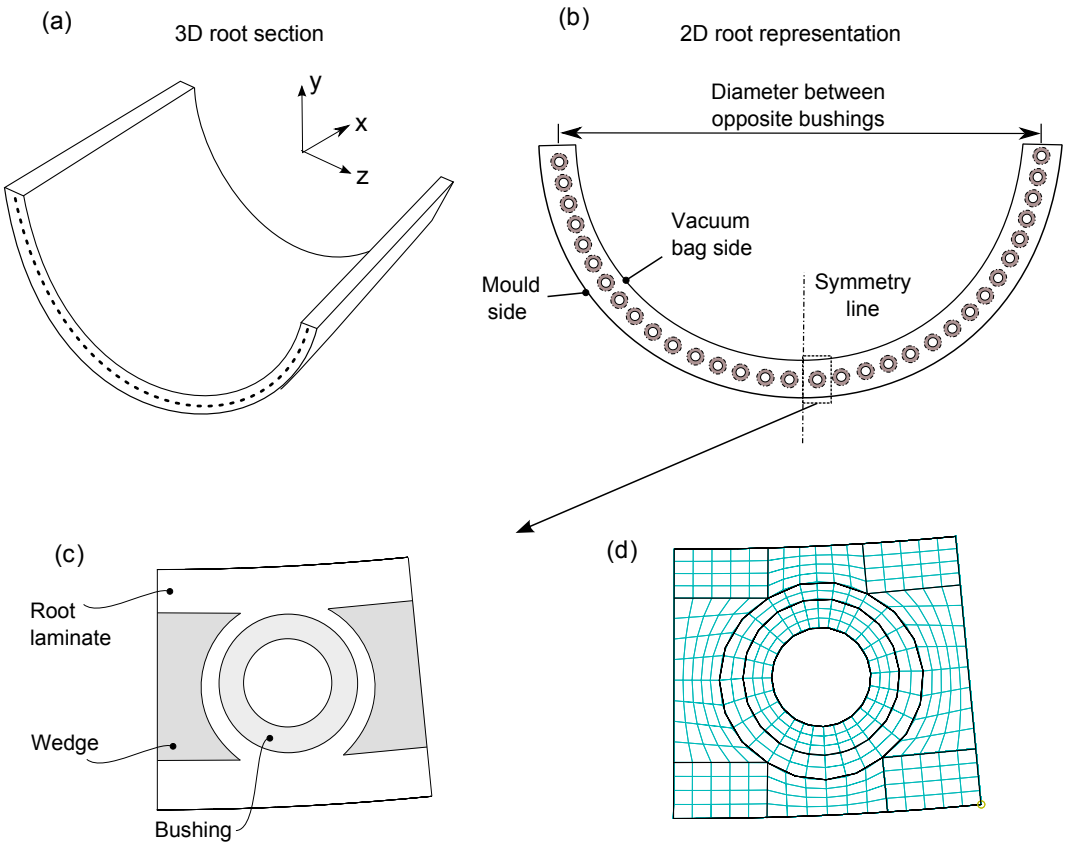

Figure 7.19: *(a) Schematic of 3D root structure, (b) 2D representation of structure disregarding length-wise (x-direction) effects, (c) close-up of bushing, wedge and root laminate material regions and (d) analysis model mesh utilized.*

- *Inner surface:* The *thin layer* inner surface, composing of a vacuum bag, distribution net, peel ply etc. is assumed to have a low thermal capacity and a corresponding low thermal resistance, with the latter being mainly due to the small layer thickness, see Eq. 5.4. Hence low heat transfer coefficients are prescribed here.
- *Mould (outer) surface:* At the part/mould contact interface, the composite mould is assumed to have a somewhat high thermal resistance due to the composite material low thermal conductivity, but a higher thermal capacity than at the inner surface due to the mould size and thickness. Hence the mould is assumed to result in a lag in heating and cooling at the part surface.
- *Bushing inner surface:* The high thermal conductivity of steel as well as good thermal contact between tool/bushing means that a somewhat high heat transfer rate is expected here. However, as precise tooling size and geometry is not known here, a conservative value is chosen.

To properly understand the influence of the thermal boundary conditions, three scenarios are simulated using different effective surface film heat transfer coefficients. Throughout the analysis, the surface film scenario 2 and 3 will be dubbed as the *low* and *high* heat transfer coefficient (HTC) boundary conditions. In the curing simulations an initial

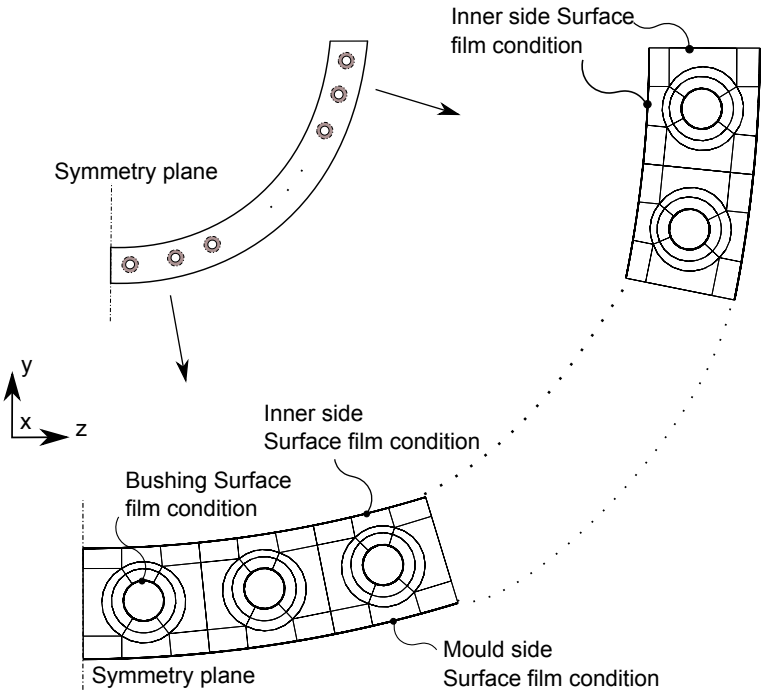

Figure 7.20: *Thermal boundary conditions considered using surface film conditions to represent real life heat transfer to the surroundings (air), mould and tooling.*

Scenario	Inner surface	Mould surface	Bushings inner surface
1	15	75	50
2 (“low HTC”)	5	75	50
3 (“high HTC”)	25	75	50

Table 7.5: *Investigated thermal boundary conditions for surface film conditions representing heat transfer coefficients. All values in* $[W/m^{2\circ}C]$

temperature of 25°C is prescribed to the entire model and held constant throughout the process simulation as sink temperatures at the boundary surfaces. Hence any increase in internal temperature is only due to heat generation. Convective heat transfer follows Newton’s convective law of cooling, expressed as [29]:

$$q = -h \cdot A(T_\infty - T_s) \tag{7.4}$$

where h is the heat transfer coefficient, A is the surface area perpendicular to the direction of heat flow. T_s and T_∞ are the temperatures of the surface of the body and the cooling fluid, respectively, with the later held constant at room temperature in this case.

In the mechanical analysis, two boundary condition cases depicting a free standing and fixed condition are considered, as illustrated in Fig. 7.21. In the free standing condition the root is allowed to freely expand and contract during curing. Contrary to this, in the fixed condition the bushings are pinned, i.e. displacements in all directions are constrained (U_y=U_z=0). This condition is chosen to represent tooling constraints from bolts screwed into the bushings. After curing, constraints on the bushings are removed, to mimic demoulding.

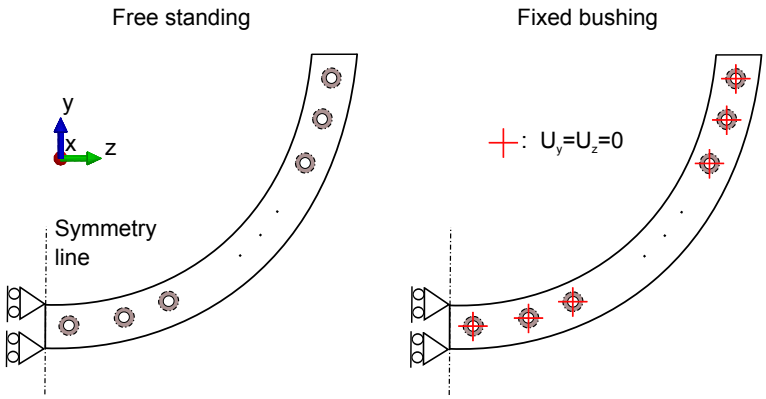

Figure 7.21: *Mechanical boundary conditions considered, (left) free standing and (right) fixed constraints at the bushing center.*

7.2.5 Results

Key results from the thermomechanical analysis conducted using the CHILE constitutive approach are presented henceforth.

Thermal analysis

Fig. 7.22 presents the curing temperature profiles for the different thermal film conditions at node 325 (see figure annotations) where the highest peak temperatures are achieved when using film condition 1 in Tab. 7.5. The presented temperatures are obtained using a reaction enthalpy equal to H_T=235[J/g]. It is seen that when a higher cooling rate is prescribed at the inner root section surface (*HTC high*), a lower peak temperature is achieved as compared to when lower surface cooling is prescribed (*HTC low*). The surface film conditions also influence how early in the cure cycle the peak exothermic temperature is achieved. With the conditions stated here, peak temperatures resembling those experienced by LM are obtained. The corresponding cure degree profiles at the same model point (node 325) are seen in Fig. 7.23. It is seen that the resin develops a fully cured state at a higher rate at this particular point when a lower cooling rate at the inner surface exists. This is a direct result of the higher temperatures and internal heat generation rates experienced. Recall that the cure rate behaviour is autocatalytic and *self-accelerating*.

In Fig. 7.24, temperature distributions along the through-thickness model symmetry plane (see e.g. Fig. 7.21) are presented at the process times when peak temperatures using the different boundary conditions are achieved. Note that the temperatures are highest towards the inner root surface and lowest near the root mid thickness region where the pultruded wedges are situated. This is due to low thermal conductivity of the composite wedge material, resulting in poorer heat conduction towards the mid thickness regions. At the depicted instants where the exothermic peak temperatures are achieved, the thermal- and cure degree gradient within the root section is largest, hence it is at this instant that the largest mismatch in thermal expansion and cure shrinkage behaviour is expected.

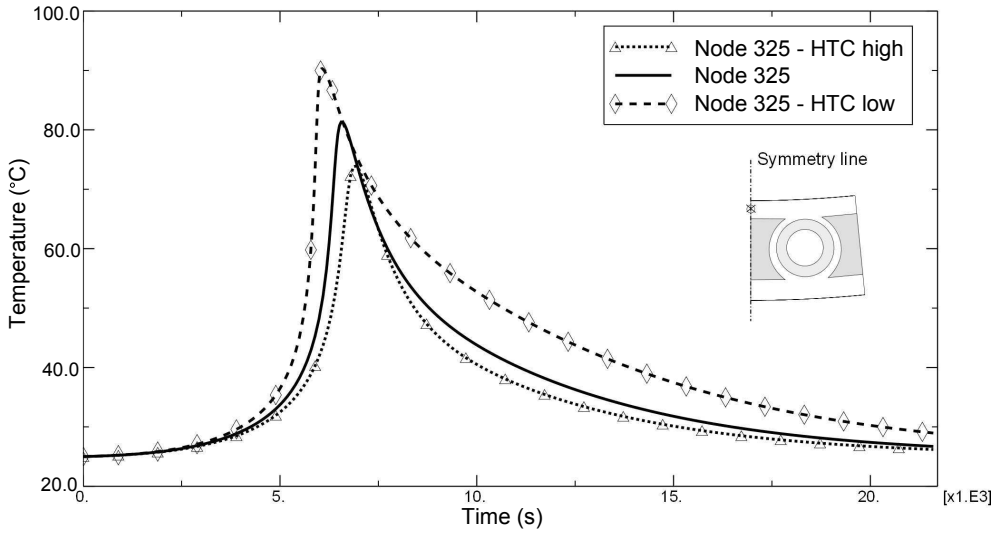

Figure 7.22: *Temperature profile at node 325 (see inserted illustration) where the largest peak temperatures are achieved using the different thermal boundary conditions.*

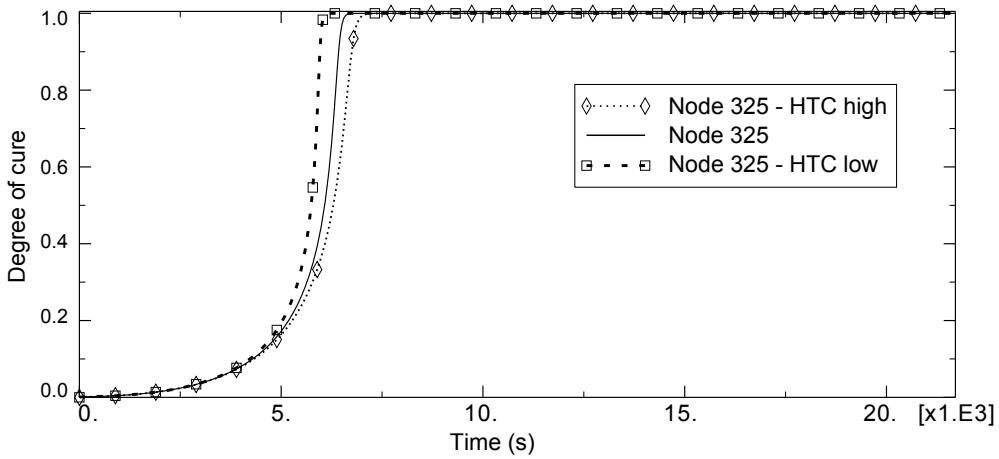

Figure 7.23: *Corresponding cure degree profile at node 325 for the temperatures shown in Fig. 7.22.*

To give an idea of the cross-section temperature distribution at the moment the peak temperature is achieved, a contour plot is presented in Fig. 7.25 with the corresponding cure degree distribution shown in Fig. 7.26. The thermal surface film condition 1 in Tab. 7.5 is used in both cases. In Fig. 7.25 it is seen that the bushings cool the mid thickness regions of the structure, while the regions comprising of the root laminate material, experience higher temperatures due to internal heat generation. The corresponding cure degree contour plot seen in Fig. 7.26, shows that some regions of the root laminate material are already fully cured while other regions, for instance around the bushings and towards the outer surface, are only cured approximately 26-74%. Hence the large thermal gradients result in large cure degree gradients within the part as expected. These gradients can greatly influence the internal strain and residual stress development, as some material re-

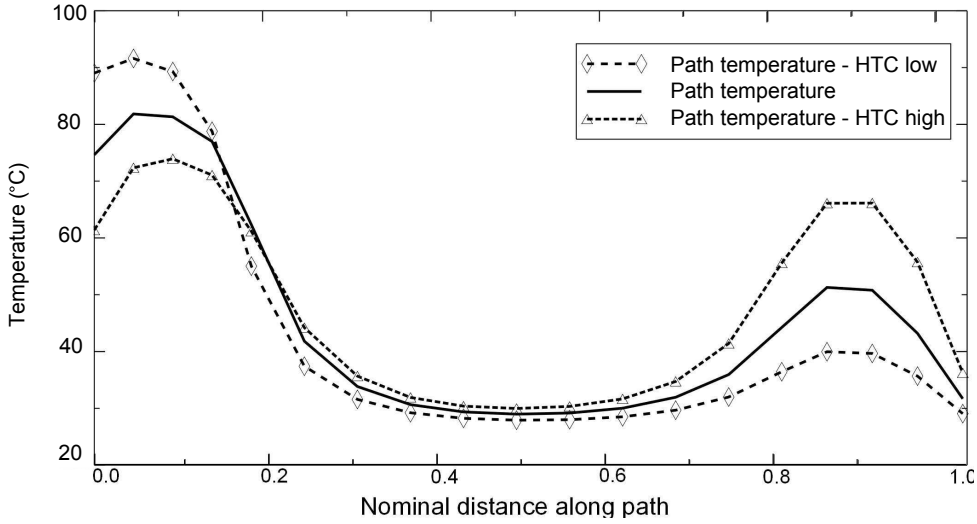

Figure 7.24: *Temperature along symmetry line path during peak exothermic temperatures using all surface film scenarios.*

gions obtain a fully developed stiffness much earlier than others, effectively constraining expansion or contraction within the material.

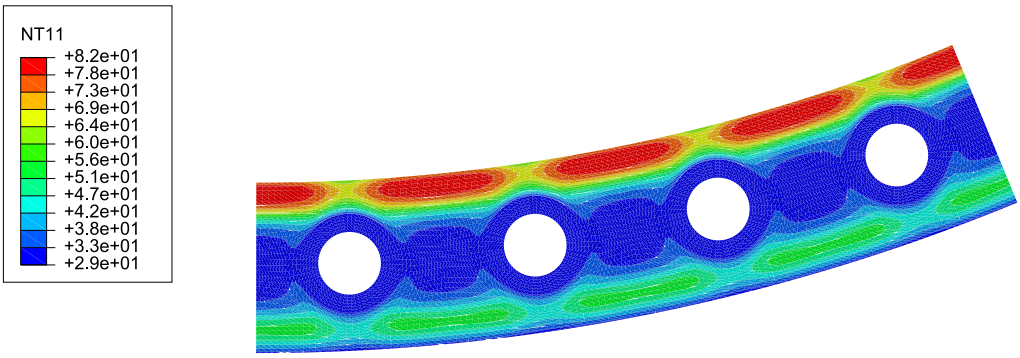

Figure 7.25: *Temperature contour plot at the instant the peak exothermic temperature is achieved at node 325 during the process, using thermal surface film condition 1.*

Mechanical analysis

Ultimately in the mechanical analysis, predictions of manufacturing induced shape distortions are conducted by analyzing the origins of the process induced internal strains and residual stresses. In doing so, determination of the mechanisms that result in the largest effects, is possible. First, the process induced thermal and chemical strains are analyzed. This is done at various key nodal points in the structure, shown in Fig. 7.27, which represent the root laminate material behaviour within the root section in general.

In Fig. 7.28, the process induced transverse thermal and chemical strains at the chosen model nodal points are presented. Also seen are the transverse total process induced

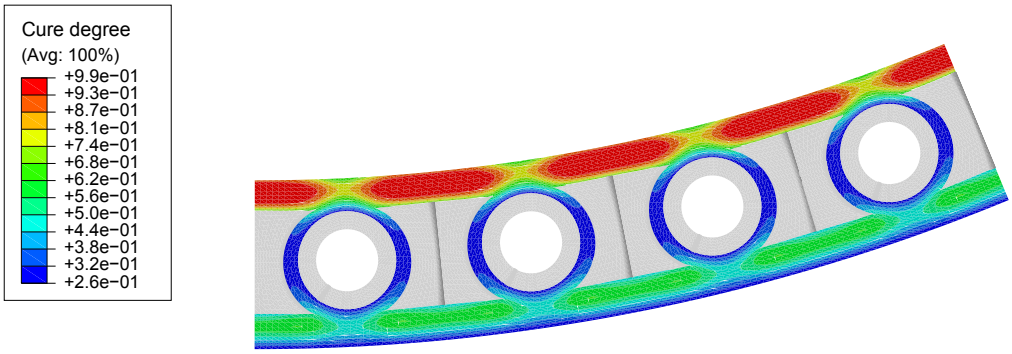

Figure 7.26: *Corresponding degree of cure contour plot at time of peak exothermic temperature using thermal surface film condition 1.*

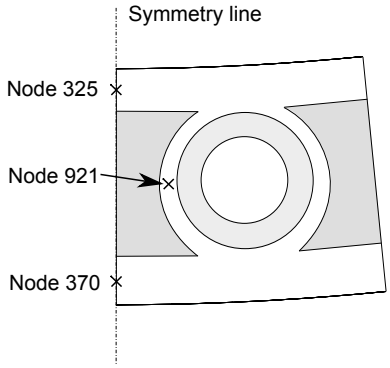

Figure 7.27: *Model nodal points of interest in the mechanical analysis, used to analyze process induced strains henceforth.*

strains, i.e. $\varepsilon_{22}^{Pr} = \varepsilon_{22}^{th} + \varepsilon_{22}^{ch}$ (not to be confused with total strains ε^{Tot}). As curing proceeds, thermal strains develop due to the increase in temperature from internal heat generation. Note that the matrix material thermal expansion coefficient is larger in rubbery state than in glassy state, hence higher thermal strain increments per temperature increase are experienced earlier in the process when the resin is assumed to be in the rubbery state. This explains why the final thermal strains seen in Fig. 7.28 are positive, even though the part is cooled back to its initial temperature. Furthermore, the larger thermal strain increments in the rubbery resin material state experienced at nodes 325 and 370 towards the surfaces result in higher final thermal strains, as opposed to the mid thickness region, where lower exothermic peak temperatures are achieved.

The chemical cure shrinkage strains depicted in Fig. 7.28 follow the cure degree evolution at the chosen nodal points. It is seen that the nodal point 921 has lower cure shrinkage curve gradients, reflecting the slower curing development experienced at this point, see e.g. Fig. 7.26. Since larger cure shrinkage strains develop, as opposed to the thermal strains, the final total process induced internal transverse strains seen at the analyzed nodal points are negative. Hence the volumetric shrinkage of the matrix material has a significant influence on the final strains induced in the root laminate composite material.

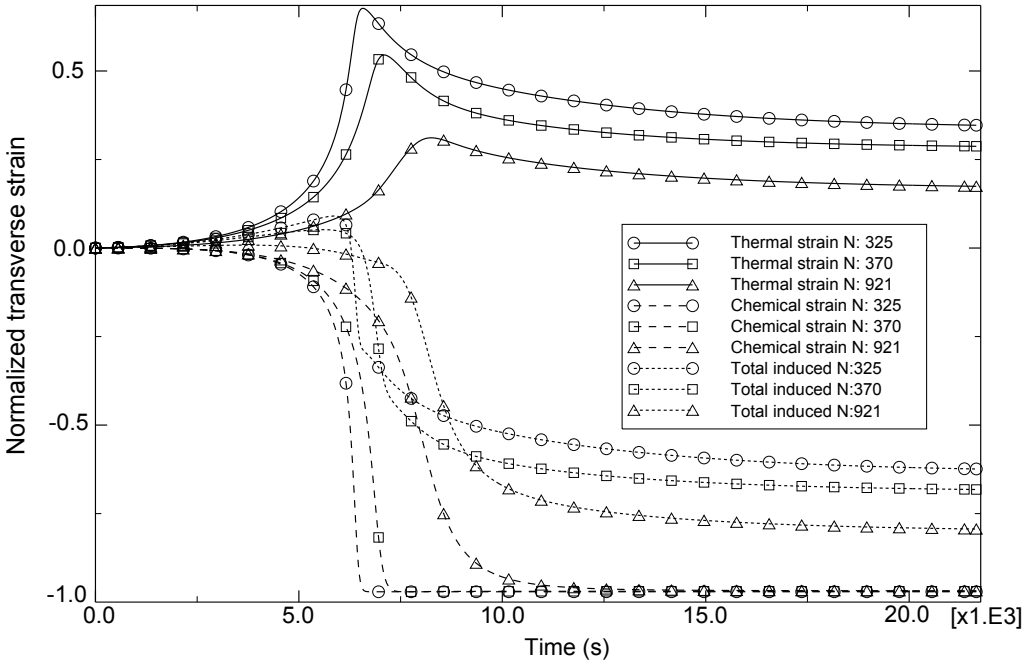

Figure 7.28: *Normalized process induced transverse thermal-, chemical- and total strains (thermal + chemical) using thermal boundary scenario 1.*

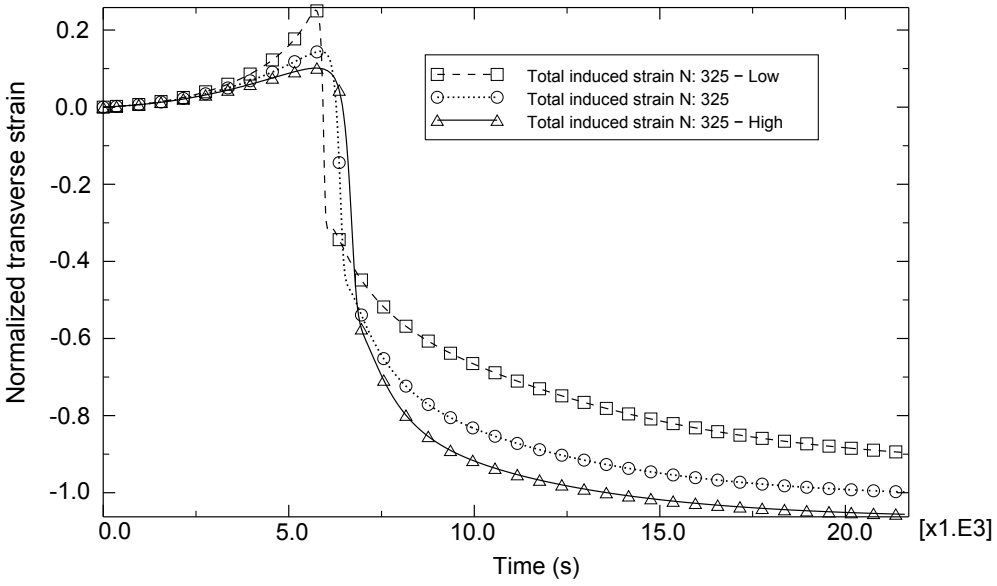

Figure 7.29: *Normalized process induced transverse total strains (thermal + chemical) at nodal point 325 using the different thermal boundary cases.*

The total transverse process strains (i.e. ε_{22}^{th} + ε_{22}^{ch}) from the different thermal surface film scenarios are compared in Fig. 7.29. Due to the higher peak temperatures induced when using a surface film condition with a lower cooling rate (low HTC), higher thermal strains are achieved, resulting in lower negative total strains as a larger magnitude of the negative shrinkage strains are up-weighed. Essentially this means that lower temperatures induce higher negative total process strains which in turn would result in larger shape

distortions due to contraction. Hence higher temperatures towards the inner surface of the root section may induce distortions resulting in a decrease in the root section radius, due to larger total negative strains. When constrained, e.g. in the fixed case, some of these process-induced strains would result in the build-up of internal stresses. The driving factor is therefore the through-thickness thermal- and corresponding cure degree gradients that determine the direction of distortion, be it an increase or decrease in part diameter.

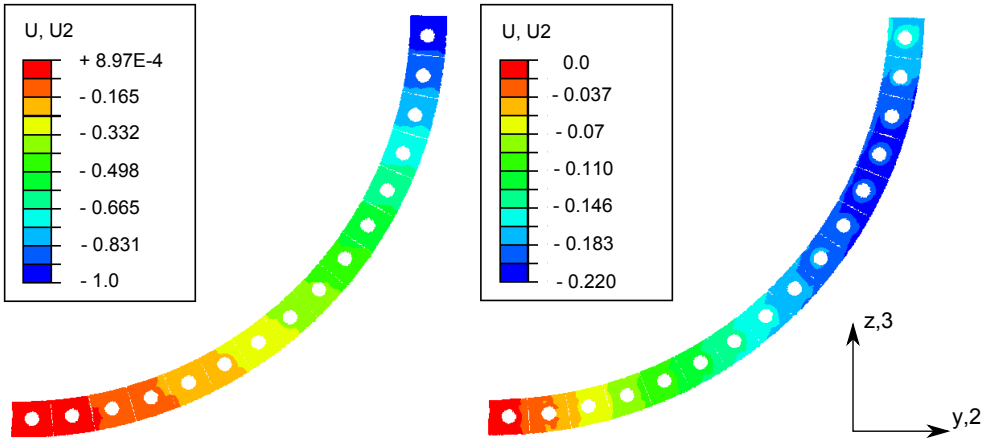

Figure 7.30: *Normalized horizontal (y,2-axis) part displacement for (left) free standing case and (right) fixed mechanical boundary condition (after demoulding). A deformation scale factor of 15 is used here.*

An analysis of the influence of tooling constraints on the final deformation of the entire root section symmetric half is conducted using the thermal surface film conditions from scenario 1 in Tab. 7.5. This is conducted for the free standing and fixed mechanical boundary conditions, and presented in Fig. 7.30. A decrease in radius in both cases is generally seen. Furthermore, it is seen that a larger decrease in radius along the part length is exhibited when using the free condition, as opposed to the fixed case. This is similarly illustrated in Fig. 7.32 as the change in radius of the root curvature along a through-thickness center-line path. The fixed case results in smaller distortions, mainly because not all process-induced stressess are readily released as distortions once the tooling constraints are suppressed, which transverse residual stress contour plots show, see Fig. 7.31. In the stresses seen in Fig. 7.31, tensile stresses are generally seen along the inner and outer surface boundaries, while compressive stresses are found primarily around the bushings.

In Fig. 7.32, the changes in radius for the two cases presented represent the bounds of which distortions are to be expected, without the need to model the tool/part contact interaction behaviour. A comparison of the predicted shape distortions, overlaid with the measured variations in roundness, presented earlier in Fig. 7.15, is presented in Fig. 7.33. While the free standing case is seen to overestimate the final change in radius along the root circumference, the fixed case is seen to agree somewhat with the general tendencies seen from the experimental data. Note that in the experimental data, an asymmetric variation exists along the root half circumference, which the model does not capture. This may mainly be a result of the simplified root section model geometry used in the model, where lengthwise and circumferential geometric non-uniformities do not exist. However,

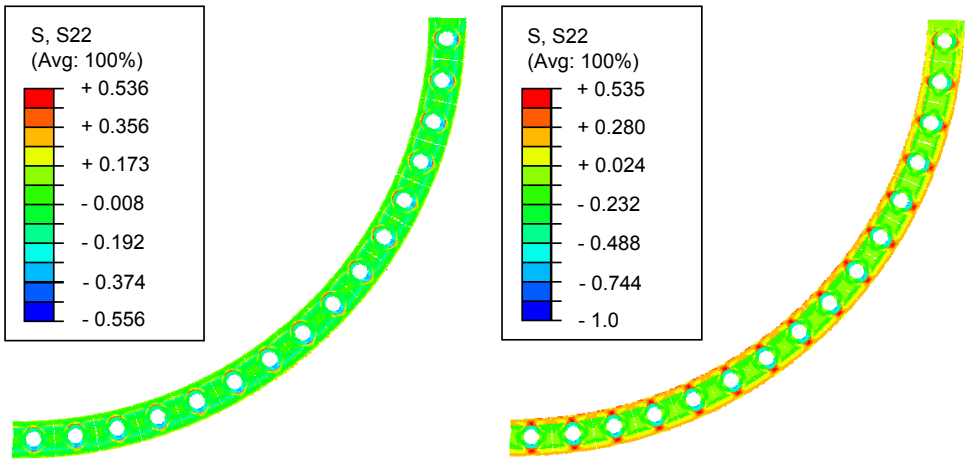

Figure 7.31: *Normalized transverse residual stresses for (left) free standing case and (right) fixed mechanical boundary condition (after demoulding).*

in general, the largest distortions arise near the trailing- and leading edge of the root half due to the sum of the contractions around the root symmetry plane along the chord of the root section substructure.

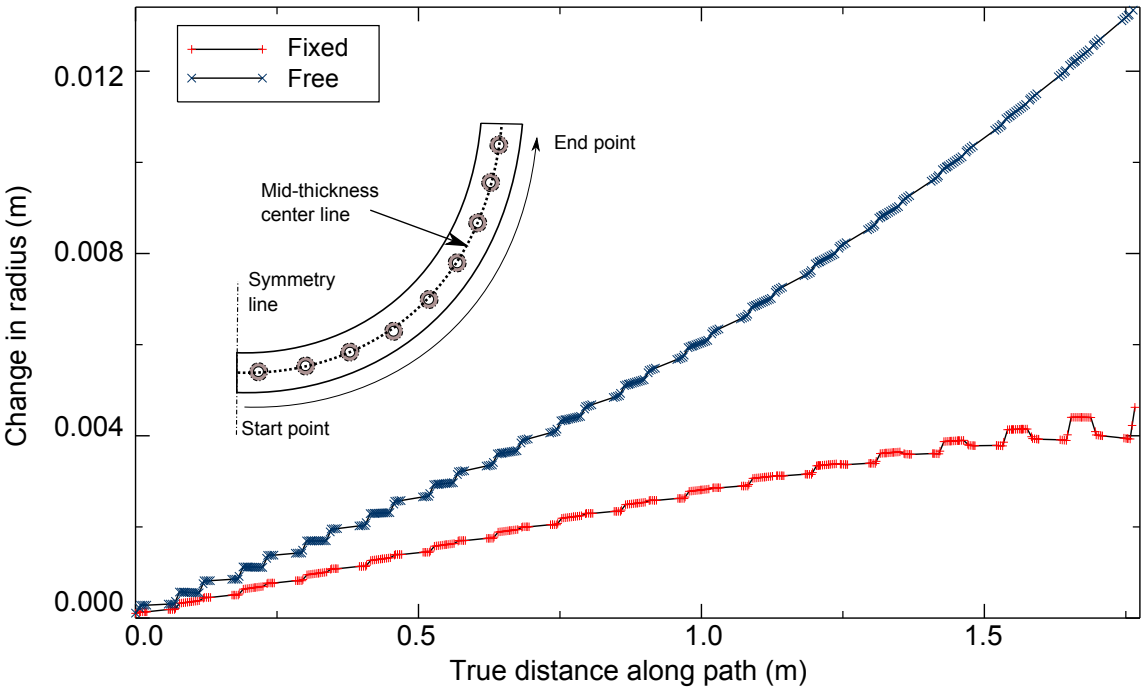

Figure 7.32: *Absolute change in root model radius along the through-thickness center-line path, for the free standing and fixed mechanical boundary condition Note that the fixed case results are after demoulding.*

In the work presented above, it is generally assumed that perfect contact prevails between the different material subsections (root laminate, bushing, pultruded wedge) throughout the process, through use of tied modelling constraints between the different model segments. Whether this sufficiently represents the actual interactions taking place between

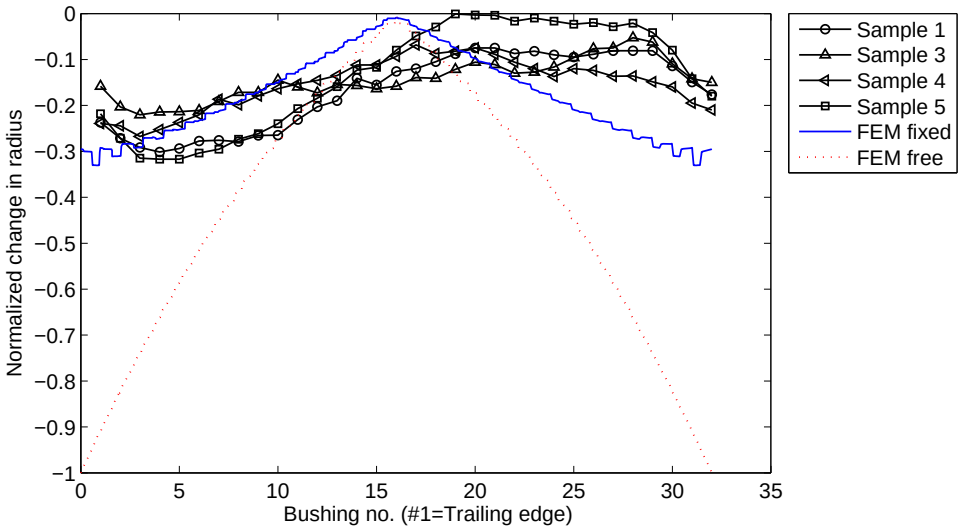

Figure 7.33: *Comparison between measured and predicted normalized change in root section radius. Note that Sample 2, shown earlier in Fig. 7.15.*

the different materials is difficult to say, since in real life conditions, the various sections within the mould and vacuum bag cavity are kept in place by the vacuum pressure and material weight. However, in order to accurately predict the interactions that may occur between inserts, pre-fabricated composites and the composite segments undergoing curing, the use of contact formulations is necessary. This can be cumbersome, since accurate orthotropic cure- and temperature dependent contact friction coefficient- and maximum interfacial shear stress properties are needed. However, as a first approximation using tied constraints, as done in the current study, is assumed to be sufficient in order to capture the main mechanisms taking place during processing.

7.3 Summary

In the first case study, it has been shown that the PD and CHILE constitutive modelling approaches are well capable of predicting process strains in a thick laminate plate as no significant viscoelastic effects are seen to exist. Note that this is valid for the simple geometry and tooling conditions examined where fairly small process induced stresses are achieved. In such cases, use of more complex and difficultly characterized viscoelastic models is not viable. This is seen even considering the length of the cure cycle used in the investigation (app. 20 hours). Hence the need for using viscoelastic models for low temperature cure cycles where *hard* mechanical constraints do not exist, is not present for the thermoset epoxy considered in this work. However, a shortcoming of the modelling approach taken in this case study is the accurate representation of the contact interactions between the glass tool and laminate plate, clearly seen during the final cooling stage.

In the second case study concerning the wind turbine blade root section, it has been shown how thermal- and cure- gradients drive the non-uniform through-thickness process in-

duced strains and govern the nature of the shape distortion experienced in the root section analyzed. The driving factors behind these non-uniform distortions are shown to mainly be due to thermal boundary conditions and non-uniform geometry of the root structure. In this analysis, the CHILE constitutive approach was utilized.

Chapter 8

Conclusions and Future work

In this chapter, the most important results from the current work and their consequences are drawn together as concluding remarks. Furthermore any reservations or limitations met during the work are presented, followed naturally by recommendations for future work.

8.1 Conclusions

The work presented in this thesis focuses on numerical modelling of thermomechanical phenomena occurring during curing in the manufacture of large fibre reinforced polymer matrix composites with thick laminate sections using vacuum assisted resin transfer moulding (VARTM). The main application of interest in the current study concerns modelling manufacturing induced shape distortions and residual stresses in commercial wind turbine composite blades.

In the preliminary review, key mechanisms known to contribute to manufacturing induced distortions and residual stress build-up were identified. The main known mechanisms of thermal-, chemical- and mechanical origin are; (i) the thermal expansion mismatch of the constitutive composite materials, laminate layers and tooling, (ii) the chemical cure shrinkage of the matrix material during cross-linking and (iii) tooling influence on the composite part, i.e. from the mould part, inserts etc.

In the first modelling study, a 1D thermomechanical curing model in a finite difference framework is implemented in MATLAB. In this model, process induced in-plane thermal- and chemical cure shrinkage strains are accounted for. Through classical laminate theory (CLT), through-thickness laminate in-plane total strains and residual stresses are calculated. It is shown that the 1D model is capable of predicting internal heat generation, resin cure degree development, the effective thermal expansion and chemical cure shrinkage, as well as the development of process induced in-plane strains and residual stresses. This 1D model is further developed and used as the framework for a void growth model, where instantaneous process conditions, resin cure kinetics and viscosity evolution are coupled in order to predict void (here a spherical gas bubble) size development. This is conducted by

solving a 1st order non-linear differential equation, expressing the through-thickness spatially distributed void bubble radius, in an incremental manner, for a prescribed composite laminate cure cycle. Void growth development is dependent of equilibrium pressure conditions, strain-displacement relations, the constitutive behaviour of the surrounding resin rich regions as well as stress equilibrium equations. Hence a first attempt is made at predicting the laminate through-thickness discretized void size distribution, as a function of processing parameters. Using this model, it has been shown how through-thickness thermal and cure gradients can influence the void size distribution within a composite laminate. The ability to predict void growth in composites is important, considering several reports in literature on the detrimental effects on the strength and fatigue life that voids can pose on fibre reinforced composite structures. It is also well known that non-uniform heating and curing can have an effect on the presence of defects and a decrease in the load carrying capacity of a laminate. Similarly, heating and curing non-uniformities affect void growth, as approximated by the developed visco-mechanical model. Specifically it is shown that variations, although still relatively small, in the final void size distribution through the laminate thickness are seen in thick laminates as a result of large gradients in temperature and curing during processing. Furthermore, selecting an appropriate temperature cycle can help reduce void growth, by suiting the temperature ramps and dwells to the laminate thickness, curing behaviour and resin viscosity.

Besides the 1D modelling efforts, a 3D thermomechanical model in ABAQUS is presented. Using this model, different constitutive modelling approaches are investigated, including a Cure Hardening Instantaneous Linear Elastic (CHILE) approach, a viscoelastic approach and a Path-dependent (PD) approach. The latter is a limiting case of viscoelasticity. These approaches are investigated with regards to their accuracy in predicting the evolution of the composite thermoset polymer matrix mechanical behaviour during the phase transitions experienced under curing. It is shown how the different approaches each predict cure hardening and thermal softening of the matrix material as a result of the material state transition at elevated temperatures.

The different constitutive approaches are utilized in a case study regarding curing of a thick glass/epoxy laminate plate. Model predictions are compared to experimental *in situ* measurements of internal total strains in the laminate plate using embedded fibre Bragg grating (FBG) sensors. It is concluded that, due to reasonable model accuracy, ease of implementation and use of relatively simply obtained material characterization data, the CHILE and PD approaches are most favorable. More specifically, it is shown that use of the viscoelastic approach to accurately predict process induced strains and stresses in modelling manufacturing cases where mild tooling constraints on the composite part exist, is not viable.

In a final case study, process induced shape distortions in a commercial wind turbine blade root subsection, courtesy of LM Wind Power A/S, are analyzed using the CHILE constitutive approach for a low temperature curing thermoset resin system. The analyzed root section consists of steel inserts, fabricated composite wedges and a root laminate material. It is shown how large non-uniform through-thickness part thermal- and corresponding cure gradients are the main driving factors behind the nature of the exhibited process induced shape distortions, be it resulting in an increase or decrease in root section

geometry radius. This is mainly a result of the differential cooling effects that the different boundary layers and inserts have on the structure during processing.

8.2 Future work

Several recommendations for future studies that could positively contribute to the current work are presented henceforth.

The 1D void growth model presented in the current work does not account for the transport of volatiles through the void bubble/resin interface due to diffusion effects. This can be included through use of Fick's law. However, for the void model in general, experimental validation cases are recommended, in order to quantify the numerous model assumptions used. However, the size scale of the investigated voids can prove difficult to control experimentally. Finally, coupling the void growth model with fracture and material strength predictions could further improve the application of the model in composites research and an understanding of effects of void dependent defects.

A general shortcoming with the presented thermomechanical models in the current work, is the lack of modelling precise tool/part interaction behaviour. This can be conducted using, for instance, contact formulations such as classical coulomb friction. Through experimental studies, relations concerning the (orthotropic) cure- and temperature dependency of effective contact friction coefficients may be obtained and modelled.

A second shortcoming concerns obtaining accurate matrix material cure kinetics material characterization data. For future studies with previously non-published resin system cure kinetics, a natural approach prior to modelling should include DSC characterization work. However, this can be cumbersome for highly reactive resin systems. The importance is however apparent, since a majority of the matrix dominant composite material behaviour is cure dependent during curing.

By directly applying the determined process induced residual stresses in loading modelling scenarios, e.g. in static of dynamic load analyses, the effects of process induced residual stresses on the in-service performance of the part can be analyzed. Hence, a means of determining where unwanted residual stresses may be developed is gained through a more integrated part analysis approach. Lastly for the induced shape distortions which are not readily minimized by changing process parameters (heating/cooling cycles, process length etc.), mould compensation analyses are necessary.

Chapter 9

Summary of Appended papers

Paper I

M.W. Nielsen, J.H. Hattel, T.L. Andersen, K. Branner, P.H. Nielsen, *A 1D coupled curing and visco-mechanical void growth model of thick thermosetting composite laminates*, Proc.: 18^{th} International Conference of Composite Materials (ICCM), Korea, 2011.

This paper focuses on a 1D void growth model implemented using the finite volume method with a through-thickness spatial domain discretization of a thick composite laminate. The model enables prediction of manufacturing induced void growth as a function of the thermal and curing evolution through the thickness of a laminate.

Paper II

M.W. Nielsen, J.H. Hattel, T.L. Andersen, K. Branner, P.H. Nielsen, *Experimental Determination and Numerical Modelling of Process Induced Strains and Residual Stresses in Thick Glass/Epoxy Laminate*, Proc.: 15^{th} European Conference of Composite Materials (ECCM), Italy, 2012.

In this paper, numerical modelling comparisons using different constitutive approaches are conducted for the prediction of process induced strains in a thick laminate plate. The approaches evaluated are the CHILE approach and the Path-dependent approach. Model predictions are compared to experimentally determined internal strains obtained using embedded optical fibre FBG sensors with good agreement. The differences between the two approaches are highlighted.

Paper III

M.W. Nielsen, J.W. Schmidt, J.H. Hattel, T.L. Andersen, C.M. Markussen, *In situ Measurement Using FBGs of Process-Induced Strains During Curing of Thick Glass/Epoxy*

Laminate Plate: Experimental Results and Numerical Modelling, Wind Energy, DOI: 10.1002/we.1550, 2012. In Press.

This paper presents a detailed experimental and numerical modelling analysis of the development of process induced strains in a thick glass/epoxy laminate plate. Numerical analyses are presented of different mechanical boundary conditions representing tooling influences, as well as the influence of part thickness and tooling configuration on the laminate part residual stresses and strains. Numerical model predictions are compared to in situ total strains from embedded fibre optic FBG sensors.

Paper IV

M. W. Nielsen, J. W. Schmidt, J. H. Høgh, J. P. Waldbjørn, J. H. Hattel, T. L. Andersen, C. M. Markussen, *Life cycle strain monitoring from manufacturing to failure in GFRP laminates using embedded FBG sensors*, Journal of Composite Materials, DOI: 10.1177/0021998312472221, 2012. In Press.

A life cycle strain monitoring approach is presented. Embedded FBG sensors are utilized to monitor resin flow front progression during infusion, curing induced strains, as well as interan strains during demoulding and loading of laminate beam specimens.

Technical Report I

M.W. Nielsen, *Implementation of Temperature- and Cure Dependent Viscoelastic Curing Model*, 2011.

In this technical report, a study of composites process modelling viscoelastic modelling is conducted. In this report, a review of existing modelling works is given. Moreover, a detailed analysis is given of different approaches used for viscoelastic process modelling of thermoset polymer matrix composites.

Bibliography

[1] Abaqus Version 6.11. *Analysis User's Manual, Vol. VI: User Subroutines & Parametric Studies*. Abaqus, Inc., 1 edition, 2004.

[2] D. Abraham and R. McIlhagger. Investigations into various methods of liquid injection to achieve moulding with minimum void contents and full wet out. *Composites Part A*, 29:533, 1998.

[3] X.A. Aduriz, C. Lupi, N. Boyard, J.-L. Bailleul, D. Leduc, V. Sobotka, N. Lefevre, X. Chapleau, C. Boisrobert, and D. Delaunay. Quantitative control of rtm6 epoxy resin polymerisation by optical index determination. *Composites Science and Technology*, 67:3196–3201, 2007.

[4] M. Amon and C.D. Denson. A study of the dynamics of foam growth: Analysis of the growth of closely spaced spherical bubbles. *Polymer Eng. and Science*, 24-13:1026–1034, 1984.

[5] Fiberline Composites A/S. Reinforcement profiles for turbine blades. *www.fiberline.com*, 2012.

[6] F. W. Jr. Billmeryer. *Textbook of Polymer Science*. John Wiley and Sons Inc. NY, 2 edition, 1971.

[7] F. Boey and S. Lye. Void reduction in autoclave processing of thermoset composites, part 1: High pressure effects on void reduction. *Composites*, 23(4):261–265, 1992.

[8] T.A. Bogetti and J.W. Gillespie. Process-induced stress and deformation in thick-section thermosetting composites laminates. *21st SAMPE Technical Conference, September*, 1989.

[9] T.A. Bogetti and J.W. Gillespie. Process-induced stress and deformation in thick-section thermoset composite laminates. *Journal of Composite Materials*, 26:626–659, 1992.

[10] B.A. Boley and J.H. Weiner. *Theory of thermal stresses*. Dover Publications, 1 edition, 1960. ISBN: 0-486-69579-4.

[11] H.F. Brinson and L.C. Brinson. *Polymer Engineering Science and Viscoelasticity*. Springer Science, 2008. ISBN: 978-0-387-73860-4.

[12] P. Brøndsted, H. Lilholt, and A. Lystrup. Composite materials for wind power turbine blades. *Annual Review of Materials Research*, 35:505–538, 2005.

[13] Z. Cai, S. Movva, N. Chiou, D. Guerra, Y. Hioe, J.M. Castro, and L.J. Lee. Effect of polyaniline surface modification of carbon nanofibers on cure kinetics of epoxy resin. *Journal of Applied Polymer Science*, 118:2328–2335, 2010.

[14] A. Cheung and Y.K. Pochiraju. Three-dimensional finite element simulation of curing of polymer composites. *Finite elements in analysis and design*, 40:895–912, 2004.

[15] A.S. Crasto, R.Y. Kim, and J.D. Russell. In-situ monitoring of residual strain development during composite cure. *Polymer Composites*, 23(3):454–463, 2002.

[16] Q. Dai. Two- and three-dimensional micromechanical viscoelastic finite element modelling of stone-based materials with x-ray computed tomography images. *Construction and Building Materials*, 25:1102–1114, 2010.

[17] Q. Dai et. al. A micromechanical finite element model for linear and damage-coupled viscoelastic behaviour of asphalt mixture. *Int. Journal for Numerical and Analytical Methods in Geomechanics*, 30:1135–1158, 2006.

[18] R. de Oliviera, S. Lavanchy, R. Chatton, D. Costantini, V. Michaud, R. Salathe, and J.-A.E. Månson. Experimental investigation of the effect of the mould thermal expansion on the development of internal stresses during carbon fibre composite processing. *Composites: Part A*, 39:1083–1090, 2008.

[19] F. Dunne and N. Petrinic. *Introduction to Computational Plasticity*. Oxford University Press, 1st edition, 2005. ISBN: 0-13-301458-4.

[20] N. Ersoy, T. Garstka, K. Potter, M.R. Wisnom, D. Porter, M. Clegg, and G. Stringer. Development of the properties of a carbon fibre reinforced thermosetting composite through cure. *Composites: Part A*, 41:401–409, 2012.

[21] J.P Favre. Residual thermal stresses in fibre reinforced composite materials - a review. *Journal of the mechanical behaviour of materials*, 1(1-4):37–53, 1988.

[22] G. Fernlund, N. Rahman, R. Courdji, M. Bresslauer, A. Poursartip, K. Willden, and K. Nelson. Experimental and numerical study of the effect of cure cycle, tool surface, geometry, and lay-up on the dimensional fidelity of autoclave-processed composite parts. *Composites Part A*, 33:341–351, 2002.

[23] R. Flanagan. *The dimensional stability of composite laminates and structures*. PhD Thesis, Queens's University of Belfast, 1 edition, 1997.

[24] J. K. Gillham. Formation and properties of thermosetting and high tg polymeric materials. *Polymer Engineering and Science*, 26:1429–1433, 1986.

[25] O.H. Griffin. Three-dimensional curing stresses in symmetric cross-ply laminates with temperature-dependent properties. *Journal of Composite Materials*, 17:449–463, 1983.

[26] L.K. Grunenfelder and S.R. Nutt. Void formation in composite prepregs - effect of dissolved moisture. *Composites Science and Technology*, 70:2304–2309, 2010.

[27] H.T Hahn. Effects of residual stresses in polymer matrix composites. *Journal of the Astronautical Sciences*, 32:253–267, 1984.

[28] H.T. Hahn and N.J. Pagano. Curing stresses in composite laminates. *Journal of Composite Materials*, 9:91–108, 1975.

[29] J.H. Hattel. *Fundamentals of Numerical Modelling of Casting Processes*. Polyteknisk Forlag, Kgs. Lyngby, 1st edition, 2005.

[30] J.J. Hermans. The elastic properties of fiber reinforced materials when the fibers are aligned. *Konigl. Nederl. Akad. van Wetenscheppen, Amsterdam*, B70, 1967.

[31] C.M.D. Hickey and S. Bickerton. Cure kinetics and rheology characterisation and modelling of ambient temperature curing epoxy resins for resin infusion/vartm and wet layup applications. *Journal of Material Science*, DOI 10.1007/s10853-012-6781-8, 2012.

[32] R. Hill. A self-consistent mechanics of composite materials. *Journal Mech. Phys. Solids*, 13:213–222, 1965.

[33] R.R. Hill, S.V. Muzumdar, and L.J. Lee. Analysis of volumetric changes of unsaturated polyester resin during curing. *Polymer Engineering Science*, 35(10):852–9, 1995.

[34] H. Huang, J.W. Gillespie, and T. Bogetti. Process induced stress for woven fabric thick section composite structures. *Composite Structures*, 49:303–312, 2000.

[35] H. Huang and R. Talreja. Effects of void geometry on elastic properties of unidirectional fibre reinforced composites. *Composite Science and Technology*, 65(13):1964–1981, 2005.

[36] P. Hubert. *Aspects of flow and compaction of laminated composite shapes during cure*. PhD Thesis, Department of Metals and materials Engineering, The University of British Columbia, 1st edition, 1996.

[37] P. Hubert, A. Johnston, A. Poursartip, and K. Nelson. Cure kinetics and viscosity models for hexcel 8552 epoxy resin. *Int. SAMPE Symposium and Exhibition (Proc.)*, 46:2341–2354, 2001.

[38] Holmberg J.A. Influence of chemical shrinkage on shape distortion of rtm composites. *19th Int. SAMPE European Conference of the Society for the Advancement of Material and Process Engineering, Paris*, 30:13–34, 1998.

[39] Ferry J.D. *Viscoelastic Properties of Polymers*. John Wiley & Sons, Inc., 2 edition, 1961.

[40] F.M. Jensen. *Ultimate strength of a large wind turbine blade*. PhD Thesis, Risø National Laboratory for Sustainable Energy, 1st edition, 2008.

[41] A.A. Johnston. An intergrated model of the development of process-induced deformation in autoclave processing of composite structures. *PhD Thesis, University of British Columbia*, 1997.

[42] M.R. Kamal and S. Sourour. *Polymer Engineering Science*, 13:59, 1973.

[43] J. Kardos, D. Dudukovic, and R. Dave. Void growth and resin transport during processing of thermosetting matrix composites. *Composites*, 2:289–298, 1971.

[44] J.M. Kenny. Application of modeling to the control and optimization of composites processing. *Composite Structures*, 27:129–139, 1994.

[45] J.M. Kenny, A. Maffezzoli, and L. Nicolais. A model for the thermal and chemorheological behaviour of thermoset processing: (ii) unsaturated polyester based composites. *Composites Science and Technology*, 38:339–358, 1990.

[46] L. Khoun. *Process-induced stresses and deformation in woven composites manufactured by resin transfer moulding*. PhD Thesis, Department of Mechanical Engineering, McGill University, Montreal, Canada, 1st edition, 2009.

[47] L. Khoun, T. Centea, and P. Hubert. Characterization methodology of thermoset resins for the processing of composite materials - case study: Cycom 890rtm epoxy resin. *Journal of Composite Materials*, 44:1397–1415, 2009.

[48] L. Khoun, R. deOliviera, V. Michaud, and P. Hubert. Investigation of process-induced strains development by fibre bragg grating sensors in resin transfer moulded composites. *Composites Part A*, 42:274–282, 2011.

[49] C. Kim, H. Teng, C.L. Tucker, and S.R. White. The continuous process for thermoset polymer composites. *Journal of Composites Materials*, 29:1222–53, 1995.

[50] J.K. Kim and Y.W. Mai. *Engineered Interfaces in Fiber Reinforced Composites*. Elsevier, 1st edition, 1998. ISBN: 0-08-042695-6.

[51] J.W. Kim, J.H. Lee, H.G. Kim, H.S. Kim, and D.G. Lee. Reduction of residual stresses in thick-walled composite cylinders by smart cure cycle with cooling and reheating. *Composite Structures*, 75:261–266, 2006.

[52] K.S. Kim and H.T. Hahn. Residual stress development during processing of graphite/epoxy composites. *Composites Science and Technology*, pages 121–132, 1989.

[53] Y.K. Kim and S.R. White. Stress relaxation behavior of 3501-6 epoxy resin during cure. *Polymer Engineering and Science*, 36(23):2852–2862, 1996.

[54] Y.K. Kim and S.R. White. Viscoelastic analysis of processing-induced residual stresses in thick composite laminates. *Mechanics of Composite Materials and Structures*, 4:361–387, 1997.

[55] P. Kotas. *Integrated Modeling of Process, Structures and Performance in Cast Parts*. PhD Thesis, Technical university of Denmark, 1st edition, 2011.

[56] J. Lange, S. Toll, J.A. Månson, and Hult A. Residual stress build-up in thermoset films cured above their ultimate glass transition temperature. *Polymer*, 36(16):3135–3141, 1995.

[57] Y. Ledru. *Etude de la porosite dans les materiaux composites statifies aeronautiques*. PhD Thesis, Universite de Toulous, 1st edition, 2009.

[58] Y. Ledru, G. Bernhart, R. Piquet, and L. Michel. Coupled visco-mechanical and diffusion void growth modelling during composite curing. *Composite Science and Technology*, 70:2139–2145, 2010.

[59] C.L. Lee and K.H. Wei. Curing kinetics and viscosity change of a two-part epoxy resin during mold filling in resin-transfer molding process. *Journal of Applied Polymer Science*, 77:2139–2148, 2000.

[60] C. Li, K. Potter, M.R. Wisnom, and G. Stringer. In-situ measurement of chemical shrinkage of my750 epoxy resin by a novel gravimetric method. *Composite Science and Technology*, 64:55–64, 2004.

[61] L. Liu, B. Zhang, D. Wang, and Z. Wu. Effects of cure cycles on void content and mechanical properties of composite laminates. *Composite structures*, 73:303–309, 2005.

[62] A. Loos and G. Springer. Curing of graphite/epoxy composites. *Technical report*, 1983.

[63] A.C. Loos, J. Sayre, R. McGrane, and B. Grimsley. Vartm process model development. *Int. SAMPE Symposium*, 46:1049–1060, 2001.

[64] A.C. Loos and G.S. Springer. Curing of epoxy matrix composites. *Journal of Composite Materials*, 17:135–169, 1983.

[65] J. Lopez, C. Ramirez, A. Torres, M.J. Abad, L. Barral, J. Cano, and F.J. Diez. Isothermal curing by dynamic mechanical analysis of three epoxy resin systems: Gelation and vitrification. *Journal of Applied Polymer Science*, 83:78–85, 2001.

[66] Voet E. Lammens N. Luyckx, G. and J. Degrieck. Strain measurements of composite laminates with embedded fibre bragg gratings: Criticism and opportunities for research. *Sensors*, 11:384–408, 2011.

[67] Haider M., Hubert P., and Lessart L. Cure shrinkage characterization and modelling of a polyester resin containing low profile additives. *Composites Part A*, 38:994–1009, 2007.

[68] A.R. Maligno, N.A. Warrior, and A.C. Long. Effects of interphase material properties in unidirectional fibre reinforced composites. *Composites Science and Technology*, pages 36–44, 2009.

[69] P.K. Mallick. *Fiber Reinforced Composites - Materials, Manufacturing and Design*. CRC Press, 3rd edition, 2007. ISBN: 978-0-8493-4205-9.

[70] R.V.N. Melnik. Models for coupled kinetics and heat transfer in processing polymeric materials with applications to biomechanical engineering. *Modelling and Simulation in Materials Science and Engineering*, 10:341–357, 2002.

[71] Z. Ming, A. Xuefeng, T. Bangming, and Y. Xiaosu. TTT Diagram Used to Control Phase Structure of 2/4 Functional Epoxy Blends for Advanced Composites. *Chinese Journal of Aeronautics*, 22:449–452, 2009.

[72] T.S. Montgomery and W.J. MacKnight. *Introduction to Polymer Viscoelasticity*. Wiley-Interscience, 3rd edition, 2005. ISBN: 0-471-74045-4.

[73] A.W Morey et al. Fibre optic bragg grating sensors. *Fibre optic laser sensors VII*, pages 98–107, 1989.

[74] S. Movva, X. Ouyang, J. Castro, and L.J. Lee. Carbon nanofiber paper and its effect on cure kinetics of low temperature epoxy resin. *Journal of Applied Polymer Science,*, 125:223–2230, 2012.

[75] M. Mulle, F. Collombet, P. Olivier, R. Zitoune, C. Huchette, L. Laurin, and Y. Grunevald. Assessment of cure-residual strains through the thickness of carbon-epoxy laminated using fbgs partii: Technological specimen. *Composites: Part A*, 40:1534–1544, 2009.

[76] M.R. Nedele and M.R. Wisnom. Three-dimensional finite element analysis of the stress concentration at a single fibre break. *Composites Science and Technology*, pages 517–524, 1994.

[77] P. Parlevliet, H.E.N. Bersee, and A. Beukers. Residual stresses in thermoplastic composites - a study of the litteratire. part iii: Effects of thermal residual stresses. *Composites Part A*, 38:1581–1596, 2006.

[78] P Parlevliet et al. Process monitoring with fbg sensors during vacuum infusion of thick composite laminates. *16th International Conference on Composite Materials, ICCM 16*, 2007.

[79] P Parlevliet et al. Measurement of (post-)curing strain development with fibre bragg gratings. *Polymer Testing*, 29:291–301, 2010.

[80] P. Prasatya, G.B. McKenna, and S.L. Simon. A viscoelastic model for predicting isotropic residual stresses in thermosetting materials: Effects of processing parameters. *Journal of Composite Materials*, 35:826–848, 2001.

[81] S.Y. Pusatcioglu, A.L. Fricke, and J.C. Hassler. Heats of reaction and kinetics of a thermoset polyester. *Journal of Applied Polymer Science*, 24:937–946, 1979.

[82] C. Ridgard. Accuracy and distortion of composite parts and tools: Causes and solutions. *SME Tech Paper, Tooling Compos. '93*, -:341–51, 1993.

[83] K. Rueggeberg, F. anf Tamareselvy. Resin cure determination by polymerization shrinkage. *Dental Materials*, 11:265–268, 1995.

[84] E. Ruiz and F. Trochu. Thermomechanical properties during cure of glass-polyester rtm composites: Elastic and viscoelastic modeling. *Journal of Composite Materials*, 39:881–915, 2005.

[85] E. Ruiz and F. Trochu. Multi-criteria thermal optimization in liquid composite molding to reduce processing stresses and cycle time. *Composites Part A*, 37(6):913–924, 2006.

[86] J.D. Russell, M.S. Madhukar, M.S. Genidy, and A.Y. Lee. A new method to reduce cure-induced stresses in thermoset polymer composites, part iii: correlating stress history to viscosity, degree of cure, and cure shrinkage. *Journal of Composite Materials*, 34(22):1926–1947, 2000.

[87] S.M Sabzevari. *Cure kinetics and process modeling of a carbon-fiber thermoplastic-toughened epoxy resin prepreg*. M.Sc. Thesis, Department of Mechanical Engineering, Wichita State University, 2005.

[88] S.L. Simon and G.B. McKenna. Modeling the evolution of the dynamic mechanical properties of a commercial epoxy during cure after gelation. *Journal of Applied Polymer Science*, 76:495–508, 1999.

[89] X. Song. *Vacuum assisted resin transfer molding (VARTM): Model development and verification*. PhD Thesis, Virginia Polytechnic Institute and State University, 2003.

[90] R. Stewart. Wind turbine blade production - new products keep pace as scale increases. *Reinforced plastics*, January:18–25, 2012.

[91] Y. Sung and H.H. Hilton. Effects of thermo-mechanical properties of composites on viscosity, temperature and degree of cure in thick thermosetting composite laminate during curing processes. *Journal of Composite Materials*, 32(7):1333–1342, 1998.

[92] J.M. Svanberg. *Predictions of manufacturing induced shape distortions - high performance thermoset composites*. PhD Thesis, Luleå University of Technology, 2002.

[93] J.M. Svanberg. Shape distortions of non-isothermally cured composite angle bracket. *Plastics, Rubber and Composites*, 9:1–9, 2002.

[94] J.M. Svanberg and J.A. Holmberg. An experimental investigation on mechanisms for manufacturing induced shape distortions in homogeneous and balanced laminates. *Composites Part A*, 32:827–838, 2001.

[95] J.M Svanberg and J.A. Holmberg. Predictions of shape distortions part i. fe-implementation of a path dependent constitutive model. *Composites Part A: Applied science and manufacturing*, 35:771–721, 2004.

[96] J.M. Svanberg and J.A. Holmberg. Predictions of shape distortions. part ii. experimental validation and analysis of boundary conditions. *Composites Part A: Applied Science and Manufacturing*, 35:723–734, 2004.

[97] Dassault Systemes. *Writing User Subroutines with ABAQUS*. Dassault Systemes, 1st edition, 2010. ISBN: 0-13-301458-4.

[98] S. Teplinsky and E.M. Gutman. Computer simulation of process induced stress and strain development during cure of thick-section thermosetting composites. *Computational Materials Science*, 6(1):71–76, 1996.

[99] G. Twigg, A. Poursartip, and G. Fernlund. Tool-part interaction in composites processing. part i: experimental investigation and analytical model. *Composites: Part A*, 35:121–133, 2004.

[100] Y. Weitsman. Optimal cool-down in linear viscoelasticity. *Journal of Applied Mechanics*, 47:35–39, 1980.

[101] X. Wen, X. Wang, Z. Cai, P. Pi, J. Cheng, and Z. Yang. Cure kinetics and chemorheological behavior of a wind epoxy resin system and its viscoelastic properties reinforced by glass fiber matt with process of vacuum assisted resin transfer molding. *High Performance Polymers*, 23(6):477–484, 2011.

[102] S.R. White and Y.K. Kim. Process-induced residual stress analysis of as4/3501-6 composite material. *Mechanics of Composite Materials and Structures*, 5:153–186, 1998.

[103] J.M. Whitney and R.L. McCullough. *Micromechanical Material Modelling, Delaware Composites Design Encyclopedia - Vol2*. Technomic Pub. Co. Inc., 2nd edition, 1990.

[104] M. Wisnal, T. Reynolds, and N.G William. Reduction in ilss by discrete and distributed voids. *Composites Science and Technology*, 56:93–101, 1996.

[105] M.R. Wisnom, M. Gigliotti, N. Ersoy, M. Campbell, and K.D. Potter. Mechanisms generating residual stresses and distortion during manufacture of polymer-matrix composite structures. *Composites Part A*, 37:522–529, 2006.

[106] J. Wood and M. Bader. Void control for polymer-matrix composites (1): theoretical and experimental methods for determining the growth and collapse of gas bubbles. *Composites Manufacturing*, 5:139–147, 1994.

[107] S. Yi, H.H. Hilton, and M.F. Ahmad. A finite element approach for cure simulation of thermosetting matrix composites. *Computers and Structures*, 64(1-4):383–388, 1997.

[108] H. Yu, S.G. Mhaisalkar, E.H. Wong, and G.Y. Khoo. Time-temperature transformation (ttt) cure diagram of a fast cure non-conductive adhesive. *Thin Solid Films*, 504:331–335, 2005.

[109] D. Zenkert and M. Battley. *Foundations of Fibre Composites*. Technical University of Denmark, 2nd edition, 2009.

[110] H. Zhao, J. Gao, Y. Li, and S. Shen. Curing kinetics and thermal property characterization of bisphenol-f epoxy resin and methpa system. *Journal of thermal analysis and calorimetry*, 74:227–236, 2003.

[111] L.G. Zhao, N.A. Warrior, and Long A.C. A micromechanical study of residual stress and its effect on transverse failure in polymer-matrix composites. *Int. Journal of Solid Structures*, 43:5449–67, 2006.

[112] M.A. Zocher. *A Thermoviscoelastic Finite Element Formulation for the Analysis of Composites*. PhD. Thesis. Texas A&M University, 1995.

[113] M.A. Zocher, S.E. Groves, and Allen D.H. A three-dimensional finite element formulation for thermoviscoelastic orthotropic media. *Int. Journal for Numerical Methods in Engineering*, 40:2267–2288, 1997.

Paper I

"'A 1D coupled curing and visco-mechanical void growth model of thick thermosetting composite laminates"'

M.W. Nielsen, J.H. Hattel, T.L. Andersen, K. Branner, P.H. Nielsen

Proceedings at the 18^{th} International Conference of Composite Materials (ICCM), Jeju, Korea, 2011.

A 1D COUPLED CURING AND VISCO-MECHANICAL VOID GROWTH MODEL OF THICK THERMOSETTING COMPOSITE LAMINATES

M.W. Nielsen[1*], J. H. Hattel[1], T. L. Andersen[2], K. Branner[2], P.H. Nielsen[2]
[1]Department of Mechanical Engineering, Process Modelling Group,
Technical University of Denmark, Kgs. Lyngby, Denmark,
[2]Risø National Laboratory for Sustainable Energy,
Technical University of Denmark, Roskilde Denmark,
* Corresponding author (mwni@mek.dtu.dk)

Keywords: *1.Curing 2.Laminate 3.Voids 4.Numerical modelling*

1. General Introduction

In the production of composite laminate parts, Vacuum Infusion (sometimes referred to as Vacuum Assisted Resin Transfer Moulding (VARTM)) is widely used in the manufacture of large structures such as wind turbine blades [1]. Vacuum infusion is a closed mould process in which resin is pulled into the mould by applying a vacuum at the outlet vent, consequently impregnating dry pre-laid fibres in the mould cavity. Vacuum infusion differs from conventional autoclave-RTM in the sense that no external hydrostatic pressure is applied which helps inhibit void growth during the final consolidation of the resin matrix with the fibres.

It is generally known that voids have a detrimental effect on the strength and fatigue life of composite laminate structures [2, 11]. Several authors have also reported that voids in composite laminates accelerate crack initiation and propagation [3-8]. Liu et al. [2] investigated the void content effect on carbon/epoxy laminate mechanical properties. A decrease of approximately 20% in shear-, flexural- and tensile strength was observed with an increase in void content by approximately 2.6%. Similar tendencies are also observed for the flexural- and tensile moduli as well as the inter-laminar shear strength (ILSS). The mean decrease in ILSS was estimated to average 6% per unit volume of void ratio for carbon/epoxy laminates [15]. Boey & Lye [11] investigated void reduction in processing of thermoset composites. Using vacuum bagging alone, a reduction of the void content below 10% was not possible without applying an external pressure, as done in autoclave processing, where a void content below 3% is possible due to the imposed hydrostatic autoclave pressure before final resin curing.

2. Void growth models

Several void growth models for composite laminates exist, e.g. [7-8],[10]. Kardos *et al*. [10] presented a general time-dependent diffusion-controlled void growth model as well as a model of the void stability at equilibrium as a function of pressure and temperature. Ledru *et al*. [8] presented a coupled visco-mechanical and diffusion model to predict the final void size at the end of polymerization. In their model the resin cure cycle viscosity variation, as a function of temperature and cure degree is taken into account, as well as the process- and gas void pressure difference and gas temperature variation for a unit cell spherical void.

3. Model Formulation

An extension of the 1D thermomechanical model presented by Bogetti & Gillespie [9], based on incremental elastic classical laminated plate theory, is employed to include void growth during VARTM, disregarding resin flow. A visco-mechanical void growth model is implemented, presented by Ledru *et al*. [8] and adapted from Wood & Bader [13] and Kardos *et al*. [10]. Void growth will follow perfect gas law behaviour without taking transport of species across the void/resin interface into account. As a novelty, this is implemented using the finite volume method with a through-thickness spatial domain discretization of the laminate. The model is programmed numerically in Matlab®.

3.1 Main model assumptions

- Constant isotropic thermal material properties are assumed
- Voids are assumed to be initially present in resin after infusion as a result of gas bubbles being trapped in the inter-roving spaces

- An initial mean void radius (R_o) and distribution is assumed through the laminate thickness
- The gas void is assumed to be perfectly spherical
- The perfect gas law applies for describing the gas inside the void
- No diffusion takes place, i.e. void and resin are assumed to be non-miscible.

3.2 Thermal model

The governing equation utilized is Fourier's heat conduction equation, reduced to one-dimension:

$$\rho c_p \frac{\partial T}{\partial t} = k_z \left(\frac{\partial^2 T}{\partial z^2} \right) + \dot{q} \qquad (1)$$

for $T(z, t)$ in $0 < z < h$ the laminate thickness, and where k_z, ρ and c_p are the through thickness thermal conductivity, density and specific heat capacity respectively. $\dot{q}$ is the heat source term, which in this case represents the exothermic heat generation rate during resin polymerization. The laminate is discretized through the thickness with the surface control volume (CV) being prescribed the imposed process cycle temperature. The remaining CVs experience temperature change due to the combined effect of curing and conduction. In this work symmetric thermal loading is considered, why only half of the laminate thickness is modelled.

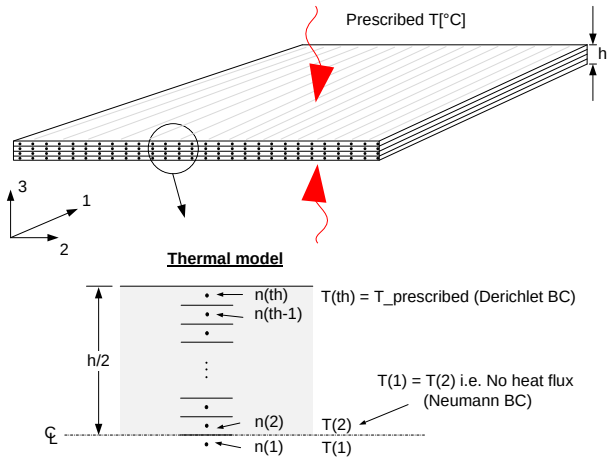

Fig.1. Thermal model discretization and boundary conditions.

The thermal model is discretized spatially in a finite volume framework with a backward Euler finite difference time discretization, see e.g. [17] for details. The resulting equation system is solved implicitly in each time step with Neumann and Dirichlet boundary conditions (BCs) at the centreline and laminate surface boundary respectively see Fig.1.

3.3 Cure kinetics and viscosity

The curing process of thermosetting epoxy resins is exothermic - a result of the drop in energy of the chemical system during polymerization. The degree of cure $\alpha(t)$, at a material point is expressed as the ratio of the cumulative mass specific heat liberated from the chemical reaction, $H(t)$, to the total heat of the reaction H_r. This is expressed as:

$$\alpha(t) = \frac{H(t)}{H_r} \qquad (2)$$

The heat liberated at any point in time t is expressed in integral form as:

$$H(t) = \int_0^t \frac{1}{\rho} \left(\frac{dq}{dt} \right) dt \qquad (3)$$

Where dq/dt is the volume specific rate of heat generation (or $\dot{q}$) from the cure reaction. Using (2-3) the heat generation rate in eq.(1) is expressed as a function of the cure rate:

$$\dot{q} = \frac{d\alpha}{dt} \rho H_r \qquad (4)$$

The cure rate of epoxy resins can be expressed (depending on the resin system) using the Kamal and Sourour kinetic model [14]:

$$\frac{d\alpha}{dt} = (k_1 + k_2 \alpha^m)(1 - \alpha)^n \qquad (5)$$

$$with \quad k_i = k_{io} \exp\left(-\frac{E a_i}{R_b T} \right) \qquad (6)$$

The degree of cure is calculated from 0 to 1, where 1 is fully cured. The resin rheology is modelled via the viscosity being a function of temperature and cure

Table 1. Epoxy thermal and cure kinetic parameters

Notation	c_p	k_z	α_{CTE}	k_{o1}	k_{o2}	E_{a1}	E_{a2}	H_r	m	n
Unit	J/W.K	W/m.K	$°C^{-1}$	s^{-1}	s^{-1}	kJ/mol	kJ/mol	kJ/kg	-	-
Value	942	0.2163	5.7E-5	1528	1.6	59.4	26.3	198.9	0.51	1.49

degree using:

$$\eta(T,\alpha) = \eta_g \exp\left[-\frac{C_1\left(T - T_{go}\right)}{C_2 + T - T_o}\right]\left(\frac{\alpha_g}{\alpha_g - \alpha}\right)^a \quad (7)$$

which is a combination of the Williams-Landel-Ferry (WLF) expression and the Castro and Macosko conversion term. η_g is the resin viscosity at gelation, C_1 and C_2 are model parameters and α_g is the crosslinking ratio at gelation. A viscosity limit of 10e6[Pa s] is used, corresponding to solidification of the resin [15].

3.4 Void growth in viscous media

The void growth model used is largely developed by Amon and Denson [16]. The model entails a spherical gas bubble developing in a polymer matrix, see Fig. 2. A spherical gas void is studied. The bubble size variation is described using the radial velocity component only ($v = [u,0,0]^T$) due to isotropic growth or contraction.

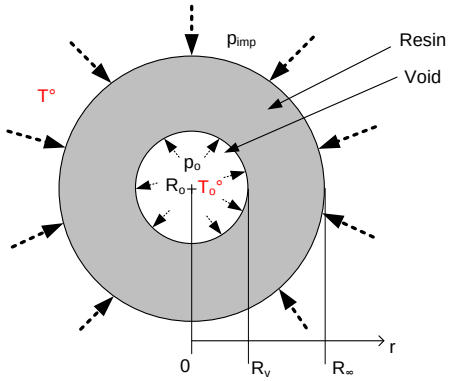

Fig.2. Schematic of gas bubble surrounded by resin with imposed pressure and temperature.

Using the standard strain-displacement relations in spherical coordinates as well as incompressibility, the strain rate tensor is given as:

$$\underline{\dot{\epsilon}} = \frac{\dot{R}_v R_v^2}{r^3}\begin{bmatrix} -2 & 0 & 0 \\ 0 & 1 & 0 \\ 0 & 0 & 1 \end{bmatrix} \quad (8)$$

where $\dot{R}_v$ is the void growth velocity. Taking the strain rate tensor into account, the equilibrium equations are hence:

$$\begin{cases} \dfrac{\partial \sigma_{rr}}{\partial r} + \dfrac{1}{r}\left[2\sigma_{rr} - \sigma_{\theta\theta} - \sigma_{\varphi\varphi}\right] = 0 \\ \sigma_{\theta\theta} = \sigma_{\varphi\varphi} \end{cases} \quad (9)$$

The boundary conditions at the limits (see Fig.1) are:

$$\begin{cases} \sigma_{rr}(R_v) = -p_g + \dfrac{2\gamma_{LV}}{R_v} \\ \sigma_{rr}(R_\infty) = -p_{imp} \end{cases} \quad (10)$$

which are found using Laplace-Young relationship where surface tension forces γ_{LV} are taken into account as well as the internal void gas pressure p_g and imposed hydrostatic pressure p_{imp}. In the case of vacuum infusion, no external hydrostatic pressure is applied in which case p_{imp} corresponds to atmospheric pressure. Finally, the polymer resin behaviour is assumed to exhibit Newtonian behaviour expressed via the Cauchy tensor as:

$$\underline{\sigma} = 2\eta\underline{\dot{\epsilon}} - p\underline{I} \quad (11)$$

Inserting (8) in (11) we get:

$$\begin{cases} \sigma_{rr} = -4\eta\dfrac{\dot{R}_v R_v^2}{r^3} - p_{imp} \\ \sigma_{\theta\theta} = \sigma_{\varphi\varphi} = 2\eta\dfrac{\dot{R}_v R_v^2}{r^3} - p_{imp} \end{cases} \quad (12)$$

Considering initial pressure, temperature, radius and viscosity conditions, from the presented equations (inserting (12) in (9)) the following differential equation is obtained:

$$\frac{\dot{R}_v}{R_v(t)} - \frac{p_g(t) - p_{imp}(t)}{4\eta(T,\alpha)} + \frac{\gamma_{LV}}{2\eta(T,\alpha)R_v(t)} = 0 \quad (13)$$

where the void gas pressure p_g at time t is:

$$p_g(t) = p_o\frac{T(t)}{T_o}\left(\frac{R_o}{R_v(t)}\right)^3 \quad (14)$$

p_o, T_o and R_o are the initial void pressure,

Table 2. Epoxy resin viscosity parameters and initial void settings

Notation	η_g	T_{go}	C_1	C_2	α_g	a	R_o	p_o	T_o	γ_{LV}	ρ
Unit	Pa.s	K	-	-	-	-	µm	Pa	°C	Pa.m	kg/m^3
Value	10e12	235	29.9	30.0	0.345	2.1	10	1.1e5	30	0.05	1280

temperature and radius respectively. The 1st order non linear differential equation (13) is solved implicitly in each finite volume in each time step but close attention should be paid when determining the roots. Once the viscosity limit of 10e6[Pa s] is reached during solidification, it is assumed that the void size follows the thermal strain of the resin, governed by the resin coefficient of thermal expansion α_{CTE} and the variation in temperature and radius from this point on.

$$R_v(t) = R_{v@\eta^{max}} + R_{v@\eta^{max}}(\alpha_{CTE}\Delta T) \qquad (15)$$

where $R_{v@\eta^{max}}$ is the void radius when the viscosity limit is reached and ΔT is the temperature variation after this point.

4. Results

A 40.0[mm] thick glass/epoxy laminate plate is modelled. The model material parameters used are summarized in Table 1 and 2. In Fig. 3 the temperature cycle at the laminate surface as prescribed in the model is seen. The temperatures at the laminate thickness centre and between the centre and surface (quarter) are also seen. The temperature peaks at app. 3000 and 9000[s] represent the exothermic heat generation during polymerization which causes a rise in temperature due to poor material conductivity, i.e. more heat is generated than can be conducted away from the source.

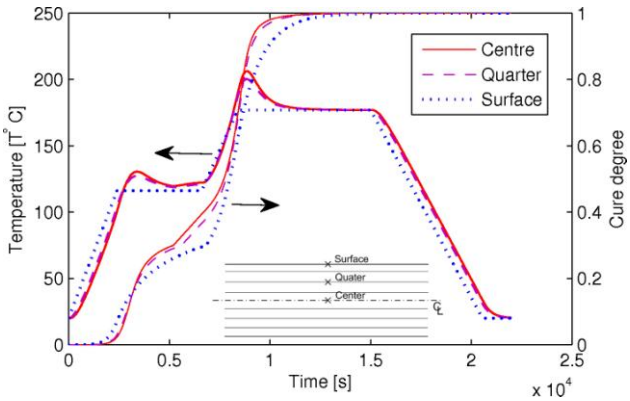

Fig.3. Temperature and cure degree at different thickness intervals during the cure cycle.

Also seen in Fig. 3 are the calculated cure degrees at the same regions (surface, quarter and centre). Notice that it is the centre of the laminate that fully cures first. The resin viscosity development is similarly seen in Fig.4. Initially, the resin viscosity drops due to the increase in temperature. As polymerization proceeds, so too does the viscosity. The programmed viscosity limit of 10e6[Pa s] is obtained at the centre of the laminate first - a result of the high curing rate here.

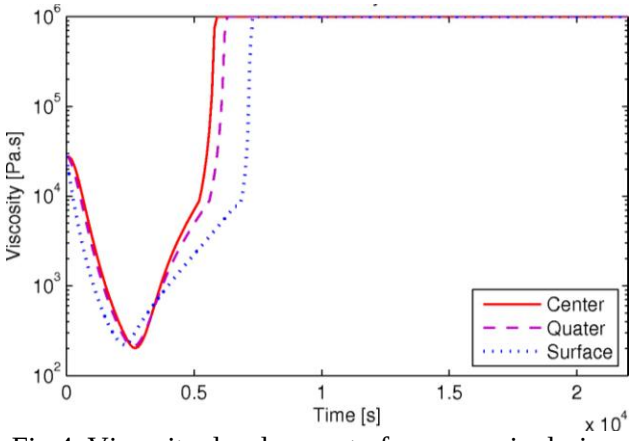

Fig.4. Viscosity development of epoxy resin during the cure cycle.

The non-isotropic through-thickness temperatures and cure degrees drive the non-uniform growth of voids resulting in a non-isotropic through-thickness void diameter as seen in Fig.5. As the resin is not fully cured at the laminate surface after approximately t=5000[s], only an increase in void radius is experienced here due to the second temperature ramp starting at time t=6600[s]. It can be said that the main contribution to the increase in void radius is the initial increase in temperature before the first dwell.

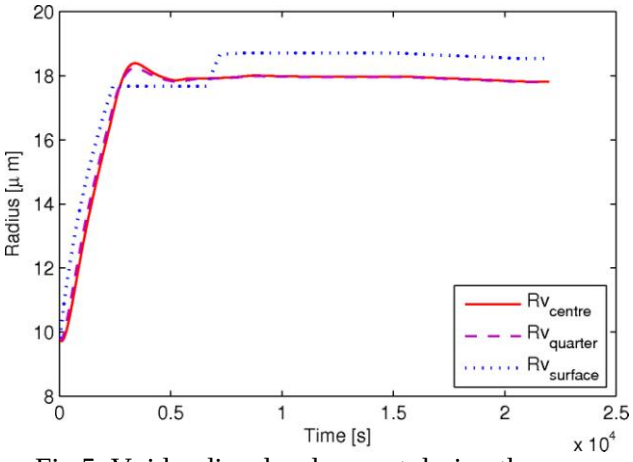

Fig.5. Void radius development during the cure cycle.

A parameter study is conducted to investigate the influence of the initial laminate thickness on void growth. A similar cure cycle as seen in Fig.3 ($T_{surface}$) is prescribed laminates of different thicknesses as this is known to influence the temperature peak during the curing exothermic reaction. In Fig. 6 the final void size variation across the laminate thickness is depicted. It is seen that the thicker laminates exhibit a larger variation in void size through the thickness, although still relatively small, as is expected due to larger through-thickness temperature and cure degree gradients during the cure cycle. Also noticeable is the change in the parabolic-shaped profile, seen for the 20 and 30[mm] laminates, to a W-shaped reversed parabolic profile within the centre for the 40 and 50[mm] laminates. This reversal in the parabolic profiles for thicker laminates is also seen when modelling in-plane residual stress development (see [9]) and is caused by changing from a nearly uniform outside-to-inside cure history for thinner laminates to an inside-to-outside cure history for thicker thermosetting laminates.

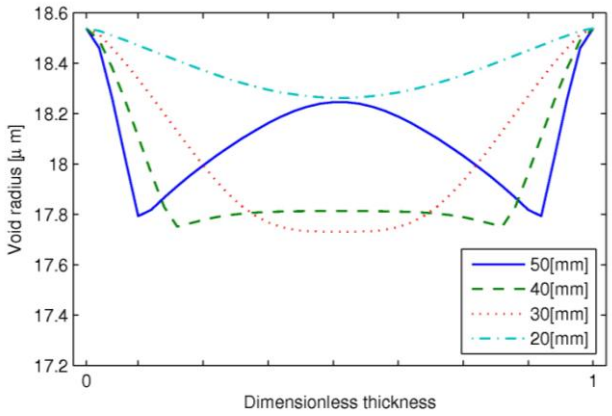

Fig.6. Laminate thickness influence on final void size distribution.

A better understanding of the void radius variations at the centre of the laminates is also gained when analyzing the void radius and viscosity during the entire cure cycle, presented in Fig.7. A higher void radius peak is achieved for thicker laminates due to higher peak temperatures at the centre of the laminate during polymerization, as seen in Fig.7(a). This higher peak is caused by a higher cure rate making a larger part of the curing phase take less time. This is also seen in the earlier occurring abrupt increase in viscosity for the thicker laminates, as seen in Fig.7(b). This alone is not necessarily an unwanted effect when purely considering the void size. As the 20[mm] laminate takes a longer time to cure, seen in Fig. 7(b) by the late increase in viscosity compared to the thicker laminates, this allows a final increase in void radius to take place due to the second cure cycle temperature ramp up, seen in Fig. 7(a) after approximately 6600[s]. Essentially this indicates that the choice of cure cycle temperature (either from a heated mould or oven) should be chosen with care so as to minimize void growth during curing by allowing a specific increase in resin viscosity before the final temperature ramp up that is normally used to fully consolidate the matrix material.

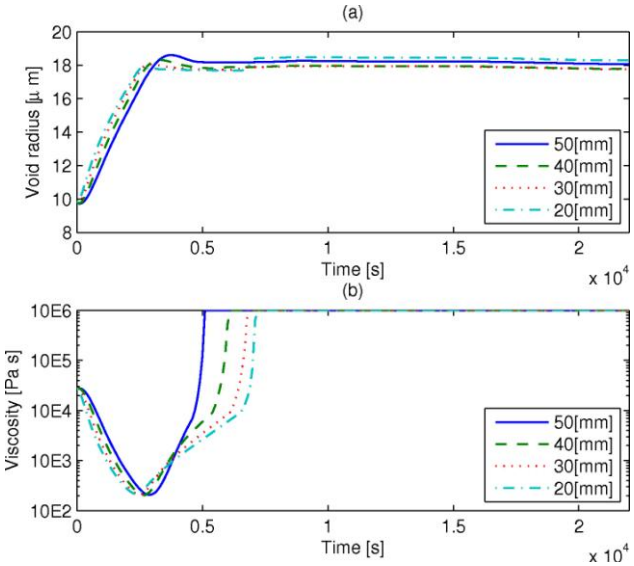

Fig.7.(a) Void radius development at laminate centre during cure cycle as a function of laminate thickness, (b) resin viscosity development for same case

5. Conclusion

In the present work, a model for predicting void growth and void size distribution in a composite laminate through-thickness direction is presented. The model is based on a coupled curing visco-mechanical void growth model mainly based on perfect gas law behaviour. The variation in void size across the laminate thickness is dependent on processing parameters as well as initial laminate thickness. It is known that non-uniform heating and curing can have an effect on the presence of defects, shape and load carrying capacity of a laminate. This

is also true for void growth, as approximated by this visco-mechanical model. Specifically it is found that variations, although still relatively small, in final void size distribution through the laminate thickness is seen in thick laminates, as a result of larger gradients in temperature and curing during processing. Furthermore, selecting an appropriate temperature cycle can help minimize void growth, by suiting the temperature ramps and dwells to the laminate thickness, curing behaviour and viscosity.

Of interest in future work is the inclusion of diffusion in the voids growth model. A non uniform distribution of initial void radii through the thickness as well as non-symmetric heating is also of interest to capture non-uniform process-induced effects. Essentially the model can be used in the prediction of process induced effects and their influence on the in-service mechanical performance of large composite parts manufactured using vacuum infusion.

Acknowledgments

The project is supported by Danish Energy Agency through the Energy Technology Development and Demonstration Program (EUDP). The supported EUDP-project is titled "Demonstration of new blade design using manufacturing process simulations" and has journal no. 64009-0094. The support is gratefully acknowledged.

References

[1] W. Brouwer and E. Herpt "Vacuum injection moulding for large structural applications" *Composites Part A: Applied Science and Manufacturing*, Vol. 34, No. 6, pp 551-558, 2003.

[2] L. Liu, B. Zhang, D. Wang and Z. Wu "Effects of cure cycles on void content and mechanical properties of composite laminates". *Composite Structures*, Vol. 73, pp 303-309, 2005.

[3] H. Huang and R. Talreja "Effects of void geometry on elastic properties of unidirectional fibre reinforced composites". *Composites Science and Technology*, Vol. 65, No.13, pp 1964-1981, 2005.

[4] D. Abraham and R. McIlhagger "Investigations into various methods of liquid injection to achieve mouldings with minimum void contents and full wet out". *Composites Part A: Applied Science and Manufacturing*, Vol. 29, pp 533, 1998.

[5] M. Wisnal, T. Reynolds and N. Gwilliam "Reduction in ILSS by discrete and distributed voids". *Composites Science and Technology*, Vol. 56, pp 93-101, 1996.

[6] S. Almeida and Z. Neto "Effect of void content on the strength of composite laminates". *Composite Structures*, Vol. 28, pp 139-148, 1994.

[7] A. Loos and G. Springer "Curing of epoxy matrix composites". *Journal of Composite Materials*, Vol. 17 no. 2, pp 135-169, 1983.

[8] Y. Ledru, G. Bernhart, R. Piquet, F. Schmidt and L. Michel "Coupled visco-mechanical and diffusion void growth modelling during composite curing". *Composite Science and Technology*, Vol. 70, pp 2139-2145, 2010.

[9] T. Bogetti and J. Gillespie "Process-induced stress and deformation in thick-section thermoset composite laminates". *Journal of Composite Materials*, Vol. 26, No. 5, pp 626-660, 1992.

[10] J. Kardos, M. Dudukovic and R. Dave "Void growth and resin transport during processing of thermosetting matrix composites". *Composites*, Vol. 2, pp 289-298, 1971.

[11] F. Boey and S. Lye "Void reduction in autoclave processing of thermoset composites, Part 1: High pressure effects on void reduction". *Composites*, Vol. 23, No. 4, pp 261-265, 1992.

[12] O. Sicot, X. L. Gong, A. Cherouat and J. Lu "Influence of residual stresses on the mechanical behaviour of composite laminate materials". *Advancements in Composite Materials*, Vol. 14-4, pp. 319-342, 2005.

[13] J. Wood and M. Bader "Void control for polymer-matrix composites (1): theoretical and experimental methods for determining the growth and collapse of gas bubbles". *Composites Manufacturing*, Vol. 5, No. 3, pp 139-147, 1994.

[14] M. Ivankovic, L. Incarnato, J.M. Kenny and L. Nicholais, "Curing Kinetics and Chemorheology of Epoxy/Anhydride System". *Journal of Applied Polymer Science*, Vol. 90, pp 3012-3019, 2003.

[15] J. Ledru, "Etude de la porosite dans les Materiaux Composites Stratifies Aeronautiques". *PhD Thèse, Université de Toulouse*, 2009.

[16] M. Amon and C.D. Denson, "A Study of the Dynamics of Foam Growth: Analysis of the Growth of Closely Spaced Spherical Bubbles". *Polymer Eng. and Science*, Vol. 24, No. 13 pp 1026-1034, 1984.

[17] J.H. Hattel, "Fundamentals of Numerical Modeling of Casting Processes". Polyteknisk Forlag, 1st Edition, 2005.

[18] J.M. Svanberg and J.A. Holmberg "Predictions of shape distortions, Part I. FE-implementation of a path dependent constitutive model". *Composites: Part A: Applied Science and Manufacturing*, 2002.

Paper II

"'Experimental Determination and Numerical Modelling of Process Induced Strains and Residual Stresses in Thick Glass/Epoxy Laminate"'

M.W. Nielsen, J.H. Hattel, T.L. Andersen, K. Branner, P.H. Nielsen

Proceedings at the 15^{th} European Conference of Composite Materials (ECCM), Venice, Italy, 2012.

EXPERIMENTAL DETERMINATION AND NUMERICAL MODELLING OF PROCESS INDUCED STRAINS AND RESIDUAL STRESSES IN THICK GLASS/EPOXY LAMINATE

M. W. Nielsen[1*], J. H. Hattel[1], T. L. Andersen[2], K. Branner[2], P.H. Nielsen[2]

[1]*DTU Mechanical Engineering, Technical University of Denmark, Kgs. Lyngby, Denmark*
[2]*DTU Wind Energy, Technical University of Denmark, Roskilde, Denmark*
**Corresponding author mwni@mek.dtu.dk*

Keywords: 1. Numerical modeling, 2. Shape distortions, 3. FBG sensoring, 4. Curing

Abstract
In this work, a cure hardening instantaneous linear elastic (CHILE) model and a path dependent (PD) constitutive approach are compared, for the case of modelling strain build-up during curing of a thick composite laminate part. The PD approach is a limiting case of viscoelasticity with path dependency on temperature and cure degree. Model predictions are compared to experimentally determined in-situ strains, determined using FBG sensors. It was found that both models offer good approximations of internal strain build-up. A general shortcoming is the lack of capturing rate-dependent effects such as creep.

1. Introduction
In the manufacture of large commercial wind turbine blades, usually multiple blade components such as the blade root, shear web, suction- and pressure shells, are initially moulded separately then joined together using epoxy adhesives to form the complete wind turbine blade [1]. A general challenge involves ensuring precise dimensional accuracy of the various parts, such that the final assembly time needed is minimal. In large composite structures with thick laminate sections, avoiding large thermal and cure gradients through the thickness during processing is cumbersome. These through-thickness thermal and cure gradients are known to induce shape distortions and residual stresses [2]. Other mechanisms responsible include, the mismatch in thermal expansion of the constituent composite materials, laminate lay-up, curing temperatures, resin chemical shrinkage and tool-part interface interaction (see [3-7]. In large wind turbine blades, laminate thicknesses can be as much as 150mm at the blade root section in 40+ meter long blades. Processing of these thick composite laminates requires long cure cycles at elevated temperatures. Generally, E-glass/epoxy composites are the material of choice for laminates in commercial blades. Thermosetting epoxy resins are known to exhibit viscoelastic effects at elevated temperatures [8]. Hence creep and stress relaxation can occur during processing. Different viscoelastic (VE) numerical process models have been proposed for modelling curing of composites, see e.g. [4, 9-10]. These models offer good accuracy as they capture the matrix material behaviour well during curing. However, VE models require extensive material characterization in order to determine discrete relaxation times, weighting terms and temperature-time-cure shift functions. Furthermore, VE models are computationally heavy due to the added need of storing internal state variables. The number of these variables is directly dependent on the size of the Weichert- or Prony series used and their goodness of fit to experimental data – usually better fit is equal to larger series. Alternatives to VE models

include the well known Cure Hardening Instantaneous Linear Elastic (CHILE) approach, originally proposed by Bogetti & Gillespie (1991)[2], and the path-dependent (PD) model, proposed by Svanberg (2002)[11]. The PD model is a limiting case of linear viscoelasticity where rate dependency is replaced by a path-dependency on cure degree and temperature history. Both these approaches require less material data and are computationally fast. In this work, we investigate how adequate the above-named non-viscoelastic approaches are, at predicting process-induced internal strains in slow curing thick laminates. Model strain predictions are compared to experimentally determined process strains from a 52ply UD E-glass/epoxy laminate (app.46mm thick) using embedded Fibre Bragg Grating (FBG) sensors.

2. Constitutive model formulation

The main differences in the analysed constitutive approaches lies within their respective incremental matrix material stiffness expressions. Thermoset epoxy resins exhibit temperature- and cure degree dependent phase transformation within the liquid, rubbery and glassy states during curing [8, 12]. In the subsequent sections, a brief description of the two modelling approaches used to capture the mechanical behaviour of the epoxy matrix is given. In both approaches, the self-consistent field model micromechanics approach for a unidirectional continuous fibre reinforced composite was used to calculate effective laminate thermal expansion and chemical shrinkage.

2.1 CHILE approach

The CHILE approach is a further development of the incremental linear elastic model originally proposed by Bogetti & Gillespie (1992) [2]. In the CHILE approach, the epoxy matrix material is cure- and temperature dependent and expressed as:

$$E_m = \begin{cases} E_m^0 & T^* < T_{C1} \\ E_m^0 + \left(\dfrac{T^* - T_{C1}}{T_{C2}^* - T_{C1}}\right)(E_m^\infty - E_m^0) & T_{C1} \le T^* \le T_{C2} \\ E_m^\infty & T^* > T_{C2} \end{cases} \quad (1)$$

where cure dependency is included in the temperature: $T^* = \left(T_g^0 + a_{Tg} * \alpha\right) - T$ (2).

In the equations above, E_m^o and E_m^∞ are the fully uncured (rubbery) and fully cured (glassy) resin modulus respectively. The critical temperatures T_{C1} and T_{C2} mark the bounds determining the linear variation of the modulus with *T**, which is cure dependent. The coefficients used in Eq. (1) and (2) are fit to the temperature dependent elastic response provided by the resin supplier [13]. In essence, Eq. (1) and (2) express a two-step temperature- and cure degree dependent resin modulus. This approach also allows softening of the fully cured resin if the cure temperature *T* is large enough to allow *T** to be smaller than T_{C2}. Physically this represents increasing the temperature of the vitrified resin resulting in transition back from glassy to rubbery state.

2.2 PD approach

The path-dependent constitutive material model approach is a limiting case of viscoelasticity. Linear viscoelastic materials, such as epoxy resins, are most commonly described using Weichert or Maxwell-Zener spring-damper models. These models are adequate because thermosetting polymers exhibit a bound in stress relaxation due to unbreakable cross-links in the polymer structure. Svanberg's simplified approach involves replacing the rate dependence by a path dependence on the strain, temperature and cure degree. In effect this results in an instantaneous stress relaxation at temperatures above *Tg*:

$$\sigma_{ij} = \begin{cases} C^r_{ijkl} \cdot (\varepsilon_{kl} - \varepsilon^E_{kl}) & ,T \geq T_g(\alpha)\,,\ \eta \to 0 \\ C^g_{ijkl} \cdot (\varepsilon_{kl} - \varepsilon^E_{kl}) - (C^g_{ijkl} C^r_{ijkl}) \cdot (\varepsilon_{kl} - \varepsilon^E_{kl}) & ,T < T_g(\alpha)\,,\ \eta \to \infty \end{cases} \quad (3)$$

where C^r_{ijkl} and C^g_{ijkl} are the rubbery and glassy state stiffness tensors, ε_{kl} and ε^E_{kl} are the mechanical and expansion (chemical + thermal) strains. The cure dependent glass transition temperature is determined using the DiBenedetto equation. In order to allow numerical implementation, incrementalization of the constitutive model is necessary, resulting in the following equation system:

$$\Delta\sigma_{ij} = \begin{cases} C^r_{ijkl} \cdot \Delta(\varepsilon_{kl} - \varepsilon^E_{kl}) - \beta^l_{ij}(t) & ,T \geq T_g(\alpha) \\ C^g_{ijkl} \cdot \Delta(\varepsilon_{kl} - \varepsilon^E_{kl}) & ,T < T_g(\alpha) \end{cases} \quad (4)$$

where the internal state variable $\beta^l_{ij}(t)$ is updated in each time increment as:

$$\beta^l_{ij}(t + \Delta t) = \begin{cases} 0 & ,T \geq T_g(\alpha) \\ \beta^i_{ij}(t) + (C^g_{ijkl} - C^r_{ijkl}) \cdot \Delta(\varepsilon_{kl} - \varepsilon^E_{kl}) & ,T < T_g(\alpha) \end{cases} \quad (5)$$

Through the equation above, the stress history of the resin matrix is stored at temperatures below *Tg* and fully relaxed above *Tg*. For model requirements that must be fulfilled, see [11]. To sum up, the presented constitutive approaches estimate the resin stiffness behaviour as a function of temperature and cure degree. This is shown for the different models overlaid the fully cured resin modulus from the resin supplier in Fig 1. The main difference between the different constitutive models is the ability of the PD approach to relax stresses instantaneously once in glassy state once the cure temperature is larger than *Tg*.

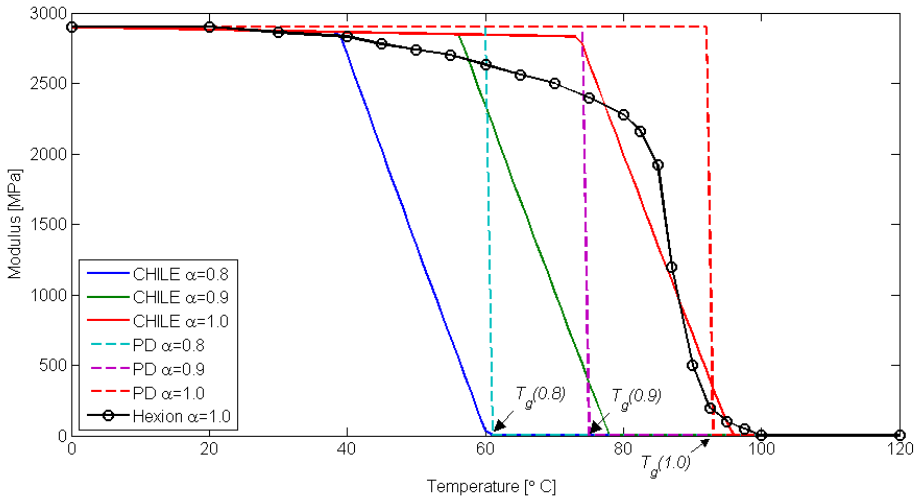

Figure 1. CHILE and PD approach resin modulus temperature and cure degree dependence

3. Experimental in-situ strain measurements

3.1 Experimental setup

A glass/epoxy laminate plate measuring 400x600mm consisting of 52-layers (app. 46mm thick) UD E-glass fiber mats was vacuum infused on a 10mm tempered glass plate. Epikote RIM R 135/R 137 epoxy resin/hardener is used, which is a slow curing resin system developed for the wind turbine industry. J-type (Fe-CuNi) 2x0.5mm thermocouples and three optical fibres, consisting three FBG sensors each, were placed at the bottom-, mid- and top planes of the laminate plate, see Fig. 2. The optical fibres were placed perpendicular to the longitudinal reinforcement fibre direction. Data from the thermocouples were used for the de-

convolution of the thermal strains in order to obtain the mechanical strains measured by the wavelength shifts in the FBG sensors, for more details see Nielsen *et. al*. 2012 [14]. The entire layup (laminate and 10mm thick tempered glass plate) was placed on an electric heating plate with a digital temperature control unit, kept at a constant prescribed temperature of 40°C. During the entire process, data was logged from the mid-plane FBG sensors and all three thermocouples. The main goal with the experiment was to achieve a high exothermic peak temperature at the laminate centre with large temperature and cure degree gradients through the thickness. Furthermore, a long temperature hold was chosen such that viscoelastic creep or stress relaxation behaviour would be visible.

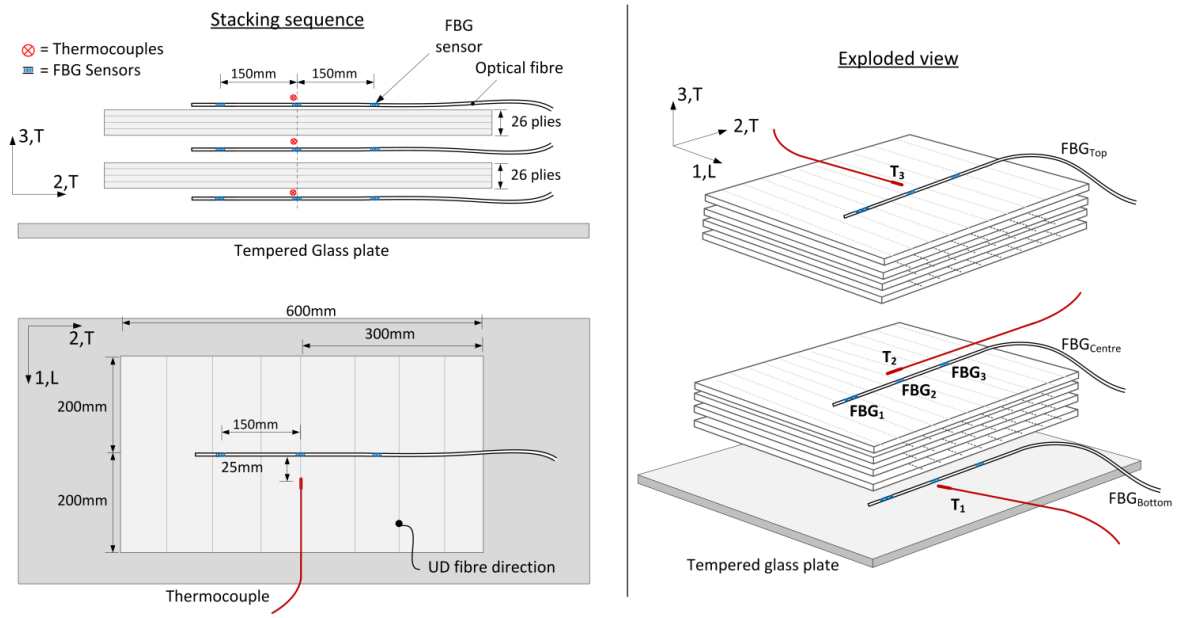

Figure 2. Laminate plate stacking sequence and sensor placement schematic

3.2 Experimental results

The total transverse strain variation $\Delta\varepsilon_{tot}$ during infusion at the laminate middle plane is seen in Fig. 3. The fluctuations seen at the beginning of the process mark the instants when the resin flow front reaches the FBG sensors. After app. 55 minutes into the infusion process, the resin flow front reaches the outlet hose, marked in Fig. 3 by the sudden decrease in strain measurements as flow is drastically reduced. Finally, after app. 65 minutes the vacuum pressure is reduced to 60% to allow complete impregnation of the reinforcement fibres. The variations in strain measurements have mainly been driven by to resin flow. In the early stages of infusion prior gelation, caution should be taken in evaluating the measured strains, as perfect bonding between the host material and optical fibres does not yet exist. After gelation, temperature changes, resin chemical shrinkage effects and tool/part interaction primarily drive the changes measured. After the exothermic reaction takes place, compressive strains are measured, showing a difference in strains dependent of the FBG placement. During the constant temperature hold (i.e. between 500 and 1050minutes) a slight slope of the strain curves is seen. As app. 60% of chemical shrinkage is known to occur in epoxies prior gelation [15], it is mostly likely that the slope is due to viscoelastic creep of the polymer matrix.

Also seen in Fig. 3 are the fluctuations which arise during cooling. The build-up of high shear stresses formed at the tool/part interface is known to cause a stick-slip effect or separation, usually experienced during cooling [15,16].

Finally, the total transverse strain from all three optical fibres (FBG_{Bottom} , FBG_{Centre} *and* FBG_{Top} in Fig. 1) at various intervals is seen in Fig. 4. These measurements were carried out to further verify any viscoelastic behaviour. The intervals shown include: (i) prior infusion with the vacuum pressure applied, (ii) after infusion, (iii) after 2 months (iv) after demoulding. At each interval the laminate was at ambient temperature. In the figure, the strain state from the previous graph (dotted lines) are overlaid the current strains. The largest changes in strains occur during infusion, visible by the increase in compressive strains after infusion. A slight increase in strains is also seen after 2 months in ambient temperature, possibly due to creep or separation at the tool/part interface. Finally after demoulding, no significant change in strains is experienced.

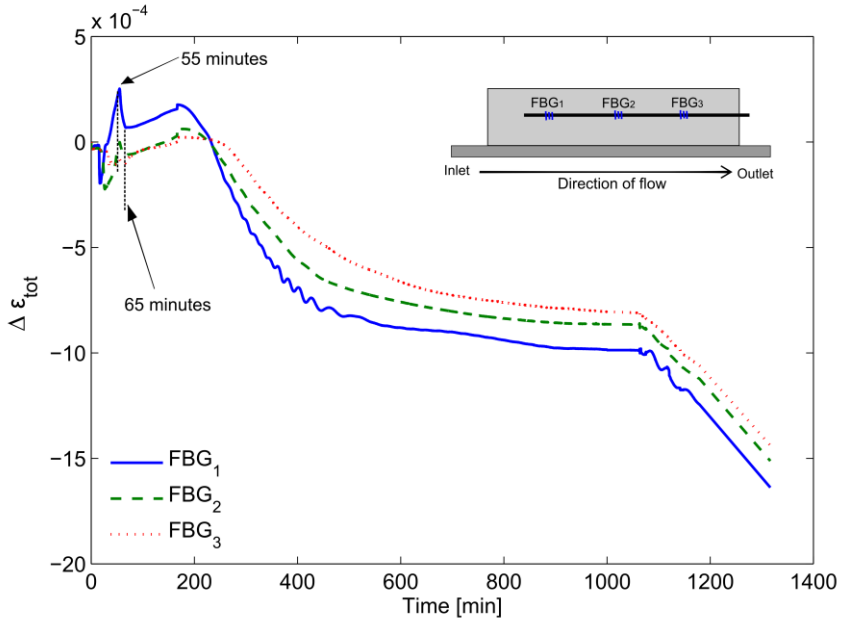

Figure 3.Variation in process-induced total transverse strains at the laminate mid plane during infusion

4. Numerical model predictions

A 46[mm] thick glass/epoxy laminate plate is modelled using a sequentially coupled thermomechanical analysis setup. In the thermal step, all thermochemical aspects of the problem are calculated, i.e. the temperature, cure degree evolution and volumetric heat generation. In the mechanical step, chemical shrinkage, thermal expansion and the instantaneous laminate mechanical property evolution is calculated leading to predictions of process strains and stresses. The same thermal step is used for the CHILE and PD approaches. Further information on model settings and material parameters used is summarized elsewhere, see [14]. The different constitutive model total transverse strain predictions are seen in Fig. 5 compared to experimental data. As one can see, both models offer good predictions of the strain history during infusion. The largest compressive strains are measured at the model node corresponding to the FBG_1 position in the experiment. This coincides well with the experimental data, although in real life the strain measurements show some dependency to resin flow. In the models, the larger strains away from the laminate mid region are a result of the part contraction during cooling and as chemical shrinkage progresses.

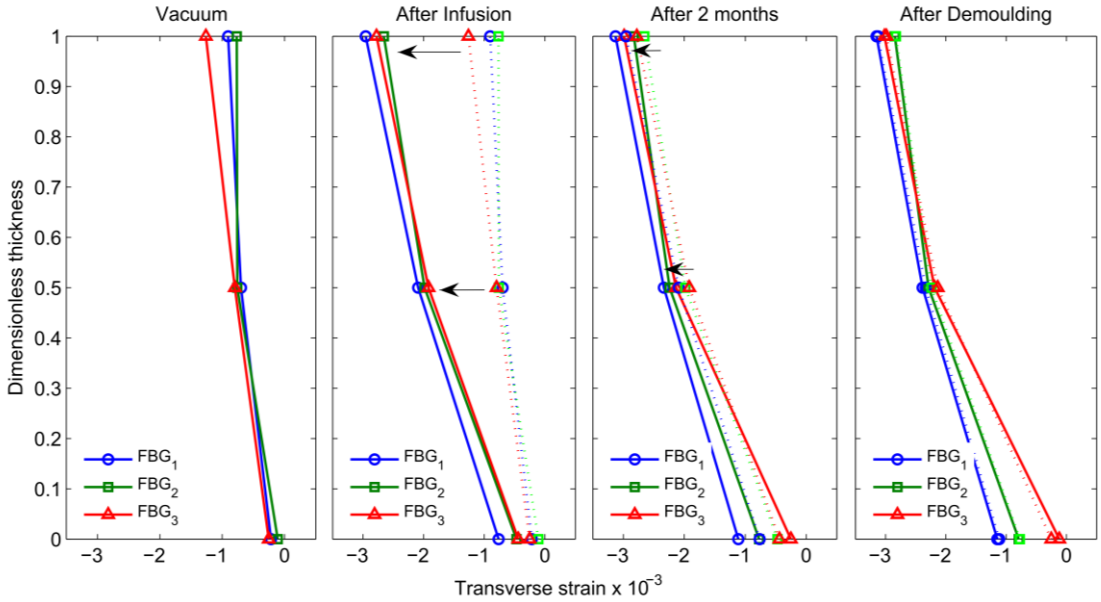

Figure 4. Total transverse strains from all embedded FBGs at various intervals during manufacturing. The dotted lines show the previous strain state overlaid the current strains at the measured time

When comparing the results from the different constitutive approaches, slightly larger compressive strains are achieved when using the path dependent (PD) approach. This is not due to stress relaxation but rather due to the fact that the *Tg* dependent transition from rubbery to glassy state occurs later than in the CHILE approach, resulting in a softer material for a longer period. The reason no stress relaxation occurs is because the cure temperature is not higher than the resin *Tg* at any time after gelation occurs. Hence even though the simplified approach taken in the PD model accounts for stress relaxation in its constitutive relations, the need to further capture creep-type behaviour, as described earlier, still exists when considering processes where low temperatures are mainly used. Fig. 6 illustrates the temperature evolution at the laminate centre for the initial 500minutes of the process, comparing the PD approach curing temperature $T_{Mid\ Ref}$ to $Tg(\alpha)$ and the CHILE approach T^* to the bounding temperatures *Tc1* and *Tc2*. From the figure, one can see that the PD approach has a transition from rubbery to glassy state later than in the CHILE model.

In the FE models, a tied mechanical boundary condition at the tool/part interface was used, which physically represents perfect bonding between the surfaces. This is not entirely descriptive of the tool/part interaction taking place during infusion where sliding and sticking conditions exist at various phases of the infusion process, governed by the resin material phase transition and thermal expansion, as shown in [17].

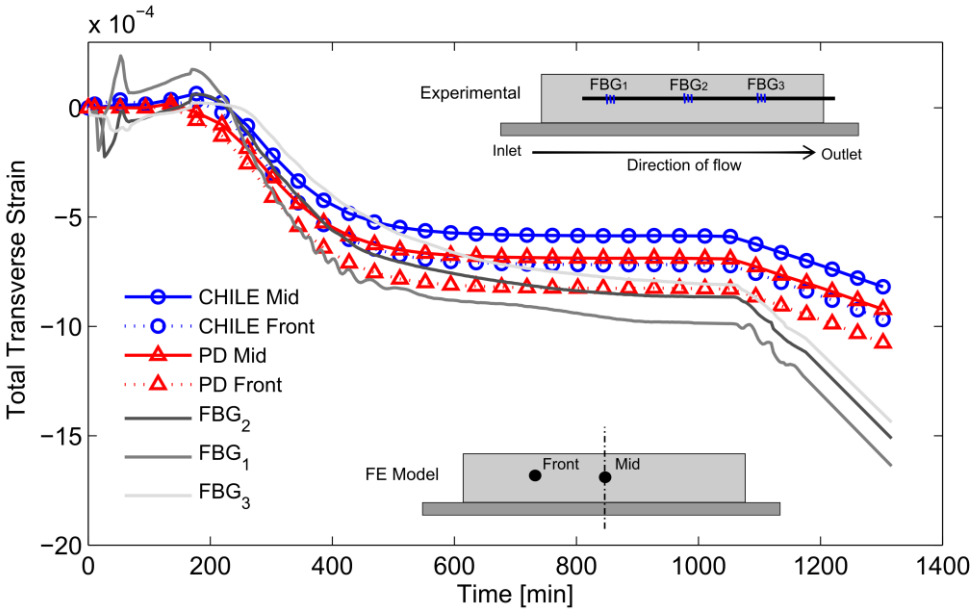

Figure 5. FE CHILE and PD model predictions og total transverse strains during infusion compared to experimental FBG measurements

5. Conclusion

In the present work, two different constitutive approaches used to model curing of composite laminates and the resulting process induced residual stresses and strains build-up were investigated. As a case, a 52 ply thick laminate plate was modelled and compared to experimentally determined in-situ strain measurements. Regarding the cure hardening, instantaneous linear elastic model approach, generally good predictions of the process strains were achieved, though the model underestimates the compressive strains that build up during infusion.

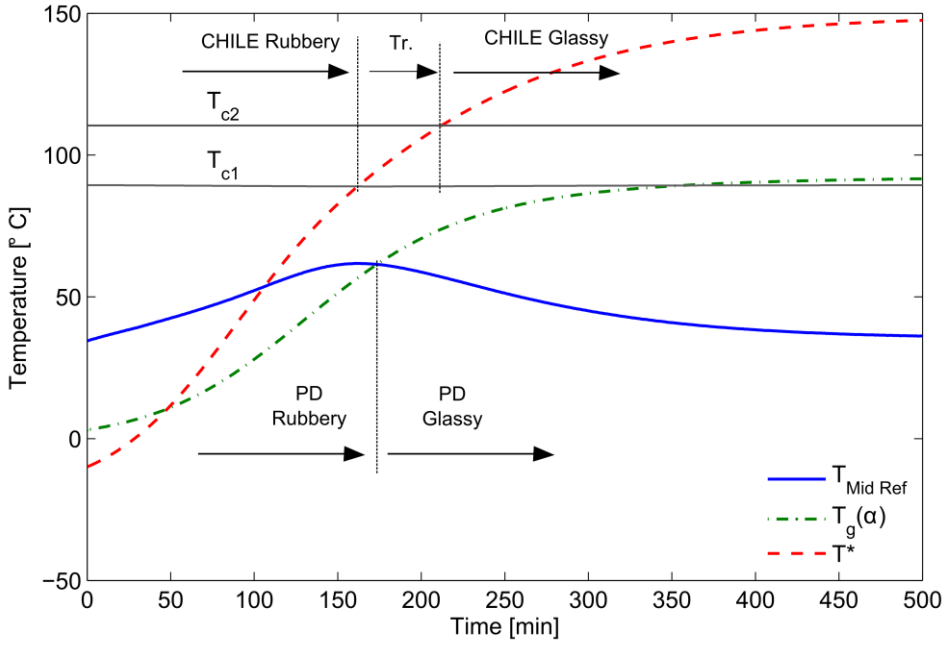

Figure 6. Comparison of the transition temperature governing the resin modulus stiffness evolution in the PD and CHILE constitutive approches. "Tr." Denotes the CHILE approach transition zone, see also Fig.1.

Regarding the path dependent model, which is a limiting case of linear viscoelasticity, slightly better strain predictions were achieved. This was however not due to calculation of transition dependent stress relaxation. I.e. for slow curing infusion processes, where cure temperatures are not that high, time dependency is needed to accurately predict process strains. Furthermore, a more accurate model of the tool/part interface is needed, taking sliding and sticking contact behaviour into account, if trustworthy modelling results are to be achieved.

Acknowledgments

The project is supported by Danish Energy Agency through the Energy Technology Development and Demonstration Program (EUDP). The supported EUDP-project is titled "Demonstration of new blade design using manufacturing process simulations" and has journal no. 64009-0094. The support is gratefully acknowledged.

References

[1] F. Jensen, "Ultimate Strength of a Large Wind Turbine Blade", PhD Thesis, Risø National Laboratory for Sustainable Energy, Roskilde, Denmark, 2008.

[2] T. Bogetti and J. Gillespie "Process-induced stress and deformation in thick-section thermoset composite laminates". *Journal of Composite Materials,* **Vol. 26- 5**, pp 626-660, 1992.

[3] J. Favre "Residual Thermal Stresses in Fibre Reinforced Composite Materials – A Review". *Journal of the Mechanical Behaviour of Materials,* **Vol. 1- 1-4**, pp 37-53, 1988.

[4] Y. Kim and S. White "Stress Relaxation Behaviour of 3501-6 Epoxy resin During Cure". *Polymer Engineering and Science,* **Vol. 36-23**, pp 2852-2862, 1996.

[5] J.M. Svanberg "An Experimental Investigation on Mechanisms for Manufacturing induced Shape Distortions in Homogeneous and Balanced Laminates". *Comp: Part A:* **Vol 32**, pp.827-838, 2001.

[6] Johnston, A. "An integrated model of the development of process-induced deformation in autoclave processing of composite structures". PhD Thesis, University of British Columbia,Vancouver, Canada, 1997.

[7] Twigg G., Poursartip A. and Fernlund G. "Tool-part interaction in composites processing. Part II: Numerical Modeling". *Composites Part A*;**Vol.35**, pp.135-141, 2004.

[8] J.D. Ferry, "Viscoelastic Properties of Polymers" John Wiley & Sons, inc., 2nd Edition, 1961.

[9] S.L. Simon, et. al. "Modeling the evolution of the dynamic mechanical properties of a commercial epoxy during cure after gelation". *Journal of Applied Polymer Science,* **Vol. 76**:pp.495–508, 1999.

[10] M.A. Zocher, S.E. Groves and D.H Allen " A three-dimensional Finite element Formulation for Thermoviscoelastic Orthotropic Media". *Int.Journal for Numerical Methods in Engineering,* **Vol. 40**:pp.2267–2288, 1997.

[11] J.M. Svanberg "Predictions of Shape Distortions Part I: FE Implementation of a Path Dependent Constitutive Model ". *Composites: Part A:* **Vol 35**, pp.771-721, 2004.

[12] J. K. Gillham. Formation and Properties of Thermosetting and high Tg Polymeric Materials. *Polymer Engineering and Science,* Volume:**Vol.26**:p.1429–1433, 1986.

[13] Momentive Speciality Chemicals Inc. Epikote RIMR 135 Technical Data Sheet, 2006.

[14] M.Nielsen, J.Schmidt, J.Hattel, T.Andersen and C. Markussen "In-situ measurement using FBGs of process-induced strains during curing of thick glass/epoxy laminate plate: Experimental results and Numerical modelling". *Wind Energy,* **Submitted** April 2012.

[15] L. Khoun, R. de Oliveira, V. Michaud and P. Hubert, " Investigation of process-induced strains development by fibre Bragg grating sensors in resin transfer moulded composites" *Composites: Part A,* **Vol. 42**, pp.274-282, 2011.

[16] R. de Oliveira, S. Lavanchy, R. Chatton, D. Costantini, V. Michaud R. Salathe and J.-A.E. Manson, "Experimental Investigation of the effect of the mould thermal expansion on the development of internal stresses during carbon fibre composite processing" *Composites: Part A,* **Vol. 39**, pp.1083-1090, 2008.

[17] Twigg G., Poursartip A. and Fernlund G. "Tool-part interaction in composites processing. Part I: Experimental investigation and analytical model". *Composites Part A*;**Vol.35**, pp.121-133, 2004.

Paper III

"'In situ Measurement Using FBGs of Process-Induced Strains During Curing of Thick Glass/Epoxy Laminate Plate: Experimental Results and Numerical Modelling"'

M.W. Nielsen, J.W. Schmidt, J.H. Hattel, T.L. Andersen, C.M. Markussen

Wind Energy, DOI: 10.1002/we.1550, 2012.

WIND ENERGY
Wind Energ. (2012)
Published online in Wiley Online Library (wileyonlinelibrary.com). DOI: 10.1002/we.1550

RESEARCH ARTICLE

In situ measurement using FBGs of process-induced strains during curing of thick glass/epoxy laminate plate: experimental results and numerical modelling

Michael Wenani Nielsen[1], Jacob Wittrup Schmidt[2], Jesper Henri Hattel[1], Tom Løgstrup Andersen[3] and Christen Malte Markussen[3]

[1] Department of Mechanical Engineering, Technical University of Denmark, 2800 Kgs. Lyngby, Denmark
[2] Department of Civil Engineering, Technical University of Denmark, 2800 Kgs. Lyngby, Denmark
[3] Department of Wind Energy, Technical University of Denmark, 4000 Roskilde, Denmark

ABSTRACT

For large composite structures, such as wind turbine blades, thick laminates are required to withstand large in-service loads. During the manufacture of thick laminates, one of the challenges met is avoiding process-induced shape distortions and residual stresses. In this paper, embedded fibre Bragg grating sensors are used to monitor process-induced strains during vacuum infusion of a thick glass/epoxy laminate. The measured strains are compared with predictions from a cure hardening instantaneous linear elastic (CHILE) thermomechanical numerical model where different mechanical boundary conditions are employed. The accuracy of the CHILE model in predicting process-induced internal strains, in what is essentially a viscoelastic boundary value problem, is investigated. A parametric study is furthermore performed to reveal the effect of increasing the laminate thickness. The numerical model predicts the experimental transverse strains well when a tied boundary condition at the tool/part interface is used and the tool thermal expansion is taken into account. However, the CHILE approach is shown to overestimate residual strains after demoulding because of the shortcomings of the model in considering viscoelastic effects. The process-induced strain magnitude furthermore increases when the laminate thickness was increased, owing mainly to a decrease in through-thickness internal transverse stresses. Copyright © 2012 John Wiley & Sons, Ltd.

KEYWORDS

blades; composites; manufacturing; shape distortions; numerical analysis; process monitoring; curing

Correspondence

Michael Wenani Nielsen, Department of Mechanical Engineering, Technical University of Denmark, 2800 Kgs. Lyngby, Denmark.
E-mail: mwni@mek.dtu.dk

Received 24 April 2012; Revised 24 July 2012; Accepted 28 July 2012

1. INTRODUCTION

Composite structures are seen to be used more extensively during the last decades in the civil industry. For instance, in the manufacture of wind turbine blades, glass fibre reinforced resin matrix composites are the principal material of choice. Such large composite structures (+50 m in length) contain thick laminates in order to withstand large in-service loads. When considering the manufacture of thick laminates, one of the challenges met is avoiding or reducing the development of process-induced shape distortions and residual stresses. Geometric variations may exist between the *as-designed* and *as-manufactured* part, for instance in laminate thicknesses, but often process-induced shape distortions and residual stresses are seen, too. Residual stresses can help initiate matrix cracking and delaminations, which reduce the structural strength of the composite.[1] In literature, a number of different mechanisms responsible for the development of these distortions and residual stresses are identified. Of these mechanisms, the fundamental include: (i) the mismatch in constituent material (*micro* level) and ply (*macro* level) thermal expansion,[1,4,6] (ii) matrix chemical shrinkage[2,4,6] and (iii) interactions at the tool/part interface.[3–7] Other mechanisms include the cure cycle design and how heating and cooling rates are prescribed, as well as which cure temperatures are used. For instance, in thick laminates, large through-thickness temperature and cure

degree gradients can result in non-uniform curing such that internal constraints arise.[2] These constraints can exist at inter-laminar and intra-laminar levels. Hence, it is generally perceived that residual stresses should be avoided, or kept at a minimum, if one wishes to manufacture good quality parts.

Another challenge relates to the size of these composite structures and the large laminate thicknesses, as they necessitate the need for longer curing cycles at lower temperatures than otherwise would be required for thinner parts during processing. This is mainly because the curing exothermic reaction can result in higher peak temperatures in thick laminates than in thin ones, resulting in non-uniform through-thickness curing (see e.g. Bogetti and Gillespie[2]). This would then result in non-uniform shrinkage and matrix material mechanical properties at different periods during the process, which induce residual stresses and strains. Polymer materials, such as the thermosetting epoxy resins used in blades, also exhibit viscoelastic (VE) material behaviour, which is especially exaggerated at elevated temperatures.[8] Hence, creep or stress relaxation behaviour by the resin may occur, taking the long process times and temperatures into account. This further amplifies the complexity of predicting the residual stress state and, from an industrial point of view, accounting for post-production shape distortions, especially for thick composites.

A shortcoming is the ability to measure, *in situ*, the process-induced strains accurately. Revealing these strains opens the possibility to include them in the design phase of the structure. Fibre optic sensors for health and *in situ* process monitoring in different mechanical applications have gained acceptance as a desirable tool for such measurements, in research[9–18] as well as in an industry, over the last decade. The main advantage with fibre optic sensors is that they can be embedded in a *host* material with minimal disturbance to the structure.[9] In composites processing, optical fibre sensors are mainly used to measure temperatures and/or strains.[10–15]

In this study, embedded fibre Bragg grating (FBG) sensors are used to monitor process-induced internal strains during the manufacture of a thick glass/epoxy laminate using vacuum infusion. The measured strains are compared with predictions from a 3D cure hardening instantaneous linear elastic (CHILE) thermomechanical numerical model with origins from classical laminate theory. Focus is primarily on investigating the accuracy of the 3D linear elastic thermomechanical model in predicting internal process strains, in what is essentially a VE problem. Hence, it is investigated whether it is feasible to use a CHILE-type process model when considering thick composites in slow curing processes where VE effects in the matrix material are inevitably at play.

Mulle *et al.*,[16,17] de Oliveira *et al.*[18] and Khoun *et al.*[15] worked with *in situ* strain monitoring and numerical modelling of composites during curing. Tool/part interaction effects were found to influence the development of internal stresses. Furthermore, large residual strains were experienced when tools with large thermal expansion coefficients were used.[18] In Khoun *et al.*,[15] it was found that modelling the tool/part interaction by using a frictional contact interaction described well the evolution of the measured strains during curing. However, common for these works is that (i) laminates thicknesses are <8 mm, (ii) uniform temperatures and cure degree although the thickness are assumed and (iii) demoulding is not considered in the numerical models. These points are considered in the current research.

2. STRAIN MEASUREMENT USING FBGs

An optical fibre with an axial Bragg grating back-reflects light when a broadband light spectrum is transmitted from a source through the optical fibre. The Bragg grating is a pattern created in the core of the optical fibre, which acts as wavelength selective mirrors.[13] This local modulation of the refractive index in the photo-sensitive optical fibre can be created as patterns in the fibre using UV light.[9] The reflected light spectrum, which is transmitted into an interrogator for data acquisition, is centred on the Bragg wavelength (λ_B) according to the Bragg equation[9]:

$$\lambda_B = 2n_{\text{eff}}\Lambda \tag{1}$$

where n_{eff} is the effective index of refraction and Λ is the Bragg period of the grating. The Bragg period changes during expansion or contraction of the FBG under mechanical or thermal loading, resulting in a change in the reflected Bragg wavelength (λ_B). Considering only the optical fibre, the change in Bragg wavelength $\Delta\lambda_B$ can be related to a change in applied axial strain $\Delta\varepsilon_{\text{app}}$ and a thermal load T as follows:

$$\Delta\lambda_B = \lambda_B^0\left[(1-p_e)\Delta\varepsilon_{\text{app}} + (\alpha_f + \xi)\Delta T\right] = \lambda_B^0\left[K_\epsilon\Delta\varepsilon_{\text{app}} + K_T\Delta T\right] \tag{2}$$

where $\Delta\lambda_B = \lambda_B^i - \lambda_B^0$. Here, λ_B^i s the current or final Bragg grating wavelength, λ_B^0 is the initial unstrained grating wavelength, p_e is the optical fibre photoelastic constant, and α_f is the optical fibre's coefficient of thermal expansion (CTE) and is the fibre thermo-optic coefficient. K_ϵ and K_T denote the mechanical strain and temperature sensitivities of the sensor. Equation (2) describes the linear mechanical and thermal response of the bare FBG optical sensor. When the FBG is embedded in a composite (host) material, as we wish to do, perfect bonding is assumed between the optical fibre and the host material if the FBG sensor

is to capture any strains from the host. Hence, any mechanical straining and thermal expansion of the *host* material governs the response of the FBG sensor. Equation (2) is then modified:

$$\frac{\Delta\lambda_B}{\lambda_B^0} = K_\epsilon\left[\Delta\varepsilon_{app}^{host} + \Delta\varepsilon_{th}^{host}\right] + K_T\Delta T = K_\epsilon\Delta\varepsilon_{tot} + K_T\Delta T \tag{3}$$

where $\Delta\varepsilon_{tot}$ is the change in total strain including the effect of the applied strain and the change in host thermal strain $\Delta\varepsilon_{th}^{host}$. The host thermal strain is here simply the host CTE multiplied by the change in temperature (ΔT). We will refer to the applied strain from the host material simply as $\Delta\varepsilon_{app}$ henceforth.

In this work, silica optical fibres provided by FOS&S (Geel, Belgium) are used, with draw tower grating (DTG) FBG sensors with an Ormocer coating (cladding diameter 125 μm). DTG FBGs are known to exhibit little variation in strain-optic coefficients when loaded which is advantageous. Furthermore, the coating helps reduce sensitivity to external transverse loading, increasing the accuracy of the axial strain measurements. A review of criticism and opportunities with embedded FBG sensors explaining more on this subject is found in Luyckx *et al.*[9] In this work, the silica optical fibre thermal expansion is equal to $5.5 \times 10^{-6}\,°C^{-1}$ and the strain sensitivity factor K_ϵ is equal to $0.775 \times 10^{-6}\,\mu\varepsilon^{-1}$. K_ϵ is known to be between 0.77 and $0.78 \times 10^{-6}\,\mu\varepsilon^{-1}$.[15,18,19] It was shown that the strain sensitivity does not exhibit temperature dependency between 0°C and 180°C.[17] The fibre thermo-optic coefficient ξ is $6.27 \times 10^{-6}\,°C^{-1}$,[20] but typically lies between 5.0 and $8.6 \times 10^{-6}\,°C^{-1}$ for similar FBG sensors.[21] Comparing the values for α_f and ξ, it is clear that the wavelength variations are mostly dependent on the fibre thermo-optic coefficient, whereas in some literature, α_f is neglected as a first approximation. An I-MON E interrogator, from Ibsen Photonics (Farum, Denmark), was used for data acquisition. The I-MON E is a stand-alone interrogation monitor with a wavelength bandwidth of 85 nm, capable of assessing <70 FBG sensor signals. This interrogator offers a wavelength accuracy of 5 pm with a sampling rate of up to 970 Hz.

It is an important general assumption that average strains are measured where no localized gradients exist or are so small that an average is a good approximation. The grating length used in this work is chosen to 4 mm. In other works[13,19] where a similar length is used, no peak splitting of the back-reflected wavelength spectrum was experienced. Peak splitting is generally attributed to the existence of transverse loading of the sensor. This is most likely to occur when using long gratings where a large transverse local force is present in the vicinity of the sensor. By having a short grating length and using a coated fibre, this problem is greatly reduced.[9] Furthermore, out-of-autoclave vacuum infusion is used; hence, the only transverse loading present would be a result of the vacuum pressure and resin curing shrinkage and assumed to be negligible. Parlevliet *et al.*[13] found that, using a similar setup, good predictions of the total chemical shrinkage in neat resin were achieved (i.e. good bonding), and no peak splitting was observed during infusion of a thick laminate.

3. VACUUM INFUSION PROCEDURE

Figure 1 shows the experimental setup. A glass/epoxy laminate plate measuring 400×600 mm consisting of 52-layers unidirectional (UD) E-glass fibre mats type L1200/G50F-E06-A from Devold AMT (Langevåg, Norway) with a nominal area weight of 1246 g m^{-2} was vacuum infused on a 10 mm tempered glass plate, which was pre-coated with release agent, resulting in a final laminate thickness of 52 mm. A glass plate as the infusion tool was chosen in order to visibly ensure full impregnation of the reinforcement fibres in the thick laminate. A glass plate does not represent what is used in an industry (glass/epoxy or glass/polyester composite moulds) but is adequate in an experimental environment where more control over process parameters is desired. The stacking sequence from bottom to top (excluding sensors) is as follows: glass plate, 52 UD plies, peel-ply, perforated release foil, distribution net and vacuum bag. During the layup process, prior vacuum bagging, three J-type (Fe–CuNi) 2×0.5 mm thermocouples and three optical fibres, consisting of three FBG sensors each, were placed at the bottom, centre and top planes of the laminate plate, as illustrated in Figure 1. Since the laminate is mostly constrained internally by the reinforcement fibres in the longitudinal direction (Figure 1), the optical fibres are placed transverse to the fibre direction in order to capture the resin-driven process-induced strains. Data from the thermocouples are used to account for the thermal strains in equation (3) in order to calculate the total strains from the wavelength shifts measured by the FBG sensors. The thermocouples are positioned approximately 25 mm from the FBG sensors, enabling measurements of the same thermal history as the FBGs. The entire layup (laminate and 10 mm thick tempered glass plate) is placed on an electric heating plate (1000×1500 mm) with a digital temperature control unit, where the infusion process takes place.

Epikote RIMR 135 (Momentive Speciality Chemicals Inc) epoxy resin is used, which is a slow curing resin system developed for the wind turbine blade manufacturing industry. A 100:30 epoxy/hardener parts by weight mixing ratio was used, and before infusion, the resin was degassed as prescribed by the manufacturer. During degassing, the dry laminate was preheated. Data logging was commenced once infusion was started. During infusion, the heat plate was kept at a constant prescribed temperature of 40°C. The laminate was assumed fully impregnated once a substantial amount of resin reached the outlet hose. At this point, the inlet hose was blocked, and further consolidation was allowed under vacuum. After approximately 17 h, the heat

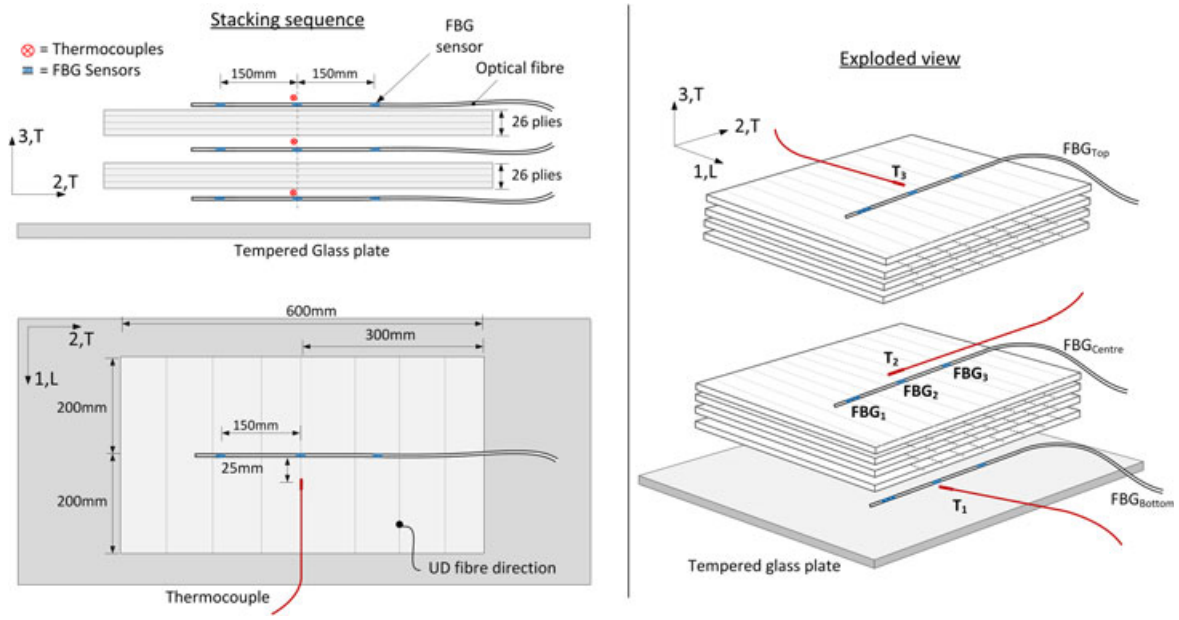

Figure 1. Experimental setup showing the laminate plate ply stacking sequence and sensor placement orientation.

plate was switched off, and free cooling was commenced. During the entire process, data were logged from the FBG sensors at the laminate mid-plane (FBG_{Centre}, see Figure 1) as well as all three thermocouples by using an I-MON E Interrogator (provided by Ibsen Photonics) and a digital thermometer, respectively.

Wavelength measurements from all three optical fibres (bottom, centre and top plane) were performed at specific intervals: (i) after vacuum bagging, (ii) prior applying vacuum at the outlet, (iii) after infusion and cooling and (iv) after demoulding. From this, information revealing the strain evolution at critical discrete times throughout the manufacturing process was measured in the thick laminate plate.

4. EXPERIMENTAL RESULTS

4.1. Temperature measurements

Figure 2 shows the measured temperatures during the vacuum infusion process, logged by the embedded thermocouples (T_1, T_2, T_3). Also shown are the room and heat plate surface temperatures (T_4 and T_5). As infusion is commenced, the

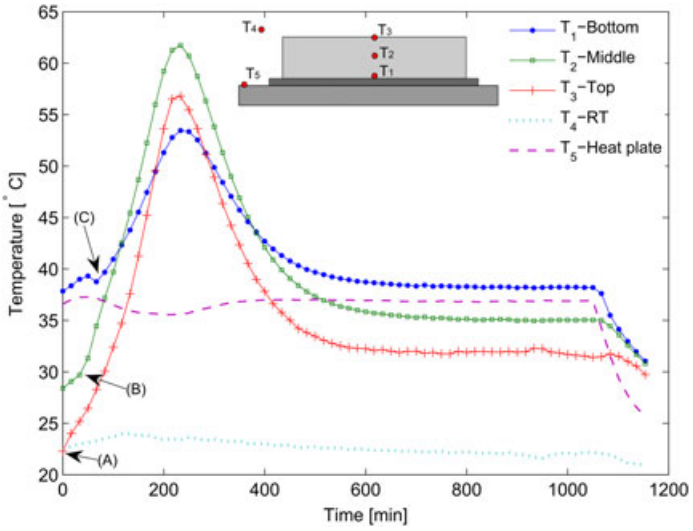

Figure 2. Thermocouple temperature data measured during vacuum infusion of laminate plate.

bottom temperatures at the laminate plate bottom (T_1) are highest because of pre-heating of the dry laminate, whereas the top of the laminate plate has the lowest temperature (T_3) because of free convection to the surroundings. Also visible in Figure 2 is the change in curve gradients at points (A), (B) and (C) as the resin flow front reaches the thermocouples. The larger decrease in temperature at point (C) indicates that the resin temperature is lower than the preheated preform temperature at the tool/part interface at this instant, yet higher than the temperature at the mid and top plane, i.e. between 30°C and 38°C. The highly porous distribution net used allows a top-down flow front as the resin flows over the laminate plate and is pulled down through the ply stack. After points (A), (B) and (C), an increase in temperature is experienced as a result of the exothermic reaction during cross-linking taking place. After the exothermic reaction peaks, the laminate plate cools, and a steady-state temperature is upheld. Finally, after approximately 1050 min, the heat plate is turned off, and the laminate plate cools by natural convection. From Figure 2, it can also be deduced that an inside-out curing is experienced as the exothermic reaction induces the highest temperatures at the centre of the laminate thickness. This is also experienced for thick thermoset matrix composites in the work of Bogetti and Gillespie.[2] The highest temperatures are experienced at the centre (T_2) because of the high heat generation rate compared with the composite's poor thermal conductivity—i.e. more heat is generated than the material can conduct away.

It should be noted that the temperature measurements were stopped before the part fully cooled, after approximately 1150 min. A linear extrapolation of the temperature to room temperature was therefore done resulting in a total process time of approximately 1316 min. The temperatures measured by the thermocouples are used subsequently to account for the thermal strains in equation (3) when calculating the total strains.

4.2. *In situ* total transverse strain variation

The *in situ* total laminate transverse strain variation $\Delta\varepsilon_{tot}$ during infusion at the laminate mid-plane is seen in Figure 3. Note that the temperature at the middle plane (T_2 in Figure 2) is used to calculate the thermal strains, hereby assuming that the temperatures at the vicinity of FBG_1 and FBG_3 are similar to the temperature at FBG_2. The total transverse strain variation in Figure 3 from the time infusion is commenced following well the temperature history presented in Figure 2, with slight discontinuities mainly at the beginning. The initial 200 min of the strain measurements in Figure 3 is shown in Figure 4.

The negative strain variation in Figure 4, at the beginning of infusion, is due to the compressive stress state that the laminate layup is in, imposed by the vacuum pressure prior infusion. In Figure 4, one can see the instances when the resin flow front reaches the FBG sensors, marked by the sudden discontinuities in the strain curves after approximately 16, 24 and 34 min for FBG_1–FBG_3, respectively. As the flow front approaches each FBG sensor, the resin flow and the existing constraints on the optical fibres from the surrounding reinforcement fibres result in compressive strains. After the flow front passes the FBG sensor, the strains change to tensile strains, which may be a result of the pulling forces emitted by the flowing resin under pressure. After approximately 55 min, the resin flow front reaches the outlet hose, marked in Figure 4 by the sudden decrease in strain measurements as flow is drastically reduced. Finally, after approximately 65 min, the vacuum pressure is reduced to 60%. Up to this point in time, variations in strain measurements have mainly been due to the resin flow. After this, temperature and resin chemical shrinkage effects primarily govern the changes measured.

A sudden jump in measured strains is observed in Figure 4 after approximately 165 min. This jump may be due to the realignment or settling of the optical fibre, or the UD reinforcement fibre in the layup, caused by a sudden stress release or spring back. Note that the resin is still in liquid/rubbery state at this point, which means that the main mechanical constraints on the optical

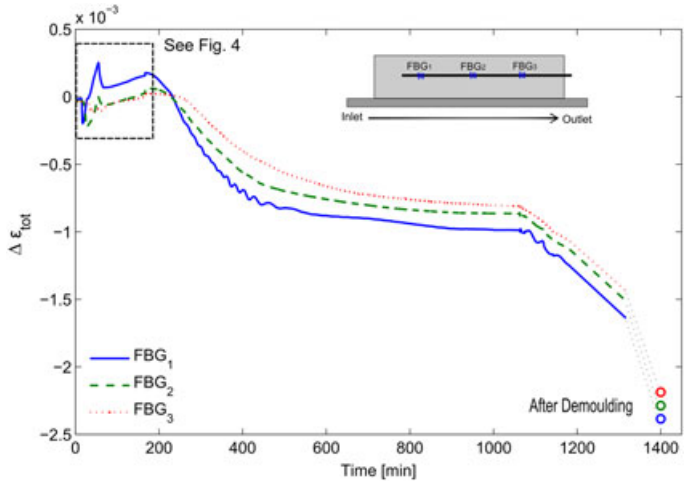

Figure 3. Variation in process-induced total transverse strains at the laminate mid-plane during infusion.

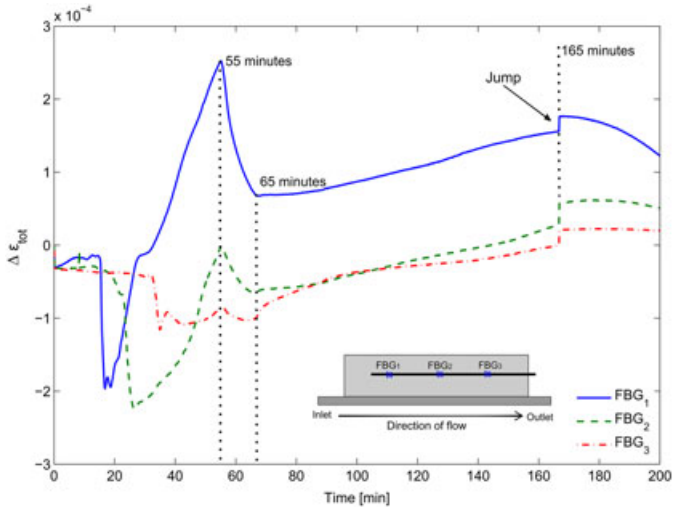

Figure 4. Initial 200 min of process-induced total transverse strains shown in Figure 3.

fibre exist from the ply stack and vacuum pressure. In other literature, where jump discontinuities are found in experimental process strain measurements (see e.g. Hahn[3]), the measured data are simply shifted vertically to cancel out any uncertainties due to similar sudden effects. This approach is omitted here, but instead it is noted that a potential error margin of +0.20 to 0.29×10^{-4} (equal to the magnitude of the jump) in the final transverse strain measurements exists. Hence, perfect strain transfer between the optical fibre and the resin or reinforcement fibres does not exist yet, whereas interpretation of any phenomena seen should be done with caution. Also seen in Figure 3 are the fluctuations that arise during cooling, most pronounced at FBG_1. During the final cool-down stage, the matrix is assumed to be fully cured. The fluctuations observed may be a result of high shear stresses formed at the glass plate/composite interface causing separation or a stick–slip effect. This is further underlined by the crackling sounds heard during cool down. Similar phenomena are experienced by Khoun *et al.*[15] and de Oliviera *et al.*[18]

Finally, the total transverse strain after demoulding was measured from all three optical fibres (FBG_{Bottom} , FBG_{Centre} and FBG_{Top} in Figure 1) . The results are given in Table I. The measured final process-induced residual strains are all compressive and largest at the top plane and smallest at the bottom plane where the plate has been constrained by the glass tool. Furthermore, the final strains are largest at each measured plane towards the infusion inlet at FBG_1. The FBG strain measurement results show that differences exist in measurements along the same line, between the same plies. It is however not certain whether these differences singularly originate from the non-symmetric loading present during infusion where resin flow and pressure changes within the vacuum bag between the inlet and outlet exist.

4.3. Thermal expansion

The thermal expansion of the laminate plate was analysed during the cooling phase of the infusion process. If we assume that the resin is fully cured *towards the end* of the infusion process, which is confirmed later in this work, then it can be stated that no more chemical shrinkage takes place. If this is correct, then any changes in the measured total strain $\Delta\varepsilon_{tot}$ would solely be due to changes in the host material thermal strain, $\Delta\varepsilon_{th}^{host}$. Hence, where the variations in total strains in equation (3) are primarily driven by mechanical straining of the optical fibre at the *beginning* of infusion (e.g. from movement of the reinforcement fibres or due to resin flow), changes to the total strain *towards the end* of infusion are driven primarily by thermal loads. This is because the resin is in liquid state initially and therefore cannot sustain any stresses. Contrary to this, the resin is in glassy state after curing and is essentially a solid. Assuming perfect bonding of the optical fibre to the laminate when fully cured, and knowing both the temperature change during cooling and the total strain variation, equation (3) can be rearranged to determine the host material thermal expansion as

Table I. Final total transverse strains measured in the laminate plate after demoulding.

		FBG_{Top}	FBG_{Centre}	FBG_{Bottom}
$\Delta\varepsilon_{tot}$	FBG_1	−3.149E−3	−2.385E−3	−1.145E−3
	FBG_2	−2.847E−3	−2.287E−3	−0.791E−3
	FBG_3	−3.019E−3	−2.187E−3	−0.117E−3

$$\Delta\varepsilon_{\text{tot}} = \Delta\varepsilon_{\text{th}}^{\text{host}} = \alpha_{\text{T}}^{\text{host}}\Delta T = \left[\left(\frac{\Delta\lambda_{\text{B}}}{\lambda_{\text{B}}^{0}}\right) - K_{\text{T}}\Delta T\right]\frac{1}{K_{\epsilon}} \tag{4}$$

Hence,

$$\alpha_{\text{T}}^{\text{host}} = \left[\left(\frac{\Delta\lambda_{\text{B}}}{\lambda_{\text{B}}^{0}}\right) - K_{\text{T}}\Delta T\right]\frac{1}{K_{\epsilon}\cdot\Delta T} \tag{5}$$

where $\alpha_{\text{T}}^{\text{host}}$ is more specifically the effective laminate *transverse* thermal expansion coefficient. This coefficient may be calculated using the well-known self-consistent field model approach (see e.g. Bogetti and Gillespie[2] and Whitney and McCullough[22]) for a UD continuous fibre reinforced composite if CTE parameters for both constituents were known *a priori*.

During cooling (i.e. between approximately 1100 and 1300 min in Figure 3), a wavelength change of -0.292 nm and a corresponding temperature change of -4.51°C is measured at FBG_2. Using equation (5), we found the host material effective transverse CTE to be $46.07 \times 10^{-6}\,^{\circ}\text{C}^{-1}$. Using the self-consistent field model, one can find that the effective transverse thermal expansion coefficient is

$$\alpha_{\text{T}}^{\text{host}} = (\alpha_{2\text{f}} + v_{12\text{f}}\,\alpha_{1\text{f}})V_{\text{f}} + (\alpha_{\text{m}} + v_{\text{m}}\,\alpha_{\text{m}})(1 - V_{\text{f}}) - [v_{12\text{f}}V_{\text{f}} + v_{\text{m}}(1 - V_{\text{f}})]\left[\frac{\alpha_{1\text{f}}E_{1\text{f}}V_{\text{f}} + \alpha_{\text{m}}E_{\text{m}}(1 - V_{\text{f}})}{E_{1\text{f}}V_{\text{f}} + E_{\text{m}}(1 - V_{\text{f}})}\right] \tag{6}$$

where E, α and v are the respective constituent modulus, CTE and Poisson's ratio, respectively, and V_{f} is the reinforcement fibre volume fraction. The subscripts f and m denote fibre and matrix specific quantities. Knowing $\alpha_{\text{T}}^{\text{host}}$ from equation (5) and using the constituent material properties summarized in Table II, the resin CTE is isolated in equation (6) and calculated to be equal to $65.41 \times 10^{-6}\,^{\circ}\text{C}^{-1}$. Returning to the assumption that the resin in the laminate plate is fully cured (or at least vitrified), this CTE value corresponds to the resin glassy CTE and resembles coefficients used elsewhere for thermoset infusion epoxies well.[2,4,23]

5. NUMERICAL MODELS

Two different numerical models are used to model the infusion process; a 1D implicit finite volume (FV) thermal model programmed in MATLAB (MathWorks Inc., Natick, Massachusetts, U.S.A) and a 3D thermomechanical CHILE model implemented in the commercial finite element software ABAQUS (Dassault Systèmes, Vélizy-Villacoublay, France).

5.1. 1D thermal model

The 1D model is used mainly to validate the resin thermal behaviour and cure kinetics model used. A 1D model offers a quick and simple platform for this purpose and is justified by the relatively small thickness of the laminate plate and the relatively large heat flow through the thickness. In the 1D model, Fourier's heat conduction equation with a heat source term, reduced to one dimension, is solved:

$$\rho c_{\text{p}}\frac{\partial T}{\partial t} = k_z\left(\frac{\partial^2 T}{\partial z^2}\right) + \dot{q} \tag{7}$$

for $T(z, t)$ in $0 < z < h$ the laminate thickness ($h = 52$ mm), and where k_z, ρ and c_p are the effective composite through-thickness thermal conductivity, density and specific heat capacity, respectively. $\dot{q}$ is the heat source term, which in this case represents the exothermic heat generation rate during resin polymerization. The model is discretized spatially in a FV framework with a backward Euler finite difference time discretization; see e.g. Hattel[24] for details. The resulting equation system is solved implicitly in each time step with Dirichlet boundary conditions (BCs) at the laminate surface boundaries,

Table II. Mechanical properties for E-glass fibre and RIMR 135 resin.

Volume fraction $V_{\text{f}} = 50\%$	Young's modulus (GPa)	Poisson's ratio	CTE ($\times 10^{-6}\,^{\circ}\text{C}^{-1}$)
Glass fibre	$E_{1\text{f}} = 73.0$	$v_{12\text{f}} = 0.22$	$\alpha_{1\text{f}} = \alpha_{2\text{f}} = 5.04$
Epoxy resin (glassy state)	$E_{\text{m}} = 2.9$	$v_{\text{m}} = 0.38$[a]	$\alpha_{\text{m}} = 65.41$[b]

[a]Referred to as the fully cured Poisson's ratio later in this work.
[b]Calculated from measurements.

respectively. This essentially omits the need to model the vacuum bag and tool with precise heat transfer coefficients, which can be cumbersome to determine. More discussion on the model structure is found in Nielsen *et al.*[25] The experimentally measured temperatures at the laminate surfaces (e.g. T_1 and T_3 in Figure 2) were used as prescribed boundary temperatures in the 1D model. Knowing the thermal BCs, the cure kinetic behaviour of the matrix material could be approximated by comparing predicted temperatures with the experimentally measured temperature at the laminate centre (e.g. T_2 in Figure 2). It is assumed here that the preform is totally saturated at the beginning of the simulations.

The resin degree of cure $\alpha(t)$ is expressed as the ratio of the cumulative mass specific heat, $H(t)$, liberated from the chemical reaction, to the total heat of the reaction H_r during curing. This is expressed as

$$\alpha(t) = \frac{H(t)}{H_r} \tag{8}$$

The heat liberated at any point in time t is expressed in integral form as

$$H(t) = \int_0^t \frac{1}{\rho}\left(\frac{dq}{dt}\right)dt \tag{9}$$

where dq/dt is the volume specific rate of heat generation (or $\dot{q}$) from the cure reaction. Using equations (8) and (9), the heat generation rate in equation (7) is expressed as a function of the cure rate:

$$\dot{q} = \frac{d\alpha}{dt}\rho H_r(1 - Vf) \tag{10}$$

where V is the fibre volume fraction. In this work, the cure rate of the epoxy resin is expressed using the Kamal and Sourour kinetic model[26]:

$$\frac{d\alpha}{dt} = (k_1 + k_2\alpha^m)(1 - \alpha)^n \tag{11}$$

With

$$k_i = A_{ci}\exp\left(-\frac{Ea_i}{R_b T}\right), \qquad \text{for } i = 1, 2 \tag{12}$$

where m and n are exponents ($m+n=2$), A_{ci} is the pre-exponential coefficient, Ea_i is the activation energy and R_b is the universal gas constant. The RIMR 135 epoxy thermal and cure kinetic parameters used in the model are given in Table III. The values used in equations (11) and (12) are taken from Cai *et al.*,[31] except the resin heat of reaction H_r and activation energy Ea_i, which are modified as the original values, for the given kinetic model, which resulted in drastically different cure temperatures. Using the 1D thermal model, with prescribed boundary temperatures, we employed numerical curve fitting until good laminate mid-thickness temperatures were determined. To validate the modified parameters, we compared temperature measurements from an E-glass/epoxy laminate plate consisting of only 40 plies with predictions from the 1D model with good results. A similar approach is used by Svanberg.[32]

5.2. 3D CHILE thermomechanical model

The development of internal strains during the vacuum infusion process was investigated numerically using a sequentially coupled thermal–mechanical 3D CHILE model, coined by Johnston.[3] The CHILE approach in composite process

Table III. RIMR 135 epoxy resin thermal and cure kinetic material properties.

	Notation								
	c_p [J (W K)$^{-1}$]	k_z [W (m K)$^{-1}$]	A_{c1} (s^{-1})	A_{c2} (s^{-1})	E_{a1} (kJ mol^{-1})	E_{a2} (kJ mol^{-1})	H_r (kJ kg^{-1})	m	n
Value	1240	0.24	3.89E−6	2.24E−3	16.28	11.08	85.8	0.78	1.12

Parameters are taken from Cai *et al.*[31] for the same resin, except E_{a1}, E_{a2} and H_r.

modelling has gained acceptance as a fast and fairly accurate approach, as opposed to more cumbersome VE approaches. Although being the *gold standard* regarding accuracy, VE models have the disadvantage of requiring extensive resin characterization *a priori* as well as being computationally heavy. Discussions concerning both CHILE and VE approaches, their pros and cons, material characterization requirements and so on, can be found in some studies.[3,23,27]

A sequentially coupled thermomechanical analysis was performed. In the thermal step, the temperature, cure degree evolution and volumetric heat generation were calculated. In the mechanical step, chemical shrinkage, thermal expansion and the instantaneous laminate mechanical property evolution were calculated using results from the thermal step. Finally, a separate mechanical step is conducted by modelling the removal of all tooling constraints, representing demoulding, effectively yielding the final equilibrium part shape. A short summary of the mechanics involved in the CHILE approach is given henceforth.

Throughout the infusion process, it is assumed that the reinforcement fibre material properties remain constant. The cure-dependent and temperature-dependent resin modulus evolution was modelled as[3]

$$E_{\mathrm{m}} = \begin{cases} E_{\mathrm{m}}^{0} & T^{*} < T_{\mathrm{C1}} \\ E_{\mathrm{m}}^{0} + \dfrac{T^{*} - T_{\mathrm{C1}}}{\left(T_{\mathrm{C2}}^{*} - T_{\mathrm{C1}}\right)}\left(E_{\mathrm{m}}^{\infty} - E_{\mathrm{m}}^{0}\right) & T_{\mathrm{C1}} \leq T^{*} \leq T_{\mathrm{C2}} \\ E_{\mathrm{m}}^{\infty} & T^{*} > T_{\mathrm{C2}} \end{cases} \tag{13}$$

where

$$T^{*} = \left(T_{\mathrm{g}}^{0} + a_{\mathrm{Tg}} * \alpha\right) - T \tag{14}$$

In the preceding equations, $E_{\mathrm{m}}^{\mathrm{o}}$ and E_{m}^{∞} are the fully uncured (rubbery) and fully cured (glassy) resin modulus, respectively. The critical temperatures T_{C1} and T_{C2} mark the bounds determining the linear variation of the modulus with T^{*}, which is cure degree dependent. The coefficients used in equations (13) and (14) are fit to the temperature-dependent elastic response provided by the resin supplier.[28] The cure-dependent and temperature-dependent resin modulus overlaid the elastic response provided by the resin supplier, as shown in Figure 5. Material properties used are found in Table IV. Knowing the instantaneous resin modulus, we calculated the instantaneous Poisson's ratio as follows[3]:

$$\nu_{\mathrm{m}} = \frac{E_{\mathrm{m}}^{\infty} - E_{\mathrm{m}}\left(1 - 2\nu_{\mathrm{m}}^{\infty}\right)}{2E_{\mathrm{m}}^{\infty}} \tag{15}$$

where $\nu_{\mathrm{m}}^{\infty}$ is the fully cured (glassy) resin Poisson's ratio (Table II).

The self-consistent field model micromechanics approach for a UD continuous fibre reinforced composite was used to calculate effective laminate thermal expansion and chemical shrinkage coefficients. Starting with the thermal expansion, for a thermoset resin, the resin CTE in rubbery state is known to be approximately 2.5 times larger than the CTE in glassy state.[4]

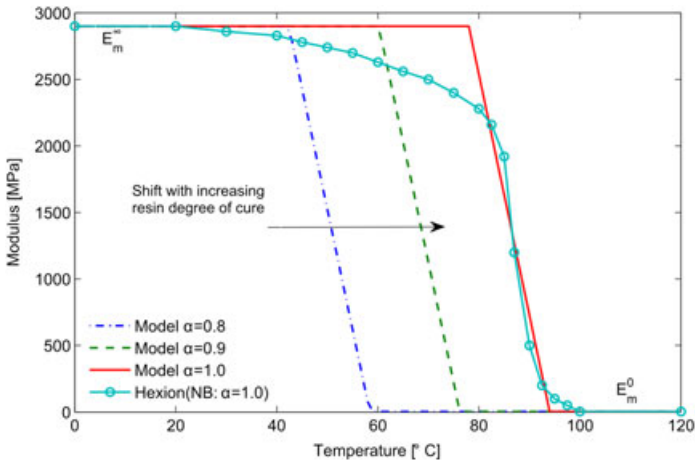

Figure 5. Fully cured resin elastic response (Hexion RIMR 135 epoxy) compared with cure-dependent and temperature-dependent resin modulus model given in equations (13) and (14).

Table IV. RIMR 135 epoxy resin mechanical material properties used in equations (13)–(14) and (17)–(18).

	Notation									
Unit	E_m^{∞} (GPa)	E_m^0 (GPa)	T_{C1} (°C)	T_{C2} (°C)	T_g^0 (°C)	a_{Tg} (°C)	A	$V_m^{Sh\infty}$ (%)	α_{C1}	α_{C2}
Value	2.9	0.0029	84.0	100.4	0.0	178.0	0.173	7[a]	0.055	0.651

[a]Assumed value for infusion epoxy resin.[4,6,23]

Contrary to CHILE-type approaches elsewhere,[3,15,17] cure-dependent resin thermal expansion is in this work implemented, as a first approximation, using a rules-of-mixture approach, on the basis of the different resin CTEs found experimentally:

$$CTE_m = \alpha \cdot CTE_m^{glassy} + (1-\alpha) CTE_m^{rubbery} \tag{16}$$

where CTE_m is the instantaneous resin thermal expansion coefficient and CTE_m^{glassy} and $CTE_m^{rubbery}$ are the resin glassy and rubbery thermal expansion coefficients, respectively.

Lastly, the resin chemical shrinkage is generally known to be cure dependent in the sense that most shrinkage strains are developed relatively early in the cure process.[3,23,29,30] In this work, the model proposed by Johnston[3] is used. The volumetric resin shrinkage V_m^{Sh} is determined as

$$V_m^{Sh} = \begin{cases} 0.0 & \alpha < \alpha_{C1} \\ A \cdot \alpha_s + \left(V_M^{Sh\infty} - A\right)\alpha_s^2 & \alpha_{C1} \le \alpha \le \alpha_{C2} \\ V_m^{Sh\infty} & \alpha \ge \alpha_{C2} \end{cases} \tag{17}$$

where

$$\alpha_s = \frac{\alpha - \alpha_{C1}}{\alpha_{C2} - \alpha_{C1}} \tag{18}$$

In equations (17) and (18), α_{C1} and α_{C2} are the critical cure degrees marking the bounds of shrinkage during curing, A is a factor accounting for the non-linear cure degree dependent shrinkage and $V_m^{Sh\infty}$ is the total resin volumetric cure shrinkage (here equal to 7%). The linear resin shrinkage strain was then found as $\varepsilon_r^{sh} = \sqrt[3]{1 + V_m^{Sh}} - 1$.

The resin instantaneous properties summarized earlier are updated in the model in each time increment. Throughout the process, the reinforcement fibre properties are assumed to remain constant. The effective laminate properties are then calculated using the self-consistent field micromechanics approach.

5.2.1. Thermal BCs

In the thermal step, temperature BCs on the top and bottom surfaces of the laminate plate are prescribed, corresponding to the temperature measurements experimentally determined (T_1 and T_3 in Figure 2). Hence, it is assumed that any variation in temperature in real life between the infusion inlet and outlet hose is negligible. This assumption is similarly justified by the relatively large heat flow through the plate thickness direction primarily driven by the heat plate and resin exothermic reaction. The reader should note that we are mainly interested in comparing numerically predicted and experimentally determined *in situ* total transverse strains at the laminate centre mid-plane.

5.2.2. Mechanical BCs

Three different mechanical BCs are employed: (i) free standing, (ii) fixed at the tool/part interface and (iii) tied contact condition at the tool/part interface (Figure 6). The first two cases represent the bounds of what can physically exist mechanically. In the case of the *tied* contact conditions, we wish to predict the laminate response, assuming the only allowable deformation present at the tool/part interface is driven by the tool thermal expansion. In order to do this, the tempered glass plate, on which the laminate is moulded, is modelled. In this way, a middle-ground condition between the *free* and *fixed* conditions can be analysed. In all models, only half of the laminate plate is modelled, assuming symmetry conditions on the 2–3 plane (or T–T plane). Finally, for the *fixed* and *tied* models, demoulding was simulated, conducted by suppressing any mechanical constrains and removing the glass tool part, respectively.

A total of $15 \times 5 \times 7$ linear brick elements are used for the laminate plate and $15 \times 5 \times 1$ elements for the 10 mm thick tempered glass plate considered in mechanical BC (3). 8-node linear heat transfer brick (DC3D8) and 8-node linear brick (C3D8) elements are used in thermal and mechanical analyses, respectively. A mesh sensitivity analysis using a model with a finer mesh by a factor of 4 in each direction (i.e. $60 \times 60 \times 28$ elements) revealed no significant change in strain measurements

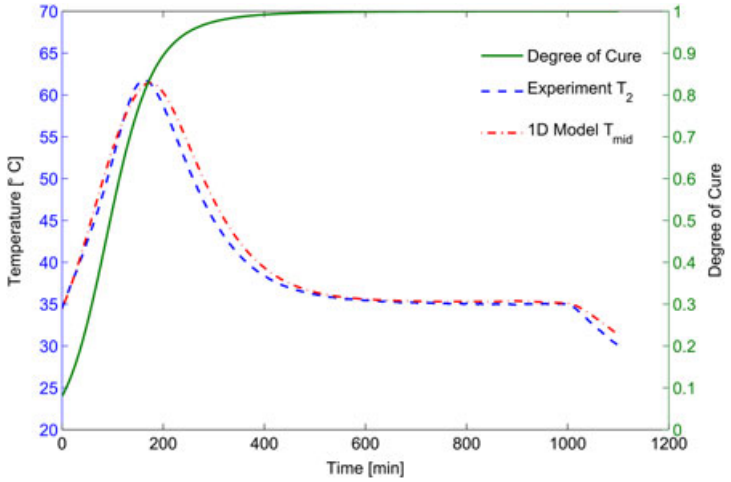

Figure 6. Experimental mid-thickness temperature (T_2) and predicted 1D model temperature. Also seen is the cure degree evolution at the middle corresponding to the temperature prediction.

at the laminate mid-thickness centre region. Some mechanical BC-related stress singularities were reduced using the finer mesh, but no significant difference in mid-plane strains was seen. Hence, the coarse mesh was used. The computational times for the thermal and mechanical steps using a max allowable time step size of 10 s are presented in Table V. For the sake of comparison, the finer mesh mechanical (fixed BC) model took 37,827 s (approximately 360 min) to calculate.

6. RESULTS AND DISCUSSION

6.1. 1D model temperature and cure degree

The 1D thermal model temperature prediction is compared with the experimentally determined mid-plane temperature, T_2, in Figure 7 using the resin cure kinetic parameters determined earlier. Also shown is the predicted cure degree at the laminate plate mid-plane. It should be noted that the initial 50 min of the measured temperature history, where resin flow is still taking place, was disregarded—i.e. the simulation is started where it is assumed that the preform is totally saturated. The initial cure degree was assumed to be equal to 0.08. A mesh sensitivity analysis showed that only a temperature variation of 0.76°C of the maximum mid-plane exothermic peak temperature was obtained when using between 10 and 52 control volumes (CVs), with the latter coinciding with one CV per ply. Hence, 10 CVs are used, having a total calculation time of only 23.78 s using a constant time step size of 1 s. In relation, the corresponding 52 CV model with the same time step takes 59.18 s.

The thermal material properties validated using the 1D thermal model (Table III) are used henceforth in the 3D thermomechanical model. From the model, it is predicted that the laminate fully cures at the mid-plane after approximately 500 min (Figure 7).

6.2. 3D model total transverse strain predictions

The final total transverse residual strain distribution for the different mechanical BC cases analysed is seen in Figure 8. Note that the results shown are prior demoulding. For the free standing case (Figure 8(a)), the maximum compressive transverse strains are predicted to be approximately 5.15×10^{-3}, compared with only 3.70×10^{-3} and 4.38×10^{-3} for the fixed (b) and tied (c) BC

Table V. 3D model calculation times for thermal and mechanical steps.

	Thermal		Mechanical		
		Incl. glass plate	Free	Fixed	Tied (incl. glass plate)
Calculation time (s)	106.20	151.40	320.90	303.03	284.57

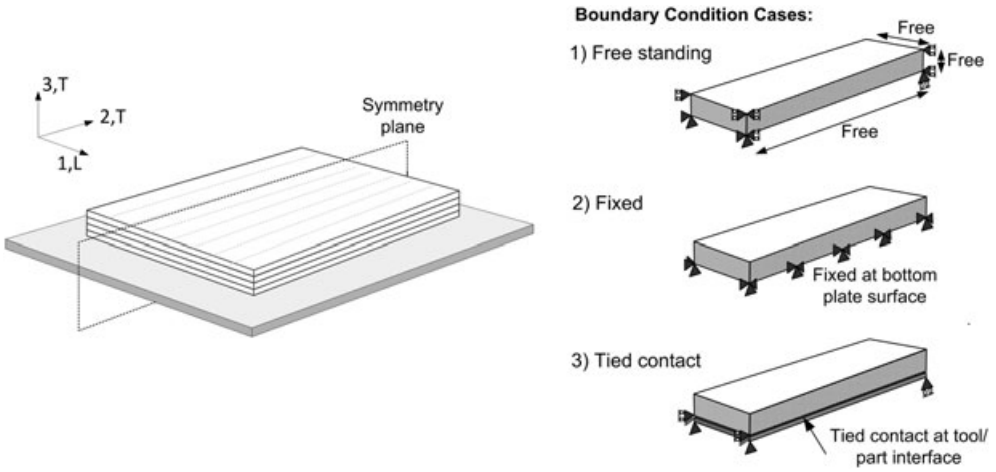

Figure 7. Different mechanical boundary conditions employed in the 3D thermomechanical process simulations.

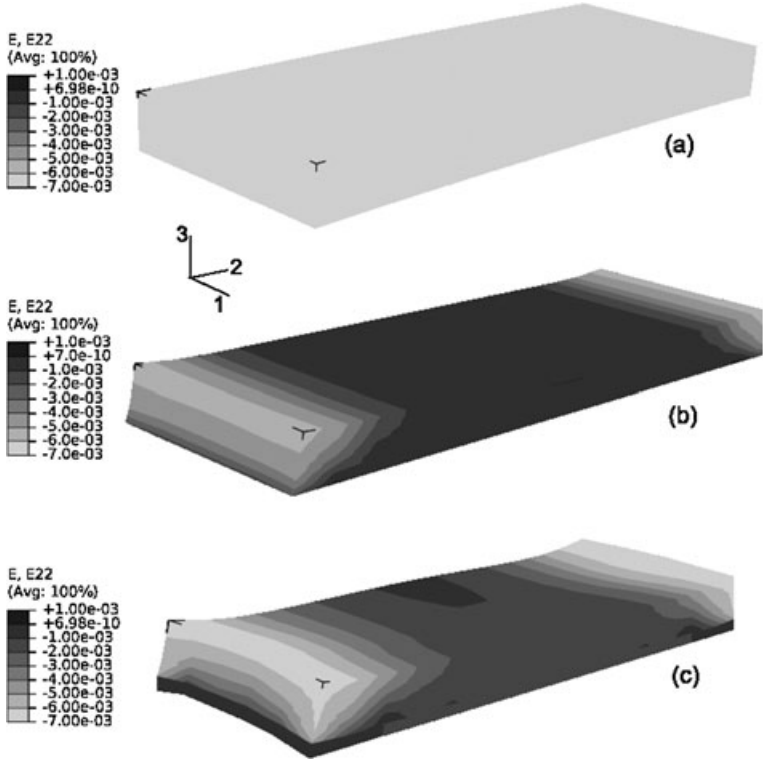

Figure 8. Total transverse strain distribution for (a) free standing BC, (b) fixed BC and (C) tied mechanical boundary condition cases prior demoulding. Note that a deformation scale factor of 20 is used.

cases, respectively. For the fixed and tied cases, the largest deformations take place at the top surface edges, in an inwards direction, mainly driven by the chemical shrinkage. As expected, the largest strains are predicted for the model with the least stringent constraints (i.e. Figure 8(a)).

The predicted *in situ* total transverse strains at the laminate centre are compared with the experimentally determined strain (FBG_2) at the laminate mid-plane. Results for the different BCs (free, fixed and tied) are shown in Figure 9. For the *free* standing case, the final transverse compressive strain is an order of approximately 2.8 larger than experimentally measured (-3.741×10^{-4} and -1.512×10^{-3}). Initially disregarding demoulding, for the *fixed* BC case, the final compressive strain is only 1.583×10^{-6}, which is significantly smaller than the experimental results. Finally, in the case of the *tied* BC, a good approximation to the experimentally measured strains was obtained. In the tied case, the influence of the tempered glass plate

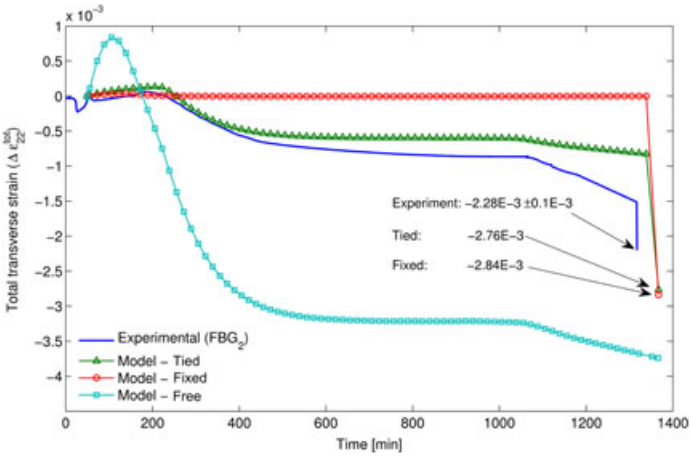

Figure 9. Comparison of experimental and predicted *in situ* total transverse strains at the laminate mid-plane centre for different mechanical boundary conditions. The final strains after demoulding are also seen and values compared.

is visible upon cooling (between approximately 1050–1300 min) where a smaller gradient on the strain curve ('Model–Tied') is predicted compared with the experimental results. This is due to the lower CTE of the tempered glass plate ($9.0 \times 10^{-6}\,^{\circ}C^{-1}$) as compared with the transverse CTE of the laminate plate in the glassy state ($46.07 \times 10^{-6}\,^{\circ}C^{-1}$). The differences in cool-down strain gradients between the model and experiment may also be due to the phenomena occurring at tool/part interface, as previously discussed in this work. In Figure 9, one can also observe the non-constant curve gradient of the experimental results (FBG_2) between approximately 500 and 1050 min, as compared with the model predictions. From the 1D model, it was predicted that the resin is fully cured after approximately 500 min into the infusion process (Figure 6). The curvature observed from the experimental measurements is therefore not caused by residual chemical shrinkage, as the cross-links are fully developed. Hence, the increase in transverse compressive strains during the constant temperature hold is due to VE creep behaviour of the composite. This is a shortcoming of the CHILE model.

When considering the released transverse strains from the demoulding simulations, predictions for the *fixed* and *tied* cases are seen in Figure 9. When comparing the predicted residual strains with the experimentally determined strains at the mid-plane, presented in Table I, the measured value (-2.287×10^{-3}) is smaller in magnitude than the *fixed* and *tied* case predictions, respectively (-2.837×10^{-3} and -2.762×10^{-3}). Essentially, all cases experience the same internal constraints governed by temperature and cure degree gradients; hence, any differences in strains can only be a result of differences in external constraints and the stresses these constraints would induce. As mentioned earlier, a potential error margin of $+0.20 \times 10^{-4}$ to 0.29×10^{-4} in the final transverse strain measurements might exist because of the jump discontinuities observed during the infusion experiment after approximately 165 min.

A better understanding, of why the differences in predicted strains are obtained after demoulding, is achieved by analysing the corresponding transverse stress state through the laminate thickness. The stress distribution, for the fixed and tied cases, before and after the demoulding simulation, is seen in Figure 10. For the fixed BC case, an almost uniform stress distribution through the laminate thickness exists prior demoulding. These stresses are then almost entirely released after demoulding, resulting in the large increase in compressive strains seen in Figure 9. When considering the stresses for the *tied* BC case in Figure 10, the tensile stresses (approximately 14–16 MPa) are smaller in magnitude than in the fixed case and vary through thickness. The tensile stresses are smaller because of the equilibrium stress state between the laminate and the tempered glass plate, which is able to sustain some of the process-induced stresses. Once demoulding occurs, these stresses are released back into the laminate, albeit they are smaller because of the less stringent BCs. However, both the *fixed* and *tied* cases result in an overestimation of the compressive residual strains when compared with the experimental measured values. This overestimation may indicate the inadequacy of the CHILE approach in capturing the VE behaviour, for instance the stress relaxation, which may occur when the laminate is mechanically constrained at elevated temperatures.

7. PARAMETRIC STUDY

A parameter study was carried out using the 3D thermomechanical model to investigate the effect of increasing the laminate plate thickness on the predicted total transverse strains. Three different laminate thicknesses are considered: 52, 100 and 150 mm. These thicknesses represent what is found in commercial wind turbine blade laminate sections. Apart from an increase in thickness, no other changes were done to the laminate plate or the model thermal and mechanical BCs. In Figure 11, the

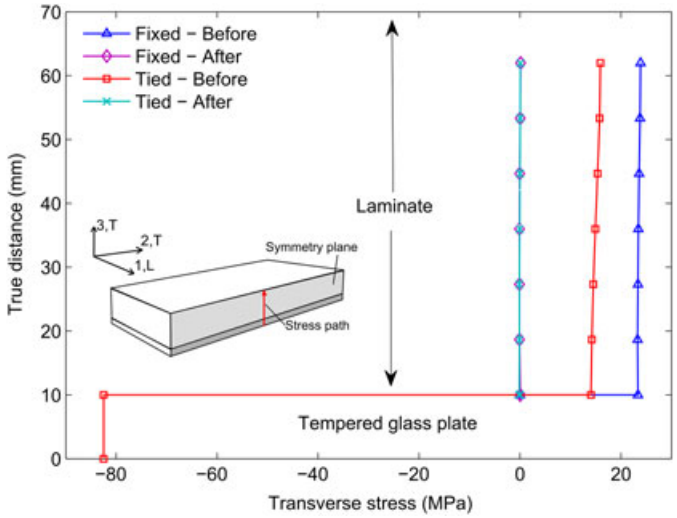

Figure 10. Through-thickness laminate transverse stresses before and after demoulding for fixed and tied boundary condition cases.

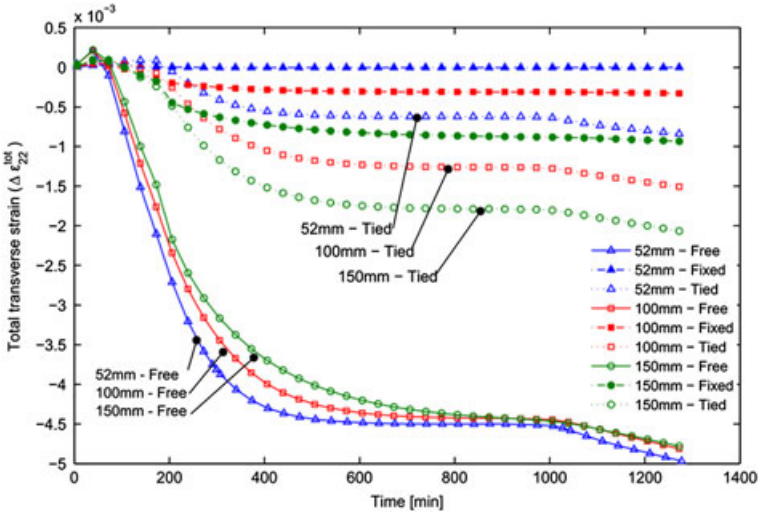

Figure 11. Total transverse strains as a function of laminate thickness for different mechanical boundaries. The arrows shown represent the tendencies in results for the different BCs used when increasing the laminate thickness.

process-induced total transverse strain for the different laminate thicknesses is seen, using the different mechanical BCs employed earlier. For the fixed and tied BC cases, an increase in laminate thickness results in a corresponding increase in the total transverse strains. This is expected, as the larger the thickness, the larger the distance of the laminate mid-plane from the tool/part interface where the BCs are enforced. On the contrary, for the results using the free BC, an increase in thickness results in a decrease in total transverse strains, albeit the difference in results is small.

Predictions of the through-thickness stresses at the laminate centre for the tied BC case are found in Figure 12. Note that demoulding is not considered here. The tensile stresses in the laminate decrease with an increase in thickness because the tempered glass plate sustains compressive stresses in order to uphold an equilibrium stress state. Hence, the ability of the tool to sustain the process-induced stresses mirrors the deformations experienced by the part.

An evaluation of the influence of composite moulds on internal strains and residual stresses is also done. A glass/epoxy mould is analysed, which would correspond to mould materials used in the wind turbine industry for large structures. In the study, three mould layup configurations are analysed: $[0,90]_s$, $[0]_4$ and $[90]_4$. In all cases, a 10 mm thick tool plate is used, and a tied-type mechanical BC at the tool/part interface is prescribed. Model predictions for the transverse in situ strains are seen in Figure 13 where, for all composite tool layup cases, higher compressive strains are achieved at the laminate plate centre when compared with the tempered glass plate tool used in the experiments. This is mainly due to the lower composite tool stiffness

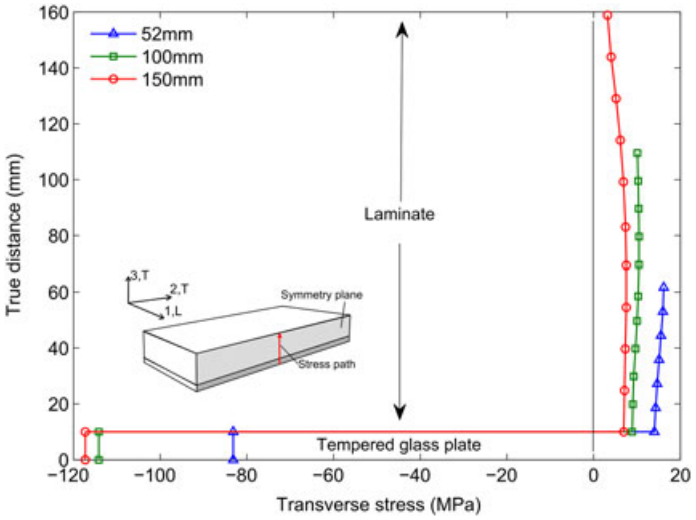

Figure 12. Through-thickness laminate transverse stresses before demoulding using tied boundary condition for different thicknesses.

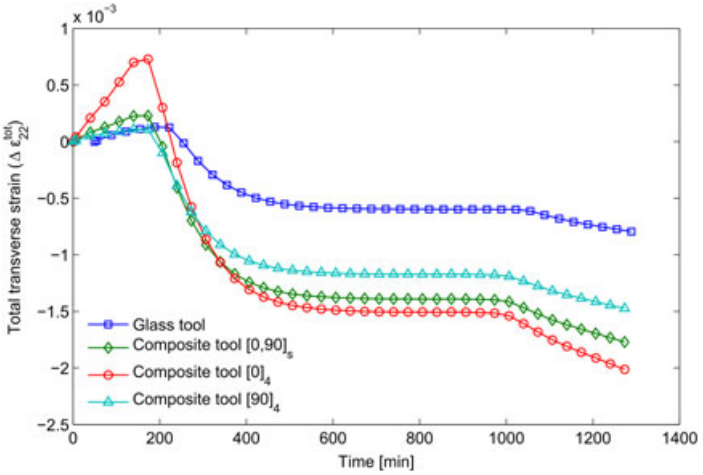

Figure 13. Total transverse strains during curing using different composite tool configurations, compared with predictions using a tempered glass plate.

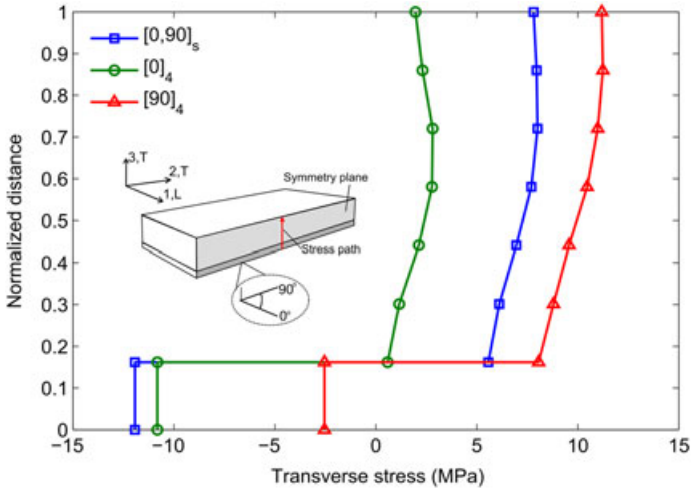

Figure 14. Through-thickness laminate transverse stresses after curing using different composite tool configurations.

and higher thermal expansion as compared with the glass tool (e.g. $\alpha_{glass} = 9.0 \times 10^{-6}\,^{\circ}C^{-1}$, $\alpha_{11,comp} = 5.04 \times 10^{-6}\,^{\circ}C^{-1}$, $\alpha_{22,comp} = 4.73 \times 10^{-5}\,^{\circ}C^{-1}$). The influence of the tool stiffness on the final residual stress predictions along a centre-line through-thickness path is seen in Figure 14 for the different composite tool configurations. For comparative purposes, stresses as high as 14–16 MPa are predicted when the tempered glass tool is used (Figure 10). The high tool stiffness in the transverse ('22') direction results in lower internal compressive transverse strains and larger residual stresses. Hence, this may indicate that the use of a more compliant tool can help reduce residual stresses in part at the cost of an increase in process-induced shape distortions.

8. CONCLUSIONS

This paper aimed to assess the accuracy of a CHILE numerical model in modelling the slow curing process-induced transverse strain development of a thick laminate plate—which is essentially a VE boundary value problem. *In situ* experimental measurements during vacuum infusion from embedded fibre optic FBG sensors are used to determine process-induced strains. These strains are compared with the 3D numerical model based on the CHILE approach where different mechanical BCs are employed. Results from the experimental measurements show the thermal expansion and shrinkage effects known to occur during curing of thick glass/epoxy composites. However, some uncertainties may exist in the interpretation of the strain measurements prior gelation, owing to the complex nature of the process in its early stages. In order to distinguish between any experimental FBG sensoring errors and physical phenomena, multiple experiments should be carried out in future where statistical significance can be determined.

The numerical model predictions of the process-induced transverse strains are reasonable when a tied mechanical BC approach at the tool/part interface is used and the tool thermal expansion is taken into account. This indicates that process-induced distortions are largely influenced by the tool thermal expansion behaviour when a tied BC is prescribed. From the experiment, it was observed that the laminate exhibited VE creep behaviour during the constant temperature hold. One of the CHILE model's shortcomings is in predicting time-dependent effects. When considering demoulding, it was shown that the CHILE model overestimates the residual strains when compared with the experimental results. This is also thought to be due to a time-dependent stress relaxation.

Finally, a parameter study concerning the effects on process-induced strains when increasing the laminate plate thickness was investigated. It was shown that external constraints to the model, for instance from the tool/part interaction, play a major role in the outcome of the process-induced strains predicted numerically. Furthermore, the use of tools with greater compliance results in lower residual stresses but at the cost of larger process-induced shape distortions.

ACKNOWLEDGEMENTS

The project is supported by Danish Energy Agency through the Energy Technology Development and Demonstration Program (EUDP). The supported EUDP-project is titled 'Demonstration of new blade design using manufacturing process simulations' and has journal no. 64009-0094. The support is gratefully acknowledged.

REFERENCES

1. Hahn HT. Effects of residual stresses in polymer matrix composites. *The Journal of the Astronautical Sciences* 1984; **32**: 253–267.
2. Bogetti TA, Gillespie JW. Process-induced stress and deformation in thick-section thermoset composite laminates. *Journal of Composite Materials* 1992; **26**: 626–659.
3. Johnston A. An integrated model of the development of process-induced deformation in autoclave processing of composite structures. PhD Thesis, University of British Columbia, Vancouver, Canada, 1997.
4. Svanberg JM. An experimental investigation on mechanisms for manufacturing induced shape distortions in homogeneous and balanced laminates. *Composites Part A-Applied Science and Manufacturing* 2001; **32**: 827–838.
5. Twigg G, Poursartip A, Fernlund G. Tool–part interaction in composites processing. Part II: numerical modelling. *Composites Part A—Applied Science and Manufacturing* 2004; **35**: 135–141.
6. Wisnom MR, Gigliotti M, Ersoy N, Campbell M, Potter KD. Mechanisms generating residual stresses and distortion during manufacture of polymer–matrix composite structures. *Composites Part A—Applied Science and Manufacturing* 2006; **37**: 522–529.
7. Ruiz E, Trochu F, Gauvin R. Internal stresses and warpage of thin composite parts manufactured by RTM. *Advanced Composites Letters* 2004; **13**: 49–57.

8. Ferry JD. *Viscoelastic Properties of Polymers*. John Wiley & Sons, Inc., 1961; 2.
9. Luyckx G, Voet E, Lammens N, Degrieck J. Strain measurements of composite laminates with embedded fibre Bragg gratings: criticism and opportunities for research. *Sensors* 2011; **11**: 384–408.
10. De Waele W. Structural monitoring of composite elements using optical fibres with Bragg sensors. PhD Thesis, Ghent University, Ghent, Belgium, 2002.
11. Guemes JA, Mendez JM. Response of Bragg grating fiber-optic sensors when embedded in composite laminates. *Composites Science and Technology* 2002; **62**: 959–966.
12. Eum SH, Kageyama K, Murayama H, Uzawa K, Ohsawa I, Kanai M, Igawa H. Process/health monitoring for wind turbine blade by using FBG sensors with multiplexing techniques. Proceedings of SPIE 2008 Conference, Perth, Australia, 2004; 5B1–5B4.
13. Parlevliet P, Voet E, Bersee H, Beukers A. Process monitoring with FBG sensors during vacuum infusion of thick composite laminates. Proceedings of ICCM 16 Conference, Kyoto, Japan, 2007.
14. Tsai L, Cheng T, Lin C, Chiang C. Application of the embedded optical fibre Bragg grating sensors in curing monitoring of Gr/epoxy laminated composites. Proceedings of SPIE 2009 conference, San Diego, USA, Vol. **7293**, 2009; 071–078.
15. Khoun L, de Oliviera R, Michaud V, Hubert P. Investigation of process-induced strains development by fibre Bragg grating sensors in resin transfer moulded composites. *Composites Part A—Applied Science and Manufacturing* 2011; **42**: 274–282.
16. Mulle M, Collombet F, Olivier P, Grunevald Y-H. Assessment of cure residual strains through the thickness of carbon-epoxy laminates using FBGs, part I: elementary specimen. *Composites Part A—Applied Science and Manufacturing* 2009; **40**: 94–104.
17. Mulle M, Collombet F, Olivier P, Zitoune R, Huchette C, Laurin L, Grunevald Y. Assessment of cure-residual strains through the thickness of carbon-epoxy laminated using FBGs part II: technological specimen. *Composites Part A-Applied Science and Manufacturing* 2009; **40**: 1534–1544.
18. de Oliviera R, Lavanchy S, Chatton R, Costantini D, Michaud V, Slathe R, Månson J. Experimental investigation of the effect of the mould thermal expansion on the development of internal stresses during carbon fibre composite processing. *Composites Part A—Applied Science and Manufacturing* 2008; **39**: 1083–1090.
19. Parlevliet P, Bersee H, Beukers A. Measurement of (post-)curing strain development with fibre Bragg gratings. *Polymer Testing* 2010; **29**: 291–301.
20. Hagemann VJ. Untersuchungen zum dynamischen Enzelspuls-Einschreiben von Faser-Bragg-Gittern un zu deren Anwendung. PhD Thesis, Friedrich-Schiller University, Germany, 2001.
21. Kreuzer M. Strain measurement with fiber Bragg grating sensors. Technical Report HBM, Darmstadt Germany, 2011.
22. Whitney RJ, McCullough JM. *Micromechanical material modelling. Delaware Composites Design Encyclopedia*. Technomic Pub. Co. Inc., 1990; 2.
23. Svanberg JM. Predictions of manufacturing induced shape distortions—high performance thermoset composited. PhD Thesis, Luleå University of Technology, Luleå, Sweden, 2002.
24. Hattel JH. *Fundamentals of Numerical Modeling of Casting Processes*. Polyteknisk Forlag, 2005.
25. Nielsen MW, Hattel JH, Andersen TL, Branner K, Nielsen PH. A 1D coupled curing and visco-mechanical void growth model of thick thermosetting composite laminates. Proceedings of ICCM 18 Conference, Jeju, Korea, 2011.
26. Ivankovich M, Incarnato L, Kenny JL, Nicholais L. Curing kinetics and chemorheology of epoxy/anhydride system. *Journal of Applied Polymer Science* 2003; **90**: 3012–3019.
27. Zobeiry N. Viscoelastic constitutive models for evaluation of residual stresses in thermoset composites during cure. PhD Thesis, The University of British Columbia, Vancouver, Canada, 2006.
28. Momentive Speciality Chemicals Inc. Epikote RIMR 135 and RIMH 134-137 Technical Data Sheet, 2006.
29. Mijovic J, Wang HT. Modelling of processing of composites part II—temperature distribution during curing. *SAMPE Journal* 1988; **24**: 42–55.
30. White SR, Hahn HT. Process modelling of composite materials: residual stress development during curing. Part II—experimental validation. *Journal of Composite Materials* 1992; **26**: 2423–2453.
31. Cai Z-Q, Movva S, Chiou N-R, Guerra D, Hioe Y, Castro JM, Lee LJ. Effect of polyaniline surface modification of carbon nanofibers on cure kinetics of epoxy resin. *Journal of Applied Polymer Science* 2010; **118**: 2328–2335.
32. Svanberg JM. Shape distortion of non-isothermally cured composite angle bracket. *Plastics, Rubber and Composites* 2002; **31**: 1–7.

Paper IV

"'Life cycle strain monitoring from manufacturing to failure in GFRP laminates using embedded FBG sensors"'

M. W. Nielsen, J. W. Schmidt, J. H. Høgh, J. P. Waldbjørn, J. H. Hattel, T. L. Andersen, C. M. Markussen

Journal of Composite Materials,
DOI: 10.1177/0021998312472221, 2012. In Press.

Original Article

JOURNAL OF COMPOSITE MATERIALS

Journal of Composite Materials
0(0) 1–17

DOI: 10.1177/0021998312472221
jcm.sagepub.com
SAGE

Life cycle strain monitoring in glass fibre reinforced polymer laminates using embedded fibre Bragg grating sensors from manufacturing to failure

MW Nielsen[1], Jacob W Schmidt[2], Jacob H Høgh[3], Jacob P Waldbjørn[2], Jesper H Hattel[1], Tom L Andersen[3] and Christen M Markussen[3]

Abstract

A holistic approach to strain monitoring in fibre-reinforced polymer composites is presented using embedded fibre Bragg grating sensors. Internal strains are monitored in unidirectional E-glass/epoxy laminate beams during vacuum infusion, curing, post-curing and subsequent loading in flexure until failure. The internal process-induced strain development is investigated through use of different cure schedules and tool/part interactions. The fibre Bragg grating sensors successfully monitor resin flow front progression during infusion, and strain development during curing, representative of the different cure temperatures and tool/part interfaces used. Substantial internal process-induced strains develop in the transverse fibre direction, which should be taken into consideration when designing fibre-reinforced polymer laminates. Flexure tests indicate no significant difference in the mechanical properties of the differently cured specimens, despite the large differences in measured residual strains. This indicates that conventional flexure testing may not reveal residual strain or stress effects at small specimen scale levels. The internal stresses are seen to influence the accuracy of the fibre Bragg gratings within the loading regime. This study confirms the effectiveness of composite life cycle strain monitoring for developing consistent manufacturing processes.

Keywords

Strain monitoring, fibre Bragg grating sensors, curing, process-induced strains, life cycle, composite

Introduction

Fibre-reinforced polymer (FRP) composites are widely used in various industrial applications. Such materials provide low weight, excellent corrosion resistance and high strength, which are beneficial properties in, for instance, the construction of commercial wind turbine blades and civil structures. The manufacturing process of the composite structure can, however, greatly influence the performance of the part, which is dependent on the presence of voids, dry spots, matrix cracks, waviness of the ply stack and other manufacturing-related defects. Such defects can result in crack initiation when the structure is loaded and premature failure at lower loads than expected when designing the structure.

During the manufacture of thermosetting matrix composites, a material state transition of the resin occurs, from a viscous, to rubbery and glassy state during curing. It is within this transition that various mechanisms result in the development of process-induced stresses in the composite structure, which when unconstrained result in shape distortions.[1–3]

[1]Department of Mechanical Engineering, Technical University of Denmark, Denmark
[2]Department of Civil Engineering, Technical University of Denmark, Denmark
[3]Department of Wind Energy, Technical University of Denmark, Denmark

Corresponding author:
MW Nielsen, Department of Mechanical Engineering, Technical University of Denmark, Produktionstorvet, Bygning 425, 2800 Kongens Lyngby, Denmark.
Email: mwni@mek.dtu.dk

In cases where these process-induced stresses are sufficiently large and unavoidable, for instance due to strong internal or external constraints, they can result in various strength reducing mechanisms that support premature failure. For instance, large process-induced residual stresses are known to induce matrix cracking, interfacial debonding and delamination in fibre-reinforced composites[1,4–6] demonstrated that for thick-walled composite tubes, residual stresses can be so great that matrix cracking was promoted. At a micromechanic level, Nedele and Wisnom[7] showed that process-induced stresses at the fibre–matrix interface can be as large as 30 MPa, due to the combination of hoop and radial stress components. This stress magnitude is substantial considering that the typical tensile strength of epoxy matrix materials is approximately 60–65 MPa. Furthermore, due to the viscoelastic nature of the polymer matrix material, large process-induced residual stresses can also influence the long-term dimensional stability of the part, due to creep or stress relaxation behaviour.

The main mechanisms responsible for process-induced shape distortions and residual stresses are: (a) the thermal expansion mismatch of the constituent materials; (b) matrix chemical shrinkage during curing; and (c) interactions at the tool/part interface.[2,3,8–11] Of particular interest, when considering thick laminate composites is also the manufacturing cure cycle design. High cure temperatures and fast heating/cooling rates can result in highly non-uniform temperature and cure gradients within the part resulting in differential curing and subsequent development of internal stresses.[3,4–6,11] Similar effects in the form of a non-uniform distribution of in-plane shear stresses can arise due to constraints posed by tooling during processing.[10,12] A combination of the above-named residual stress mechanisms and manufacturing defects can cause local premature failure at lower load magnitudes than would otherwise be predicted in a defect-free composite structure.

In order to experimentally monitor the internal strain development during manufacturing, the use of fibre optic sensors has gained approval as a desirable in situ method.[13–24] Apparent advantages include their ease of integration structurally during the composite manufacturing phase and the minimal influence to the host part structural properties. In recent works by the authors, fibre Bragg grating (FBG) sensors were successfully embedded in a laminate composite for cure strain monitoring purposes.[19] As opposed to the use of conventional non-intrusive strain/deformation monitoring methods (e.g. using strain gauges (SGs) or digital image correlation (DIC)), embedded optical fibre sensors offer the advantage of being able to monitor local internal strains in the composite readily. Moreover, FBG sensors offer the capability to accurately monitor resin flow front progression during infusion.[14,23,24]

This study focuses on investigating the development of internal strains in glass FRP (GFRP) composites in a holistic manner during the composite life cycle using embedded FBG sensors. The term *life cycle* in this context refers to the composite life time from manufacturing using vacuum infusion and until mechanical testing, as illustrated in Figure 1. Thus, using this approach, we wish to monitor the development of process-induced internal strains and investigate the influence of these strains and residual stresses in the composite during manufacturing and testing. This study provides an approach to monitor and gain knowledge during the manufacturing procedure of FRP composites. Such manufacturing control is important if consistency in the quality of the composite is desired. In addition, information of the residual strain and stress state in the structure is important if these are to be accounted for in the design of a structural component.

FBG sensor principle

Strain monitoring using optical fibres with FBG sensors requires a light source, an interrogator unit and an appropriate data acquisition software tool. The light source transmits a broadband light spectrum through the optical fibre and the axially placed FBG sensors back-reflects light within a specific pre-defined wavelength. This back-reflected light is fed into the interrogating unit designed to measure the reflected light signal. Modulation of the reflected signal, centred along the Bragg wavelength, is linearly related to mechanical or thermal loads. The FBG wavelength variation is hence determined using[13]

$$\frac{\Delta\lambda_B}{\lambda_B^0} = K_\epsilon\left[\Delta\varepsilon_{app}^{host} + \Delta\varepsilon_{th}^{host}\right] + K_T\Delta T = K_\epsilon\Delta\varepsilon_{tot} + K_T\Delta T \tag{1}$$

where $\Delta\lambda_B$ is the change in Bragg grating wavelength and λ_B^0 the initial unstrained grating wavelength, K_ϵ and K_T the optical fibre mechanical strain and temperature sensitivities, specific for the type of sensor used. $\Delta\varepsilon_{tot}$ is the change in total strain – a summation of the increments from the applied strain $\Delta\varepsilon_{app}^{host}$ and the host thermal strain $\Delta\varepsilon_{th}^{host}$. Equation (1) describes the linear mechanical and thermal response of the FBG sensor. When the FBG is embedded in a composite material, here on termed the host material, complete strain transfer is achieved once bonding between the optical fibre and the host material occurs. Subsequently, any mechanical straining and thermal expansion of the host material would govern the response of the FBG sensor. Knowing the temperature

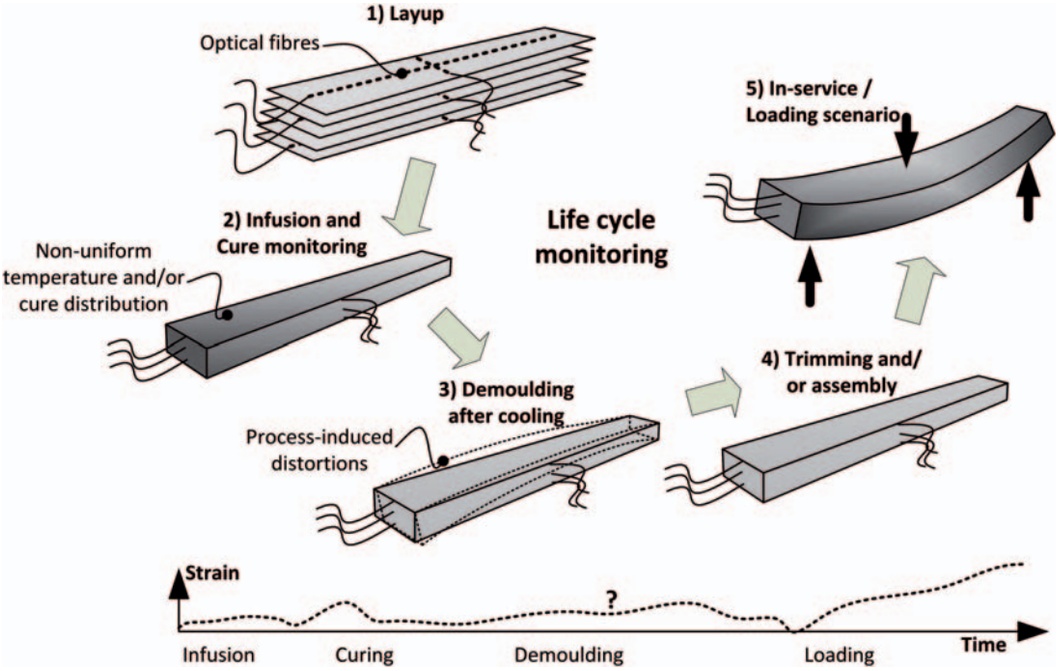

Figure 1. Schematic of life cycle monitoring approach for a GFRP laminate using embedded optical fibres where internal strains are monitored from manufacture to loading.
GFRP: glass fibre reinforced polymer.

and sensor wavelength variation, the corresponding change in host material total strain in the optical fibre axial direction can be determined using equation (1) by isolating $\Delta\varepsilon_{tot}$.

In this study, silica optical fibres provided by FOS&S, Belgium, were used, with multiple draw tower grating (DTG®) FBG sensors with an Ormocer® coating (cladding diameter 125 µm). The sensitivity coefficients K_ϵ and K_T are equal to $0.775\text{E}-6\,\mu\varepsilon^{-1}$ and $6.27\text{E}-6^{\circ}\text{C}^{-1}$, respectively. When considering the magnitudes of the mechanical strain and temperature sensitivity coefficients, it is clear that accurate temperatures at the vicinity of the sensors is needed in order to determine precise strains. It has been shown that the strain sensitivity remains constant below 180°C for this optical fibre.[20] Furthermore, DTG FBGs are known to exhibit little variation in strain-optic coefficients when loaded which is advantageous. The Ormocer coating helps reduce the sensor sensitivity to external transverse loading, hence increasing the accuracy of the axial strain measurements. An I-MON E interrogator, from Ibsen Photonics, Denmark, was used for data acquisition. The I-MON E is a stand-alone interrogation monitor with a wavelength bandwidth of 85 nm, capable of assessing <70 FBG sensor signals. The interrogator wavelength accuracy lies within 5 pm with a sampling rate of up to 970 Hz. The grating length used in this work, i.e. the effective strain measurement region, spans 4 mm of the optical fibre length at each sensor positioned along the optical fibre. In other works, where a similar length is used, no peak splitting of the back-reflected wavelength spectrum was experienced.[21,22] Peak-splitting is generally attributed to the existence of transverse loading of the sensor causing a local distortion of the reflected signal spectra. This is most likely to occur when using long gratings where a large transverse local load is present in the vicinity of the FBG sensor. By having a short grating length and using a coated fibre, this problem is greatly reduced. Studies found that good predictions of process strains in neat resin and composite laminates were achievable using a similar setup.[13,16,19]

Experimental procedure

Materials

The composite constituent materials used in this study comprise of unidirectional (UD) fibre reinforcement fabric type L1200/G50F-E06-A, from Devold AMT, with a nominal area weight of 1246 g/m^2 and a thermoset epoxy resin matrix material type Airstone 760E mixed 100 : 32 parts-by-weight with Airstone 776H hardener, from Dow Chemicals Company. The reinforcement fibre and resin matrix material used in this study are representative of materials commonly

used in commercial wind turbine blades. Material properties are summarised in Table 1. As mentioned in the introduction, epoxy resins exhibit volumetric chemical shrinkage during cross-linking, generally known to lie between 3% and 7%.[9–11] Both constituent materials used exhibit isotropic thermal expansion behaviour, as observed from Table 1.

Manufacturing procedure

In order to investigate the influence of the cure cycle profile and boundary conditions on the process-induced strain development and subsequent part performance, two different manufacturing procedures were employed, as summarised in Figure 2 and Table 2. The tool used was a transparent tempered glass plate, chosen in order to visibly ensure full wetting of the reinforcement fibres during infusion. Vacuum infusion was performed as edge infusion with resin flow in the longitudinal fibre direction in the entire length of the specimens. An Enka channel mesh and highly porous distribution net (Figure 2) are used in order to allow fast flow along the top surface of the reinforcement fabric and subsequent through-thickness wetting. Fibre layup was established using 22 layers of UD glass fibre fabric each cut to $500 \times 100\,\text{mm}^2$ $(l \times b)$ and stacked symmetrically on the glass tool with the fibre backing material faced outwards. During the layup procedure, placement of optical fibres and thermocouples was conducted as described in the subsequent section. After layup, a vacuum leak test was carried out prior to infusion. The epoxy resin was mixed with the hardener and degassed in a vacuum chamber with a vacuum pressure above 95 kPa, until all foaming had subsided. Infusion was carried out at ambient temperature with a vacuum pressure of 95 kPa. The inlet hose was closed once resin flowed through the outlet hose and full impregnation of the reinforcement fibres was visible. Full wetting of the reinforcement fibres took approximately 45 min. The vacuum pressure was then reduced to 60 kPa and pressure equalisation and further compaction of the laminate was allowed for 15 min before the outlet was closed. The vacuum infused specimens were placed into pre-heated ovens at 50°C and 80°C for approximately 5 and 3 h, respectively, for the different cure cycles investigated (Table 2). The in-mould cure periods were chosen such that the resin was nearly fully cured based on differential scanning calorimetry isothermal scan data at various temperatures.[25] Different cure temperatures were chosen in order to achieve different thermal residual stresses.

Table 1. Material properties of E-glass reinforcement fibre and epoxy resin.

	Density (kg/m^3)	Young's modulus (GPa)	Poisson's ratio	CTE ($\times 10^{-6}\,°C^{-1}$)
UD E-glass fibre	2600	72.0[a]	0.22	5.04[a]
Epoxy resin (cured)	1040	3.116	0.32[b]	65.41[b]

CTE: coefficient of thermal expansion; UD: unidirectional.
[a]Isotropic for E-glass, i.e. $E_1 = E_2$, $CTE_1 = CTE_2$.
[b]Approximated value from the literature.
[c]Resin supplier data sheet.

Table 2. Experimental design matrix showing layup, cure schedules and boundary conditions.

	Type A	Type B
Layup	$[0]_{22}$	$[0]_{22}$
Cure temperature[a] (°C)	50	80
Temperature hold[b] (min)	300	180
Cooling	Natural convection	Natural convection
Post-cure temperature[a] (°C)	90	–
Post-cure hold[b] (min)	120	–
Tool/part interface	Release agent[c]	Perforated release foil

[a]Pre-heated oven temperature.
[b]Temperature hold period includes heating from ambient- to pre-heated oven temperature.
[c]The tool surface was treated with release agent prior to the experiments.

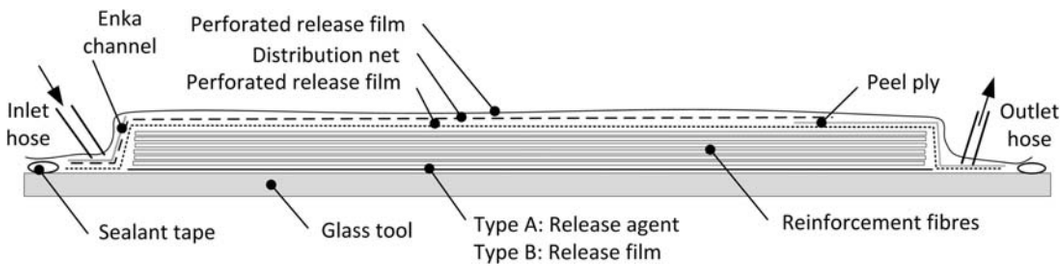

Figure 2. Schematic of vacuum infusion setup.

The cured in-mould laminates were cooled by natural convection to ambient temperature. Cooling in this manner took approximately 3.5 h and 5.5 h, respectively, for the 50°C and 80°C cure cycles. After cooling, demoulding was carried out and type A specimens were post-cured in a pre-heated oven at 90°C for 2 h. Type B specimens were not post-cured. All specimens were then cut into $500 \times 45\,\text{mm}^2$ ($l \times b$) beams. Trimming of the beam sides was done in order to ensure a constant cross section of each specimen, necessary in the mechanical tests. The manufactured specimens had a final average thickness of 19.04 mm with a variation of approximately 0.20 mm, and a fibre volume fraction of approximately 55%.

During manufacturing, two different tool/part interfacial interactions were investigated using release agent and release film (Table 2). This was done to investigate non-uniform through-thickness strain variations during manufacturing as well as the possible occurrence of locking.[11] A total of 10 laminates were manufactured using the different cure cycle and boundary conditions summarised in Table 2 evenly divided between the specimens.

Optical fibre and thermocouple sensor embedment

During the layup process, optical fibres consisting each of three FBG sensors were placed in the laminate, as illustrated in Figure 3. The optical fibres were placed along the UD reinforcement fibre direction (i.e. longitudinally) as well as perpendicular to the reinforcement fibres (transversely). This was done at three different interlayer locations along the ply stack thickness direction: between the 1st and 2nd, 11th and 12th and 21st and 22nd plies representing the laminate beam specimen top, middle and bottom planes (*Top*, *Mid* and *Bot* henceforth). In order to ensure that the optical fibres remained in place, they were *sewn* in place using the backing fibres of the reinforcement fibre fabrics, as an alternative to using adhesives, etc. In this manner, the optical fibres remained aligned but at the same time not entirely constrained. Temperature monitoring during processing was conducted using type-J (Fe-CuNi) $2 \times 0.5\,\text{mm}^2$ thermocouples, placed at various regions on the outer surface and within different layers approximately 10 mm from the edge of the laminate. Temperature data was collected using an eight-channel DaqPRO data acquisition system (Fourier systems, Barrington, USA), with a sampling frequency of 10 Hz. Data logging were commenced once infusion was initiated, as well as at different intervals at ambient temperatures between the various manufacturing steps. Hence, information revealing the internal strain development at discrete times throughout the manufacturing process was obtained from the specimens at different through-thickness layers in different reinforcement fibre directions. Strain and temperature monitoring was carried out in three 'Type A' and two 'Type B' laminate beam specimens, respectively. The remaining laminate beams without embedded sensors were solely used for mechanical test verification purposes.

Temperature logging conducted during the experiments served two purposes. First, the temperatures are used in equation (1) in order to compensate for the thermal expansion of the optical fibre and determine the total mechanical strains from the FBG data. The thermocouples are also used to monitor the exothermic reaction of the resin during curing and ensure that the specimens were cooled to the ambient temperature at the data sampling intervals. Figure 4 shows some of the specimens manufactured at various stages during the experiments.

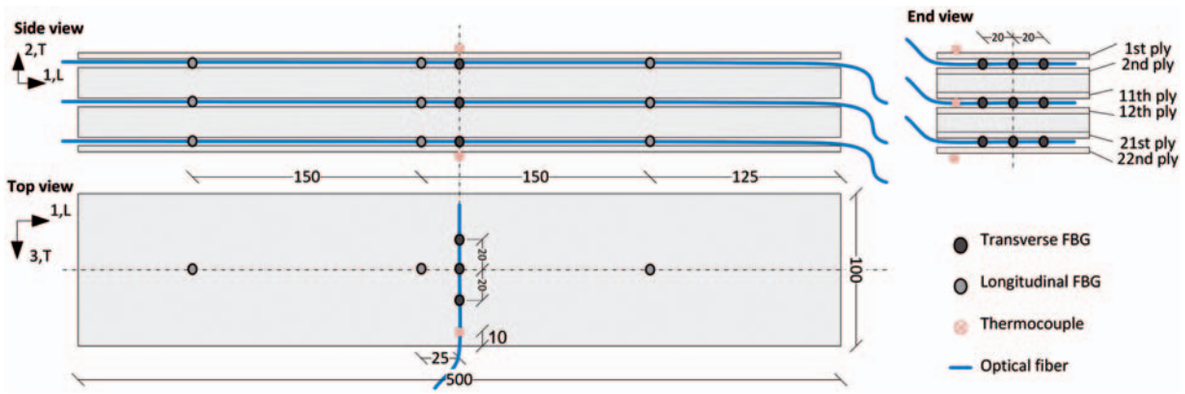

Figure 3. Schematic of laminate beam layup with FBG and thermocouple sensor placement.
FBG: fibre Bragg grating.
All dimensions are in mm.

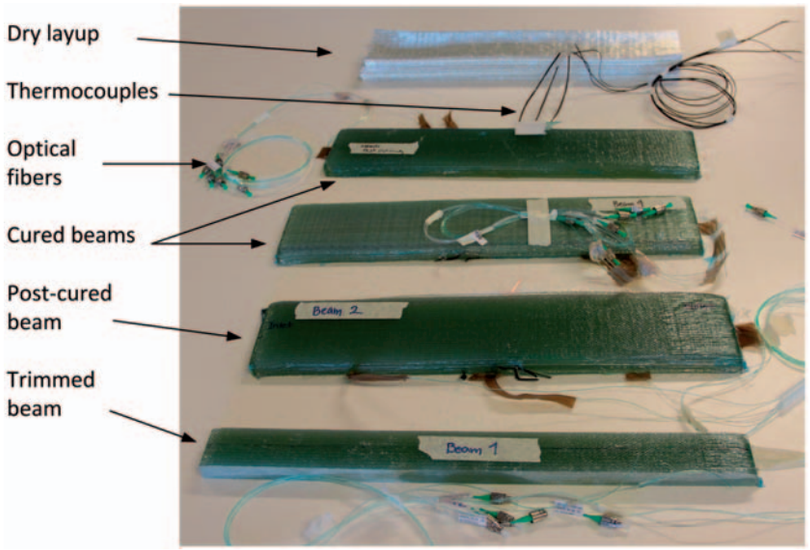

Figure 4. Laminate beam specimens at different stages in the manufacturing procedure, seen with embedded FBG sensors and thermocouples.
FBG: fibre Bragg grating.

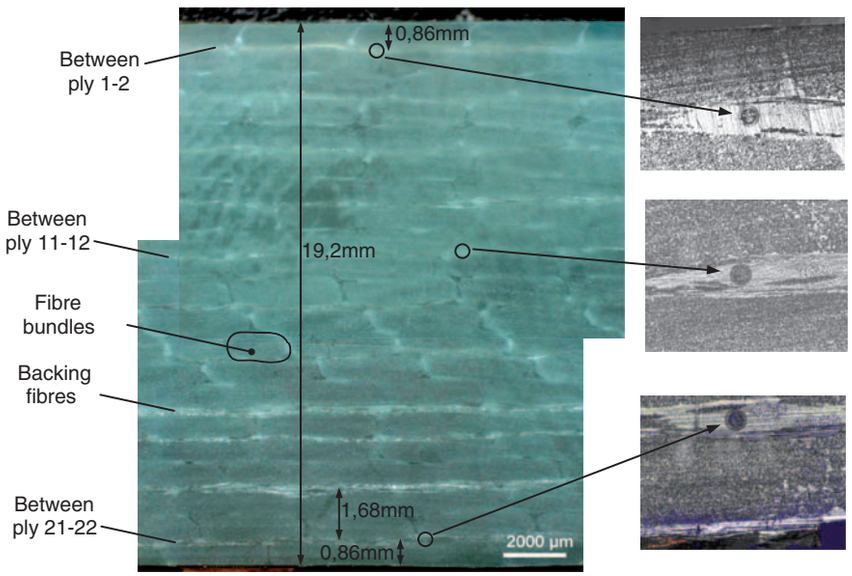

Figure 5. Image of laminate specimen cross section with zoom of inter-ply placement of optical fibres.

To ensure that the optical fibres remained at their respective laminate inter-ply locations during layup and vacuum infusion, a cross-sectional microscope analysis was conducted, after mechanical testing. Knowing the exact depth of each optical fibre is, for instance, vital for correct comparison of surface mounted SGs and embedded optical fibres. Figure 5 shows microscope images of the laminate beam cross section, showing placement of optical fibres after manufacturing. The optical fibres were found to be situated at the same inter-ply regions as during layup. It has been reported in some studies that standard 125 µm optical fibres produce a insignificant perturbation of the host material when embedded parallel to the reinforcing fibres in laminates.[26,27]

Experimental results and discussion

Strains at discrete periods during manufacturing

Figures 6 and 7 show measured total strains at discrete periods during manufacturing for type A and B

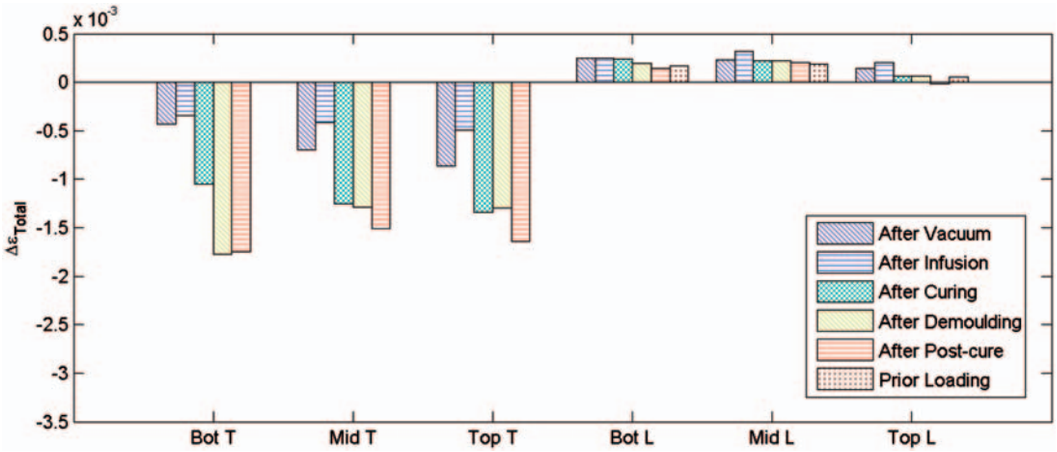

Figure 6. Average total strains at manufacturing intervals, measured at ambient temperature for type A laminate beam specimens.

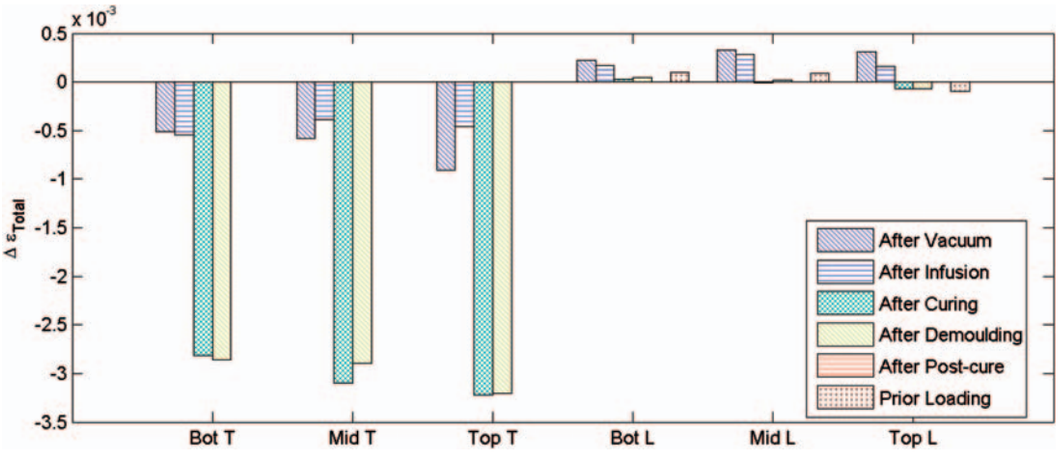

Figure 7. Average total strains at manufacturing intervals, measured at ambient temperature for type B laminate beam specimens.

laminate beams, respectively, at ambient temperature. The values presented are averages of type A and B specimens for all three FBG sensors on each optical fibre at discrete stages during manufacturing. Total strains are shown: (a) after vacuum pressure is applied; (b) after infusion (resin flow); (c) after curing; (d) after demoulding; (e) after post-curing (type A only); and finally (f) prior loading. Note that the transversely embedded optical fibres were no longer usable after cutting, hence no transverse measurements are conducted prior loading.

In both cure cycle cases shown (Figures 6 and 7), transverse total strains which are matrix dominated are seen to have higher magnitudes as compared to the longitudinal strains, which are fibre dominated, i.e. more constrained. General tendencies are as follows: upon applying vacuum pressure, a negative increment in strains are seen in the transverse direction, while a small positive increment in tensile strains arise in the longitudinal direction (here onwards *T*- and *L*-directions). The elongation longitudinally is believed to be due to re-alignment of fibres from a wavy to straight state when under pressure effectively straining the optical fibre in tension. After infusion, a slight decrease in strain magnitudes is exhibited in general. After curing, a significant negative strain increment in the *T*-direction occurs in type A and B specimens throughout the beam thickness, as well as a slight negative strain increment in the *T*-direction. This is an indication of prevailing compression/shrinkage due to the inherent mechanisms present, i.e. matrix shrinkage and thermal compression upon cooling. A significant difference in strain magnitudes after curing is seen between type A and B specimens, with larger negative strains in type B specimens. Assuming that both specimens are fully cured such that total chemical shrinkage has taken place, the difference in magnitudes owes to larger thermally induced strains in type B beams. The through-thickness strain

distribution in both cases is largest near the top surface as compared to at the tool/part interface (Bot) where tool/part interaction constrains movement. Upon demoulding, a larger strain release is exhibited at Bot T in type A specimens, as opposed to Bot T in type B beams. This is an indication that better bonding at the tool/part interface existed during curing when release agent is used at the tool/part interface as opposed to when using the perforated release foil.

Figure 8 shows the total strains for type A and B beams in the *L*- and *T*-directions compared to each other. Results are shown for stages after curing, where it is assumed that perfect bonding between the composite and optical fibre exists. After curing, a non-uniform strain distribution through the thickness is seen in both *L*- and *T*-directions. After demoulding, negative strain increments are seen at the laminate bottom plane in the *T*-direction for both beam types (Figure 8 (T-2)), indicating a tensile stress state at the bottom laminate plane after curing. This implies that a compressive stress state exists at the laminate centre while tensile stresses exist at the surfaces, which is a common stress state when an inside-out cure occurs due to exothermic peak temperatures at the centre, as also seen in Bogetti and Gillespie.[3] Moreover, for type B specimens, this is also seen at the top plane, while at the middle plane a positive strain increment is seen. When considering the through-thickness strain gradients, a more uniform distribution is generally seen in type B specimens. This indicates that weaker bonding at the tool/part interface exists when using release film, allowing for more sliding friction behaviour. This observation is supported by the fact that all type B specimens were significantly easier to separate from the glass tool during demoulding.

When considering the free-standing change in type B longitudinal strains from demoulding and prior loading (Figure 8 (L-2 to L-4)), an increase in tensile strains is seen near the beam bottom plane. This is due to visco-elastic creep, exhibited by the composite during the 6 week period in time before loading tests were commenced. Contrary to this, a decrease in tensile strains (compressive creep) is seen for type A beams after post-curing and prior loading. Positive creep strains indicate

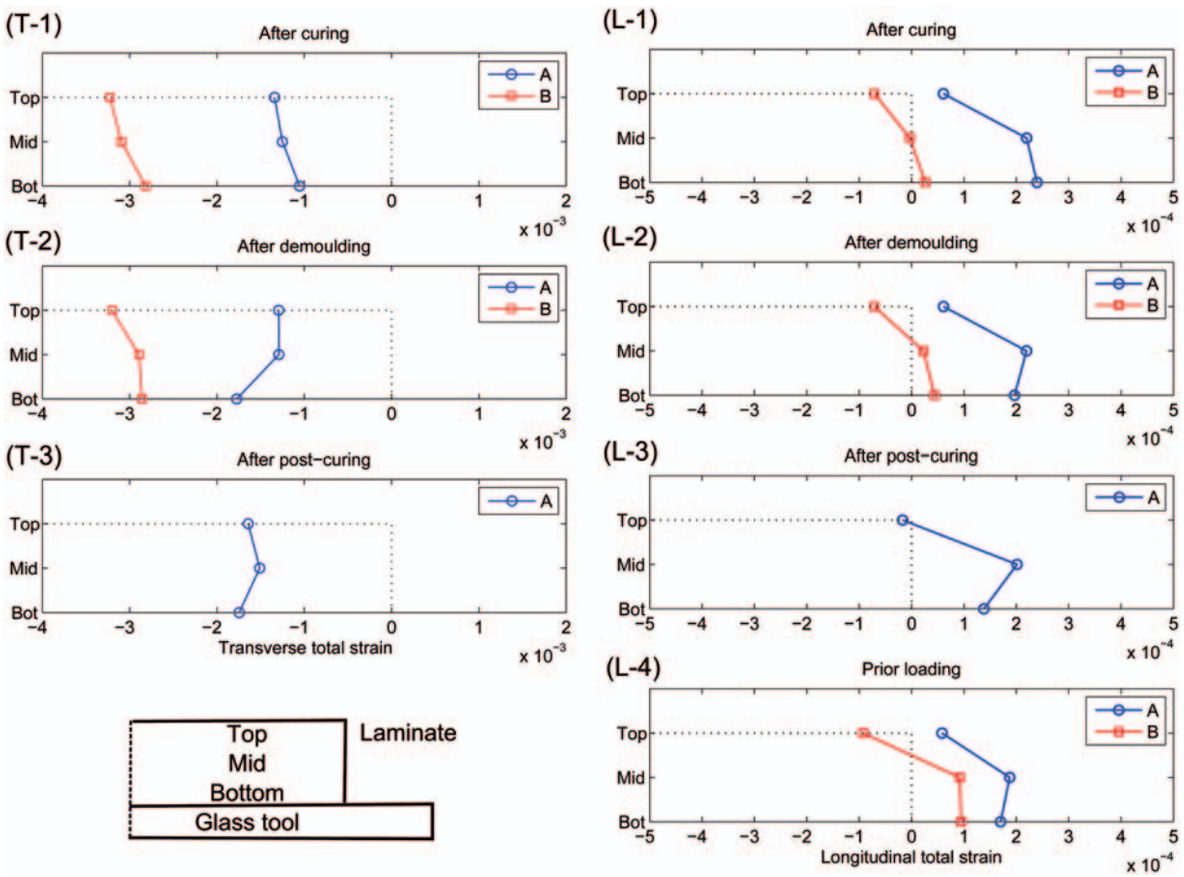

Figure 8. Average laminate type A and B transverse (T) and longitudinal (L) strains after various manufacturing stages compared to non-strained (dashed line) laminate beam state.

that a compressive stress state exists, that is not readily released as distortions after curing, but gradually with time. Nedele and Wisnom[7] and Wisnom et al.[11] found that residual stresses at a micromechanic level may not normally readily cause distortions because they may arise at a very local scale, where any deforming effects are averaged out over the larger volume of material. Hence inter-ply or microscale compressive stresses may still exist in the beams.

Strain monitoring signal quality

The quality of the strain measurements was monitored during this study by constant evaluation of the reflected light signal spectrum. This is presented for a type B laminate after curing at ambient temperature in Figure 9, compared to the reflected signal prior vacuum-bagging and infusion for longitudinally and transversely embedded FBG sensors. Due to the large compressive strains in the transverse direction after curing, the signal peaks have been shifted left to lower wavelength values. Furthermore, some distortion of the FBG spectrum is seen in the form of birefringence (peak splitting) of the Bragg peak. The peak-splitting seen indicates development of transverse loads at the vicinity of the sensors.[13,18] This could be the result of backing-fibres or perpendicular UD fibre bundles that are locally loading the optical fibres not to mention resin shrinkage stresses around each optical fibre (Figure 10). Broadening of the spectrum is also

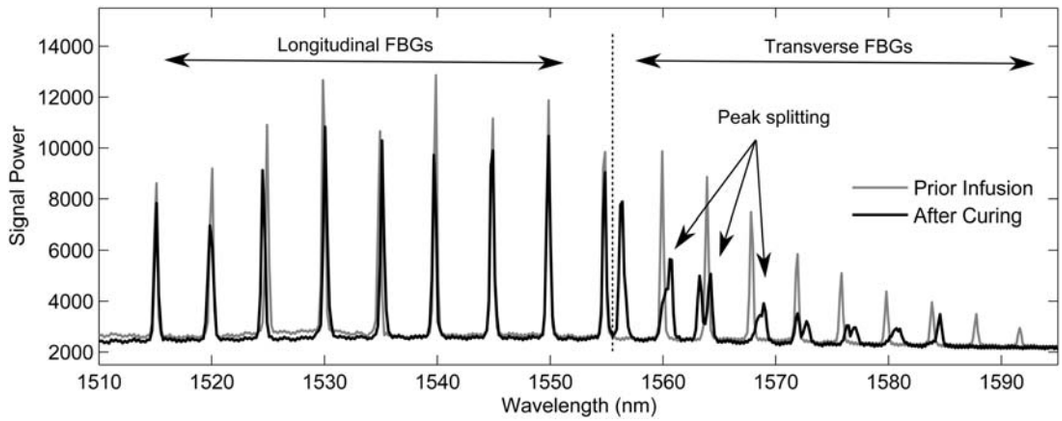

Figure 9. Wavelength signal spectrum for type B laminate after curing, showing clear signs of birefringence of the light signal (peak splitting).

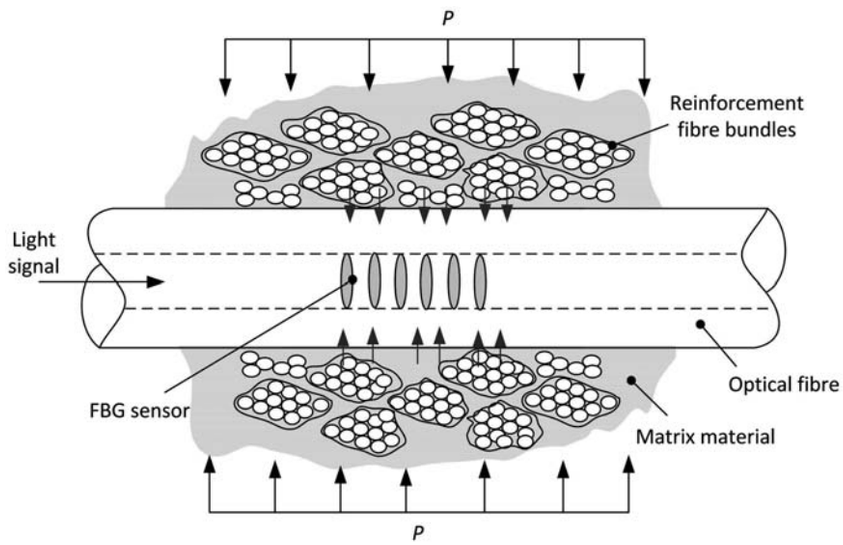

Figure 10. Illustration of mechanisms causing transverse loading of optical fibre from reinforcement fibre tows perpendicular to the optical fibre during processing.

observed, which is also an indication that transverse stress may exist.[13] Distortion is not seen in any of the signals from longitudinal sensors, but only in Type B transverse signals. Acquiring the correct discrete wavelength shift in order to determine the mechanical strain variation must, therefore, be interpreted with caution where peak-splitting of the signal is present. The data acquisition software seeks only the signal peaks above a user-defined threshold found using an *n*th-order polynomial fit for a prescribed number of expected peak signals (here 18). In this study, in order to account for these signal distortions, an approach is used where averaging of multiple peaks within a common base is performed for the discrete ambient strains presented in the previous section. The spectrum data shows that larger stresses are generally present in Type B specimens as opposed to Type A.

In situ strains during infusion

Flow front monitoring is conducted during resin infusion by monitoring the shift in wavelength of the embedded FBG sensors during vacuum infusion. Figures 11 and 12 show the strain variations during infusion for a beam specimen representative of general tendencies occurring in the *L*- and *T*-directions, respectively.

After approximately 100 s, infusion is commenced and the resin flow front reaches the L-embedded sensors near the inlet first, seen as changes in sensor 3 wavelengths at the top, mid and bottom (Figure 11). As the flow front progresses along the laminate top surface and gradually through the thickness towards the outlet, changes in wavelengths are seen in the L-embedded sensors and the corresponding T-embedded sensors (Figure 12). Hence, at different times during

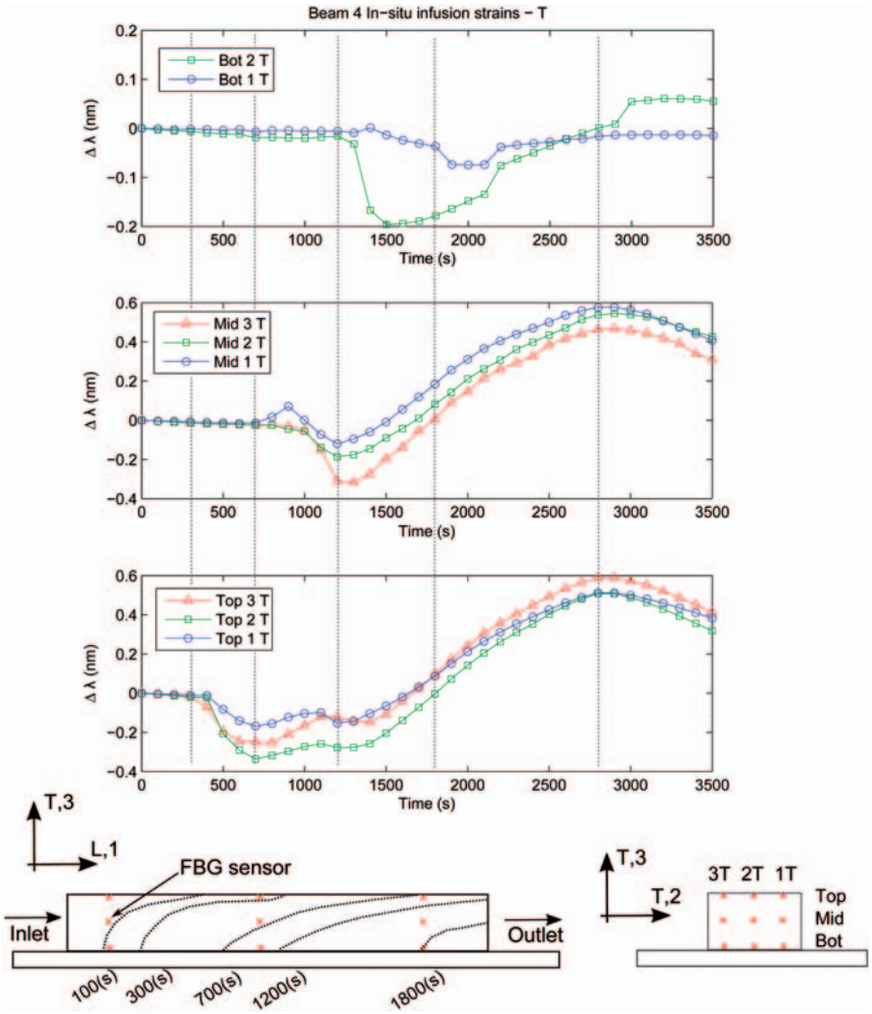

Figure 11. Variations in longitudinally embedded FBG sensor wavelengths during infusion.
Also seen is a schematic of the sensor placement from inlet to outlet and the expected flow front development.
FBG: fibre Bragg grating.

infusion, through-thickness tracking of the resin flow front in different directions is possible. After approximately time $t = 2800$ s, the inlet hose is closed, marked by changes in wavelength in all embedded sensors as the flow speed is drastically reduced.

In situ strains during curing

In Figure 13, experimentally measured temperatures for type A and B cure cycles are presented. A gap in the acquired type A temperature data is seen between time $t = 180$ and 300 min. For the sake of continuity, estimated temperature development curves are drawn, following tendencies from type B data. In both cases, the exothermic reaction during resin cross-linking as the matrix cures results in peak temperatures that are higher than the prescribed oven cure temperatures of 50°C and 80°C for type A and B, respectively. The large increase in temperatures is accredited to high heat generation rates as the matrix cures. The peak exothermic

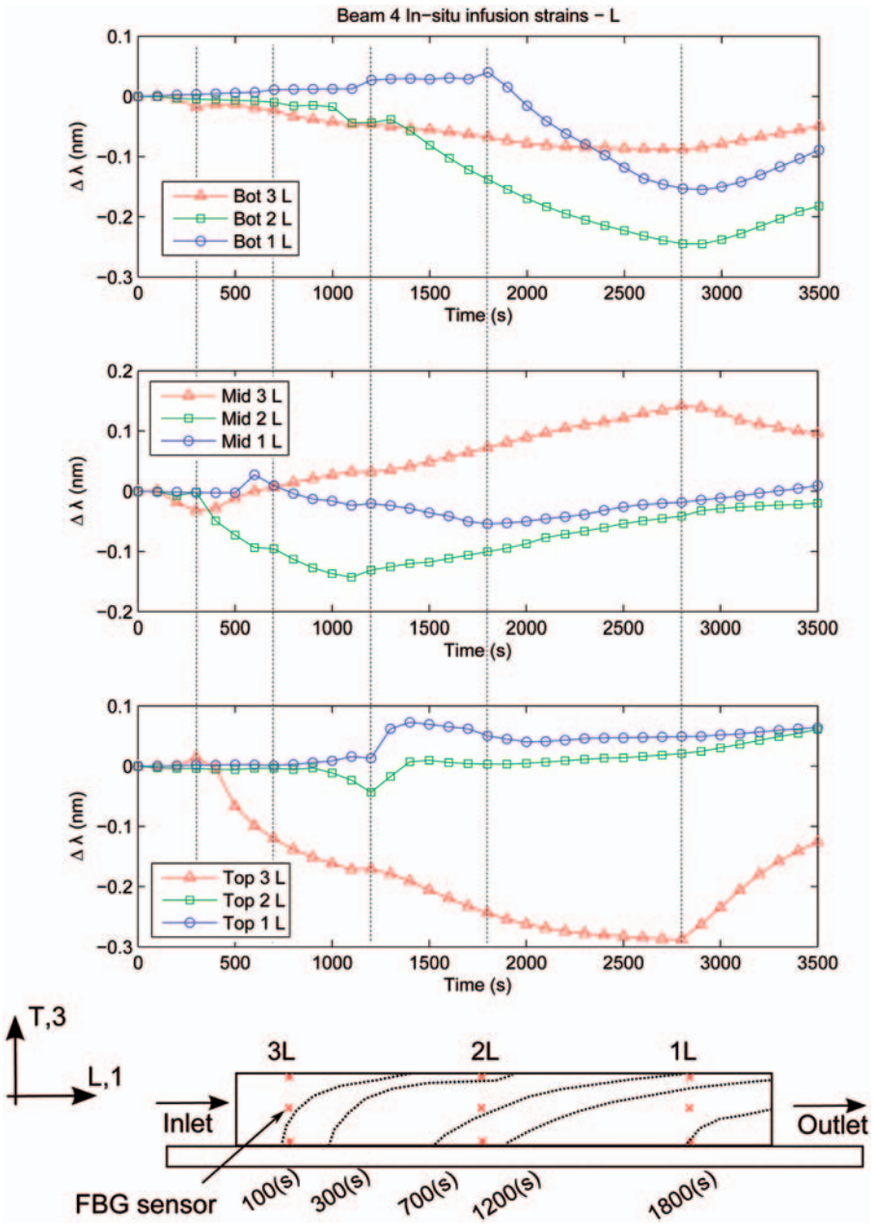

Figure 12. Variations in transversely embedded FBG sensor wavelengths during infusion.
Similarly, a schematic of the sensor placement is given and the expected flow front development, as shown in Figure 11.
FBG: fibre Bragg grating.

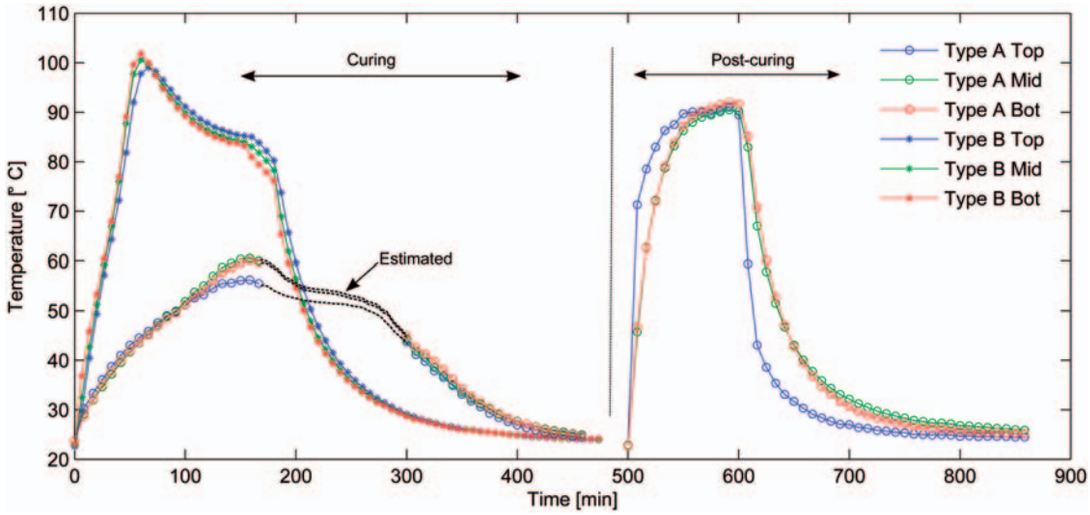

Figure 13. Temperature profiles for type A and B cure cycle laminate beam samples during curing. Note that only type A specimens are post-cured.

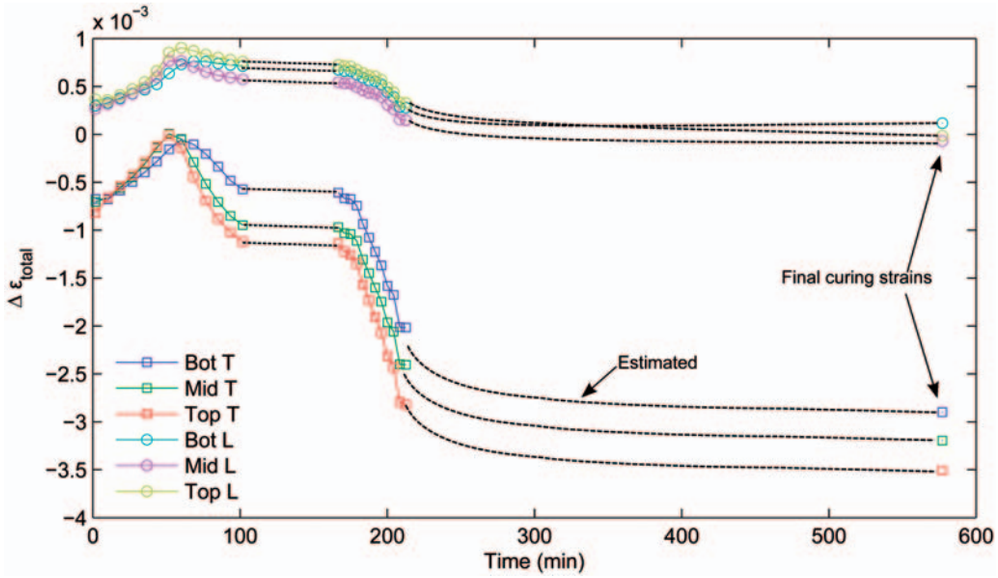

Figure 14. In situ total strain measurements during curing for type B specimen. Dotted lines are added for continuity where loss of signal occurred.

temperatures are approximately 60.1°C and 100.6°C during in mould cure, while the peak post-cure temperature is 98.3°C measured towards the end of the 90°C post-cure temperature hold for type A beam specimens. The peak temperatures are measured at the laminate mid-layer. The temperature peaks during post-curing is due to the release of residual latent heat which was not fully released during the first heating cycle.

In situ strain monitoring during curing is shown in Figure 14 for a type B beam using averaged values for top, mid and bot (T and L) sensor measurements as calculated using equation (1). Where loss of signal from the interrogator unit was encountered, dotted lines are added for the sake of continuity based on the temperature profiles observed from Figure 13 during cooling. The in situ strain development generally follows the temperatures for type B specimens well (Figure 13) depicting an increase upon heating, a peak, dwell and decrease in strains during cooling. Early in the process, thermal expansion- and chemical cure shrinkage strains occur simultaneously, resulting

in negative strains after the exothermic reaction has occurred. This is mainly seen in the transverse (matrix driven) direction. In both the *L*- and *T*-directions, the higher mechanical constraints at the bottom layer, in both *T*- and *L*-directions, result in lower negative and positive strains, respectively, as compared to strain magnitudes at mid and top. Upon the onset of cooling after approximately 160 min, negative strain increments in the *T*- and *L*-directions are seen, owing primarily to thermal contraction, assuming the resin is fully cured and total chemical cure shrinkage has occurred. The strains after cooling are also shown, corresponding to the 'after curing' strains previously shown in Figures 6 and 7.

Simple analytic calculations based on the self-consistent field micromechanic model are made to validate the cure strain magnitudes found. The effective laminate longitudinal and transverse thermal strain increments can be calculated using[3]

$$\Delta\varepsilon_L^{th} = \left[\frac{\alpha_f E_f V_f + \alpha_m E_m (1 - V_f)}{E_{1f} V_f + E_m (1 - V_f)}\right] \cdot \Delta T \tag{2}$$

$$\begin{aligned}\Delta\varepsilon_T^{th} = \Big\{&\big(\alpha_f + \nu_{12f}\alpha_f\big)V_f + (\alpha_m + \nu_m\alpha_m)\big(1 - V_f\big) \\ &- \big[\nu_{12f}V_f + \nu_m\big(1 - V_f\big)\big] \\ &\times \left[\frac{\alpha_f E_f V_f + \alpha_m E_m\big(1 - V_f\big)}{E_f V_f + E_m\big(1 - V_f\big)}\right]\Big\} \cdot \Delta T\end{aligned} \tag{3}$$

where E, α and ν are the respective constituent modulus, coefficient of thermal expansion (CTE) and Poisson's ratio and V_f the reinforcement fibre volume fraction. The subscripts f and m denote fibre and matrix specific quantities and ΔT the change in temperature. Assuming that the resin is in glassy state the instant the peak exothermic temperature is achieved, the temperature variation during the cooling phase (i.e. from the peak cure temperature to ambient) can be used to calculate the thermal strain increments. Results are summarised in Table 3.

The analytically determined transverse thermal strains coincide well with the experimentally determined FBG strain values, measured at the least constrained laminate layer, namely the top layer. A large discrepancy is seen when comparing the longitudinal strains, which could be due to the larger influence of the tool interaction along the length of the beam. It is believed that the poor agreement in analytical and experimental strains in the longitudinal fibre direction may generally owe to the positive pre-straining of the fibres in this direction once the vacuum pressure was applied and during infusion (Figures 6 and 7). Note that the analytical calculations do not take into account gelation, differential resin material CTE in rubbery and glassy state or chemical shrinkage strains. If one wishes to accurately predict these effects, numerical process models could be used.

Table 3. Analytical thermal strain increment during cooling compared to measured total strains at the laminate beam top plane.

	Type A	Type B
ΔT (°C)	−38.6	−79.6
$\Delta\varepsilon_L^{th}$	−0.281E − 3	−0.579E − 3
$\Delta\varepsilon_T^{th}$	−1.80E − 3	−3.60E − 3
$\Delta\varepsilon_L^{tot}$ − FBG	−0.06E − 3	−0.001E − 3
$\Delta\varepsilon_T^{tot}$ − FBG	−1.34E − 3	−3.50E − 3

FBG: fibre Bragg grating.

Flexural tests – Three-point bending

Although large process-induced strains were seen to develop in the *T*-direction during curing, only small strains were measured in the *L*-direction. Hence, large residual stresses in the *L*-direction may still exist that are not released into distortions upon demoulding or relaxed during post-curing. At a micromechanical level, resin cure shrinkage and contraction upon cooling result in a tensile stress state in the *L*-direction in the matrix, due to constraints posed by the reinforcement fibres. In turn, the reinforcement fibres are in a compressive stress state upholding equilibrium. Whether these residual stresses influence the composite mechanical behaviour during loading is investigated using simple flexure tests. Figure 15 shows a schematic of the flexure test beam samples and sensor placement.

The tests were conducted in a custom made three-point test rig with adjustable rolling cylindrical supports (Figure 15), using an MTS 810 axial servo-hydraulic table top test, with a ±180 mm stroke and force capacity of 25 kN. The loading and support nose cylinder diameters are 40 and 25 mm, respectively. A large nose radius was used to avoid excessive indentations and failure due to stress concentrations directly under the loading point. The test rig is connected to the load cell and hydraulic piston by serrated grips. The piston is controlled through the MTS FlexTest system by a servo valve model 525-15A-04 with a maximum flow of 10 L/s and load cell model 662.10A-05. A cross-head rate of 0.5 mm/min is used and tests are conducted until a substantial drop in the specimen load-carrying capacity is exhibited. The strain at the top and bottom surface of the test specimen is acquired from four SG located at the top and bottom surface along the same beam cross section as the embedded FBG sensors (Figure 15). Strains are measured along the laminate

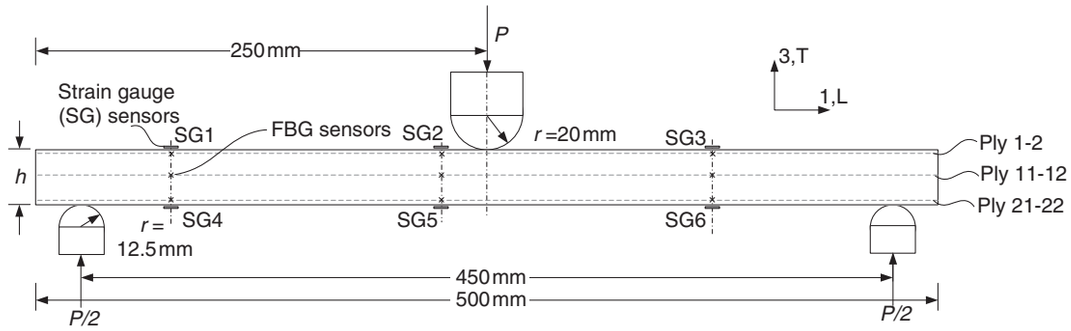

Figure 15. Schematic of three-point flexure test setup of laminate beam specimens.
Also seen are the embedded FBG fibres and SGs (SG1–SG4).
FBG: fibre Bragg grating; SG: strain gauge.

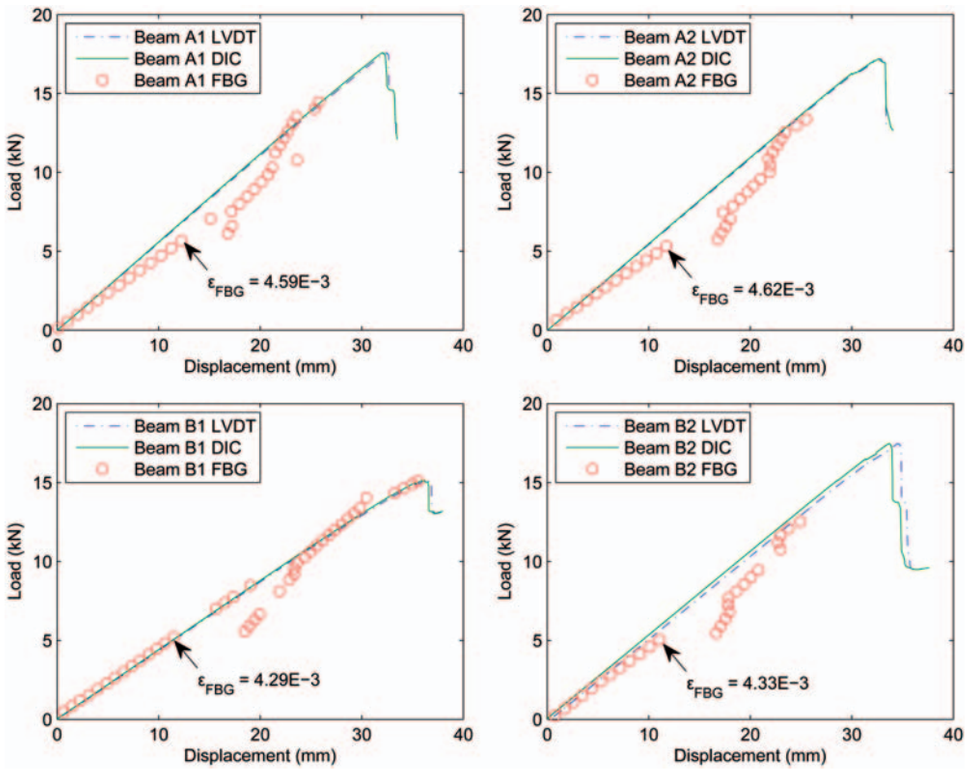

Figure 16. Flexural test load–displacement results for type A and B specimens using displacement measurements from test rig LVDT, DIC and embedded FBG sensors at laminate top centre point.
LVDT: linear variable differential transformer; DIC: digital image correlation; FBG: fibre Bragg grating.

beam longitudinal direction. Furthermore, DIC as well as the test rig linear variable differential transformer (LVDT) sensor is used to measure displacements during loading. DIC measurements are performed in order to avoid using inaccurate LVDT displacement results that may also take into account deformation of the test rig.

Results and discussions

Figure 16 shows the flexural response of beam specimens type A and B using load–displacement plots. Displacements are shown for the embedded FBG, DIC and the test rig LVDT data for comparison. The data represents vertical displacements at the

laminate/loading nose contact point. The LVDT and DIC displacements correspond well throughout the loading range, which indicates that no significant deformations occur in the test rig itself. FBG strains measured at the laminate top centre (and bottom centre for validation) are converted to vertical displacements using the following geometric relations

$$\delta = \rho[1 - \cos(\theta)]$$

where

$$\rho = \frac{h/2}{\Delta\varepsilon_{\{FBG\}}} \text{ and } \theta = \sin^{-1}\left(\frac{L/2}{\rho}\right) \quad (4)$$

In equation (4) δ is the vertical displacement, ρ the chord length and θ is the angle of curvature. A good agreement between the FBG, DIC and LVDT displacements is seen in the early stages of loading, albeit gradually diverging. The FBG displacements increase linearly with the load until a threshold strain is reached (ε_{FBG} in Figure 16) after which the signal becomes sporadic and inconsistent, marking sensor failure. The strain is also seen to be lower in type B beams due to the higher initial process-induced strains which lower the fracture strain of the optical fibre. The strain range of the FBG is given by the supplier to be approximately 5000 με, which both type A and B specimens in Figure 16 lie below, more so for type B beams. This may indicate that the slight compressive pre-straining of the FBG sensors in the *L*-direction during processing (see Figure 8 (L-4)) decreases the strain to failure of the sensors.

Flexural test results from all beam specimens were collected using load–DIC displacement data. From the test results, the flexural modulus E_f of each beam is found using the slope of the load–displacement curves along the linear regime as[28]

$$E_f = \frac{S^3 m}{4bh^3} \quad (5)$$

where S is the support span, b the width and h the thickness of the beams. The flexural strength of the respective specimens is the stress at the surface upon failure, calculated assuming a linear stress–strain relationship up to failure as[28]

$$\sigma_{cr} = \frac{3P_{cr}S}{2bh^2} \quad (6)$$

Table 4. Flexural test modulus, failure load and flexural strength for all tested specimens.

	Type A					Type B				
	A 1	A 2	A3	A 4	Average	B 1	B 2	B 3	B4	Average
h (mm)	19.10	18.56	19.17	19.10	18.98	19.56	19.45	19.05	19.42	19.37
E_f (GPa)	39.26	40.60	39.36	38.06	39.32	37.86	38.45	38.65	38.70	38.23
P_{cr} (kN)	17.583	16.593	17.198	15.992	16.84	18.312	17.156	17.468	17.930	17.72
σ_{cr} (MPa)	708.04	722.55	701.89	657.54	697.53	717.92	680.24	721.88	712.92	708.32

Respective beam specimen thickness (h) measured at the laminate centre, are also seen.

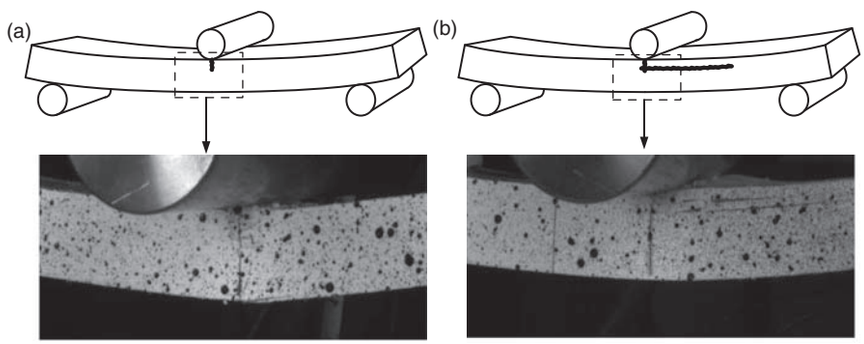

Figure 17. Images capturing failure progression using DIC during fracture. Failure starts for most specimens as compressive fracture at the top laminate layer (a), and later develops to compressive fracture with interlaminar shear (b).
DIC: digital image correlation.

where P_{cr} is the load at the moment of fracture. The experimentally determined flexural modulus and failure load is presented for all specimens in Table 4 as well as the flexural strength of each specimen, determined using equation 6. From Table 4, beam type A and B average failure loads are 16.84 and 17.72 kN, respectively, resulting in average flexural strength values of 697.5 and 708.3 MPa, respectively. As these results highly depend on the thickness of the specimens (as h is squared in equation (6)) substitution of P_{cr} in equation (6) with normalised failure loads for 20 mm thick beam specimens is conducted resulting in average flexural strength values of 771.1 and 716.5 MPa for type A and B specimens, respectively. Note that in Table 4, no distinct differences are seen between beam specimens with embedded optical fibres (i.e. A1, A2, B1 and B2) and without.

DIC was also utilised to monitor the onset of failure (Figure 17). For all 10 beam specimens, failure modes were first visible after the maximum load was reached. From the DIC images, the first failure modes seen for a majority of the specimens was compressive fracture at the top surface, followed second by a number of specimens exhibiting compressive fracture with interlaminar shear. No distinct failure mode type accredited to only type A or B specimens was visible.

Conclusion

A life cycle approach where strain monitoring using embedded FBG sensors in E-glass/epoxy composite laminate beam specimens from manufacturing to failure in three-point bending was conducted. The embedded FBG sensors successfully monitored resin flow front progression during infusion and internal strain development during curing as well as at subsequent intervals until loading to failure. Process-induced strains were seen to reflect the differences in processing temperatures and tool/part interface interactions well. Laminates cured at 80°C for 3 h induced larger internal strains than those cured at 50°C for 5 h. It was shown that process-strains in the transverse reinforcement fibre direction were large enough to result in a decrease in FBG signal quality due to peak splitting and signal distortion for specimens cured at 80°C. No such signal distortions were seen in specimens cured at 50°C for 5 h with subsequent post-curing at 90°C for 2 h. Flexural tests were conducted showing no significant effect of the process-induced stresses and strains on the longitudinal flexural stiffness or failure strength of the specimens. This could owe to the simplicity of the analysed UD laminate beam specimens, which readily releases most residual stresses due to lack of significant internal or external constraints. Furthermore, it can be questioned whether small specimens, similar to the beams used in this study, are representative measures for the behaviour of large FRP structures. In such structures, thicker laminate sections and complex geometries incorporating internal constraints could play a role, not to mention the likelihood of including manufacturing defects such as voids, dry spots or matrix cracks to name a few. However, a difference in the failure strain of the embedded FBG sensors was seen for specimens cured at 50°C and post-cured at 90°C as compared to specimens cured at 80°C with the latter resulting in lower sensor failure strains. Hence, if embedded FBG sensors are to be used for in-service strain monitoring of composite structures where large deformations are expected, process-induced pre-straining of the FBG sensors should be taken into account.

The manufacturing and loading strain monitoring conducted in this study can be utilised to validate an integrated numerical process and loading model where the effects of process-induced residual stresses on the composite response under loading and failure strength can be analysed. Moreover, use of embedded FBG sensors offers the ability to measure and track part consistency during processing. The procedure presented in this article is applicable for strain monitoring of composite structures from manufacture to in-service use.

Funding

This study is supported by Danish Energy Agency through the Energy Technology Development and Demonstration Programme (EUDP). The supported EUDP-project is titled 'Demonstration of new blade design using manufacturing process simulations' and has journal no. 64009-0094. The support is gratefully acknowledged.

Conflict of interest

None declared.

References

1. Favre JP. Residual thermal stresses in fibre reinforced composite materials - a review. *J Mech Behav Mater* 1988; 1(1–4): 37–53.
2. Hahn HT. Effects of residual stresses in polymer/matrix composites. *J Astronaut Sci* 1984; 32(2): 253–267.
3. Bogetti TA and Gillespie JW. Process-induced stress and deformation in thick-section thermoset composite laminates. *J Compos Mater* 1992; 26: 626–659.
4. Kim KS and Hahn HT. Residual stress development during processing of graphite/epoxy composites. *Compos Sci Technol* 1989; 36: 121–132.
5. Zhao LG, Warrior NA and Long AC. A micromechanical study of residual stress and its effect on transverse failure in polymer-matrix composites. *Int J Solids Struct* 2006; 43: 5449–5467.
6. Stone MA, Schwarz IF and Chandler HD. Residual stresses associated with post-cure shrinkage in GRP tubes. *Compos Sci Technol* 1997; 57: 47–54.

7. Nedele MR and Wisnom MR. Three-dimensional finite element analysis of the stress concentration at a single fibre break. *Compos Sci Technol* 1994; 51(4): 517–524.
8. Johnston A. *An integrated model of the development of process-induced deformation in autoclave processing of composite structures*. PhD Thesis, University of British Columbia, Vancouver, Canada, 1997.
9. Svanberg JM. *Predictions of manufacturing induced shape distortions - high performance thermoset composites*. PhD Thesis, Luleå University of Techology, Luleå, Sweden, 2002.
10. Twigg G, Poursartip A and Fernlund G. Tool-part interaction in composites processing. Part II: numerical modelling. *Composites Part A* 2004; 35: 135–141.
11. Wisnom MR, Gigliotti M, Ersoy N, et al. Mechanisms generating residual stresses and distortion during manufacture of polymer-matrix composite structures. *Composites Part A* 2006; 37: 522–529.
12. Fernlund G, Rahman N, Courdji R, et al. Experimental and numerical study of the effect of cure cycle, tool surface, geometry, and lay-up on the dimensional fidelity of autoclave-processed composite parts. *Composites Part A* 2002; 33: 341–351.
13. Luyckx G, Voet E, Lammens N, et al. Strain measurements of composite laminates with embedded fibre Bragg gratings: criticism and opportunities for research. *Sensors* 2011; 11: 384–408.
14. Eum SH, Kageyama K, Murayama H, et al. Process/health monitoring for wind turbine blade by using FBG sensors with multiplexing techniques. In: *Proceedings of SPIE 2008 conference*, Perth, Australia, 14–18 April, 2008, vol. 7004, pp.5B1–5B4.
15. Khoun L, de Oliviera R, Michaud V, et al. Investigation of process-induced strains development by fibre Bragg grating sensors in resin transfer moulded composites. *Composites Part A* 2011; 42: 274–282.
16. Parlevliet P, Voet E, Bersee H, et al. Process monitoring with FBG sensors during vacuum infusion of thick composite laminates. In: *Proceedings of 16th ICCM conference*, Kyoto, Japan, 3–8 July 2007.
17. De Waele W. *Structural monitoring of composite elements using optical fibres with Bragg sensors*. PhD Thesis, Ghent University, Ghent, Belgium, 2002.
18. Guemes JA and Mendez JM. Response of Bragg grating fiber-optic sensors when embedded in composite laminates. *Compos Sci Technol* 2002; 62: 959–966.
19. Nielsen MW, Schmidt JW, Hattel JH, et al. In-situ measurement using FBGs of process-induced strains during curing of thick glass/epoxy laminate plate: experimental results and numerical modelling. *Wind Energy* 2012.
20. Mulle M, Collombet F, Olivier P, et al. Assessment of cure-residual strains through the thickness of carbon-epoxy laminated using FBGs Part II: technological specimen. *Composites Part A* 2009; 40: 1534–1544.
21. Parlevliet E, Bersee H and Beukers A. Measurement of (post-) curing strain development with fibre Bragg gratings. *Polym Test* 2010; 29: 291–301.
22. de Oliviera R, Lavanchy S, Chatton R, et al. Experimental investigation of the effect of the mould thermal expansion on the development of internal stresses during carbon fibre composite processing. *Composites Part A* 2008; 39: 1083–1090.
23. Eum SH, Kageyama K, Murayama H, et al. Resin flow front monitoring for VARTM using fiber Bragg gratings. In: *Proceedings 16th ICCM conference*, Kyoto, Japan, 8–13 July 2007.
24. Gupta N and Sundaram R. Fiber optic sensors for monitoring flow in vacuum enhanced resin infusion technology (VERITy) process. *Composites Part A* 2009; 40(8): 1065–1070.
25. Nielsen MW, Schmidt JW and Hattel JH. Process-induced residual stress predictions during vacuum infusion of thick glass/epoxy laminate beams and analysis of influence on loading. 2012.
26. Saton K, Fukuchi K, Kurosawa Y, et al. Polyimide-coated small-diameter optical fiber sensors for embedding in composite laminate structures. *Proc SPIE* 2001; 4328: 285–294.
27. Jensen DW and Sirkis JS. Integrity of composite structures with embedded optical fibers. In: Udd E (ed.) *Fiber optic smart structures*. New York: Wiley, 1995, pp.109–129.
28. Hodgkinson JM. *Mechanical testing of advanced fibre composites*. Boca Raton, FL: CRC Press, 2000.

Technical Report I

Implementation of Temperature- and Cure Dependent Viscoelastic Curing Model

M.W. Nielsen, 2011.

IMPLEMENTATION OF TEMPERATURE- AND CURE DEPENDENT VISCOELASTIC MODEL

TECHNICAL REPORT

(SEPTEMBER-NOVEMBER 2011)

Michael Wenani Nielsen

DTU/MEK/MPP

DTU Mechanical Engineering
Department of Mechanical Engineering

Preface

The work presented in this report was primarily conducted during a 3 month external research stay at the German Aerospace Center (*Deutsches Zentrum für Luft- und Raumfahrt e.V (DLR)*), at the Institute of Composites Structures and Adaptive Systems, in the Department of Structural Mechanics, in Braunschweig (BS), Germany. The work documented in this technical report supports the PhD work concerning numerical modelling of the wind turbine blade manufacturing process. The project is supported by Danish Energy Agency through the Energy Technology Development and Demonstration Program (EUDP). The supported EUDP-project is titled "Demonstration of new blade design using manufacturing process simulations" and has journal no. 64009-0094. The support is gratefully acknowledged.

Acknowledgement is also in order to Dr.-Ing. Tobias Wille and Dr.-Ing. Alexander Kling at the Department of Structural Mechanics (DLR/BS) for having me and for their hospitality. Special acknowledgement is directed to Dipl.-Ing. Robert Hein for his support and our discussions during the research stay.

Contents

1 Introduction

During the manufacture of fibre-reinforced polymer matrix composite structures, non-isothermal temperature conditions exist, typically as a result of the exothermic reaction taking place in the epoxy polymer matrix during curing (polymerization), as well as due to external heating via the mould to the part. External heating is a means to accelerate the curing process. Polymer materials are known to exhibit viscoelastic material behaviour, especially exaggerated at elevated temperatures [4][16]. For this reason, if one wishes to model the thermomechanical behaviour of an epoxy resin during the manufacture of a composite structure precisely, where relaxation or creep behaviour might take place, a viscoelastic constitutive model to represent the polymer matrix material behaviour is necessary.

Different methods exist in literature to mathematically model general viscoelastic behaviour of solid polymers. When manufacturing fibre reinforced polymer matrix composite structures (from here on simply; *composites*), the resin matrix is initially in liquid state prior to curing. During an optimal infusion process, the fibre reinforcement material (E.g. carbon- or glass fibre tows, mats etc.) are saturated with the liquid resin, after which the curing process is commenced, where the resin cures and changes state from a liquid to a solid. In order to capture the viscoelastic behaviour of the resin during this phase-change, the viscoelastic constitutive material model must include temperature- and curing dependence.

This report concerns the numerical implementation of a tamperature and cure dependent polymer viscoelastic process model. First, an introduction to polymer viscoelastic behaviour is given. Simple differential form (DF) and integral form (IF) viscoelastic models are presented and simple examples given of these. After this, an introduction to temperature and cure effects on viscoelastic behaviour is given and existing models in literature on modelling these effects are presented. Schemes for the numerical implementation of the constitutive viscoelastic equations of interest are presented and the most advantageous of these is chosen. Throughout, modelling examples in MATLAB and ABAQUS are given and validation tests are carried out and compared to analytical solutions where possible.

2 Polymer Characteristics and Properties

Classification of polymers is generally done into two groups; thermoplastics and thermosets[1]. In the manufacture of composites, specifically wind turbine blades, thermosetting resins are generally used as the matrix material of choice due to their high thermal and dimensional stability. In this section, polymer characteristics with special attention to thermosetting resins are presented. The aim of this section is to identify which material characteristics and properties it is necessary to capture in a viscoelastic thermomechanical model. The main references used in this section are Brinson & Brinson (2008)[4], Shaw & MacKnight (2005) [16] and Ferry (1961,1970)[9].

2.1 Thermoset Resin Curing Mechanisms and Transformation

Thermosetting polymers exhibit slightly different constitutive behaviour compared to thermoplastics, mainly due to their cross-linked bonds forming between the molecular chains during polymerization. As curing progresses, so to does the density of cross-links, effectively increasing the material's viscosity and ability to sustain loads. As mentioned earlier, ross-linking can be initiated and accelerated by heating, as well as by applying pressure or radiation[2].

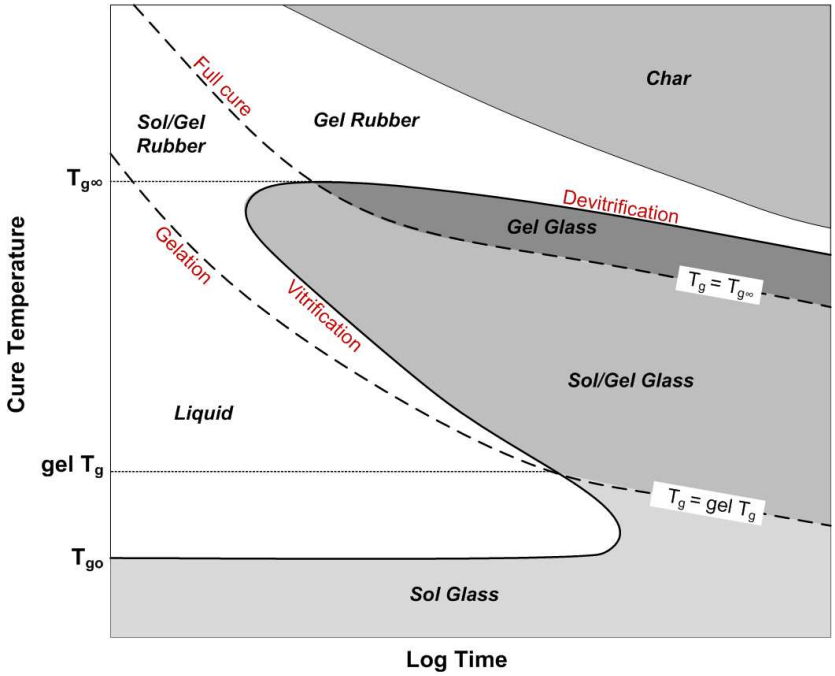

Fig. 1: *Schematic reproduction of the Time-Temperature-Transformation (TTT) isothermal cure diagram for a thermosetting polymer system, as proposed by Gillham [7].*

In the manufacture of large composites, heat is sometimes either applied to the liquid resin prior to infusion or applied directly to the mould. Initially during the process, the resin viscosity drops upon the application of heat, passes through a region of maximum flow (minimum viscosity) and then begins to increase as the chemical reactions increase and the average length and the degree of cross-linking between the constituent oligomers[2] increase. Gillham [7] was amongst the first

[1] Sometimes identified as "linear" and "cross-linked" polymers respectively [4]

[2] Polymer that contains 2, 3 or 4 monomers

to show the relations between time, temperature and transformation behaviour for thermosetting systems, using Time-Temperature-Transformation cure diagrams as shown in Fig. 1.

The resin transformation depends on the cure temperature and the cure time, as seen in Fig. 1, where the different transitions and material states as a function of time and temperature are illustrated. Upon prolonged heating of the resin a continuous network of chains are created and gelation occurs - characterized by development of the material's elastic properties and the liquid-to-rubber transition. Upon gelation, the polymer's mechanical strength increases rapidly and the ability to sustain stresses initiates. After gelation, the mobility of the polymer system is very limited, the resin micro-structure is more fixed and limitations to further cure are created. Further heating can induce vitrification - the transition of the material into a glass-like state. An increase of the process temperature is necessary such that the material glass transition temperature T_g rises to the isothermal temperature of cure T_{cure} [1; 7]. Vitrification retards chemical conversion, effectively marking the end of curing and transition to a gelled-glass. Heating past the maximum glass transition temperature $T_{g\infty}$ results in devitrification and the transition back from glassy to rubbery state. Devitrification marks the lifetime for the material to support a load. Prolonged exposure of the material to elevated temperatures can ultimately result in degradation of the material marked by a transition to a charred state.

The TTT-diagram presented by Gillham helps understand which different phases to expect during a typical cure cycle. A general understanding of the behaviour of thermosetting materials is obtained using the TTT cure diagram by understanding the transitions gelation, vitrification and devitrification [7]. The importance of the different glass transition temperatures ($T_{g\infty}$, $_{gel}T_g$, T_{g0}) and the rubbery and glassy states (disregarding the differences between soluble (sol) and insoluble/gelled (gel) fractions) will be apparent in the subsequent sections of this report.

2.2 Stress-strain Behaviour of Thermosetting Resins

In the previous section it was shown that thermosetting polymers can exist in liquid-, rubbery- and glassy-like states, depending on cure degree and temperature. In Fig. 2 and Fig. 3, the temperature and strain-rate dependency of an epoxy is illustrated. In Fig. 2 it is visible how the linear response at low temperatures changes to a non-linear response at elevated temperatures, which is an indication of glassy and rubbery behaviour respectively. Hence polymers exhibit softening as temperature increases.

In Fig. 3 it is visible that strain rate dependence exists. This is a result of the time dependence exhibited by polymers under loading, as will be discussed later.

2.3 Viscoelastic properties and Characterization

Characterization of viscoelastic time-dependent behaviour is typically conducted using relaxation and creep tests. During (stress)relaxation tests, isothermal tests are carried out by applying a constant strain quasi-statically to a uniaxial tensile bar, without inducing any dynamic or inertia effects. During this loading, the stress needed to maintain the constant strain will decrease with time marking relaxation. For a thermoplastic, the stress will eventually go to zero with time, but for thermosets, a lower non-zero bound exists due to unbreakable cross-links known as the

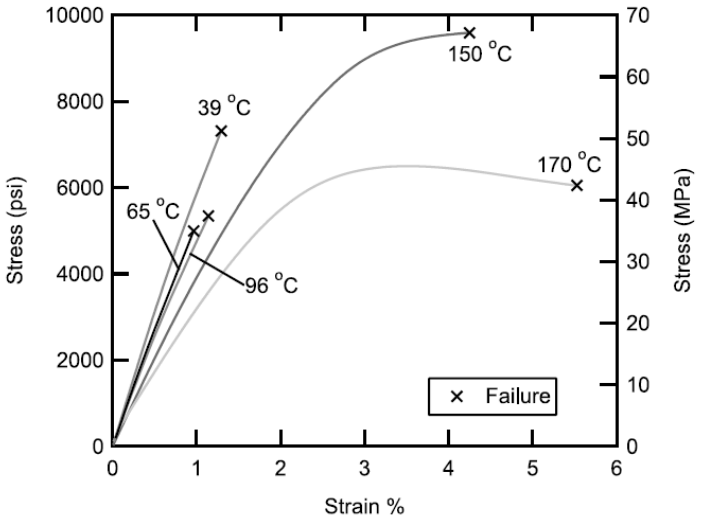

Fig. 2: *Temperature dependent stress-strain response of a typical brittle epoxy during constant strain-rate tests (Data from Hiel, et al. [4]).*

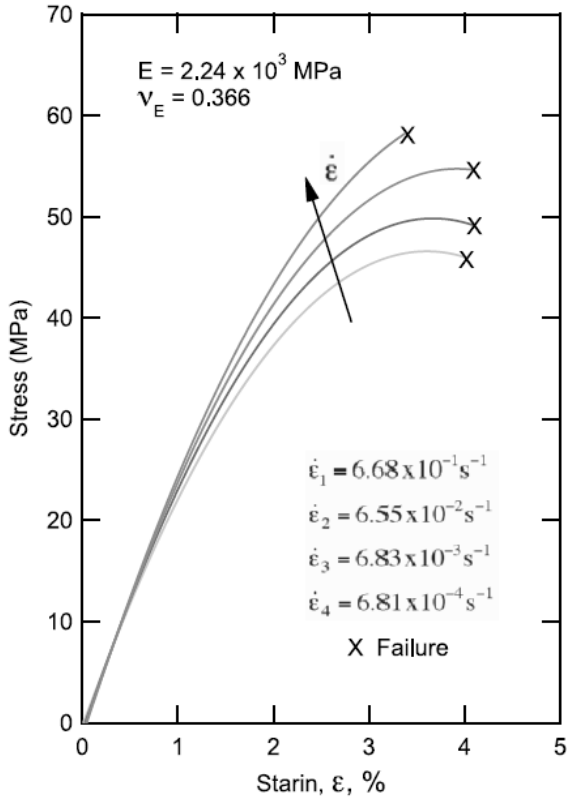

Fig. 3: *Rate dependent stress-strain response of an epoxy at room temperature (Data from Brinson, et al. [4]).*

fully-relaxed stress σ_∞. An illustration of the typical strain input and stress relaxation response of thermoplastic and thermosetting polymers is seen in Fig. 4.

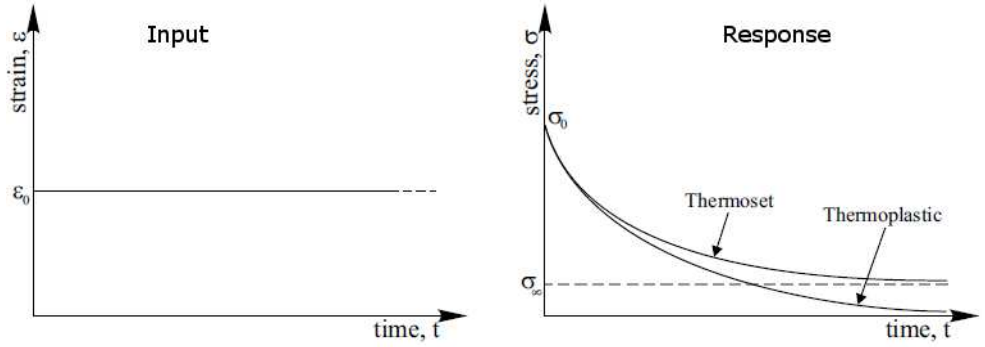

Fig. 4: *Relaxation test: Constant strain input and stress response (output), typical for thermoplastics and thermosets [4].*

As the stress varies with time, so to does the modulus. This can be expressed in a similar analogy as Hooke's law giving:

$$\sigma(t) = \epsilon_0 E(t) \tag{1}$$

where ϵ_0 is the constant strain and $E(t)$ is the time dependent modulus or relaxation modulus. For a thermosetting material, the bounds of the relaxation modulus at time $t = 0$ and $t = t_\infty$ are the initial modulus E_0 and fully relaxed (or equilibrium) modulus E_∞.

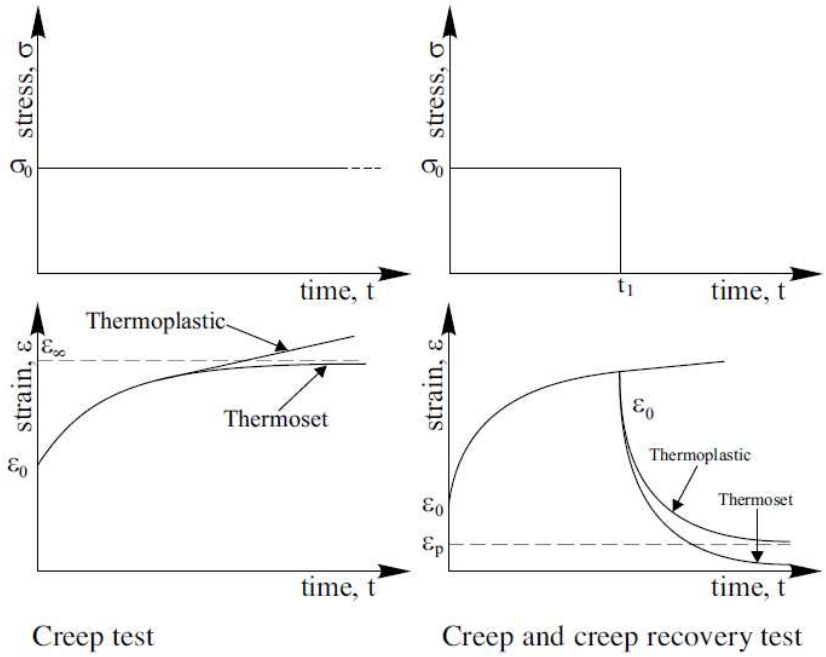

Fig. 5: *Creep (left) and creep recovery (right) tests: Constant stress input (above) and corresponding strain response (below), typical for thermoplastics and thermosets [4].*

During a creep test, a uniaxial tensile test specimen is loaded with a constant stress, applied quasi-statically as stated earlier for the relaxation test. During this test, for a viscoelastic material, the strain will increase under the constant load as time increases, see Fig. 5. The stress input and strain response during a creep recovery test is shown, where the constant stress input is instantaneously removed after some time. During a creep test, the strain response of a thermoset will tend to a

constant value after some time, while the strain for a thermoplastic material will increase without bound. During a creep recovery test, after the stress input is removed, the strain will decay to zero after some time, while a thermoplast would exhibit some residual or permanent strain. Creep behaviour is a result of the gradual rotation and unwinding of the molecular chains to accommodate the load [16][4].

During creep behaviour, the strain varies with time, as does the creep compliance such that:

$$\epsilon(t) = \sigma_0 D(t) \tag{2}$$

where σ_0 is the constant stress and $D(t)$ is the creep compliance defined as the time dependent strain divided by the constant stress.

In the following section, simple mathematical models are presented which can be used to understand and describe the viscoelastic behaviour presented above.

2.4 Phenomenological Mechanical Models

Mathematical models for the viscoelastic behaviour of a material can be obtained using combinations consisting of one or more spring and damper elements. These are typically used in Maxwell fluid- or Kelvin solid models, which consist of a linear spring and damper in series or parallel respectively. The reason this is possible is because polymers are known to exhibit viscoelastic behaviour spanning between that of viscous fluids (*Stokesian behaviour*) and elastic solids (*Hookean behaviour*). This is illustrated in the rheological classification of materials shown in Fig. 6.

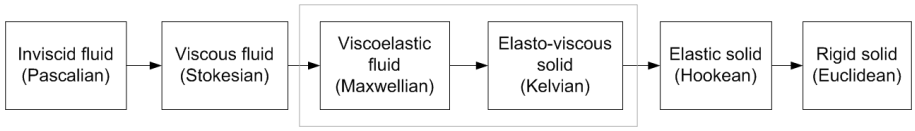

Fig. 6: *Rheological classification of materials (From Fredrickson, (1964)) [4].*

Hence a combination of Maxwell- and Kelvin elements, dampers and springs in series, parallel or both can be used to fit the desired polymer behaviour as experienced from experimental testing. The stress-strain relations for a linear elastic spring is expressed from Hooke's law as:

$$\sigma = E\epsilon \tag{3}$$

Similarly, the Newtonian law of viscoelasticity for shear is expressed as:

$$\tau = \mu \frac{d\gamma}{dt} = \mu\dot{\gamma} \tag{4}$$

where μ is the shear viscosity and $d\gamma/dt$ or $\dot{\gamma}$ is the shear strain rate. Subsequently, we will refrain from using μ and τ to represent the material viscosity and shear stress respectively and instead use η as the viscosity and do not distinguish between normal or shear stresses unless stated otherwise. As seen later, μ will represent one of the Lamé constants while τ is henceforth devoted to the viscoelastic relaxation time defined as:

$$\tau \equiv \frac{\eta}{E} \tag{5}$$

Combining spring and damper elements, one can get analogous representations of the behaviour of a Maxwell fluid or Kelvin solid model, shown in Fig. 7. Different combinations of these models can be used to develop differential form viscoelastic constitutive models, as will be described in the following section.

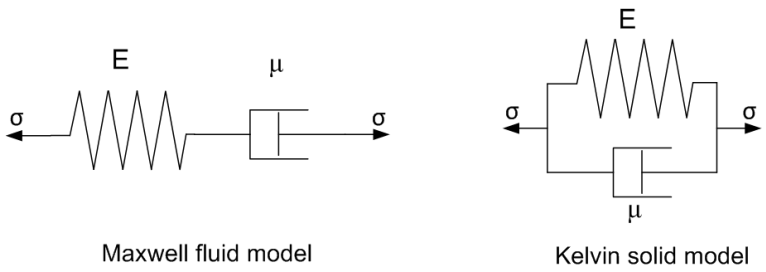

Fig. 7: *Maxwell and Kelvin model spring and damper arrangements.*

2.5 Summary

In this section, the material behaviour of polymers has been introduced with special interest in the behaviour of thermosetting polymers and their cure mechanisms using a Time-Temperature-Transformation cure diagram. Furthermore, different polymer characteristics are introduced and typical stress relaxation and creep behaviour shown. A short introduction to phenomenological mechanical models is also given, which will be used in the following section for determining expressions for constitutive equations. We now understand which material behaviour we wish to model.

3 Constitutive Equations

In this section, different viscoelastic constitutive formulations are presented in 1D. The advantages and disadvantages of each form are discussed, specifically with regards to numerical implementation in existing commercial codes such as ABAQUS. We wish to use a viscoelastic constitutive model which is straightforward to implement numerically in MATLAB as well as using user-subroutines in ABAQUS. In this section, isothermal material conditions are considered, after which temperature and cure effects are discussed in the following section.

3.1 Differential Form (DF) Constitutive Equations

Differential Form (DF) constitutive equations are developed using the simple spring-damper models presented in the previous chapter. This will be done for a Maxwell and Kelvin model henceforth.

An equation describing the relation between stress and strain is obtained by any mechanical model by using equilibrium equations and kinematic equations for the system of interest, as well as constitutive equations for the elements (damper, spring) used. This is done below for a Maxwell and Kelvin (or *Voigt*) model:

Model:	Maxwell fluid	Kelvin solid
Equilibrium Equations:	$\sigma = \sigma_s = \sigma_d$	$\sigma = \sigma_s + \sigma_d$
Kinematic Equations:	$\epsilon = \epsilon_s + \epsilon_d$	$\epsilon = \epsilon_s = \epsilon_d$
Constitutive Equations:		
Spring	$\sigma_s = E\epsilon_s = \sigma$	$\sigma_s = E\epsilon_s$
Damper	$\sigma_d = \eta\dot{\epsilon}_d = \sigma$	$\sigma_d = \eta\dot{\epsilon}_d = \eta\dot{\epsilon}$
Differential Equations	$\dot{\sigma} + \frac{E}{\eta}\sigma = E\dot{\epsilon}$	$\sigma = E\epsilon + \eta\dot{\epsilon}$

In the above table, η is the viscosity and the subscripts s and d represent spring and damper specific stress or strain components. Obtaining the differential equation for the Maxwell model requires differentiating the constitutive equation for the spring and kinematic equation, while that of the Kelvin model only requires summation of each elements constitutive equation.

In a similar fashion, differential constitutive equations for models containing additional spring and damper elements in series or parallel can be found. We are now interested in obtaining solutions for the models above for a relaxation and creep type case. Subsequently, we will refer to a Maxwell model as a Maxwell element, to avoid confusion later when multiple Maxwell and Kelvin models are combined.

3.1.1 Maxwell element response

The differential equation for a Maxwell element as given earlier is:

$$\dot{\sigma} + \frac{E}{\eta}\sigma = E\dot{\epsilon} \tag{6}$$

or

$$\frac{d\sigma}{dt} + \frac{E}{\eta}\sigma = E\frac{d\epsilon}{dt} \tag{7}$$

For a relaxation test case, a constant strain input is used, i.e. $\epsilon(t) = \epsilon_0$, and consequently $\frac{d\epsilon}{dt} = 0$. The solution for relaxation is therefore:

$$\frac{d\sigma}{dt} + \frac{E}{\eta}\sigma = 0 \Rightarrow \frac{d\sigma}{\sigma} = -\frac{dt}{\eta}E \tag{8}$$

Note that $\tau \equiv \eta/E$. Upon integration from σ_0 at time 0 to $\sigma(t)$ at time t, we get:

$$\begin{aligned} ln\sigma &= -\frac{t}{\tau}t + c_1 \\ \sigma &= e^{(-t/\tau)+c_1} \Rightarrow \frac{\sigma_0}{\epsilon_0}e^{(-t/\tau)} \end{aligned} \tag{9}$$

Dividing by ϵ_0 gives:

$$\frac{\sigma(t)}{\epsilon_0} = \frac{\sigma_0}{\epsilon_0}e^{(-t/\tau)} \Rightarrow E(t) = Ee^{(-t/\tau)} \tag{10}$$

resulting in an expression for the material relaxation modulus. The stress output is then:

$$\sigma(t) = \epsilon_0 Ee^{(-t/\tau)} = \epsilon_0 E(t) \tag{11}$$

This is represented schematically in Fig. 8

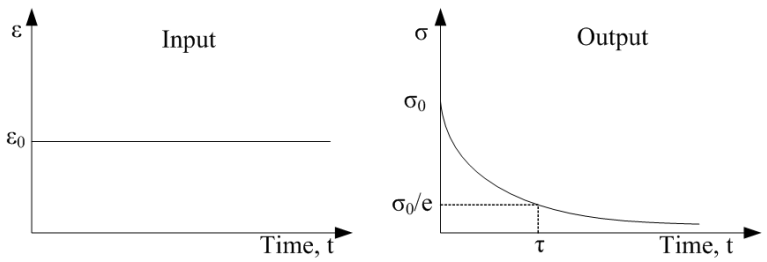

Fig. 8: *Relaxation of a Maxwell element. By dividing the initial stress σ_0 with an exponential function, the relaxation time can be determined.*

For a creep test case, a constant stress input is used, i.e. $\sigma(t) = \sigma_0$, and consequently $\frac{d\sigma}{dt} = 0$. The solution is found as:

$$\frac{d\epsilon}{dt} = \frac{\sigma_0}{\eta} \tag{12}$$

Upon integration from ϵ_0 at time 0 to $\epsilon(t)$ at time t, we get:

$$\epsilon(t) = \epsilon_0 + \frac{t}{\eta}\sigma_0 \Rightarrow \epsilon(t) = \frac{\sigma_0}{E} + \frac{t}{\eta} \tag{13}$$

Hence we get an expression for the strain response during a creep test. This is likewise represented schematically in Fig. 9, where creep-recovery is also shown, i.e. when the stress is instantaneously removed after some time. As expected, the strain increases during the constant stress loading and due to this does not fully recover to it's initial configuration.

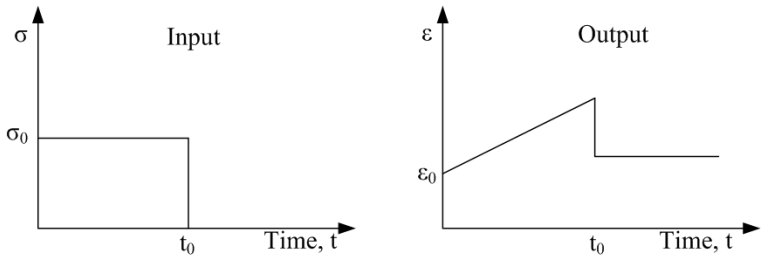

Fig. 9: *Creep and creep-recovery of a Maxwell element.*

3.1.2 Kelvin element response

The Kelvin element differential equation is:

$$\sigma = E\epsilon + \eta\dot{\epsilon} = E\epsilon + \eta\frac{d\epsilon}{dt} \tag{14}$$

The relaxation response of a Kelvin element, where a constant strain input is used, effectively reduces the above equation to Hooke's law as the strain rate is equal to zero. During a relaxation test, the constant strain is introduced quasi-statically, which would result in indefinite high stresses due to the damper response. Due to this, Kelvin elements are not adequate for relaxation modelling [16].

In the case of a creep test, $\sigma(t) = \sigma_0$, hence:

$$\sigma_0 = \epsilon E + \eta\frac{d\epsilon}{dt} \Rightarrow \frac{d\epsilon}{dt} + \frac{\epsilon}{\tau} = \frac{\sigma_0}{\eta} \tag{15}$$

Upon integration from ϵ_0 at time 0 to $\epsilon(t)$ at time t, using the integration factor $e^{(t/\tau)}$ we get:

$$\epsilon(t) = \frac{\sigma_0}{E}e^{(-t/\tau)} \tag{16}$$

where the creep compliance is:

$$D(t) = \frac{1}{E}e^{(-t/\tau)} \tag{17}$$

The Kelvin element response to creep is represented schematically in Fig. 10.

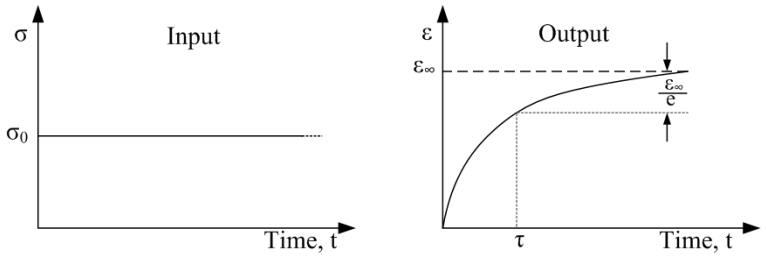

Fig. 10: *Kelvin element response during creep test. The relaxation time can be determined by division of the fully relaxed strain with an exponential function.*

3.1.3 Generalized models

The time dependent behaviour of real viscoelastic materials can be imitated by using a sufficient number of elastic and viscous elements. By increasing the number of Maxwell elements in parallel and Kelvin elements in series, generalized Maxwell and Kelvin models are achieved. These models are illustrated in Fig. 11. By having different spring moduli and damper viscosities, specific behaviour of a viscoelastic material can be approximated through parameter fitting.

The solution for a generalized Maxwell model with n Maxwell elements is found by superposition of each respective element's solution. Hence the response to creep would be:

$$\sigma(t) = \epsilon_0 \sum_{i=1}^{n} E_i \cdot exp\left[-\frac{t}{\tau_i}\right] \tag{18}$$

where E_i and τ_i are the $i'th$ element's stiffness and relaxation time respectively. The relaxation modulus is in this case:

$$E(t) = \sum_{i=1}^{n} E_i \cdot exp\left[-\frac{t}{\tau_i}\right] \tag{19}$$

Similarly the response of a generalized Kelvin model to creep is:

$$\epsilon(t) = \sigma_0 \left[\frac{1}{E_0} + \sum_{i=1}^{n} \frac{1}{E_i}\left(1 - exp\left[-\frac{t}{\tau_i}\right]\right)\right] \tag{20}$$

where the creep compliance is:

$$D(t) = \frac{1}{E_0} + \sum_{i=1}^{n} \frac{1}{E_i}\left(1 - exp\left[-\frac{t}{\tau_i}\right]\right) \tag{21}$$

The generalized Kelvin model can be used to represent a cross-linked material since the parallel arrangement of the springs and dampers does not allow complete stress relaxation [4]. This is also true for a generalized Maxwell model if one of the Maxwell elements is replaced with a spring [16], normally termed as a *Wiechert* Model. Wiechert type models are known to represent thermosetting polymer viscoelastic behaviour well, due to the single spring element representing un-breakable cross-links [4; 16].

The number of elements in the above generalized models is usually increased to fit specific material data. In doing so, the order of the differential equation grows, which can make implementation of this formulation impractical for complex material behaviour. For instance, a generalized Maxwell model consisting of n Maxwell elements (as shown in Fig. 11) will have the following differential equation:

$$p_o\sigma + p_1\frac{d\sigma}{dt} + ... + p_i\frac{d^i\sigma}{dt^i} + ... + p_n\frac{d^n\sigma}{dt^n} = q_o\epsilon + q_1\frac{d\epsilon}{dt} + ... + q_i\frac{d^i\epsilon}{dt^i} + ... + q_n\frac{d^n\epsilon}{dt^n} \tag{22}$$

where all p_i and q_i are constants consisting of damper and stiffness parameters, with i=1,...,n. For instance, for a model comprising $n = 2$ Maxwell elements in parallel we have:

$$\sigma + (\frac{\eta_1}{E_1} + \frac{\eta_2}{E_2})\frac{d\sigma}{dt} + (\frac{\eta_1}{E_1}\frac{\eta_2}{E_2})\frac{d^2\sigma}{dt^2} = (\eta_1 + \eta_2)\frac{d\epsilon}{dt} + (\frac{\eta_1^2}{E_1} + \frac{\eta_2^2}{E_2})\frac{d^2\epsilon}{dt^2} \tag{23}$$

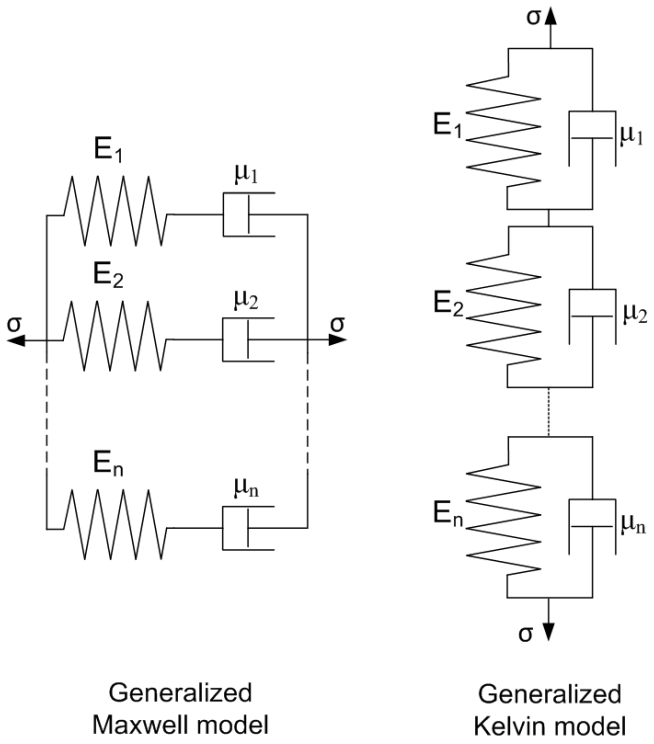

Fig. 11: *Generalized Maxwell and Kelvin models consisting of n Maxwell and Kelvin elements in parallel and series respectively.*

The increasing complexity of the above equation is apparent and makes numerical implementation of differential form viscoelastic models cumbersome and a disadvantage. A review of very limited applications in modelling where DF viscoelastic solutions are used, is given in Zobeiry [21].

3.2 Integral Form (IF) Constitutive Equations

To describe the behaviour of a linear viscoelastic material in integral form, the Boltzman superposition principle is applied (also referred to as the *Duhamel*'s integral). The constitutive equation is given as:

$$\sigma(t) = \int_0^t E(t-t')\frac{\partial \epsilon(t')}{\partial t'}dt' \tag{24}$$

Similarly:

$$\epsilon(t) = \int_0^t D(t-t')\frac{\partial \sigma(t')}{\partial t'}dt' \tag{25}$$

where D is the creep compliance. Essentially, the equations in IF represent the stress or strain output of a viscoelastic material as a sum of the output for each individual time increment up to the current time t. In order to do this, an important assumption on the material's behaviour is $linearity$ - i.e. superposition and proportionality conditions must prevail[4]. In other words, it is necessary that the response to stresses applied at any time to be superposable and that responses to different stress levels to be proportional.

In the above equation, mathematical expressions for the relaxation modulus or the creep compliance is needed. Discrete Prony series (exponential series) representations are normally used [4]. When modelling epoxy resins, the relaxation modulus can be expressed as [10; 11; 13]:

$$E(t) = E^{\infty} + (E^{u} - E^{\infty}) \sum_{i=1}^{n} w_i \cdot exp\left[-\frac{t}{\tau_i}\right] \tag{26}$$

where E^{∞} is the fully relaxed (or $rubbery$) resin modulus, E^{u} is the unrelaxed (or $glassy$) resin modulus, w_i are weight factors, τ_i are relaxation times and n is the number of Maxwell elements. A power law representation can also be used[10]:

$$E(t) = E^{u} \cdot exp\left[-\left(\frac{t}{\tau_i}\right)^{b}\right] \tag{27}$$

where b is a material constant and τ_p is the peak relaxation time. Kim & White [10] found that a single value of b is not sufficient to represent the stress relaxation behaviour of an epoxy resin over a wide temperature range. This makes the power law form unsuitable for process modelling cases. Ruiz & Trochu [12] have however, modified the power-law formulation for a polyester resin, resulting in a simple precise model for the relaxation modulus without the use of extensive least-square fitting techniques for the determination of prony series data:

$$E(t) = E^{u} \cdot exp\left[-\Omega_1 (t+\tau_0)^{\Omega_2}\right] (t+\tau_0)^{-\Omega_3} \tag{28}$$

where Ω_1,Ω_2,Ω_3 and τ_0 are material constants. However, determination of these constants can be cumbersome.

Note on recursive formulations to minimize memory needs
Before concluding, a note should be made on the practicality or ease of implementation in numerical codes of the DF and IF formulations presented above. Customary for viscoelastic models is that the entire history of the material needs to be accounted for for accurate prediction of stress or strain at the current time. If the above given expressions are to be calculated for an arbitrary FE model at each integration point, from time $t = 0$ to current time $t = t$, for every time increment as the simulation (process) time marches forward, this would be extremely computationally expensive and time consuming. Due to this, a number of recursive formulations for viscoelastic models exist in literature, designed for numerical implementation, see for instance [6; 17; 23]. These recursive formulations allow for storage of stresses from previous solutions, used for the solution at the current time step when using constitutive models in incremental form. Hence instead of recalculating the entire time history of a loading scenario at each new increment in time, only state data from the previous calculation time increment is needed, which drastically reduces data storage memory requirements.

3.3 Summary

The two main constitutive equation formulations for a viscoelastic material have been presented. The differential form viscoelastic model is simple to understand due to the mechanical analogies used with springs and dampers, but cumbersome to implement numerically for complex material behaviour due to the rapidly growing order of the general constitutive differential equation when the number of elements used is increased. On the other hand, the integral form viscoelastic model

formulation is more suitable with regards to numerical model implementation as the use of Prony series representation of the material stiffness greatly simplifies the constitutive equation.

Due to the apparent advantageous of the integral form method, the constitutive equations in this form will be used subsequently unless stated otherwise.

4 Temperature and Cure Behaviour

In the previous section, isothermal viscoelastic constitutive models are presented. In this section, temperature and cure effects are presented and methods for including these effects in the constitutive equations used to model thermosetting polymers are presented and discussed.

4.1 Temperature Effects on Viscoelastic Behaviour

In Section 2 it was shown that polymers exhibit temperature dependent viscoelastic behaviour. Generally, fully-cured polymers exhibit glassy, transition, rubbery and flow viscoelastic behaviour upon heating. Thermosets do not exhibit flow behaviour and instead degrade when submitted to prolonged elevated temperatures. This is illustrated in Fig. 12.

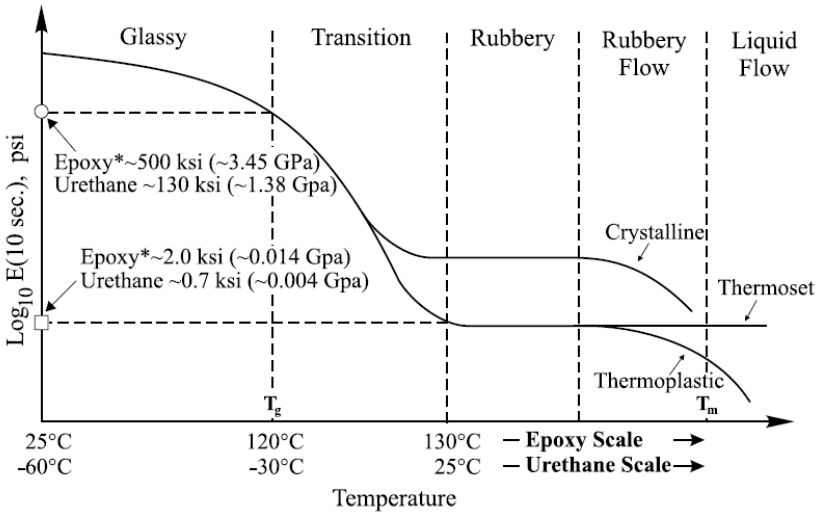

Fig. 12: *Generic temperature dependent relaxation modulus for an epoxy and urethane polymer (From Brinson (2008))[4]. Note that the Epoxy and Urethane behave similarly at different temperatures respective of their T_g.*

The Time-Temperature-Superposition-Principle is used to determine *master curves* - a complete modulus-time curve at a constant temperature, ranging many decades in time. This is needed, for instance in cases where material properties after 2, 10, 20 years are necessary. This principle builds upon the assumption that time and temperature effects on a polymer are similar. Materials exhibiting this form of temperature dependence are known as thermorheologically simple. Thus, applying the time-temperature correspondence principle to experimental data, a measure of the complete modulus-time behaviour is achieved.

During relaxation or creep tests, it is normally only possible to conduct these tests below 4 decades in time [16]. But when these isothermal tests are conducted at different temperatures, it has been shown that results can be used to form a master curve at one temperature. This is illustrated in Fig. 13, where relaxation test results at different temperatures are shifted to form a master curve for 90°C. In doing so, a continuous curve for the relaxation modulus able to describe the material behaviour for long times (in this case 2 years) is achieved.

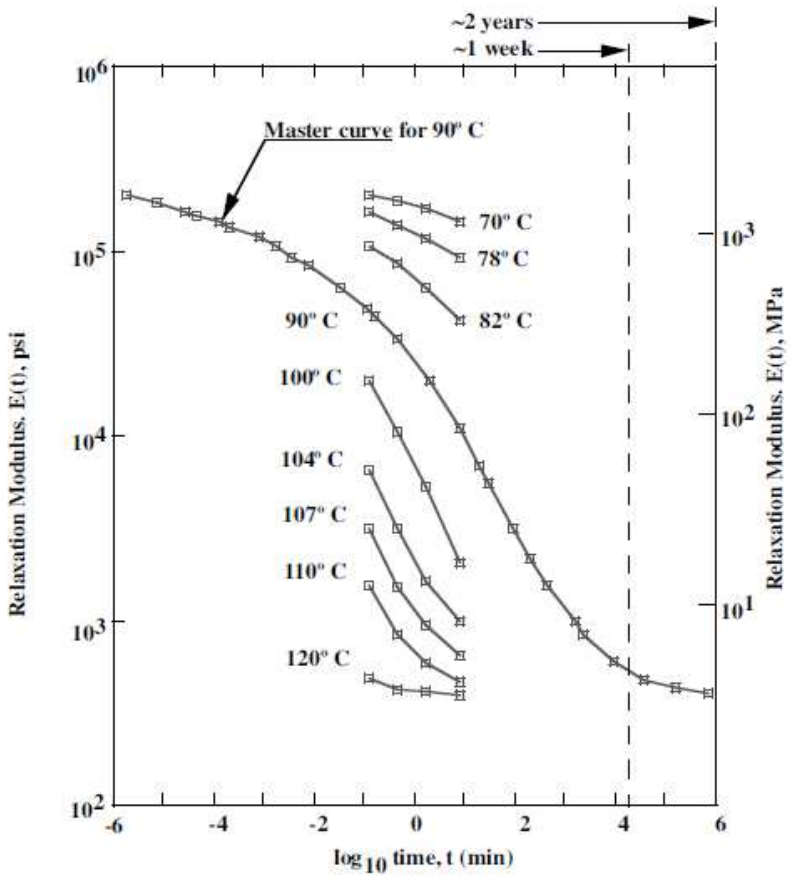

Fig. 13: *Master curve for a modified epoxy. (Data from Cartner in [4])*

Mathematically, the time-temperature equivalence can be expressed as [16]:

$$E(t, T_1) = E(t/a_T, T_2) \tag{29}$$

stating that the modulus at time t at one temperature T_1 is equal to the modulus at temperature T_2 at the time $t = t/a_T$, where a_T is the temperature shift function. The shift function is generally found using the WLF equation (from M.L. Williams, R.F. Landel and J.D. Ferry [9]):

$$log(a_T) = log\left(\frac{\tau(T)}{\tau(T_0)}\right) = \frac{-C_1(T - T_0)}{C_2 + (T - T_0)} \tag{30}$$

where the C_1 and C_2 are constants and have the "universal" values of 17.44 and 51.6 respectively under the assumption that the glass transition temperature T_g is used as the reference temperature T_0. During their work, Williams, Landel and Ferry found different values for C_1 and C_2 for different polymers. These values are found in Ref. [9]. The universal WLF values are averaged values obtained by fitting data from a large number of polymers. It should be noted that use of the universal values should only be done as a last resort in absence of other specific data, unless T_0 is substituted with the glass transition temperature T_g. The reason for choosing T_g is founded on the notion that all amorphous polymers (like thermosets) at their glass transition temperature have similar viscoelastic behaviour. In other words T_g is a good reference point, as also seen in Fig. 12, where the different polymers have similar behaviour respective of their T_g.

Having an expression for the shift factor a_T, temperature dependence can now be implemented and Equations (24) and (25) can be rewritten as:

$$\sigma(t) = \int_0^t E_{T_0}(\xi(t) - \xi(t'))\frac{\partial \epsilon}{\partial t'}dt' \tag{31}$$

and:

$$\epsilon(t) = \int_0^t D_{T_0}(\xi(t) - \xi(t'))\frac{\partial \sigma}{\partial t'}dt' \tag{32}$$

where $\xi(t)$ and $\xi(t')$ are the so called *reduced times* defined as:

$$\xi(t) \equiv \int_0^t \frac{1}{a_T}\zeta \quad and \quad \xi(t') \equiv \int_0^{t'} \frac{1}{a_T}\zeta \tag{33}$$

Essentially the function of the shift factor is to make "time run faster or slower" depending on the difference between the current temperature and reference temperature. This is illustrated in Fig. 14. As is seen, when the temperature is higher than the reference temperature ($T - T_g$ = positive), the shift factor is negative and vice versa, essentially increasing or reducing the actual time. Note that the shift factor at reference temperature ($T - T_g$ = 0) is 1.0 (log(a_T)=0).

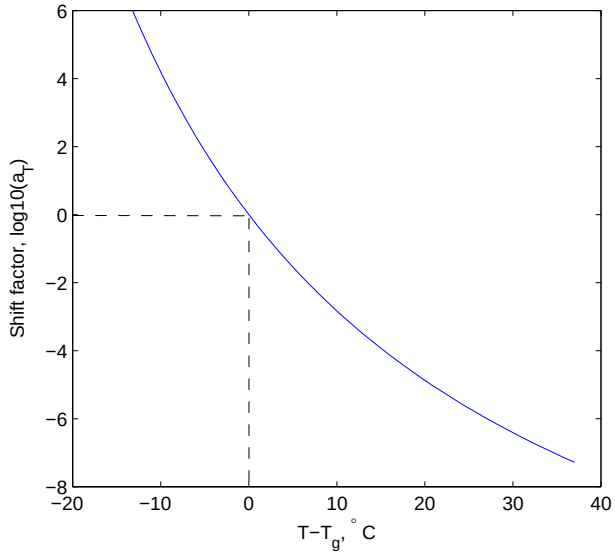

Fig. 14: *Graph of the WLF equation using C_1=17.44 and C_2=51.6*

Before carrying on to the cure dependence, a quick note on the glass transition temperature is needed. A polymer's T_g can be determined as the point where the material exhibits a change in its thermal expansion behaviour as a result of the change in the material properties at gelation, or the peak loss modulus during dynamic testing [4; 9; 16]. Due to this discontinuity, Ferry (1961) noted that the WLF equation is known to be only valid above the T_g. A shift factor below the T_g is developed based on Arrhenius activation energy equation, which is more valid [4]:

$$log(a_T) = log\frac{\tau(T)}{\tau(T_g)} = -\frac{E_a}{2.303R}\left(\frac{1}{T} - \frac{1}{T_g}\right) \tag{34}$$

where E_a is the activation energy and R is the gas constant. To account for effects above and below T_g, i.e. WLF and Arrhenius behaviour, a generalized Vogel equation is used [13]:

$$log(a_T) = log\frac{\tau(T)}{\tau(T_g)} = \frac{C}{T - T_\infty} - \frac{C}{T_{ref} - T_\infty} \tag{35}$$

where C is a constant, T_∞=0K is the absolute temperature and T_{ref} is the reference temperature for the viscoelastic master curve of the fully cured material ($\alpha = 1.0$). Before going further with the different shift factor equations, the addition of cure dependence to the viscoelastic models is described.

4.2 Cure Dependence

To describe how cure dependence in viscoelastic constitutive models for thermosets is included, two main references will be used; the work by Simon, McKenna & Sindt [13] and that of Kim & White [10]. In both studies, the evolution of mechanical properties of two different epoxy resins during cure are studied, with good correlation between experimental results and models. These works are also amongst the most referenced wrt. modelling of cure and temperature dependent polymer viscoelastic behaviour (see for instance [11; 17; 20; 21]).

As described earlier, the effects of temperature on the polymer are accounted for by applying the principles of time-temperature superposition, where a temperature shift factor a_T is used. In a similar manner, the effects of the cure degree (or $conversion$) can be accounted for by applying time-conversion superposition, using a cure shift factor a_α as done by Simon, McKenna & Sindt [13]:

$$log(a_\alpha) = log\left(\frac{\tau(T_g(\alpha))}{\tau(T_g(\alpha_{ref}))}\right) = -\left(\frac{C}{T_g(\alpha) - T_\infty} - \frac{C}{T_g(\alpha_{ref}) - T_\infty}\right) \tag{36}$$

where cure degree-dependent glass transition temperatures are used. Assuming that the reference cure degree α_{ref}=1.0 and that T_{ref}=$T_g(\alpha_{ref})$, then the cure shift factor a_α and temperature shift factor a_T can be combined to give:

$$log(a_{T,\alpha}) = log\left(\frac{\tau(T, T_g(\alpha))}{\tau(T_{ref}, T_g(\alpha_{ref}))}\right) = \frac{C}{T - T_\infty} - \frac{C}{T_g(\alpha_{ref}) - T_\infty} \tag{37}$$

In the above equation, cure degree dependence is included by having a cure dependent glass transition temperature given by the DiBenedetto equation:

$$\frac{T_g - T_{go}}{T_{g\infty} - T_{go}} = \frac{\lambda\alpha}{1 - (1 - \lambda)\alpha} \tag{38}$$

where T_{go} is the T_g of the polymer monomer, λ is a material constant (usually = 0.43). By isolating T_g in the above equation, the cure degree dependent glass transition temperature can be determined. In a similar manner, the WLF equation presented previously can be made cure dependent by using the DiBenedetto equation. Hence the relaxation modulus (Equation (26)) would become:

$$E(\alpha, T, t) = E^\infty + (E^u - E^\infty)\sum_{i=1}^{n} w_i \cdot exp\left[-\frac{t}{a_{T,\alpha} \cdot \tau_i}\right] \tag{39}$$

An alternative approach is proposed by Kim & White (1996). In this work, experimental studies of the viscoelastic behaviour of 3501-6 Epoxy resin during cure are conducted. From experimental testing at different cure degrees, it is seen that the peak stress relaxation time τ_p increases as the degree of cure increases. Assuming that this is also true for the stress relaxation behaviour at any cure degree, an expression for the discrete relaxation time at any cure degree was formulated, using discrete relaxation times at a reference degree of cure:

$$log(\tau_i(\alpha)) = log(\tau_i(\alpha^0)) + \left[f'(\alpha) - (\alpha - \alpha^0) log(\lambda_i')\right] \tag{40}$$

where τ_i is each discrete relaxation time, α^0 is the reference degree of cure where the stress relaxation is known and:

$$f'(\alpha) = \frac{T_g(\alpha)}{T_g(\alpha^0)} - 1 \tag{41}$$

$$\lambda_i' = \frac{\tau_p(\alpha^0)}{\tau_i(\alpha^0)} \tag{42}$$

where $\tau_p(\alpha^0)$ is the peak relaxation time at the reference cure degree. Having a cure dependent expression for the relation times, a separate temperature shift factor is used:

$$log(a_T) = c_1(\alpha)T + c_2(\alpha) \tag{43}$$

where:

$$c_1(\alpha) = -a_1 \cdot exp\left[\frac{1}{\alpha - 1}\right] - a_2 \tag{44}$$

$$c_2(\alpha) = -T_{ref} \cdot c_1(\alpha) \tag{45}$$

where a_1 and a_2 are constants. The above equations for the temperature shift factor are built on the assumption of a linear relation between time-temperature superposition, but with changing gradient as a function of the cure degree. Hence the relaxation modulus (Equation (26)) in this case would become:

$$E(\alpha, T, t) = E^{\infty} + (E^u - E^{\infty}) \sum_{i=1}^{n} w_i \cdot exp\left[-\frac{t}{a_T \cdot \tau_i(\alpha)}\right] \tag{46}$$

Having the different approaches presented above, a comparison of the shift factors using material parameters in [9], [13] and [10] respectively is calculated and presented in Fig. 15 for different cure degrees ranging 0.2-1.0. It should be noted that most resins encounter gelation at a cure degree of app. 0.4-0.6, why the results shown below this cure degree do not have any physical meaning but are presented here purely to catch the tendencies from the different shift factor expressions.

In Fig. 15 it should be noted that the shift factor proposed by Kim & White is calculated using the same T_g as in the other cases, which might not be strictly valid. The Kim & White model is strictly formulated for their test results where T^0=30°C is the reference temperature and where the curves intercept at [30,0] (i.e. 30degrees and shift factor equal zero).

In the Vogel-type shift function, a similar trend as observed by Kim & White is seen; the slope of the shift function increases when the cure degree decreases.

In work done by Brinson [4], $log(a_T)$ for an epoxy resin ranges from -4 to 6 in order to achieve a smoothly continuous creep compliance master curve from creep test data at different temperatures.

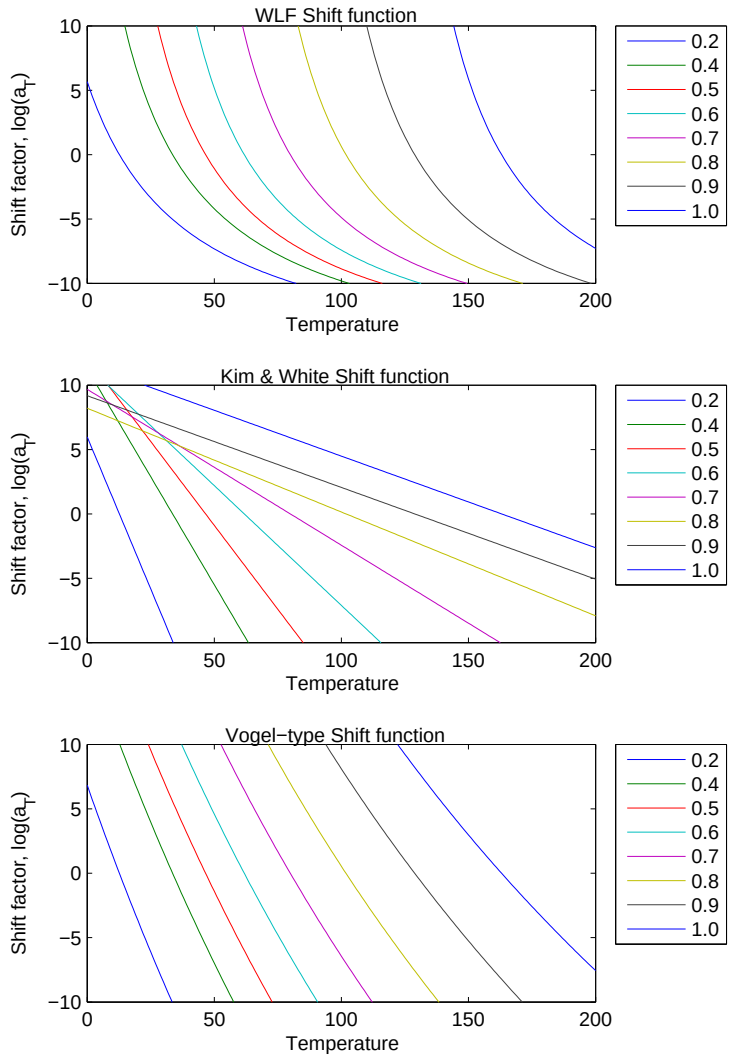

Fig. 15: *Time-temperature-cure degree shift factors as a function of temperature and cure degree using the WLF equation [9] (top), model by Kim & White (1996)[10] (center) and Vogel-type expression as done in Simon et al. (1999)[13] (bottom)*

Along this range the differences in the WLF and Vogel-type formulations in Fig. 15 are not that significantly different. However, common for the approaches presented above is that no proof of validity is present in the literature for the combination of degree of cure with time-temperature superposition, though the WLF-type expressions are very popular. In the subsequent sections, the model proposed by Kim & White will be used.

4.3 Summary

In this section, temperature- and cure-dependence has been discussed and different models have been presented. In the following sections, the viscoelastic model will be tested.

5 Numerical Implementation

In this section the approach used for the numerical implementation of the viscoelastic constitutive equations presented in the previous sections is described and validation experiments are carried out.

5.1 Overview of problem

Before a description of how the temperature and cure dependent viscoelastic constitutive equations (e.g. equation (39) or (46)) are implemented, a note on why it is necessary to convert these equations into incremental form is given. The problem which we essentially wish to solve may be referred to as a linear 3D quasi-static uncoupled thermoviscoelastic initial/boundary value problem. This problem in turn becomes orthotropic if a composite material is used. The governing equations needed to solve such a problem would be derived from:

- conservation of mass
- conservation of momentum
- kinematic constraints
- material constitutive equations
- laws of thermodynamics
- Initial and boundary conditions (mechanical and thermal)

In this work, we wish to use the user-subroutine capabilities of ABAQUS to solve the problem, why only a definition of the material constitutive equations is needed. In order to do this using the user-material subroutine UMAT, the stress increment and Jacobi matrix (tangent stiffness matrix) need to be defined. This can be efficiently done using a constitutive equation in incremental form, one for which a viscoelastic material would require minimum storage of material history dependent parameters.

5.2 Incrementalization of the viscoelastic constitutive equation

The derivation of an incrementalization of the viscoelastic constitutive equation as proposed by Zocher [22] is used subsequently due to the following key arguments:

1. The incremental form of the viscoelastic constitutive equation is accomplished in closed-form, resulting in a simple recursive relationship needed to account for material history, as linear algebraic equations
2. Constant strain rate across a time step is assumed as opposed to constant stress or strain resulting in a model capable of solving relaxation-type and creep-type behaviour. As stated in Zocher $et.al.$ [23], FE formulations, where constant stress over each time step is assumed, result in good creep-like behaviour but are poor in the prediction of relaxation behaviour.

Alternatively, formulations where a constant strain is assumed, adequately predict relaxation behaviour and are poor at creep-like behaviour.

3. Lastly, the formulation allows for simple change of the phenomenological mechanical model used, be it a generalized Kelvin model, Wiechert model etc. Along this line simple adjustment of the number of elements used in these models is possible.

The formulations proposed by Zocher are summarized subsequently. An in-depth description can be found in [14; 15; 22; 23]. The main difference here consists of the cure-dependence.

Firstly, the concept of reduced time is used and subdivided into discrete intervals such that $\xi_{n+1} = \xi_n + \Delta\xi$. The general integral form constitutive equation in 3D is:

$$\sigma_{ij}(\xi) = \int_0^{\xi} C'_{ijkl}(\xi - \xi') \frac{\partial \epsilon_{kl}(\xi')}{\partial \xi'} d\xi' \tag{47}$$

This can be written incrementally as:

$$\Delta\sigma_{ij} = C'_{ijkl}\Delta\epsilon_{kl} + \Delta\sigma^R_{ij} \tag{48}$$

where:

$$\xi(t) \equiv \int_0^t \frac{1}{a_{T,\alpha}}\zeta \quad and \quad \xi(t') \equiv \int_0^{t'} \frac{1}{a_{T,\alpha}}\zeta \tag{49}$$

$$C'_{ijkl} = C^{\infty}_{ijkl} + \frac{1}{\Delta\xi}\sum_{m=1}^{N} \eta_{ijkl_m}\left(1 - exp\left[-\frac{\Delta\xi}{\tau_m}\right]\right) \tag{50}$$

Here, a Wiechert model with N elements is used here. The viscosity of each element η_m is given as a tensor because $\eta_{ijkl_m} = \tau_m \cdot C_{ijkl_m}$. The stress residual is given as [22]:

$$\Delta\sigma^R_{ij} = -\sum_{m=1}^{N}\left(1 - exp\left[-\frac{\Delta\xi}{\tau_m}\right]\right) S_{ijkl_m} \tag{51}$$

where the internal state variable is defined as:

$$S_{ijkl_m} = exp\left[-\frac{\Delta\xi}{\tau_m}\right] S_{ijkl_m}(\xi_n - \Delta\xi) + \eta_{ijkl_m}\dot{\epsilon_{kl}}\left(1 - exp\left[-\frac{\Delta\xi}{\tau_m}\right]\right) \tag{52}$$

Here, the tensor $S_{ijkl_m}(\xi_n - \Delta\xi)$ is the "old" internal state variable from the previous step. In the above equations, a key assumption is the approximation:

$$\frac{\partial \epsilon_{kl}(\xi')}{\partial \xi'} \approx \dot{\epsilon_{kl}} \equiv \frac{\Delta\epsilon_{kl}}{\Delta\xi} \tag{53}$$

where $\Delta\epsilon_{kl}/\Delta\xi$ is known from the previous step at reduced time ξ_n. Having an expression of the stress increment, the new stress can be updated at the end of each time step as:

$$\sigma_{ij}(\xi_{n+1}) = \sigma_{ij}(\xi_n) + \Delta\sigma_{ij} \tag{54}$$

For the equations presented above, in the current work only a simple single parameter model will be used, i.e. $N = 1$. For materials where multiple discrete relaxation times and weighting factors

are needed in order to accurately describe the material behaviour, the size of the internal state variables increases with the number of parameters used. For instance, if 10 discrete τ_m values are used, 10 different sets of the internal state variable S_{ijkl_m} must be saved for each integration point in each increment. The increase in memory need is apparent.

In other works (for instance [5; 6]) a similar approach using a constant strain rate assumption is used with the exception that the general state of stress is subdivided into deviatoric and dilatoric stress tensors. Separating the stress tensor into dilatational (volumetric) and deviatoric components is a result of the observation that viscoelastic and/or plastic deformations in materials are predominantly a result of changes in shape [4]. Hence volumetric effects can be neglected simplifying the initial/boundary value problem.

5.2.1 Note on Viscoelastic Micromechanics

When considering multiple-phase materials such as composites, approximations of equivalent mechanical properties are for instance determined using micromechanic relations based on the volume fraction of each constituent (here fibre and matrix) and their respective mechanical properties. For elastic models, elastic micromechanic expressions exist, see e.g. [3; 18; 19]. However, for viscoelastic models, a more cumbersome approach exists. Here, an elastic-viscoelastic analogy is used. First, the time dependent constituents are Laplace transformed into the frequency domain, after which the effective mechanical properties of the composite are calculated using elastic micromechanical formulations in the Laplace domain. Finally, inverse Laplace transformation is applied yielding the solution in time domain of the effective modulus of the composite. Since an exact solution is not always found, approximation or numerical techniques are needed. Lastly, to be able to implement this in a recursive formulation, an additional curve-fit after obtaining the time-dependent modulus is necessary. It is clear that many steps are needed in this approach.

White & Kim [17], use an alternative approach as will be adapted in this work. In their approach, the effective stiffnesses of the composite material are modelled directly based on the response of the matrix material. Furthermore, fibre-reinforcement dominated composite mechanical properties (for instance the longitudinal stiffness in a uni-directional composite layup) remain elastic and do not vary with time. Therefore in this approach, effective composite stiffness matrices in the glassy and rubbery state (or unrelaxed and fully relaxed states) are found and the time-dependent behaviour of the composite follows the Prony series representation presented in equation (50). Essentially, we assume that the viscoelastic behaviour of the composite follows the same behaviour of the epoxy during cure.

5.3 Validation test cases

The incremental constitutive equation presented above is implemented in MATLAB for a simple 1D isotropic model, as well as in ABAQUS using the material user-subroutine UMAT, for a 3D isotropic material. Simple tests are carried out to validate the numerical model for different isothermal loading cases representing relaxation, creep and creep-recovery tests. Analytical (exact) solutions are used for comparison, adapting a similar approach here as in [22]. An illustration of the uniaxial bar used in the 1D tests is seen in Fig. 16.

In all test cases, the test bar has a unit length, unit cross-section and material parameters E_∞=0.1[MPa], E_0=0.4[MPa] and relaxation time τ=1[s].

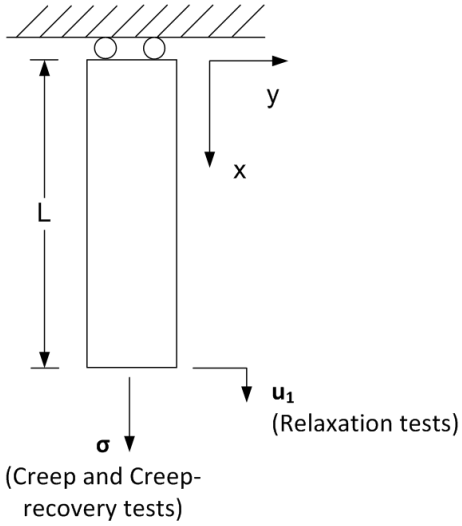

Fig. 16: *Illustration of uniaxial test bar used in test cases*

5.3.1 Relaxation test

In a relaxation test, a constant displacement $u1$ is applied resulting in a constant strain of $\epsilon(t)$= ϵ_0= $1.0E-3$. The exact analytical solution for this case is:

$$\sigma(t) = \epsilon(t)E(t) = \frac{u_1}{L}\left[E_\infty + E_0 \cdot e^{(-t/\tau)}\right] \tag{55}$$

The model prediction using a time step $dt = 0.01[s]$ and analytical solution are shown in Fig. 17; the results match well. The fairly small time step chosen is a result of the need to apply the load instantaneously.

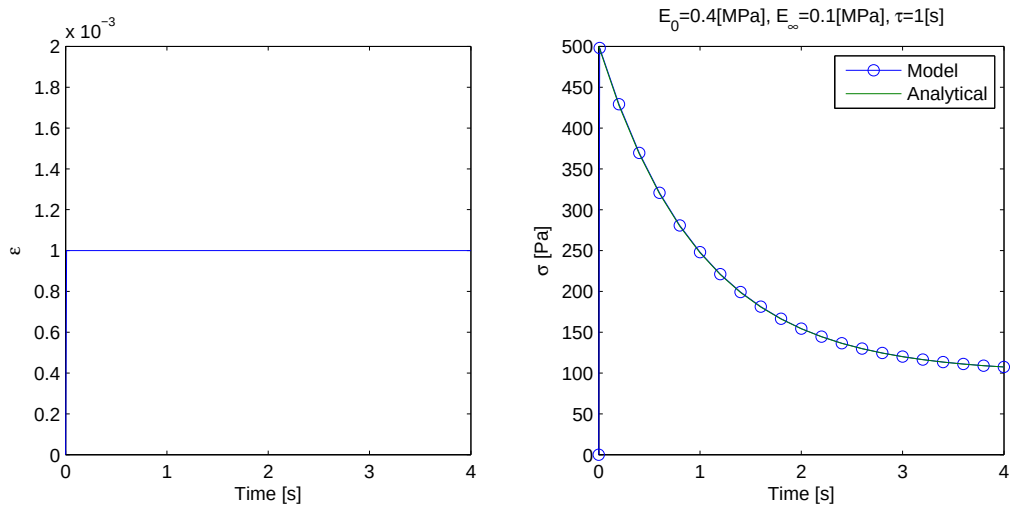

Fig. 17: *Constant strain load input (left) and stress response (right) for relaxation test.*

5.3.2 Constant strain rate test

In this test, a constantly increasing displacement is prescribed resulting in a strain rate defined by $\epsilon(t) = \epsilon_0 \cdot t = 1.0E-3 \cdot t$. This test is also referred to as a constant ramp displacement test. The analytical solution for this case is given as:

$$\sigma(t) = E_\infty \epsilon_0 t + E_0 \tau \epsilon_0 \left(1 - e^{(-t/\tau)}\right) \tag{56}$$

The numerical model prediction using a time step $dt = 1[s]$ and analytical solution are shown in Fig. 18; the results match well. In this case, no instantaneous loading is applied, why for this case, the solution is practically time step-independent - since our assumption of a constant strain rate across the time step (Equation (53)) is met.

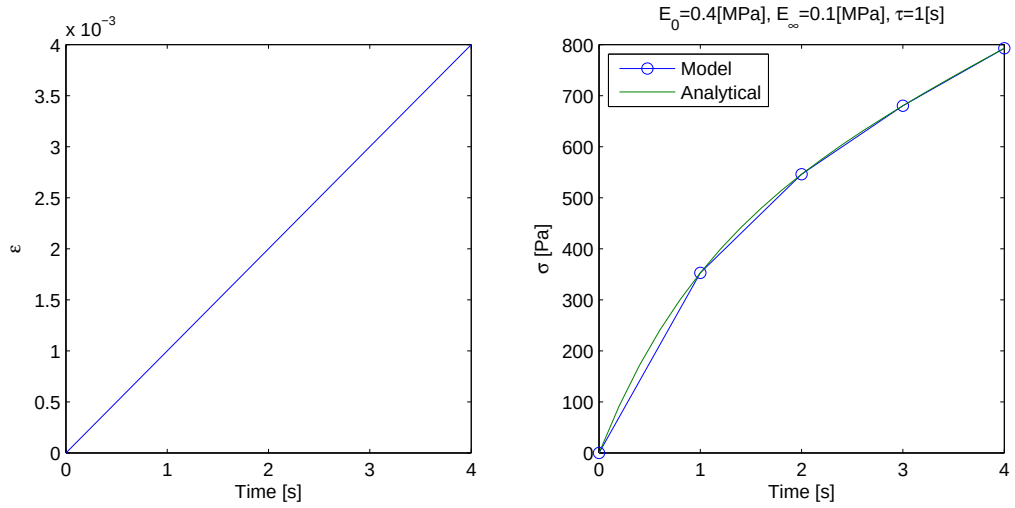

Fig. 18: *Constant strain rate load input(left) and stress response (right).*

5.3.3 Creep test

In this test, a constant stress is prescribed as $\sigma(t) = \sigma_0 = 1.0E3[Pa]$. The analytical solution for a creep test is given as:

$$\epsilon(t) = \sigma_0 D(t) = \sigma_0 \left[D_0 + D_1 \left(1 - e^{(-t/\lambda)}\right)\right] \tag{57}$$

where:

$$D_0 = \frac{1}{E_\infty + E_0} \tag{58}$$

$$D_1 = \left(\frac{1}{E_\infty} - \frac{1}{E_0}\right) \tag{59}$$

$$\lambda = \frac{E_0 \tau}{E_\infty} \tag{60}$$

The numerical model prediction using a time step $dt = 0.01[s]$ and analytical solution are shown in Fig. 19; the results match well. Once again the fairly small time step chosen is a result of the need to apply the load instantaneously.

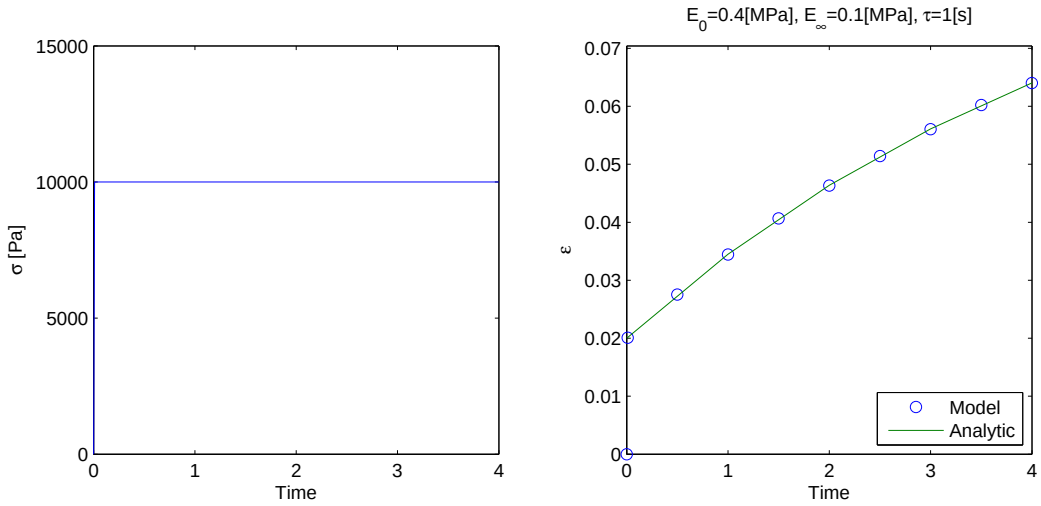

Fig. 19: *Constant stress load input (left) and strain response (right) for creep test.*

5.3.4 Creep-recovery test

In this example, the uniaxial bar is submitted to a similar initial load as done in the previous creep test. The load is then removed after 10[s] and recovery-behaviour is analysed. Such a load input can be expressed using a step-function $H(t)$, also known as the *heavy side function*. In this case, $\sigma(t) = \sigma_0 H(t)$ - $\sigma_0 H(t - t_1)$, where $t_1 = 10[s]$. The exact solution in this case is:

$$\epsilon(t) = \sigma_0 \left[D(t) + D(t - t_1) H(t - t_1) \right] \tag{61}$$

The model prediction using a time step $dt = 0.01[s]$ and analytical solution are shown in Fig. 20. Using $dt = 0.01[s]$ it is seen that the numerical model results in similar results as the analytical solution.

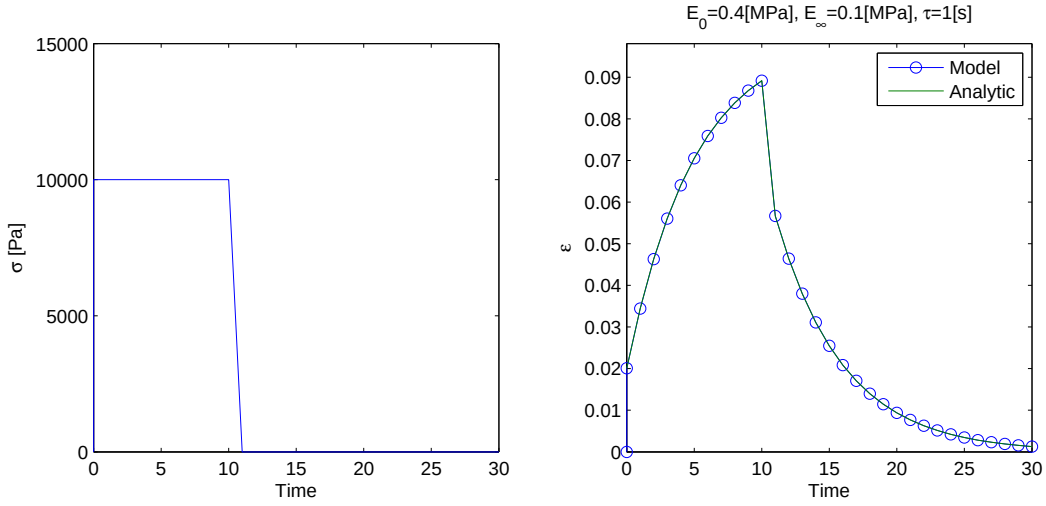

Fig. 20: *Creep-recovery stress input (left) and strain response (right).*

5.4 Time step dependence

While carrying out similar validation tests in the 3D ABAQUS model, it was found that time step (TS) dependence exists when compared to the relaxation time used. Different ratios of the relaxation time vs. time step were investigated for a similar relaxation test as presented above:

$$ratio = \frac{\tau}{\text{time step}} \tag{62}$$

with constant time steps dt ranging between 0.1 to 100[s] and relaxation times ranging between 1 to 100[s]. From the analytical solution it is known that the fully relaxed stress after a total time of 30[s] is $\sigma_\infty = 100[Pa]$. Final stress results using different ratios are shown in Tab. 1

	τ = 1[s] / ratio	τ = 10[s] / ratio	τ = 100[s] / ratio
dt=100	213.960 / 0.01	215.970 / 0.1	212.166 / 1
dt=10	213.960 / 0.1	212.452 / 1	133.844 / 10
dt=1	209.903 / 1	133.417 / 10	103.890 / 100
dt=0.1	132.845 / 10	103.537 / 100	100.359 / 1000

Tab. 1: Fully relaxed stresses using different relaxation time-time step ratios. For comparison, the exact solution is $\sigma_\infty = 100[Pa]$.

From the results presented in Tab. 1, it can be deduced that when carrying out simulations where large time steps are used compared to the material relaxation time, an error in results may be present. It should be noted of course that it is highly unlikely that the relaxation times for a real material are as small as the ones used in the tests. For instance, for the epoxy shown in Fig. 13, full relaxation occurs after a time span of approximately 2 years at 90°C and approximately 10minutes at 120°C. Due to this fairly large difference over a small difference in temperature it is important to have the above mentioned ratio in mind for accurate results during for instance stress relaxation calculations.

6 Comparison of Viscoelastic and Linear Elastic model

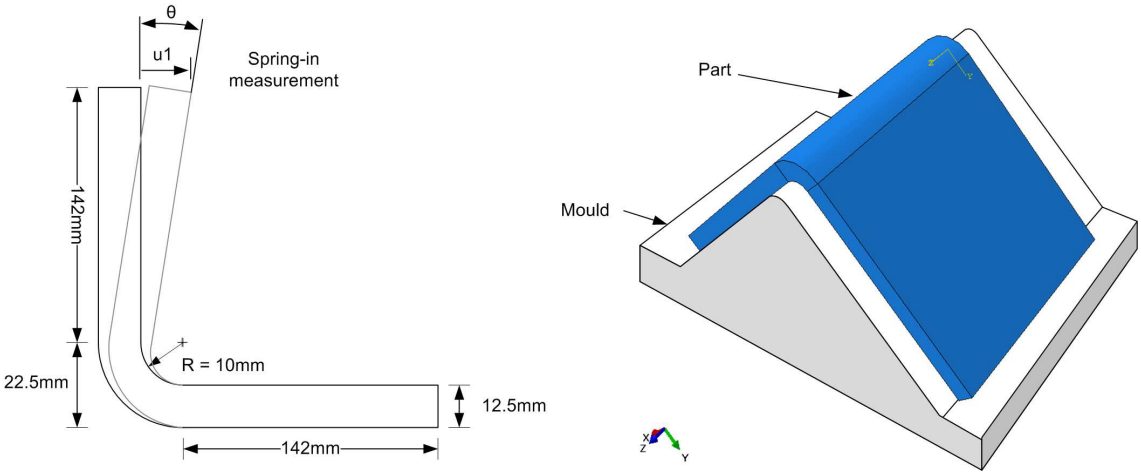

Fig. 21: *L-profile cross section geometry and illustration of part-mould configuration. Profile length (extruded) is 150[mm].*

A glass/epoxy laminate composite L-profile, similar to that in work by Svanberg [15], is modelled using the geometry illustrated in Fig. 21. The part is 150mm wide and modelled using brick elements (linear) in ABAQUS. Only the part is modelled. The mechanical properties for the woven glass fibre reinforced laminate with a volume fraction V_f=56% are shown in Tab. 2 in both glassy and rubbery state.

Property	Glassy state	Rubbery state
E_x [GPa]	26.2	21.4
E_y [GPa]	26.2	21.4
E_z [GPa]	10.1	2.7
ν_{xy} [-]	0.094	0.0021
ν_{xz} [-]	0.46	0.83
ν_{yz} [-]	0.46	0.83
G_{xy} [GPa]	3.0	0.033
G_{xz} [GPa]	2.9	0.033
G_{yz} [GPa]	3.0	0.033
α_x [10^{-6}/°C]	13.9	5.4
α_y [10^{-6}/°C]	13.9	5.4
α_z [10^{-6}/°C]	58.7	229.0
β_x [-]	-3.2·10^{-3}	-7.4·10^{-5}
β_y [-]	-3.2·10^{-3}	-7.4·10^{-5}
β_z [-]	-1.9·10^{-2}	-3.2·10^{-2}

Tab. 2: *Mechanical properties of woven glass/epoxy laminate with V_f=56% [15]. α_i is the thermal expansion coefficient and β_i the chemical shrinkage constant, given for the normal material directions.*

Using the properties given in Tab. 2, effective stiffness matrices in the glassy and rubbery state are constructed and used in a Cure Hardening Linear Elastic (CHILE) model and the viscoelastic model presented earlier. Not all aspects of the process will be presented here but to give an idea of the process, the temperature and resulting cure degree development experienced at the middle of the center plane of one of the L-profile's flat sides is shown in Fig. 22. The numerical models in ABAQUS are constructed as sequentially coupled thermal-mechanical analyses, where the thermal history is the same for both the constitutive linear elastic and viscoelastic models investigated. User subroutines HETVAL, UEXPAN and UMAT, which are programmed in FORTRAN are used to calculate the cure kinetics and volumetric heat generation, process-induced strains and mechanical properties respectively.

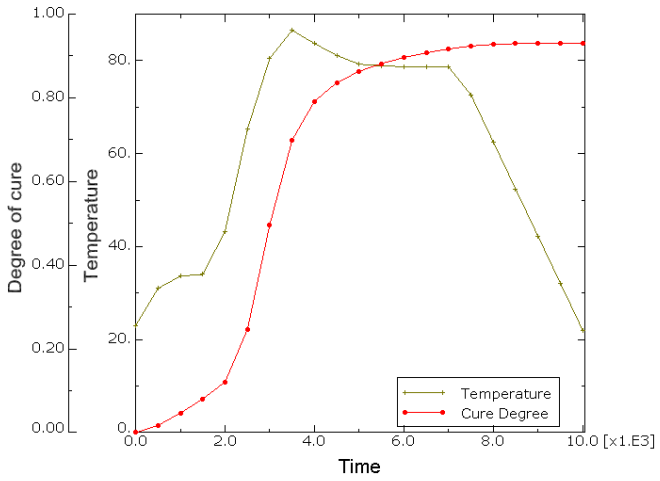

Fig. 22: *Temperature profile and cure degree development experienced at the middle of the centre plane of the flat L-profile sides. The temperature profile is similar to that measured experimentally in the work by Svanberg [15].*

Two mechanical boundary conditions are assumed in the simulations; Free standing and Fixed. In the Free mechanical boundary conditions, only the bottom of the L-profile is supported such that shape distortion of the part during a prescribed cure-cycle is still allowed. In the Fixed case, all nodes along the L-profile inner surface plane are fully constrained, resembling a fully fixed tool-part configuration to a stiff tool with negligible thermal expansion (see Fig. 21 (right)). After the cure cycle simulation is completed, the boundary conditions in the Fixed case are suppressed, allowing the release of stresses over a given time period of 5E3[s]. This replicates demoulding, where the constraints that might be present between the part and tool are removed. For more information on constituent material parameters (fibre and resin) and process settings, see [15].

Simulations of both boundary condition cases are carried out using the CHILE model and compared to results from the viscoelastic model using different relaxation times. In each simulation, the spring-in angle of the L-profile is measured and the final maximum normal stresses in the laminate, for each boundary condition case, is compared. The spring in is defined as illustrated in Fig. 21.

Results from the free boundary condition case are given in Tab. 3. Starting with the tip displacement and spring-in for both models (CHILE and VE), no significant differences in results exist. This is expected because the L-profile is free to move during the entire process. Hence no mechanical constraints are generated which are large enough to trigger stress relaxation or creep type

Free	CHILE	VE τ=1[s]	VE τ=10[s]	VE τ=100[s]	VE τ=100[s]
Tip displacement [mm]	3.950	3.985	3.984	3.982	3.984
Spring-in angle [°]	1.375	1.387	1.387	1.386	1.387
Final σ_{11} [MPa]					
Min:	-3.633	-1.099	-1.172	-1.609	-1.693
Max:	+3.139	+0.921	+0.900	+1.055	+1.442
Final σ_{22} [MPa]					
Min:	-2.833	-2.155	-2.358	-3.391	-3.284
Max:	+4.079	+1.927	+2.115	+3.145	+4.042
Final σ_{33} [MPa]					
Min:	-2.444	-3.009	-3.022	-2.984	-2.809
Max:	+1.975	+2.250	+2.319	+2.628	+3.341
τ/dt ratio	-	1	1	10	100 (dt= 1[s])

Tab. 3: *Tip displacement and spring-in angle for L-profile modelled using Fully Free boundary condition. Final normal stresses are also shown. Note that the experimentally measured spring-in is equal 1.0°(±0.1°) from [15], resulting in a tip displacement of 2.87[mm]*

behaviour in the material as the process-induced strains momentarily result in shape distortions. However, taking a look at the final normal stresses given in Tab. 3 it is clear that smaller compressive and tensile stresses are predicted using the VE model with small relaxation times compared to the CHILE model. When a longer relaxation time is used, the viscoelastic model essentially approaches linear elastic behaviour, i.e. higher stresses are predicted because minimal relaxation or creep occurs. In the CHILE model, an internal state variable erases any residual stresses present in the model whenever the cure temperature exceeds the glass transition temperature T_g. In other words, whenever we switch from a glassy to rubbery state, we reset the stress history of the model. More on this is found in [15]. Hence the VE model results in higher stresses (compressive and tensile) when using longer relaxation times as compared to the CHILE model.

Results from the fully fixed boundary condition case are given in Tab. 4. In the table it is seen how the fully fixed CHILE model has a smaller spring-in angle (=0.65°) as compared to in the fully free case (=1.375°). This is a result of frozen-in stresses which are not released when the mechanical constraints are released, as is well described in [15] and [8]. This is also understated by the higher normal stresses found in the fixed case after demoulding. Similarly, the normal stresses predicted by the viscoelastic model for the fixed case starts out high upon demoulding and is gradually released as a result of creep-like behaviour. This is seen in the table where the simulations with long relaxation times result in higher final stresses as compared to with the shorter relaxation times.

To accompany the results for the free and fixed simulations given in Tab. 3 and Tab. 4, graphs showing the tip displacements of the different models during the entire simulation are depicted in Fig. 23. It is seen how creep behaviour is exhibited by the viscoelastic results for the fully fixed case after demoulding at 10000[s].

In this modelling example, it has been shown that by modelling two some what extreme cases of mechanical boundary conditions (free and fixed), it is possible to predict shape distortions on either side of what has been experimentally measured.

Fixed	CHILE	VE τ=1[s]	VE τ=10[s]	VE τ=100[s]	VE τ=100[s]
Tip displacement [mm] 5000[s] after demoulding:	1.870	3.430	3.208	2.580	2.460
Spring-in angle [°] 5000[s] after demoulding:	0.650	1.191	1.114	0.895	0.854
Final σ_{11} [MPa]					
Min:	-15.400	-5.129	-6.501	-18.780	-17.930
Max:	+21.720	+5.473	+6.480	+12.840	+12.090
Final σ_{22} [MPa]					
Min:	-80.290	-14.460	-15.370	-37.650	-37.130
Max:	+190.20	+40.920	+41.080	+44.140	+40.530
Final σ_{33} [MPa]					
Min:	-85.580	-15.450	-14.130	-46.140	-46.240
Max:	+112.0	+22.830	+20.920	+48.540	+48.320
τ/dt ratio	-	1	1	10	100 (dt= 1[s])

Tab. 4: *Tip displacement and spring-in angle for L-profile modelled using Fixed boundary condition.*

6.1 Summary

In this section the viscoelastic model has been compared to a Cure Hardening Instantaneous Linear Elastic (CHILE) model. An L-profile laminate is modelled and the spring-in angle and predicted normal stresses compared. Different relaxation times are compared in order to see whether the viscoelastic effects are exhibited as expected, with good results.

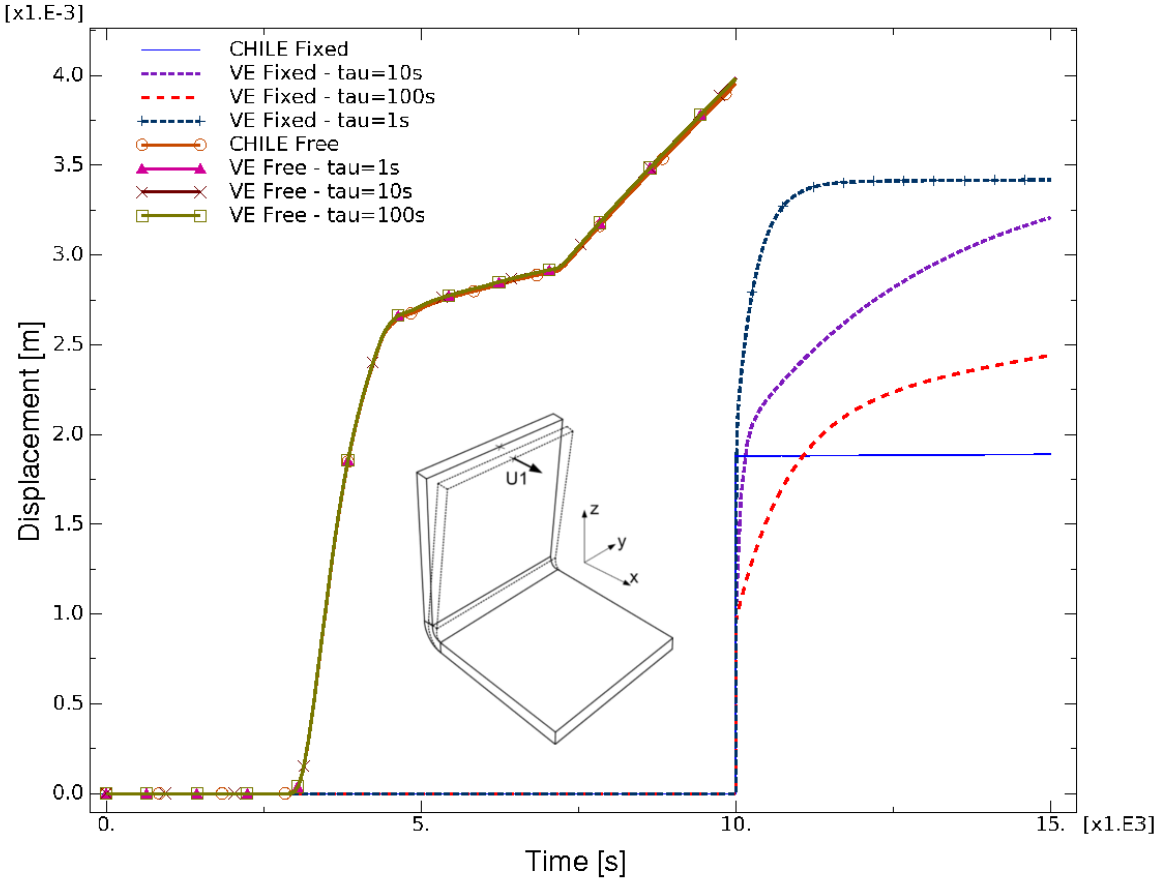

Fig. 23: *Plot of the tip displacements using the CHILE model and Viscoelastic (VE) model with different relaxation times (tau) for free and fixed mechanical BC*

References

[1] X.A Aduriz et al. Quantitative control of rtm6 epoxy resin polymerisation by optical index determination. *Composites Science and Technology*, Volume:67:p.3196–3201, 2007.

[2] F. W. Jr. Billmeryer. *Textbook of Polymer Science*. John Wiley and Sons Inc. NY, 2nd edition, 1971.

[3] T.A Bogetti and J.W Gillespie. Process-induced stress and deformation in thick-section thermosetting composites laminates. *21st SAMPE Technical Conference, September*, 1989.

[4] H.F. Brinson and L.C. Brinson. *Polymer Engineering Science and Viscoelasticity*. Springer Science, 2008. ISBN: 978-0-387-73860-4.

[5] Q. Dai. Two- and three-dimensional micromechanical viscoelastic finite element modelling of stone-based materials with x-ray computed tomography images. *Construction and Building Materials*, 25:1102–1114, 2010.

[6] Q. Dai et. al. A micromechanical finite element model for linear and damage-coupled viscoelastic behaviour of asphalt mixture. *Int. Journal for Numerical and Analytical Methods in Geomechanics*, 30:1135–1158, 2006.

[7] J. K. Gillham. Formation and properties of thermosetting and high tg polymeric materials. *Polymer Engineering and Science*, Volume:26:p.1429–1433, 1986.

[8] J.A. Holmberg. Influence of chemical shrinkage on shape distortion of rtm composites. *19th Int. SAMPE European Conference of the Society for the Advancement of Material and Process Engineering, Paris*, 30:13–34, 1998.

[9] Ferry J.D. *Viscoelastic Properties of Polymers*. John Wiley & Sons, Inc., 2nd edition, 1961.

[10] Y.K. Kim and S.R. White. Stress relaxation behavior of 3501-6 epoxy resin during cure. *Polymer Engineering and Science*, Volume:36(23):p.2852–2862, 1996.

[11] P Prasatya et al. A viscoelastic model for predicting isotropic residual stresses in thermosetting materials: Effects of processing parameters. *Journal of Composite Materials*, 35:826–848, 2001.

[12] E. Ruiz and F. Trochu. Thermomechanical properties during cure of glass-polyester rtm composites: Elastic and viscoelastic modeling. *Journal of Composite Materials*, 39:881–915, 2005.

[13] S.L. Simon, et. al. Modeling the evolution of the dynamic mechanical properties of a commercial epoxy during cure after gelation. *Journal of Applied Polymer Science*, 76:495–508, 1999.

[14] J.M Svanberg. *Predictions of manufacturing induced shape distortions - high performance thermoset composites*. PhD Thesis, Luleå University of Technology, 2002.

[15] J.M Svanberg and J.A. Holmberg. Predictions of shape distortions part i. fe-implementation of a path dependent constitutive model. *Composites Part A: Applied science and manufacturing*, 35:771–721, 2004.

[16] Montgomery T.S. and MacKnight W.J. *Introduction to Polymer Viscoelasticity*. Wiley-Interscience, 3rd edition, 2005. ISBN: 0-471-74045-4.

[17] S.R. White and Y.K Kim. Process-induced residual stress analysis of as4/3501-6 composite material. *Mechanics of Composite Materials and Structures*, 5:153–186, 1998.

[18] J.M. Whitney and R.L. McCullough. *Micromechanical Material Modelling, Delaware Composites Design Encyclopedia - Vol2*. Technomic Pub. Co. Inc., 2nd edition, 1990.

[19] D. Zenkert and M. Battley. *Foundations of Fibre Composites*. Technical University of Denmark, 2nd edition, 2009.

[20] N. Zobeiry et.al. Computationally efficient pseudo-viscoelastic models for evaluation of residual stresses in thermoset polymer composites during cure. *Composites: Part A*, 41:247–256, 2010.

[21] N. Zoberiy. *Viscoelastic Constitutive Models for Evaluation of Residual Stresses in Thermoset Composites During Cure*. PhD. Thesis, University of British Colombia, 1st edition, 2006.

[22] M.A. Zocher. *A Thermoviscoelastic Finite Element Formulation for the Analysis of Composites*. PhD. Thesis. Texas A&M University, 1995.

[23] M.A. Zocher et.al. A three-dimensional finite element formulation for thermoviscoelastic orthotropic media. *Int. Journal for Numerical Methods in Engineering*, 40:2267–2288, 1997.